

# APPLICATION OF SEMI-CLASSICAL METHODS TO DEFORMED AND SUPERDEFORMED NUCLEAR SYSTEMS

**A THESIS**

*Submitted in fulfilment of the  
requirements for the award of the degree*

*of*

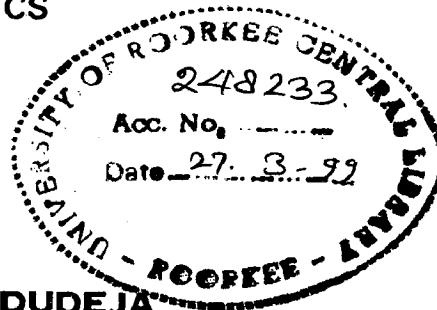
**DOCTOR OF PHILOSOPHY**

*in*

**PHYSICS**

By

**MANISHA DUDEJA**



DEPARTMENT OF PHYSICS  
UNIVERSITY OF ROORKEE  
ROORKEE-247 667 (INDIA)

JULY, 1998

## CANDIDATE'S DECLARATION

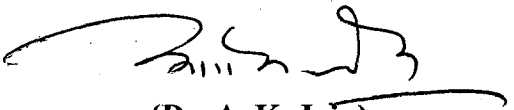
I hereby certify that the work which is being presented in the thesis entitled "*APPLICATION OF SEMI-CLASSICAL METHODS TO DEFORMED AND SUPERDEFORMED NUCLEAR SYSTEMS*" in fulfilment of the requirement for the award of the Degree of *Doctor of Philosophy* and submitted in the *Department of Physics* of the *University of Roorkee* is an authentic record of my own work carried out during a period from *January 1995 to July 1998* under the supervision of *Dr. A. K. Jain*.

The matter presented in this thesis has not been submitted by me for the award of any other degree of this or any other University.

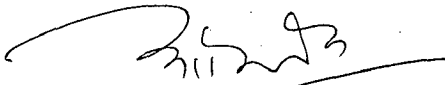
  
(MANISHA DUDEJA)


This is to certify that the above statement made by the candidate is correct to the best of my knowledge.

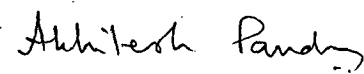
Date: 25-07-1998

  
(Dr. A. K. Jain)  
Department of Physics,  
University of Roorkee,  
Roorkee- 247 667.

The Ph.D. Viva-Voce examination of **Manisha Dudeja**, Research Scholar, has been held on 18 November 1998.

  
Signature of Supervisor

  
Signature of H.O.D.  
18.11.98

  
Signature of External Examiner

## ACKNOWLEDGEMENTS

After the preparation of this thesis, as I look back, all those people come to my mind who stood by me during the last four years and helped me contribute my bit to the world of science through my Ph.D.

At the very onset I express my deep sense of overwhelming gratitude and immense respect to my mentor and reverend teacher Dr. A. K. Jain who not only guided me but also trusted me to dabble with nuclear physics to achieve the goals I desired. The long hours of fruitful discussions, his incisive criticism, pertinent suggestions not only strengthened my skills in research methodology but also helped me a more confident personality. Right from the very beginning I have admired him for his wonderful oratory.

My heart is full of praise for Mrs. Neerja Jain who in affectionate manner boosted my morale and also fed me numerous hearty meals during these years. Her charming behaviour will last long in my memory. Also I would like to thank Kanee and Kitoo for giving me a homely atmosphere whenever I visited them and thus making my stay at Roorkee enjoyable.

I am indebted to Dr. K. C. Mathur (Former Head) and Dr. A. N. Tripathi, Head, Department of Physics, University of Roorkee for providing me the infrastructural facilities to carry out the research work.

I am extremely grateful and highly obliged to Dr. S. S. Malik, G.N.D.U. for collaborating with us and providing most sincere help whenever I needed and making this dream a reality. Also I express gratitude to Dr. S. R. Jain and Zafar Ahmed with whom we shared telephonic discussions about the research work during this course of study.

I would like to thank my friend Amita for rendering her help when needed specially in the last stages of my thesis and also by giving me numerous rides on her scooter.

Words are inadequate to express my heartfelt feelings for Hina with whom I share a

special bond of friendship and her encouraging and affable attitude will always remain a pleasant part of my memory.

It is difficult to forget the great time I spent with my friends in the Department during these years. I acknowledge Drs. Amit Rai, Kamlesh, Mithlesh and budding doctors Menakshi, Sangita, Seema, Nidhi, Vaishali, Piyush, Manoj, Yogendra, Satish and Adarsh.

I am not the only one who thinks that parents are beyond comparison in the whole world. My parents have been the strongest influence in my life, always being there as guiding stars whenever I lost direction. Thanks to my ma and papa for the wonderful gift of a fresh and untainted canvas of life and the freedom and encouragement to paint it as I liked. I am in derth of proper words to express my abounding feelings for my sister, a bundle of joy, Gifty for her support and love she showered on me at every stage.

Countless images flash through my mind when I remember the phase of time I had been through and here my husband Sanjay deserves a special mention who made the most conspicuous contribution in making this ambition a reality. This thesis belongs to him as much as it does to me. I have no words to put forth my tender feelings to another set of my parents, ever encouraging father-in-law and mother-in-law, Pankaj bhaiaa and Anju.

It would be unjustified if I fail to thank Sandeep and Raju of N.C.F. for patiently transferring my long data files from one system to the other.

I also gratefully acknowledge the financial assistance by U.G.C. (INDIA) to carry out the research work.

Also I would like to thank Sandeep, Prop. Mouze Computers, and Tarun for meticulously typing the thesis and Shri Kishan Lal for the excellent xeroxing.

  
MANISHA DUDEJA

## RESEARCH PUBLICATIONS

### A. Papers in Journals

1. **Some New Universal Features of Superdeformed Bands**  
A. K. Jain and M. Dudeja  
J. of Korean Phys. Soc. 23, S361 (1996).
2. **Nonlinear Dynamics of Particle-Rotor Model and Superdeformed Bands**  
A. K. Jain, M. Dudeja, S. S. Malik and Zafar Ahmed  
Phys. Lett. B392, 243 (1997).
3. **An Empirical Analysis of Superdeformed Bands: A Semiclassical View**  
M. Dudeja, S. S. Malik and A. K. Jain  
Phys. Lett. B412, 14 (1997).

### B. Papers in Conferences/Symposia

1. **First Evidence of a Nonlinear Effect in Nuclear Spectra**  
M. Dudeja, A. K. Jain, Zafar Ahmed and S. S. Malik  
Proc. of DAE symposium on Nuclear Physics 39B, 6 (1996).
2. **Superdeformed Bands as the Rigid Rotor Bands**  
A. K. Jain, M. Dudeja, S. R. Jain, Zafar Ahmed and S. S. Malik  
Proc. of DAE symposium on Nuclear Physics 39B, 74 (1996).
3. **Semiclassical Quantisation of Cranking Model and SD Bands**  
M. Dudeja  
Talk presented at IV National Workshop on Nuclear structure physics, Puri (1997).

# ABSTRACT

The present thesis aims at bringing the latest discoveries in nuclear physics and the new developments in semiclassical physics closer together. The low energy domain of nuclear physics has been replete with exciting observations of superdeformed (SD) bands in a number of pockets of the chart of nuclides beginning with the first discovery of a discrete high spin SD band in  $^{152}\text{Dy}$  in 1986 [1]. Since then a large number of SD bands have been seen in  $A=80, 130, 150, 190$  mass regions [2]. On the experimental side, the observation of these weakly populated and very low intensity structures represents a triumph of the modern detector arrays and data analysis capabilities of modern computing systems. It has also led to the emergence of what we may term as ultra-weak spectroscopy.

Theoretically, one expected the observation of these structures on the basis of potential energy surface calculations based on Strutinsky method which lays emphasis on the role of shell structure near the Fermi energy in stabilising specific configurations at specific shapes [3-5]. A detailed compilation of these results as applicable to SD shapes may be found in the reference [6]. Experimental discovery of SD bands thus also implies a growing confidence in the predictive capabilities of the present theoretical methods in nuclear physics.

Large deformations and high angular momenta, which are intertwined themes, have now become commonplace in nuclear physics [7]. Superdeformed structures like fission isomers were already known in 1970 [8]. There is however an important difference between SD structures and fission isomers; while the former are essentially observed at high spins, the fission isomers are observed at low spins. Moreover the SD bands display characteristics which make these structures look very simple yet very hard to understand.

Physics over the past decades, has also been witness to a resurgence in the study of non-linear features and application of semiclassical methods to quantal systems. Semiclassical techniques, first ushered in by Bohr, Sommerfeld, Einstein etc. were abandoned after the advent of quantum theory [9,10]. These have now been found to be of immense help and use in unraveling the nature of truth underlying the various phenomena exhibited by com-

plex quantum and semi-quantum (mesoscopic) systems. The study of chaotic dynamics in hamiltonian systems has become a growing discipline during the recent years. These studies are now being carried out in nuclei also with an emphasis on order-to-chaos transition in the classical dynamics of a particle in various shapes of cavities [11,12]. While earlier studies of chaos in nuclei have concentrated on statistical approaches [13], semiclassical methods have now begun to play a very important role. Developments like the periodic orbit theory [9] have brought to fore the deep connection between classical motion and quantal shell structure. Effects like superdeformation at high spin are directly linked to quantal fluctuations which tend to stabilise shapes having axes ratio 2 : 1,3 : 1, etc. The fact that these are very feeble and weak structures suggests that small nonlinear terms have a role to play in stabilising these structures with specific configurations.

Taking a lead from the classical analysis of the nuclear models [14] and combining several ideas from the theory of dynamical systems, we present in this thesis a complete dynamical scenario of the two most used models of nuclear rotation: the cranking model [15] and the particle-rotor model [16]. We also highlight the most important features of the SD bands and establish their systematics. We then proceed to show that most of these features can be understood very well from the semiclassical analysis and thus establish the role of nonlinearity in stabilising the SD structures.

Shell structure is a recurrent theme of molecular, atomic and nuclear systems. The quantal nature of a system naturally leads us to shell structure. It basically represents the grouping of levels at certain number of neutrons and protons at zero or, non-zero deformations. A quantitative way of dealing with shell structure was provided by Strutinsky [4] and forms the basis of the present day understanding of the stability of nuclei. In recent times, a new semiclassical approach has emerged in the form of Gutzwiller's periodic orbit theory (POT) [9] which relates the single particle level density of a quantum system to the classical periodic orbits. Use of periodic orbit theory to understand the properties of deformed and superdeformed systems is another major theme of this thesis. An introduction to the superdeformation and related topics is presented in Chapter I.

In chapter II, we present a complete discussion of the nonlinear dynamics of the particle-rotor model [16]. Special attention is given to the semiclassical quantization of small amplitude oscillations around the twin excited fixed points  $c_{\pm}$ , which naturally yields rotational bands whose various features such as alignment, starting angular momentum and oscillations in gamma ray energies are discussed. These twin fixed points are located in a region of nonlinearity and can be identified with the two minima in the double well potential (DWP) of  $j_3$ . The DWP, being energy dependent, gives rise to unusual features including a  $\Delta I=2$  staggering.

A close correspondence of these results with the properties of the SD bands is established in chapter III, where we establish some additional new features of SD bands from an analysis of the experimental data [17]. In particular, we show that the SD bands have almost reached the rigid rotor value of the moment of inertia [17]. Also, we highlight the negative alignment of SD bands and its saturation at a finite positive value at higher angular momenta which in turn is responsible for a saturation in the dynamic moment of inertia. The fact that SD bands begin with a finite starting angular momentum is presented as an important feature of the SD bands and its systematics are explained. An understanding of the  $\Delta I=2$  staggering is also provided [18]. A new feature of General Identical Band is also presented [19].

In chapter IV, we present a complete discussion of the dynamics of cranking model and its semiclassical quantisation is carried out [15,20]. Numerical results based on this model are presented. These results confirm the results of particle-rotor model. These studies together tend to present a view of the SD bands as structures stabilised in a sea of chaos and hence not so well connected to the normal deformed states.

We present the current general interpretation of shell structure in nuclei in chapter V. At this stage we introduce the periodic orbit theory and other necessary tools to understand the link between the shell structure and periodic orbits. We also present, as examples, simple applications of the POT to integrable systems like harmonic oscillator and spherical billiard. An expression for the level density of spherical billiards is derived and results presented [21].

We extend the POT in chapter VI to deformed systems. In particular an analysis of the



classical closed orbits in an infinitely deep ellipsoidal well is considered and its relevance to the gross-shell structure of single particle spectra in deformed nuclei established [22]. We present detailed and exact results for the planar and the 3-dimensional periodic orbits and study their consequences for the deformed and superdeformed nuclei [23]. The conclusions of the thesis are contained in chapter VII.

## REFERENCES

- [1] P.J. Twin et al., Phys. Rev. Lett. 57 (1986) 811.
- [2] B. Singh, R.B. Firestone and S.Y. Frank Chu, Nucl. Data Sheets 78 (1996) 1.
- [3] V.M. Strutinsky, Nucl.Phys. A95 (1967) 420; Nucl.Phys. A254 (1975) 197.
- [4] M. Brack et al., Rev. Mod. Phys. 44 (1972) 320.
- [5] I. Ragnarsson, S.G. Nilsson and R.K. Sheline, Physics Reports 45 (1978) 1.
- [6] T.R. Werner and J. Dudek, At. and Nucl. Data Tables 50 (1992) 179;  
ibid., 59 (1995) 1.
- [7] Z. Szymanski, Fast Nuclear Rotation, Oxford Studies In Physics (Clarendon Press, Oxford, 1983).
- [8] S. Bjorholm and J.E. Lynn, Rev.Mod.Phys. 52 (1980) 725.
- [9] M.G. Gutzwiller, Chaos In Classical And Quantum Mechanics, Springer Verlag, Berlin 1991.
- [10] M. Brack and R. K. Bhaduri, Semiclassical Physics, (Addison-Wesley, 1997).
- [11] J. Blocki, J. J. Shi and W. J. Swiatecki, Nucl.Phys. A554 (1993) 387.
- [12] T. Mukhopadhyay and Santanu Pal, Nucl.Phys. A592 (1995) 291.
- [13] J. B. French, V. K. B. Kota, Akhilesh Pandey and S. Tomsovic, Phys.Rev.Lett. 54 (1985) 2313; Phys.Rev.Lett. 58 (1987) 2400.
- [14] A. Bohr and B.R. Mottelson, Phys.Scr. 22 (1980) 461.
- [15] S.R. Jain, A.K. Jain and Z. Ahmad, Phys. Lett. B370 (1996) 1.
- [16] A.K. Jain, M. Dudeja, S.S. Malik and Z. Ahmad, Phys.Lett. B392 (1997) 243.
- [17] M. Dudeja, S.S. Malik and A.K. Jain, Phys. Lett. B412 (1997) 14.

- [18] M. Dudeja, A.K. Jain, S.S. Malik and Z. Ahmed, submitted for publication.
- [19] M. Dudeja and A.K. Jain, under preparation.
- [20] M. Dudeja, A.K. Jain, S.S. Malik, S.R. Jain and Z. Ahmed, under preparation.
- [21] S.S. Malik, M. Dudeja and A.K. Jain, to be published.
- [22] V.M. Strutinsky, A. G. Magner, S.R. Ofengenden and T. Dossing, Z. Phys. A283 (1977)  
269.
- [23] S.S. Malik, M. Dudeja and A.K. Jain, under preparation.

# CONTENTS

## CHAPTER I

### INTRODUCTION

I	Introduction to superdeformation	2
II	Experimental Information	3
III	Unusual Features Of The SD Bands	3
	A An Unusual Population and Depopulation Pattern . . . . .	4
	B Spin and Excitation Energy of SD Bands . . . . .	5
	C Unusual Behaviour of the Moment of Inertia . . . . .	6
	D $\Delta I = 2$ Staggering . . . . .	7
	E Unusually Long Chain Of Levels In SD Bands . . . . .	8
	F Phenomenon Of Identical Bands . . . . .	8
	G IB Phenomenon In Normal Deformed Nuclei . . . . .	10
IV	Shell Structure	10
V	Periodic Orbit Theory	11
VI	Present Work	13

## CHAPTER II

### PARTICLE ROTOR MODEL AND ITS SEMI-CLASSICAL QUANTISATION

I	Introduction	17
II	The Dynamics of the Particle-Rotor Model	18
	A General Structure of the Orbits . . . . .	19

III	Fictitious Hamiltonian for $j_3$	22
IV	Small Amplitude Oscillations	23
	A Double well in $j_3$ and second order Phase transition . . . . .	27
V	Aligned Angular Momentum	28
VI	Results and Discussion	30

CHAPTER III

SOME NEW UNIVERSAL FEATURES OF SD BANDS AND  
EMPIRICAL ANALYSIS OF SD BAND DATA

I	INTRODUCTION	35
II	New Empirical features of SD bands	36
	A Weak oscillations in the I vs. $E_\gamma$ plots . . . . .	36
	B Negative intercept of the I vs. $E_\gamma$ plots . . . . .	36
	C Finite angular momentum of the SD bandheads . . . . .	37
	D $\Delta I = 2$ Staggering . . . . .	38
III	An Empirical Analysis of SD bands	39
IV	Starting Angular Momentum for the Bandhead	42
V	$\Delta I=2$ staggering	44
VI	Identical Band Feature	46
	A A=190 Mass region . . . . .	50
	B A=130, 140 and 150 mass regions . . . . .	51
VII	Conclusions	51

## CHAPTER IV

### CRANKING MODEL AND ITS SEMI-CLASSICAL QUANTISATION

I	Introduction	65
II	Model Hamiltonian	65
	A Equations of motion and fixed point structure . . . . .	66
	B Fictitious Hamiltonian . . . . .	67
III	Small Amplitude Oscillations	68
	A Fixed point $a$ . . . . .	68
	B Fixed points $c_{\pm}$ . . . . .	69
IV	Aligned Angular Momentum	71
V	Numerical results and discussion	72

## CHAPTER V

### PERIODIC ORBIT THEORY AND SPHERICAL CAVITY

I	Introduction	75
II	Conditions for Shell Structure : Isotropic harmonic oscillator	76
III	Some Basic Tools For Semiclassical Periodic Orbit Theory	78
	A Level Density . . . . .	79
	B Separation Of $g(E)$ Into Smooth and Oscillatory Part . . . . .	79
	C Solvable Case of Harmonic Oscillator . . . . .	80
IV	Periodic Orbit Theory	82
	A Convergence of the Periodic Orbit Sum . . . . .	83

B	Maslov Indices . . . . .	84
C	Smooth Part of the Level Density . . . . .	86
V	Spherical Cavity	86
A	Quantum Mechanical Results . . . . .	87
B	Results Using POT . . . . .	88
1	Spherical Billiard in Spherical Polar coordinates . . . . .	89
VI	Results and Discussion	92

## CHAPTER VI

### PERIODIC ORBIT THEORY OF SPHEROIDAL CAVITY

I	Introduction	95
II	Periodic Orbits in a Spheroidal Cavity	96
III	Partial Frequencies and Periodicity Conditions	100
A	Three-Dimensional Orbits . . . . .	102
B	Frequency Of Rotation . . . . .	103
C	Planar Orbits . . . . .	104
IV	Relationship Of Planar Orbits With The Gross-Shell Structure	104
V	Trace Formula For Spheroidal Cavity	107
VI	Numerical Results And Discussion	112

## CHAPTER VII

Conclusions	117
References	124

# CHAPTER I

## INTRODUCTION



## I. INTRODUCTION TO SUPERDEFORMATION

Nuclei possessing very large deformations have been known for many years in light nuclei in terms of excited  $\alpha$ -cluster configurations, and in some actinide nuclei in terms of the so called fission isomeric states. However, these “Superdeformed” shapes could be studied only in the ground state region; for example the highest spin observed among the fission isomers is  $8\hbar$ . An important step forward in the research was taken by the observation of superdeformed high-spin states [110] first in  $^{152}\text{Dy}$  and later on in many neighbouring nuclei as well as in nuclei around  $^{192}\text{Hg}$ . Rotational bands containing up to 18 or 19 discrete superdeformed transitions could be identified ranging up to spin  $I \approx 66\hbar$ . By these observations a new and exciting field in nuclear spectroscopy has opened up allowing for detailed studies of 2:1 shapes where the pairing interaction often plays a minor role.

The experimental discovery of superdeformed high spin states was preceded by their prediction a decade earlier [9]. In fact, the underlying mechanism, namely clustering of single-particle states (particularly at the symmetric 2:1 deformation), that gives rise to a negative shell energy for specific particle numbers, is the same as for the earlier observed fission isomers [12,84]. Although the occurrence and stability of SD regions (static properties) are well reproduced by the standard model calculations [9,28,97], it is the dynamical properties that elude a complete explanation.

For the past decade, the study of superdeformed states has dominated experimental nuclear structure studies at high spin. A recent compilation [99] lists about 170 yrast and excited superdeformed bands in about 60 nuclei spread over the four mass regions with  $A=80, 130-140, 150$  and  $190$ . The list continues to expand as more data are added, for example the recently added  $^{156}\text{Dy}$  nucleus. Another recent addition is the observation of SD states in  $^{62}\text{Zn}$  [108], which corresponds to a new region of superdeformation for nuclei with neutron and proton numbers  $N, Z \approx 30-32$ . This region was predicted long ago by Sheline et al. [98].

The spectroscopic properties of the different bands in different nuclei can generally be

understood from the occupation of the highest spin orbitals ( $N = 6$ , and  $N = 7$  protons and neutrons in the case of the  $A \approx 150$  region). The  $A=130-140$  region corresponds to a 3 : 2 axis ratio, and the positions of the single particle orbitals (especially  $N = 6$  neutrons) play an important role in determining the particle numbers corresponding to shell gaps. The  $A=190$  mass region also arises for similar reasons [86].

## II. EXPERIMENTAL INFORMATION

The importance of adequate detection techniques becomes clear if one analyses the FIG. 1.1 [39]. A typical heavy ion projectile vs. target collision leads to fusion giving a compound nucleus having high excitation energy and large angular momentum. The characteristic phases of its rotation responding at the various stages of the de-excitation process are shown in FIG. 1.1. The process of particle emission is the fastest. During a characteristic time of  $\tau \approx 10^{-19}$ sec. a number of particles, like neutrons, protons or  $\alpha$ -particles are emitted, thus lowering the total excitation energy of the compound system. The electromagnetic radiation follows the particle emission with its characteristic gamma decay time of  $\tau \approx 10^{-17}$  to  $10^{-12}$ sec. Thus the main task of an experimentalist is to determine the process of de-excitation by measuring the energies, and angular correlations between the successive gamma rays. A typical heavy ion reaction used to populate the superdeformed bands in  $^{192}\text{Hg}$  can be given as  $^{160}\text{Gd}(^{36}\text{S}, 4n)^{192}\text{Hg}$  using  $^{36}\text{S}$  [78] beam energy  $\approx 159$  MeV. Future of this domain of research lies in the exploitation of the  $4\pi$  multidetector systems with high energy resolution like Eurogam and Gammasphere and the systems to follow.

## III. UNUSUAL FEATURES OF THE SD BANDS

The SD bands present several puzzles; most of these puzzles emanate from the very simple behaviour of the SD bands which defy a complete and consistent understanding [62]. Mostly two types of data have been gathered about the SD bands; one the quadrupole

transition energies of  $\gamma$  ray cascades and two, the intensity of the  $\gamma$  rays. The data have been used to arrive at a number of unusual features which we discuss briefly.

### A. An Unusual Population and Depopulation Pattern

A schematic representation of the formation and decay of the yrast SD band is shown in FIG. 1.2. The SD bands are fed from the top in HI-fusion cum evaporation reactions of the kind described above and merely 1-2 percent of the nuclei formed correspond to the SD shape; naturally the transitions of SD bands are very weak.

The population and feeding pattern of nearly all the SD bands are similar and this makes it very interesting. It has been observed that after the population at high spins, the intensity builds up slowly and attains a constant value; it then stays constant. For example, the SD yrast band in  $^{150}\text{Tb}$  builds up intensity from 20 to 80 percent in a very narrow range of spin between  $60\hbar$  to  $48\hbar$  [34] as shown in FIG. 1.3. Also the population of SD bands is observed to be nearly unaffected by changes in excitation energy and the maximum input angular momenta. Such a feeding pattern indicates that there is no side-feeding to the SD bands as opposed to the normal deformed (ND) bands which experience considerable side-feeding.

In another result from Eurogam, Petrache et al. [91] populated the ND and SD bands in  $^{151}\text{Tb}$ . It was observed that the yrast SD band and the first excited SD band depopulate at  $I = 32.5\hbar$  and  $26.5\hbar$  respectively. Interestingly, the first excited SD band is observed to selectively populate only four positive parity ND states having spins between  $35/2$  and  $45/2$  (average spin  $\langle I \rangle = 20.5\hbar$ ). The yrast SD band, on the other hand, feeds yrast states of both positive and negative parity having spins between  $45/2$  and  $63/2$  (average spin  $\langle I \rangle = 27.5\hbar$ ). The decay-out spins of the first excited SD band and the yrast SD band are  $26.5\hbar$  and  $32.5\hbar$  respectively; the difference of  $6\hbar$  in the decay out spins is thus maintained in the average value of the entry spin of ND states.

As the angular momentum decreases, the SD bands undergo a sudden depopulation over the last two or three transitions. The sudden depopulation indicates that the strength of

the SD band has got fragmented over many weak transitions which have not been resolved. These observations paint a picture of the SD bands as isolated and hanging bands with no observations of any linking transitions between the SD bands and the ND states.

### B. Spin and Excitation Energy of SD Bands

Since no linking transitions have been observed in most of the cases, there is no direct information about the spin and the excitation energy of SD bands. It became necessary to use indirect methods to make the spin assignments. In one such method [36], use is made of the fact that the gamma-ray transitions are known to be of E2 type. The level energies for these bands may be written as

$$E(I) = \frac{\hbar^2}{2\mathfrak{I}}[I(I+1) - K^2] + E_0. \quad (1)$$

One may use the Harris expansion to write  $I^* = \sqrt{I(I+1)} = 2\alpha\omega + \frac{4}{3}\beta\omega^2 + \dots$ . Here  $\hbar\omega \approx \frac{\Delta E_\gamma}{2}$ . A series of such equations are generated, one for each level, with spin value increasing by 2 units with each  $\gamma$ -ray. A least squares fit to this set of equations is then performed to obtain  $I_b$ , the spin of the lowest level. In another method [92], the VMI model was used to fit the cascade of  $\gamma$ -ray energies and obtain the spin assignments. The spin assignments in the mass-150 region are more uncertain as the  $\gamma$ -ray sequences are known to end at higher energies and spins and the methods are not so sensitive to a change of  $I$  by  $\pm 1$ . The available spin assignments are therefore uncertain by at least  $1\hbar$  to  $2\hbar$ .

The estimates of the excitation energy are likewise uncertain. Theoretical calculations, for example, done by Bonche et al. [17] yield a SD minimum which is 4 to 5 MeV above the ground state minimum. Estimates from the experimental data also suggest that the SD minimum may lie anywhere between 4 MeV to 20 MeV. The recent observations from the France-UK collaboration [96] leads to an average excitation energy of decaying SD states above ND states of  $4.3 \pm 0.9$  MeV at the average spin value of  $10\hbar$  at the decay point in the  $^{192}\text{Hg}$  nucleus. It is therefore certain that the SD minimum lies nearly 5 MeV above the

ground state minimum. Considerable effort has gone into observing the linking transitions with some success in a few such cases. Recently, the spins, parity and excitation energy of excited SD bands in  $^{194}\text{Hg}$  have been measured by Khoo et al. [76] and Hackman et al. [51]. Linking  $\gamma$ -ray transitions, highly fragmented, having energies from 3 to 5 MeV have been observed placing the two SD bands in  $^{194}\text{Hg}$  at 6.4 MeV and 7.2 MeV of excitation energy.

### C. Unusual Behaviour of the Moment of Inertia

The SD bands display a very regular energy spectrum as opposed to the energy spectrum of ND bands which are marred by significant variation in the moment of inertia with angular momentum and other features such as the backbendings. A semi-classical expression for the rotational energy of an axially symmetric rotor is given by

$$E(I) = \frac{I^2}{2\mathfrak{I}} = \frac{\hbar^2}{2\mathfrak{I}} I(I+1), \quad (2)$$

where  $\mathfrak{I}$  is the moment of inertia about the rotation axis. Also, the rotational frequency  $\omega = \frac{dE}{dI}$ . It follows that the gamma-ray transition energies  $E_\gamma(I \rightarrow I-2) = \frac{\hbar^2}{2\mathfrak{I}} 2(2I-1)$  and the second difference of energies  $\Delta E_\gamma(I) = E_\gamma(I+2) - E_\gamma(I)$ . An ideal rigid rotor band will thus display a constant increment in the successively higher gamma-ray energies. The normal deformed bands however show a strong deviation from this rule; the pairing correlations, the Coriolis anti-pairing effect and the preferential breakdown of the high- $j$  nucleon pairs accompanied by alignment lead to a complex dependence of the moment of inertia on rotational frequency.

It is instructive to plot the angular momentum  $I$  vs. the rotational frequency  $\omega$  or  $E_\gamma(I \rightarrow I-2)$  as  $\omega \approx \frac{E_\gamma}{2}$ . We show the typical behaviour observed in the ND and the SD bands in FIG. 1.4. The SD bands display a nearly linear behaviour in most of the cases in comparison to the ND nuclei which display a rapidly changing slope and backbending features. An exactly linear behaviour would imply a constant moment of inertia. We find that the SD band observed in the doubly-odd  $^{150}\text{Tb}1$  and  $^{194}\text{Tl}2$  are closest to this kind of

behaviour (see FIG. 1.5 and 1.6). The SD band in  $^{150}\text{Tb}$  is probably unique in the sense that the change in moment of inertia for this band is within 1 percent from spin  $24\hbar$  to  $60\hbar$ ; it may easily be identified as the most rigid band seen so far with an average value of moment of inertia equal to  $76\hbar^2\text{MeV}^{-1}$ . The variations in the SD bands of  $^{194}\text{Tl}$  are likewise very small, and  $\mathfrak{S}$  remains between  $100\hbar^2\text{MeV}^{-1}$  and  $106\hbar^2\text{MeV}^{-1}$  over the whole range of spins from  $11\hbar$  to  $37\hbar$ . We find in general that the variation from a linear behaviour is very small; it is about 1 to 3 percent over a range of 10 units of angular momentum in the mass-190 region. On the other hand, the change may be as much as 3 to 5 times of the ground state value over the same range of angular momentum in ND bands.

It is customary in the literature to define a second moment of inertia or, the dynamical moment of inertia as

$$\mathfrak{S}^{(2)} \equiv \frac{dI}{d\omega} \equiv \left[ \frac{d^2E}{dI^2} \right]^{-1}. \quad (3)$$

It is easy to show that

$$\mathfrak{S}^{(2)} = \mathfrak{S}^{(1)} + \omega \frac{d\mathfrak{S}^{(1)}}{d\omega}. \quad (4)$$

If  $\mathfrak{S}^{(1)}$ , the kinematic moment of inertia, does not have any  $\omega$ -dependence,  $\mathfrak{S}^{(1)} = \mathfrak{S}^{(2)}$ . The dynamical moment of inertia may thus reflect the small changes in  $\mathfrak{S}^{(1)}$  with  $\omega$  which are not obvious in the  $\mathfrak{S}^{(1)}$  vs.  $\omega$  plots. The second difference in the gamma ray energies denoted by  $\Delta E_\gamma$ , when plotted as a function of either  $I$  or  $\omega$ , also reveals these fine changes.

#### D. $\Delta I = 2$ Staggering

The term  $\Delta I = 2$  staggering [52,88] implies a systematic displacement of a sequence of states having spins  $I, I + 4...$  etc. with respect to a complementary sequence of states with spins  $I + 2, I + 6, \dots$  etc. Such a systematic displacement appears as a regular staggering pattern in the  $\mathfrak{S}^{(2)}$  vs.  $\hbar\omega$  plots. Two examples which display this feature prominently are shown in FIG. 1.7; the example of  $^{149}\text{Gd}$  band 1 has been widely discussed in the literature

and the other example where the feature is quite prominent is band 1 of  $^{193}\text{Tl}$ . Other cases with this feature over a limited range of spin have also been observed. Most recent examples, where this feature has been observed, are  $^{148}\text{Gd}$  and  $^{143}\text{Eu}$  [55]; however in both the cases the feature is observed over a range of angular momentum limited from both the sides. We discuss this feature in Chapter III in some detail.

### E. Unusually Long Chain Of Levels In SD Bands

It is understood that the SD shapes become a possibility because the large moment of inertia helps in lowering the rotational energy. These bands are located in the second minimum formed at higher angular momenta; the second minimum is not more than 3-4 MeV deep. The SD bands consist of a chain of levels ranging from say,  $15\hbar$  to  $60\hbar$ ; the topmost level lies almost 15-20 MeV above the lowest level thus extending much beyond the second well (see FIG. 1.8). There is no example of such a long chain of levels in the fission isomers where the second minimum exists at the lowest angular momenta; the highest spin known in the fission isomeric SD bands is merely  $8\hbar$ . The density of normal states is very high at 15-20 MeV of excitation energy reached in the high-spin SD bands. It is therefore amazing that the SD states exist almost isolated from these normal states. Further, the lifetime measurements have confirmed that there is no change in shape as we go up the band with increasing angular momentum. In other words, the SD bands are quite rigid in nature.

### F. Phenomenon Of Identical Bands

The most widely discussed feature of the SD bands has been the phenomenon of identical bands (IB) [25,101]. A discussion of this phenomenon will also bring up interesting questions about the presence of pairing correlations in SD nuclei.

When we go from one nucleus having mass number  $A$  to another nucleus having mass number say  $(A+1)$ , we expect some changes in the rotational energies due to a variation

in the moment of inertia and also the spin values. Since the pairing correlations play an important role, the observed changes could in fact be much more. It has however been observed that the gamma-ray transition energies of two SD bands in neighbouring nuclei are identical over a very large range of angular momenta; the differences are much less than what one would normally expect on physical grounds. This observation of identical cascades of  $\gamma$ -transitions in two neighbouring nuclei is termed as the phenomenon of identical bands.

It is known that the variation of the moment of inertia in deformed nuclei is proportional to  $\propto (A^{\frac{5}{3}}\hbar^2) \text{ MeV}^{-1}$ . For an increase in A by one unit, the increment in  $\mathfrak{I}$  is given by  $\delta\mathfrak{I} \approx \frac{5}{3}(A^{\frac{2}{3}})\hbar^2 \text{ MeV}^{-1}$ . Therefore,

$$\frac{\delta\mathfrak{I}}{\mathfrak{I}} = \frac{5}{3A} \approx \frac{1}{90}, \quad A = 150; \quad (5)$$

A 1 percent relative change in  $\mathfrak{I}$  is expected. Let us now assume that the spin of the levels involved in the identical transition (see FIG. 1.9) differ by  $\delta I = I_{A+1} - I_A$ . The change in rotational frequency for the transition may be written as

$$\delta\omega \equiv \omega_{A+1}(I_{A+1}) - \omega_A(I_A) \quad \text{or,} \quad \frac{\delta\omega}{\omega} = -\frac{\delta\mathfrak{I}}{\mathfrak{I}} + \frac{\delta I}{I}. \quad (6)$$

If A corresponds to an even-even nucleus, then A+1 will be an odd-A nucleus. The angular momenta of the two will differ by at least 1/2; the difference could however also be 3/2 or, 5/2 etc. For  $I \approx 30$  and  $I = 1/2, 3/2$  or,  $5/2$  .....,  $\frac{\delta I}{I} = 1/60, 1/20$  or,  $1/12$ ..... etc. respectively. Thus the value of  $\frac{\delta\omega}{\omega} = 1/180$  or nearly 0.5 percent for  $\delta I = 1/2$ ; it acquires a value  $7/180$  or, nearly 3.5 percent for  $\delta I = 3/2$ . Since  $\omega \approx \frac{E_\gamma}{2}$ , we expect at least 1 percent change in gamma-ray energy in going from a nucleus with mass number A to a neighbouring nucleus A+1. The observed change is however much smaller than this because there is hardly a change of 3-5 keV over a range of 3000-5000 keV implying  $\frac{\delta\omega}{\omega} \approx 1$  per thousand. Note that we have completely ignored the additional changes that might occur due to pairing correlations.



## G. IB Phenomenon In Normal Deformed Nuclei

Is this feature unique to SD bands? Probably not. Similar features were noted by Jain in 1984 [60,71] in the normal deformed nuclei of the rare-earth region and also the actinide region [66] where the identical nature of the transition energies of an even-even and its neighbouring odd-A nucleus was specifically pointed out. Similarly, a striking similarity between the energies of rotational bands of pairs of even-even nuclei with  $A=164\pm a$  was observed again for the first time by Jain and collaborators [64,65,100]. A comprehensive review of this topic may be found in Baktash et al. [5]. It is thus clear that such features are not uncommon; however, these are much more prominent in the SD bands.

Questions may also be asked about the presence of pairing correlations in the SD nuclei. It appears that the pairing may not have completely vanished in the SD bands. It is well known that the observed moment of inertia in ND nuclei is less than one-third of the rigid body value due to the presence of pairing correlations. As the angular momentum increases, the Coriolis antipairing effect leads to a large rise in the moment of inertia by a factor of 2 to 3. On the other hand, the change in the moment of inertia of mass-190 SD bands is as little as 1 to 5 percent over a range of 10 to  $20\hbar$  of angular momentum. As we shall show in this thesis, the SD bands may already have reached the rigid rotor value.

## IV. SHELL STRUCTURE

In simple terms, the shell structure means a bunchiness in the levels of a system. It is a general property of quantal systems present in diverse fields of nature, be it an atom, molecule or nucleus. This shell structure has two characteristics, one, the groupings of levels and the second is the extra stability of the system at the complete filling of the shells. Example of shell structure in atoms is the extra stability, high ionisation potential, lack of reactivity of noble gases at particular electron numbers.

A similar stability, first noticed by Mayer [82,56] exists for spherical nuclei with magic

numbers of 2, 8, 20, 28, 50, 82 and 126 (114) neutrons or protons. A large number of phenomena exhibit this special stability at these magic numbers such as stability to radioactive decay, abundance of isotopes, delayed neutron emission by these nuclei. Peaks in the binding energy also show this feature.

In the framework of single-particle models, the distribution of energy levels is usually defined in terms of shells, subshells etc. Shells can be defined as a large-scale nonuniformity in the energy distribution of the individual particle states [22].

Most nuclei are now known to be nonspherical in shape. In order to describe the effect of deformation, Nilsson [85] developed a deformed shell model, which is basically an extension of the shell model to deformed potentials. In this model an axially deformed harmonic oscillator potential was introduced and a spin-orbit term, and a term proportional to  $\ell^2$  which simulates the flat bottom and a steeper surface, were added to reproduce realistic magic numbers. In the early stages, only one deformation parameter  $\epsilon$  was used in this model. In this model also, shell structure was evident. The aspect of quantal shell effects and their relation with nuclear deformations was emphasized by Strutinsky with the introduction of his shell correction method [22,105]. A detailed description and understanding of this method may be found in Brack et al. [22]. An understanding of the shell structure and hence the spherical or deformed shapes at various nucleon numbers, plays an important role in explaining the superdeformed shapes. In the present thesis, we shall try to understand the origin of shell structure by using the powerful semiclassical technique of periodic orbit theory.

## V. PERIODIC ORBIT THEORY

It is well known that periodic orbits play an important part in going from classical mechanics to quantum mechanics. Classical action of the orbit is a major input in this theory [20]. In the beginning of quantum mechanics, this theory failed when it encountered nonintegrable system. This old quantum theory is related to the present day quantum

mechanics through the quantisation of the classical action over a periodic orbit. An early example of this is Bohr's model of atom in which the orbits with certain integral units of classical action are said to be quantized and labelled by some quantum numbers. For one dimensional systems the quantity  $\int p_x dx$  can be understood in terms of action  $S$  or the area of a closed path in the two dimensional phase space, whose two axes are represented by the position coordinate and the corresponding canonical momentum. As an example, we consider the case of one dimensional harmonic oscillator, whose Hamiltonian is given by

$$H = \frac{p_x^2}{2M} + \frac{1}{2}M\omega^2 x^2 = E. \quad (7)$$

It can also be written as

$$\left(\frac{p_x}{\sqrt{2ME}}\right)^2 + \left(\frac{x}{\sqrt{\frac{2E}{M\omega^2}}}\right)^2 = 1. \quad (8)$$

This is just the equation of an ellipse in the given phase space with semi-axes given by  $\sqrt{2ME}$  and  $\sqrt{\frac{2E}{M\omega^2}}$ . Thus the particle orbits along this ellipse in harmonic oscillator. The area of the particle over one complete period is given by

$$S = \oint p_x dx = \pi\sqrt{2ME}\sqrt{\frac{2E}{M\omega^2}} = \frac{2\pi E}{\omega}. \quad (9)$$

This area will identify action denoted by  $S$ . This action can further be quantised to have few periodic paths or orbits.

A powerful technique called periodic orbit theory has now been developed [49] which enables one to obtain gross-shell effects in the level density of a quantum system semiclassically without solving the Schrodinger's equation. This theory was originally developed for chaotic systems. As we shall see, it was later on adapted to work for integrable systems also. There are almost infinite number of orbits present in a system. The beauty of this technique is that, the inclusion of a few shortest periodic orbits reflects the correct gross-shell structure [50]. Thus it is clear that these periodic orbits give rise to shells in the density of states and thus to the shell effects as an observable effect in the energy spectrum of the system. It is a known fact that shell effects are most prominent for the systems with high degeneracy

and symmetry. But these effects can also be seen in the case of chaotic or unstable systems because some isolated orbits are still present there.

Periodic orbit theory relates the classical actions of the periodic paths to the oscillating part of level density  $\delta g(E)$ . This theory gives a Fourier decomposition of the oscillating part of the level density of single-particle states in terms of classical periodic orbits, their actions, periods and stabilities. This relation in general is quoted as 'trace formula' was proposed by Gutzwiller [50]. The periodic orbit theory or trace formula as proposed by Gutzwiller applies only to systems with isolated orbits. Balian and Bloch presented in 1972 [6] a similar formula for cavities of arbitrary shapes in two or more dimensions; their formula remains valid also to integrable systems. Berry and Tabor in 1976 [10] also presented a trace formula also applicable to integrable as well as non-integrable systems taking EBK quantisation as a basis. Strutinsky and coworkers [105] extended the Gutzwiller theory to include potentials with continuous symmetries and correspondingly degenerate periodic orbits. A more detailed description of the trace formula and some aspects of the P.O.T. will follow in the relevant chapters.

## VI. PRESENT WORK

This thesis aims at exploiting the semiclassical techniques available in the literature and applying those in the field of nuclear physics. We have tried to couple this with the study of the latest discovery in nuclear physics i.e. of superdeformed shapes.

Since the discovery of first superdeformed band in  $^{152}\text{Dy}$  by P. J. Twin in 1986 [110], the list of SD bands has expanded significantly. Till date, about 170 SD bands are known, spread over the four mass regions [99]. The gamma ray transition energies observed in these structures are very feeble. Thus the discovery of these bands depicts the a quantum leap of the advancement in the detection technology.

The study of chaotic dynamics in hamiltonian systems has become a growing discipline during the recent years. These studies are now being carried out in nuclei also with an

emphasis on order-to-chaos transition in the classical dynamics of a particle in various shapes of cavities. Moreover as mentioned in the previous section developments like the periodic orbit theory [49] have brought to fore the deep connection between classical motion and quantal shell structure. Study of SD bands, which represent examples of motion in a highly deformed cavity, therefore offers an exciting possibility to connect the two areas.

In Chapter II we present a complete semiclassical analysis of Particle-Rotor model, taking lead from Bohr and Mottelson [16]. In this chapter we have taken care of the classical fixed point structure emerging in the particle-rotor model and subsequent semiclassical quantisation at various fixed points. This SCQ naturally yields rotational bands whose various features such as alignment, starting angular momentum and oscillations in gamma ray energies are discussed. The two degenerate fixed points  $c_{\pm}$  are situated in the region of nonlinearity/chaos and can be identified with the two minima in the double well potential (DWP) of  $j_3$ . The features of the rotational bands built at the fixed points  $c_{\pm}$  are discussed in full detail in this chapter [63].

A close correspondence of these results with the properties of the SD bands is established in chapter III, where we establish some additional new features of SD bands from an analysis of the experimental data [61]. In particular, we show that the SD bands have almost reached the rigid rotor value of the moment of inertia [37]. Also, we highlight the negative alignment of SD bands and its saturation at a finite positive value at higher angular momenta which in turn is responsible for a saturation in the dynamic moment of inertia. The fact that SD bands begin with a finite starting angular momentum is presented as an important feature of the SD bands and its systematics are explained. With the help of our simple model, presented in chapter II, we have tried to identify the most significant features of a few observed SD bands, representative of the four mass regions, with those obtained from our model. An understanding of the  $\Delta I=2$  staggering is provided. A new feature of General Identical Band is also presented [61] in this chapter.

Chapter IV is a parallel to Chapter II, the difference being in the model chosen. In this chapter we have chosen the cranking model and the semiclassical analysis is repeated.

Numerical results at the degenerate fixed points  $c_{\pm}$  are presented for excitation energies and alignments [59,38].

We present the current general interpretation of shell structure in nuclei in chapter V. At this stage we introduce the periodic orbit theory and other necessary tools to understand the link between the shell structure and periodic orbits. We also present, as examples, simple applications of the POT to integrable systems like harmonic oscillator and spherical billiard [20]. An expression for the level density of spherical billiards is obtained and numerical results presented.

We now exploit the periodic orbit theory to understand deformed systems. We identify the possible classical periodic orbits in the infinitely deep ellipsoidal well. In particular an analysis of the classical closed orbits in the infinitely deep ellipsoidal well is considered and its relevance to the gross-shell structure of single particle spectra in deformed nuclei established [106]. We present detailed and exact results for the planar and the 3-dimensional periodic orbits and study their consequences for the deformed and superdeformed nuclei. The conclusions of the thesis are contained in chapter VII.

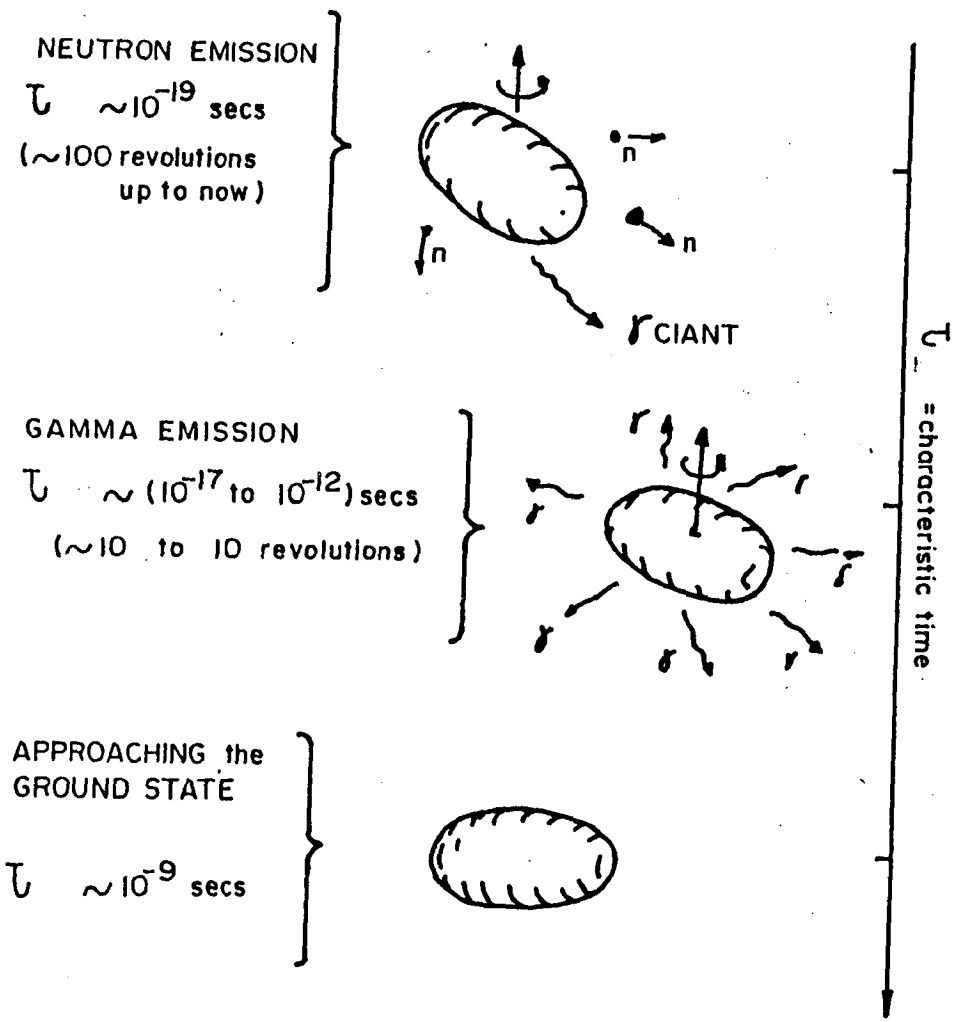
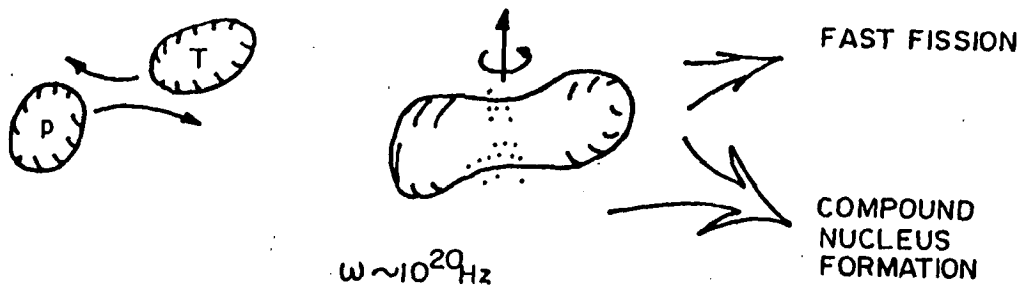


FIG. 1.1 Schematic diagram showing a heavy ion reaction as a source of high spin information. From Ref. [39]

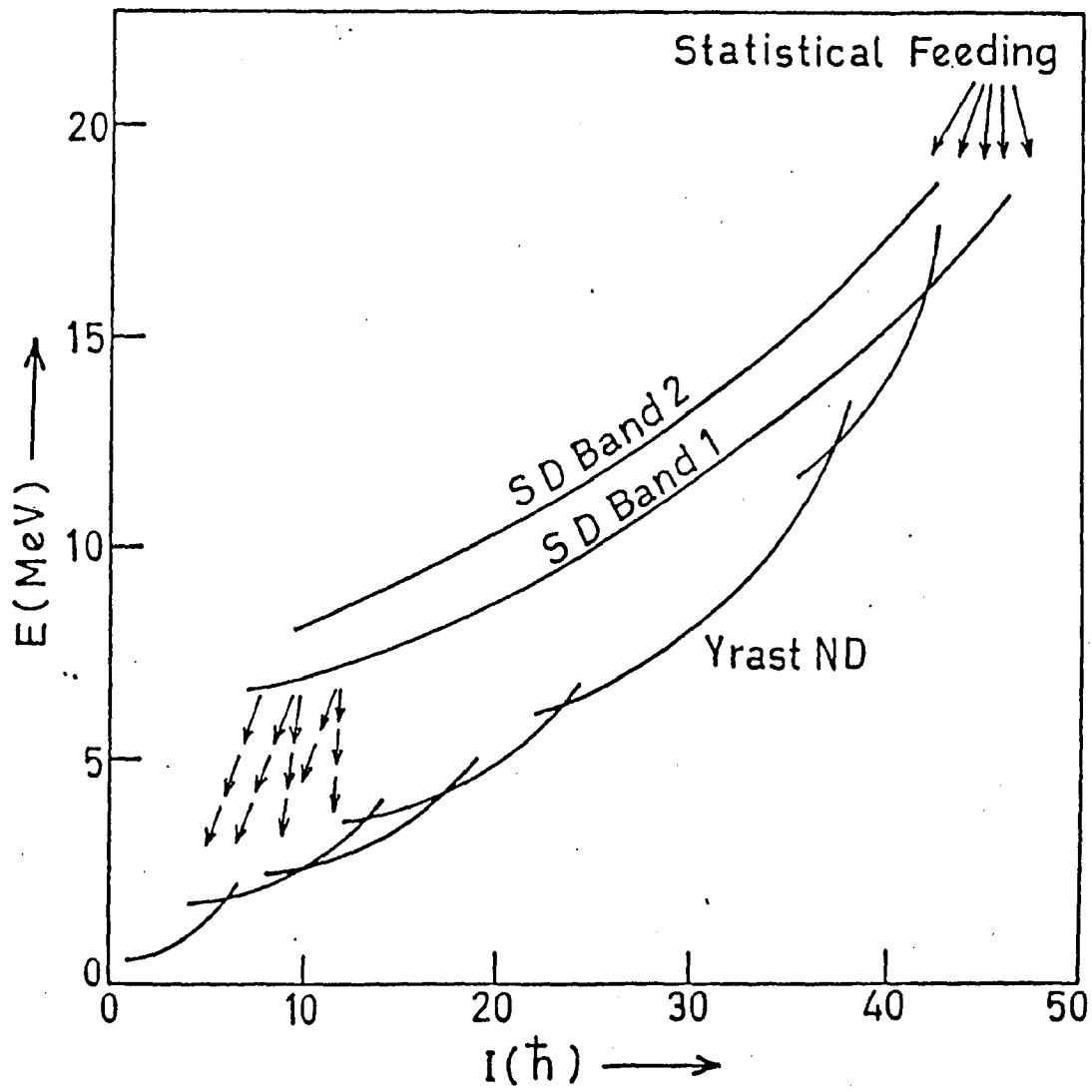


FIG. 1.2 Schematic picture of the formation and decay of SD bands. The ND yrast line is also shown.



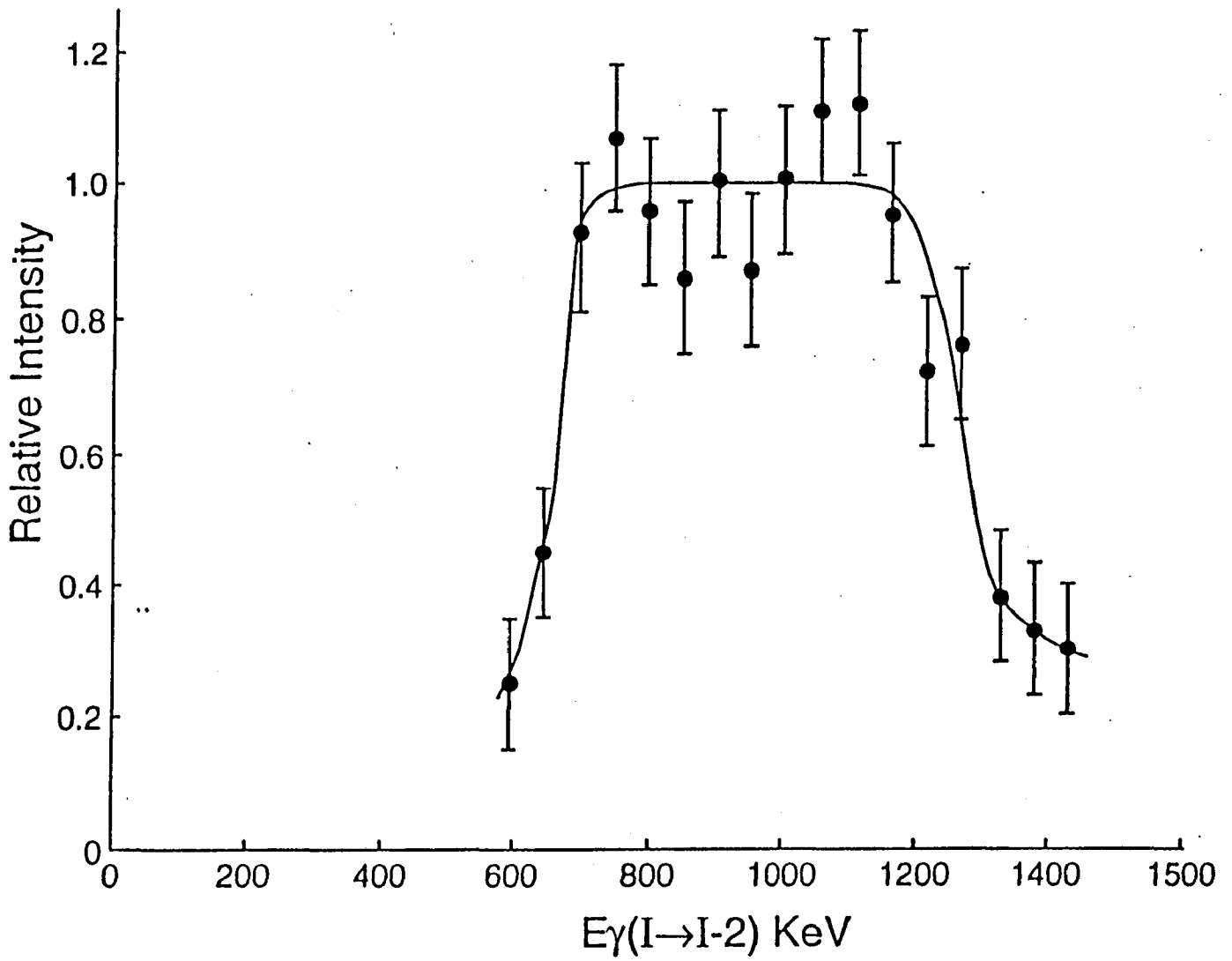


FIG. 1.3 Intensity pattern of SD band 1 of  $^{150}\text{Tb}$ .

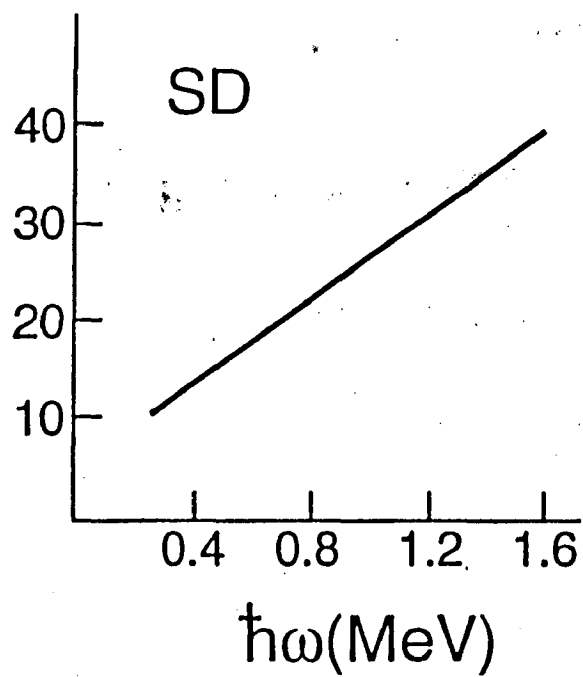
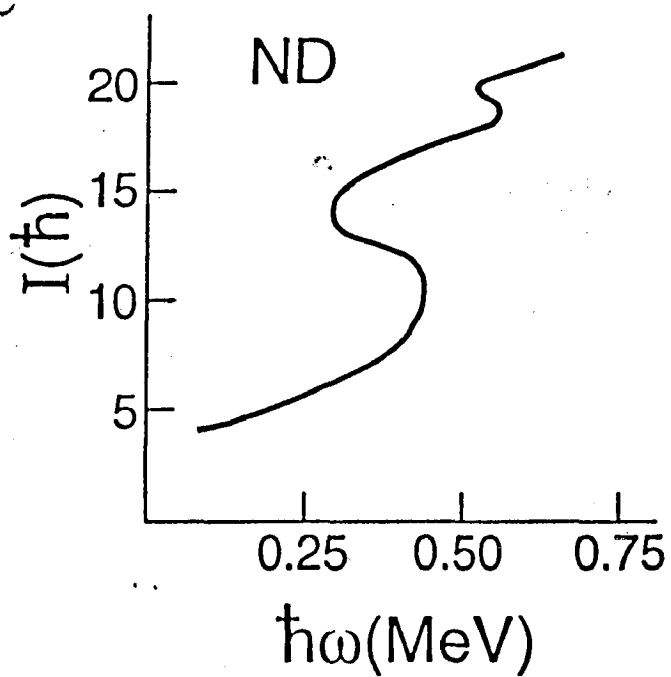


FIG. 1.4 Schematic plots of angular momentum  $I$  vs. rotational frequency  $\hbar\omega$  for ND band on the left and SD band on the right.

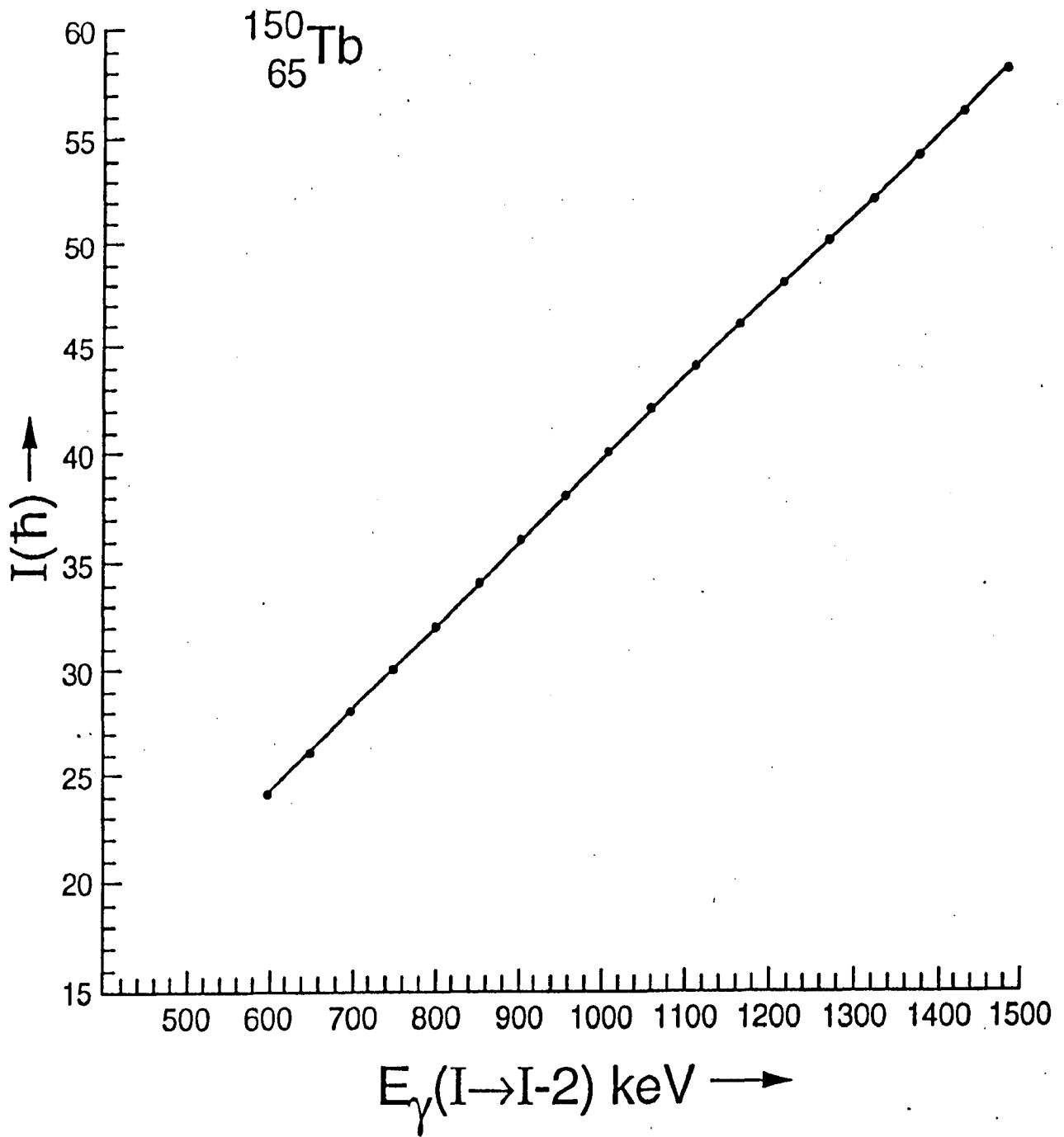


FIG. 1.5 Plot of  $I$  vs. gamma ray energy  $E_\gamma(I \rightarrow I - 2)$  for band 1 of  $^{150}\text{Tb}$ .

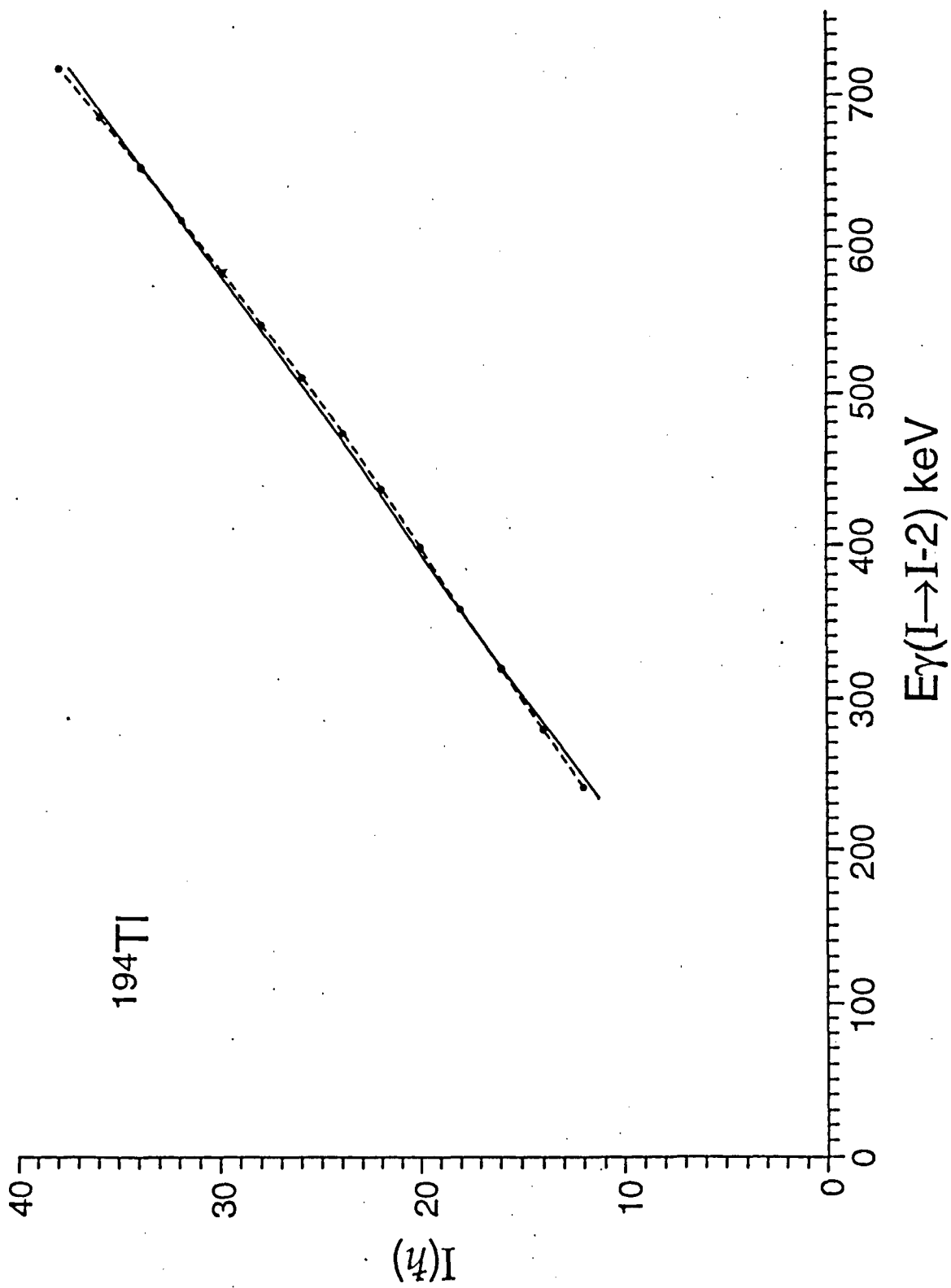


FIG. 1.6 Plot of  $I$  vs. gamma ray energy  $E_{\gamma}(I \rightarrow I - 2)$  for band 2 of  $^{194}\text{Tl}$ .

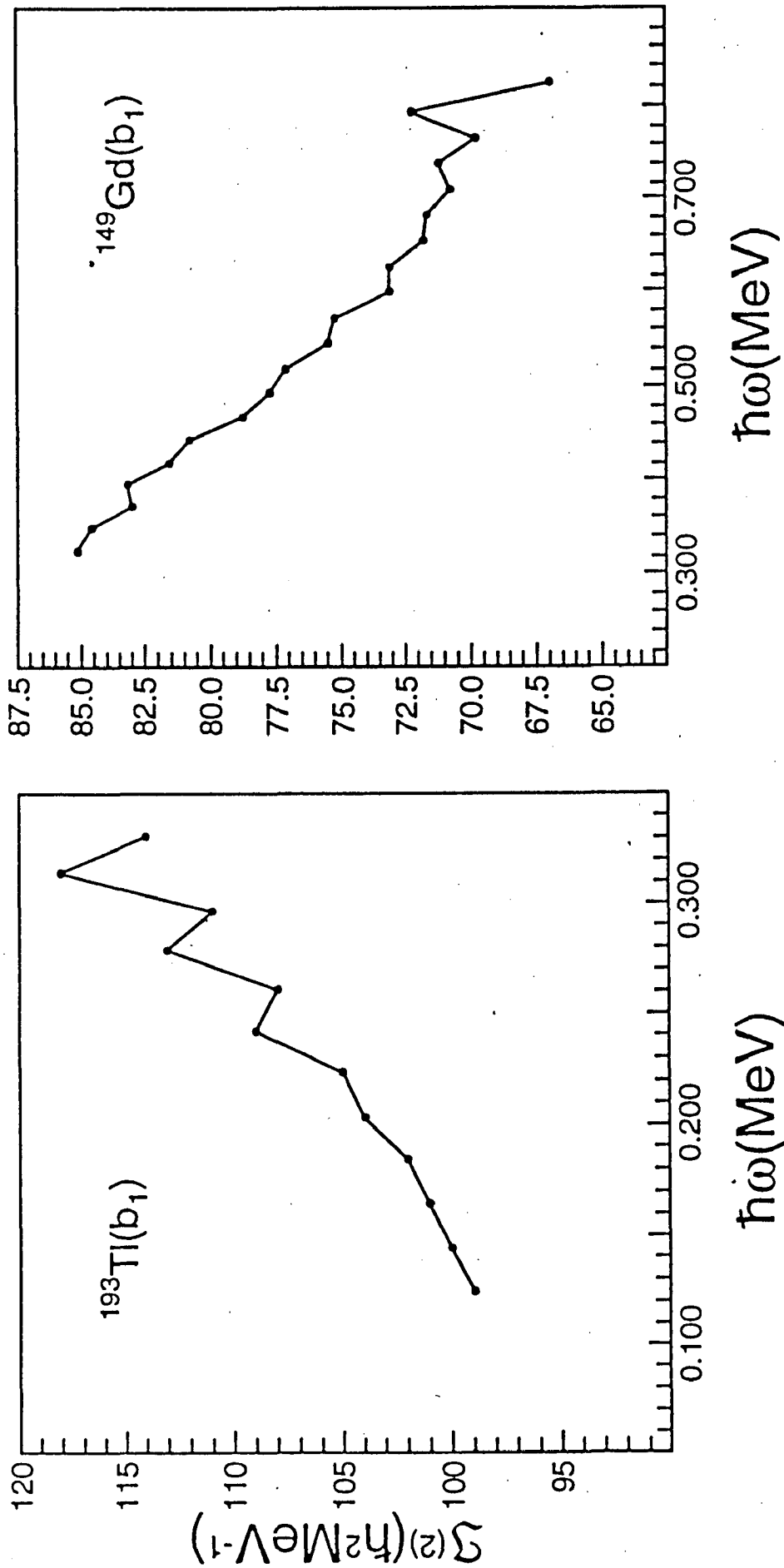


FIG. 1.7 Plots of second moment of inertia  $S^{(2)}$  vs.  $\hbar\omega$  for  $^{149}\text{Gd}$  band 1 and  $^{193}\text{Tl}$  band 1 showing  $\Delta I = 2$  staggering.

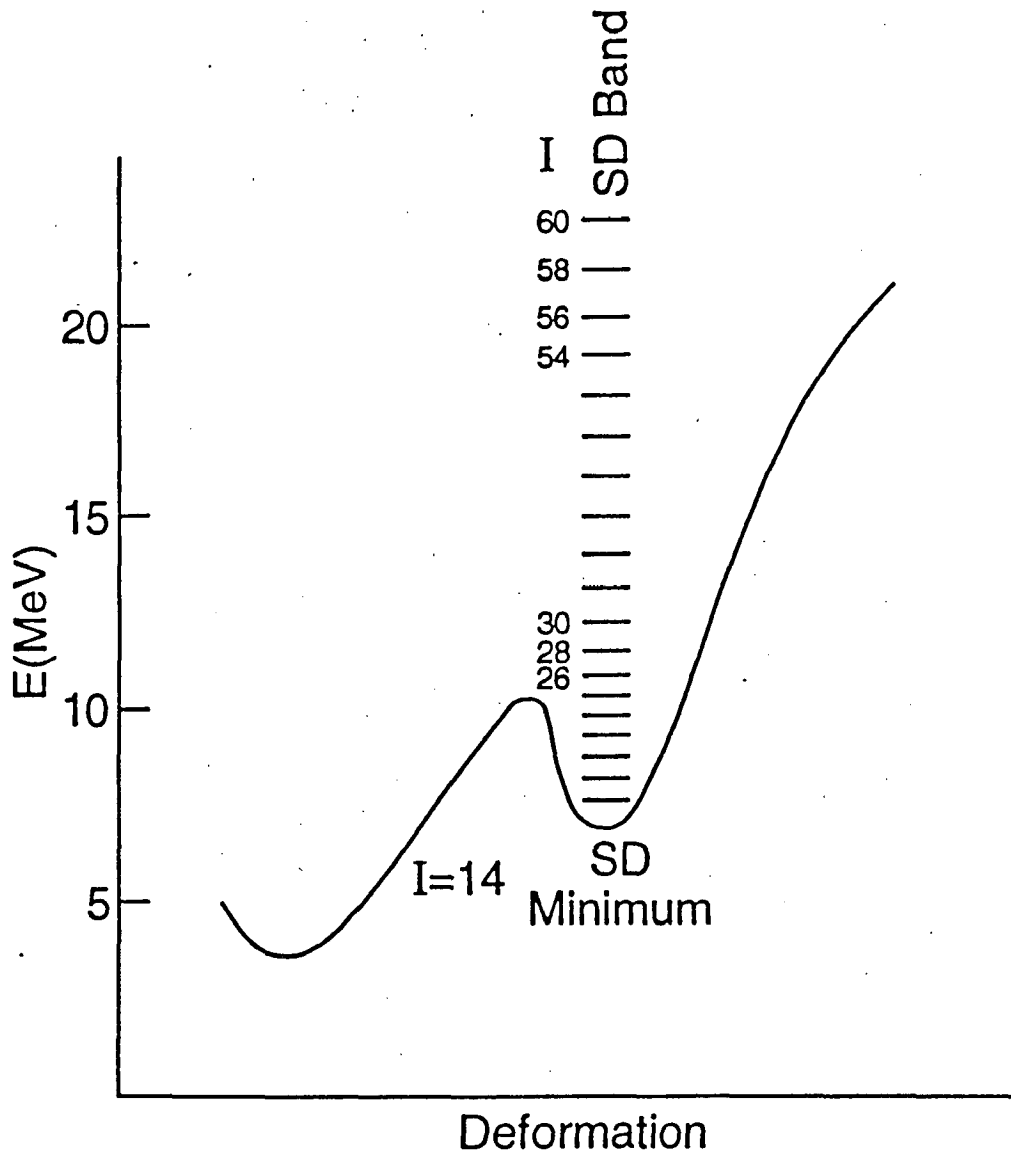


FIG. 1.8 A schematic plot of the potential energy as a function of deformation at high spins where a second minimum develops to form the SD band.

**CHAPTER II**  
**PARTICLE-ROTOR MODEL AND**  
**ITS SEMI-CLASSICAL**  
**QUANTIZATION**

## I. INTRODUCTION

The present day particle-rotor models can trace their origin to the early works of Bohr and Mottelson [13,14] and the first application of Coriolis mixing to the rotational structure of  $^{183}\text{W}$  presented by Kerman [75]. Since then the particle-rotor models have played an important role in the understanding of a large body of experimental data on rotational structures in odd-A [67], odd-odd [70] and 2qp structures in even-even [46] nuclei. Several versions of the particle-rotor model are presently in use and detailed references to these may be found in [67,70]. The basic idea of the particle-rotor model is to treat one or, more valence particles moving independently in the potential as coupled to an inert rotating core consisting of rest of the particles. An odd-A nucleus thus naturally divides into one unpaired nucleon plus an even-even core. Accordingly the Hamiltonian also breaks up into two parts,

$$H = H_{intr} + H_{rotor}, \quad (1)$$

where  $H_{intr}$  is the intrinsic Hamiltonian and  $H_{rotor}$  is the rotational Hamiltonian. One may also add to this, a residual interaction term such as pairing or, n-p residual interaction. The rotational part,

$$H_{rotor} = \frac{\hbar^2}{2\mathfrak{I}_1} R_1^2 + \frac{\hbar^2}{2\mathfrak{I}_2} R_2^2 + \frac{\hbar^2}{2\mathfrak{I}_3} R_3^2, \quad (2)$$

where  $(R_1, R_2, R_3)$  are the three components of rotational angular momentum  $\vec{R}$ . If the valence particle carries an angular momentum  $\vec{j}$ , then  $\vec{I} = \vec{R} + \vec{j}$ . For axially symmetric systems, where  $I_3 = j_3$  and  $\frac{\hbar^2}{2\mathfrak{I}_1} = \frac{\hbar^2}{2\mathfrak{I}_2} = \left(\frac{\hbar^2}{2\mathfrak{I}}\right)$ , the rotational Hamiltonian reduces to

$$H_{rotor} = A(I - j)^2, \quad (3)$$

where  $A = \frac{\hbar^2}{2\mathfrak{I}}$  is labeled as the inertia parameter. The intrinsic part of the Hamiltonian is usually taken from the Nilsson model potential or, the deformed Woods-Saxon potential. For our purpose, we shall introduce a highly simplified version of the Nilsson model.

Neglecting the spin-orbit ( $\vec{l}\vec{s}$ ) and  $\vec{l}^2$  terms, the Nilsson model for a single j-shell provides a simple expression for the single particle energies which may be written as [15],



$$\epsilon_{j_3} = \epsilon_0 - \beta \langle nljj_3 | r^2 Y_{20} | nljj_3 \rangle, \quad (4)$$

$$= \epsilon_0 + \beta \kappa \frac{3j_3^2 - j(j+1)}{4j(j+1)}, \quad (5)$$

where  $\kappa$  is the radial matrix element. We rewrite this result as

$$\epsilon_{j_3} = \epsilon_0 + Qj_3^2, \quad (6)$$

where  $\epsilon_0$  represents the energy corresponding to zero deformation and is independent of  $j_3$ , the third component of  $\vec{j}$  along the symmetry axis.

The total Hamiltonian for a particle in a single- $j$  shell therefore becomes

$$H = Qj_3^2 + A(I - j)^2, \quad (7)$$

where we drop the constant energy contribution  $\epsilon_0$  as it does not affect the dynamics of the problem. The  $Qj_3^2$  term reproduces the fan-like splitting of single particle energies for a given  $j$  as the deformation increases. A typical plot of this term is shown in FIG. 2.1; it simulates the Nilsson diagram reasonably well for a schematic model that we propose to use.

We use this Hamiltonian in the present chapter for a complete discussion of the non-linear dynamics of the particle-rotor model for a single- $j$  configuration. A semiclassical quantization procedure is then used to obtain excitation energies which group together into many rotational bands around twin fixed points  $c_{\pm}$ . A detailed analysis and discussion of the behaviour of gamma ray energies, alignment and the dynamical moment of inertia is then presented. As will be discussed in the next chapter, many observed features of the superdeformed (SD) bands resemble very closely with the properties of the bands built around the fixed points  $c_{\pm}$ .

## II. THE DYNAMICS OF THE PARTICLE-ROTOR MODEL

The particle-rotor Hamiltonian, eq. (7), introduced above was first discussed by Bohr and Mottelson [16]. The rotor is assumed to be axially symmetric and  $R_3 = I_3 - j_3$  is a

constant of motion, which is assumed to be zero. The parameter  $Q = k\beta\sqrt{\frac{5}{4\pi}}\frac{3}{4j(j+1)}$ , where  $\kappa$  is the radial matrix element which may have a value in the range of 40-50 MeV. The inertial parameter  $A$  is of the order of 10 keV for highly deformed nuclei. For  $\beta \approx 0.6$  we get a typical value of  $Q \approx \frac{14}{j^2}$  MeV. We thus have  $A \ll Q \ll Aj^2$  for the orbits of large  $j$  that are of special interest in the superdeformed nuclei. We discuss solution for  $Q > 0$ , i.e. prolate shape only. Using the Poisson brackets [47], we can write the equations of motion for the Hamiltonian (eq.(7)) by noting that the components of the angular momenta are generators of infinitesimal rotations. The time derivatives of the components of  $\vec{I}$  and  $\vec{j}$  are given by the six equations,

$$\frac{dj_1}{dt} = -2A(I_2 - j_2)j_3 - 2Qj_2j_3, \quad (8)$$

$$\frac{dj_2}{dt} = 2A(I_1 - j_1)j_3 + 2Qj_1j_3, \quad (9)$$

$$\frac{dj_3}{dt} = -2A(I_1 - j_1)j_2 + 2A(I_2 - j_2)j_1, \quad (10)$$

$$\frac{dI_1}{dt} = -2A(I_2 - j_2)I_3, \quad (11)$$

$$\frac{dI_2}{dt} = -2A(I_1 - j_1)I_3, \quad (12)$$

and

$$\frac{dI_3}{dt} = \frac{dj_3}{dt}. \quad (13)$$

### A. General Structure of the Orbits

The equations of motion along with the general conservation laws can be used to explore the dynamics of a problem. Besides the six equations of motion, the magnitude of the particle angular momentum  $\vec{j}$  and the total angular momentum  $\vec{I}$  are conserved so that

$$j^2 = j_1^2 + j_2^2 + j_3^2, \quad (14)$$

and

$$I^2 = I_1^2 + I_2^2 + I_3^2, \quad (15)$$

provide additional constraints. In addition, the total energy of the system given by eq. (7) is also a conserved quantity. The total energy defines a parabolic surface whose intersection with the sphere corresponding to constant  $\vec{j}$  defines the trajectories of the system. A fixed point analysis of the problem by putting  $\dot{j}_1$ ,  $\dot{j}_2$ , and  $\dot{j}_3$  equal to zero, provides four stationary points corresponding to a minimum, a saddle point and two distinct but degenerate maxima. For  $I > I_c$  the saddle point and maxima merge into a single maximum.

- The fixed point  $a$

The fixed point denoted by  $a$  corresponds to the full alignment of  $\vec{j}$  along  $\vec{I}$  and represents the minimum in energy. It defines the yrast line with

$$j_1 = j, \quad j_2 = j_3 = 0, \quad (16)$$

$$I_1 = I, \quad I_2 = I_3 = 0, \quad (17)$$

and the energy

$$E_a = A(I - j)^2. \quad (18)$$

We have chosen the 1-axis as the rotation axis.

- The fixed point  $b$

The fixed point  $b$ , an extremum, corresponds to an anti-aligned configuration in which  $\vec{j}$  is aligned opposite to  $\vec{I}$ . At this point,

$$j_1 = -j, \quad j_2 = j_3 = 0, \quad (19)$$

$$I_1 = I, \quad I_2 = I_3 = 0, \quad (20)$$

and the energy

$$E_b = A(I + j)^2. \quad (21)$$

• The twin stable fixed points  $c_{\pm}$

The twin stable fixed points denoted by  $c_{\pm}$  exist only for  $I < I_c$  and correspond to the situation  $j_3 \neq 0$ . It can be shown [63] that  $c_{\pm}$  are defined by the following values of  $(j_1, j_2, j_3)$  and  $(I_1, I_2, I_3)$ :

$$j_1^2 = j_2^2 = -\frac{a^2(I^2 - j^2)}{32\sqrt{1+a}(\sqrt{1+a} + \sqrt{a})} + \frac{(\sqrt{1+a} + 0.5\sqrt{a})^2}{2\sqrt{1+a}(\sqrt{1+a} + \sqrt{a})}(j^2 - j_3^2), \quad (22)$$

$$j_3^2 = I_3^2 = j^2 - \frac{a(I^2 - j^2)}{4\sqrt{1+a}(\sqrt{1+a} + \sqrt{a})}, \quad (23)$$

$$I_i^2 = \left(2\sqrt{\frac{(1+a)}{a}} + 1\right)^2 j_i^2, \quad i = 1, 2, \quad (24)$$

where  $a = \frac{4a^2}{Q(Q-4A)}$ . To obtain the energy at the fixed points  $c_{\pm}$  we rewrite the Hamiltonian eq. (7) as

$$E = (Q - 2A)j_3^2 - 2A(I_1j_1 + I_2j_2) + A(I^2 + j^2), \quad (25)$$

and use the values of  $(I_1, I_2, I_3)$  and  $(j_1, j_2, j_3)$  given by equations (22-24). We finally obtain

$$E_{c_{\pm}} = A(I^2 + j^2) + 2A\sqrt{\frac{(1+a)}{a}}j^2 - \frac{aA(I^2 - j^2)}{2\sqrt{1+a}(\sqrt{1+a} + \sqrt{a})}\left(3\sqrt{\frac{(1+a)}{a}} + 1\right). \quad (26)$$

It can be shown that the fixed point  $b$  is a saddle point for a value of the angular momentum  $I$  less than a critical value  $I_c$ . The vectors  $\vec{I}$  and  $\vec{j}$  precess around the point of minimum energy until the saddle point is reached. The orbit passing through the saddle point, the separatrix, plays a very important role in the analysis of the solutions of classical dynamical systems. Knowing the nature of the separatrices is very helpful in classifying the general structure of orbits.

### III. FICTITIOUS HAMILTONIAN FOR $J_3$

The system of equations (8-13) can be reduced to a second order differential equation in  $j_3$  as also shown by Bohr and Mottelson [16,59,63]. It follows that  $j_3$  satisfies

$$\frac{d^2 j_3}{dt^2} + K j_3 + L j_3^3 = 0, \quad (27)$$

where the coefficients

$$K = 4AQIj + 4A^2(I-j)^2 - 2(Q-2A)\tilde{E}, \quad (28)$$

$$L = 2Q(Q-4A), \quad (29)$$

and

$$\tilde{E} = E - E_a = E - A(I-j)^2. \quad (30)$$

Here  $\tilde{E}$  represents the energy with respect to the yrast line representing the fully aligned configuration. As  $\vec{j}_1$ ,  $\vec{j}_2$  and  $\vec{j}_3$  are coupled through a set of nonlinear differential equations, dynamics of  $j_3$  controls the overall dynamics of the model. The equation of motion for  $j_3$  leads to a fictitious Hamiltonian in  $j_3$  viz.,

$$H_{fictitious} = \left(\frac{dj_3}{dt}\right)^2 + K j_3^2 + \frac{L}{2} j_3^4. \quad (31)$$

It can easily be shown that

$$H_{fictitious} = (4AIj - \tilde{E})\tilde{E}, \quad (32)$$

a quantity denoted by  $C$ . The nature of solution depends on the sign of  $K$  which in turn depends on the energy. At fixed point  $a$  where  $K > 0$  and  $Lj_3^3 \ll K j_3$ , the simple harmonic oscillator regime prevails. As we move away from  $a$ , the cubic anharmonic term  $Lj_3^3$  in equation (27) becomes important with increasing energy. When  $K = 0$ , the solutions of  $j_3$  obey a purely quartic oscillator. On increasing the energy further, the constant  $K$  changes its sign becoming negative. It heralds the commencement of a most interesting

nonlinear dynamical phase governed by Duffing oscillator [94] which then prevails for all higher energies. As shown in FIG. 2.2, the orbit corresponding to  $K = 0$  and the separatrix divide the phase space into three parts.

As pointed out earlier, the maxima  $c_{\pm}$  exist only for  $I < I_c$ . To find the critical angular momentum, we should find the limit when these maxima merge with the saddle point  $b$ . Note that as soon as  $K < 0$  at  $b$ , it becomes a saddle point. Thus, the critical angular momentum corresponds to the situation when  $K = 0$  at  $b$ . Using this condition it is easy to show that

$$I_c = \frac{j}{\sqrt{a}}(\sqrt{1+a} + 1). \quad (33)$$

Thus  $K$  will be negative at  $b$  provided we do not cross the limit  $I_c$ . For  $j = 7$  and  $A = 0.005$  MeV, values typical of SD shapes,  $I_c \approx 400\hbar$ . Clearly the fixed points  $c_{\pm}$  always remain within the  $j$ -space for all meaningful values of angular momenta.

#### IV. SMALL AMPLITUDE OSCILLATIONS

Small amplitude solutions near the fixed points can be obtained by using the technique of linearization of equations of motion. The frequency of oscillations at the fixed point then plays the role of angle variable and the energy at the fixed point is provided by (action  $\times$  angle). It also provides us an avenue to introduce quantization of energy by quantizing the action. The nature of solutions around the fixed point  $a$  has been discussed by Bohr and Mottelson [16]. We give the details of solutions around  $a, b$  and  $c_{\pm}$ ; our main interest being in the fixed points  $c_{\pm}$  and a general expression for the frequency of oscillation.

- Fixed point  $a$

The frequency of small oscillation for  $j_3$  can immediately be obtained by ignoring the anharmonic term in the equation of motion to give

$$\omega_{vib} = \sqrt{K} = [4AQIj + 4A^2(I-j)^2]^{1/2}, \quad (34)$$

$$j_3 = a_3 \cos(\omega_{vib}t + \nu_0), \quad (35)$$

$$a_3^2 = \left[ \frac{4AIj}{K} \right] \tilde{E}. \quad (36)$$

The energy for small oscillations at  $a$  is given by

$$E = E_a + J\omega_{vib}, \quad (37)$$

where  $E_a = A(I - j)^2$  and  $J$  is the action for  $\omega_{vib}$ . The solutions of  $j_2$  and  $I_2$  are

$$j_2 = a_2 \sin(\omega_{vib}t + \nu_0), \quad (38)$$

$$a_2 = \frac{2}{\omega_{vib}} [Qj + A(I - j)] a_3, \quad (39)$$

$$I_2 = b_2 \sin(\omega_{vib}t + \nu_0), \quad (40)$$

$$b_2 = \frac{2}{\omega_{vib}} A(I - j) a_3. \quad (41)$$

The components  $I_1$  and  $J_1$  are obtained from  $j^2 = j_1^2 + j_2^2 + j_3^2$  and  $I^2 = I_1^2 + I_2^2 + I_3^2$ . The action  $J$  can be quantized in the sense of Bohr-Sommerfeld quantization to obtain quantized energy levels. Thus

$$J = \left( n + \frac{1}{2} \right) \hbar, \quad (42)$$

where  $n = 0, 1, 2, 3, \dots$  etc.

• Fixed point  $b$

At the unstable fixed point  $b$  which is a saddle point for  $I < I_c$  we obtain

$$\omega_{vib} = \left[ -4AQIj + 4A^2(I - j)^2 \right]^{\frac{1}{2}}, \quad (43)$$

$$j_3 = a_3 \cos(\omega_{vib}t + \nu_0), \quad (44)$$

$$a_3 = \left[ \frac{4AIj\tilde{E}_b}{\omega_{vib}^2} \right]^{\frac{1}{2}}. \quad (45)$$

The energy of small oscillations at  $b$  is given by

$$E = E_b + J\omega_{vib}. \quad (46)$$

• Fixed point  $c_{\pm}$

The twin stable fixed points  $c_{\pm}$  offer interesting possibility of supporting motion beyond the saddle point  $b$  and therefore the separatrix. Since  $K < 0$  at  $c_{\pm}$ , the equation of motion becomes that of a Duffing oscillator whose solutions are in the form of Jacobian elliptic functions [48] which decide the nature of excitations that can be sustained at or, near  $c_{\pm}$ . The energy at the fixed points  $c_{\pm}$  can be obtained by using the approximate values of  $(I_1, I_2, I_3)$  and  $(j_1, j_2, j_3)$  at  $c_{\pm}$  in the equation (25). We obtain [63],

$$E_{c_{\pm}} = A(I^2 + j^2) + 2A\sqrt{\frac{(1+a)}{a}}j^2 - \frac{aA(I^2 - j^2)}{2\sqrt{1+a}(\sqrt{1+a} + \sqrt{a})} \left(3\sqrt{\frac{(1+a)}{a}} + 1\right),$$

as in equation (26) and  $\tilde{E}_{c_{\pm}} = E_{c_{\pm}} - E_a$ .

Small oscillation analysis at  $c_{\pm}$  leads to the following results,

$$\omega_{vib} = \pm \left[ 4A^2(I^2 + j^2 - 2j_3^2) + 4A(Q - 2A) \left( 2\sqrt{1 + \frac{1}{a}} + 1 \right) \frac{a(I^2 - j^2)}{4\sqrt{1+a}(\sqrt{1+a} + \sqrt{a})} \right]^{\frac{1}{2}}. \quad (47)$$

In fact the frequency of small oscillations near the various fixed points is given by a general expression.

$$\omega_{vib} = \pm [4A^2(I_1^2 + I_2^2 + j_1^2 + j_2^2) + 4A(Q - 2A)(I_1j_1 + I_2j_2)]^{\frac{1}{2}}, \quad (48)$$

where appropriate values of  $I_1, j_1$ , etc. should be used. The energy for small oscillations around  $c_{\pm}$  can be written as

$$E = E_{c_{\pm}} + J\omega_{vib}, \quad (49)$$

where  $J$  is the action is given by

$$J = 4 \int_0^{j^+} dj_3 [C - Kj_3^2 - \frac{L}{2}j_3^4]^{\frac{1}{2}}, \quad (50)$$

and





$$j^+ = \left[ \frac{1}{L} (\sqrt{K^2 + 2LC} - K) \right]^{\frac{1}{2}}. \quad (51)$$

The quantization condition,

$$J = \left( n + \frac{1}{2} \right) \hbar, \quad (52)$$

where  $n = 0, 1, 2, \dots$  etc. is introduced to obtain the quantized energy levels. As already pointed out, as  $K$  changes sign from positive to negative, a double well potential (DWP) appears from the single well in  $V(j_3)$  of the fictitious Hamiltonian of  $j_3$  given by

$$\left( \frac{dj_3}{dt} \right)^2 + V(j_3) = C, \quad (53)$$

where  $V(j_3) = Kj_3^2 + (L/2)j_3^4$  and  $C = (4AIj - \tilde{E})\tilde{E}$ . The minima of the DWP correspond to the two isolated, fixed points  $c_{\pm}$ ; these are located in a region of nonlinearity. The DWP supports two solutions which we denote by  $p=0$  and  $p=1$ ; these correspond to the usual even and odd solutions of a potential well. On taking the tunnelling between the two wells into account, the semiclassical quantization condition for the action in  $j_3$  now reduces to

$$\frac{1}{\pi} \int_{j_-}^{j_+} \sqrt{C - V(j_3)} dj_3 - \frac{\Phi(\varepsilon) \mp \Delta\Phi(\varepsilon)}{2\pi} = \left( n_{\pm} \pm \frac{1}{4} \right), \quad (54)$$

where

$$\varepsilon(C) = \sqrt{\frac{1}{2V''(0)}} (C - V(0)) = \frac{C}{\sqrt{4K}}, \quad (55)$$

$$\Phi_{\pm}(\varepsilon) = \frac{1}{2} \left[ \arg\Gamma\left(\frac{1}{2} + i\varepsilon\right) - \varepsilon \ln |\varepsilon| + \varepsilon \pm \tan^{-1} e^{-\pi\varepsilon} \right], \quad (56)$$

and,  $\Delta\Phi = \Phi_- - \Phi_+$  and  $\Phi = \Phi_- + \Phi_+$ . The limits on  $j_3$  are the four real turning points at subbarrier energies denoted by  $-j_+$ ,  $-j_-$ ,  $j_-$  and  $j_+$ . If we choose the upper sign in equation (54) and take  $n_+ = 0, 1, 2, 3, \dots$ , we get the even solutions denoted by  $p=0$ . By taking the lower sign and  $n_- = 1, 2, 3, \dots$  we get the odd solutions denoted by  $p=1$  [2]. Fulfillment of the SCQ condition given by equation (54) yields a set of energies  $E$  for a given  $n$  and different  $I$ ; this constitutes a band which exhibits rotational features.

As pointed out by Bohr and Mottelson [16], the frequency  $\omega_{vib}$  is characteristic of motion in the intrinsic frame. Another frequency  $\omega_{rot}$  associated with the angle variable conjugate to the total angular momentum, can also be defined in the particle-rotor model,

$$\omega_{rot} = \left( \frac{\partial E}{\partial I} \right)_J, \quad (57)$$

and is characteristic of the mean rate of precession of the rotor around appropriate axis.

### A. Double well in $j_3$ and second order Phase transition

The fictitious hamiltonian for  $j_3$  contains a fictitious potential term  $(Kj_3^2 - Lj_3^4)$  which is parabolic. As  $K$  changes sign from positive to negative, there is a sudden appearance of a double well potential FIG. 2.3, which implies a spontaneous breakdown of symmetry. Such a symmetry breaking is well known to be associated with a second order phase transition [57]. Following the Landau theory, let us choose the Landau free energy as

$$\psi(j_3, \chi) = [Kj_3^2 + \frac{L}{2}j_3^4] - \frac{j_3\chi}{E}. \quad (58)$$

The term in square brackets is the potential term which is a single well potential for  $K > 0$  and a double well potential for  $K < 0$ . The Landau free energy  $\psi$  for  $\chi = 0$  is invariant under  $j_3 \rightarrow -j_3$  but this symmetry is spontaneously broken when  $K < 0$ . The transition is a second order because  $\langle j_3 \rangle$  is continuous at  $K=0$ . Here,  $j_3$  plays the role of order parameter and  $|K|$  plays the role of the intensive variable (an exact analogy can be made with magnetization and temperature respectively). The Gibbs free energy  $G$  can be defined as

$$j_3 = -\frac{\partial G}{\partial |K|}, \quad (59)$$

(note again the analogy with magnetism). The condition determining  $\langle j_3 \rangle$  is

$$2K \langle j_3 \rangle + 2L \langle j_3 \rangle^3 - \frac{\chi}{E} = 0. \quad (60)$$

For  $\chi = 0$ , the only real solution is

$$\begin{aligned} \langle j_3 \rangle &= 0 & K > 0, \\ &= \pm \sqrt{\frac{|K|}{L}} & K < 0, \end{aligned}$$

which implies that the exponent  $\beta = \frac{1}{2}$  in the Rushbrook law. This establishes that there is a second-order phase transition as  $K$  changes sign. The system has two minima; corresponding to  $\pm \sqrt{\frac{|K|}{L}}$ ; it cannot however exist simultaneously in both of them and one of these two must become the ground state. From the nature of the fixed points  $a, b$  and  $c_{\pm}$ , it is clear that the allowed  $j$ -space is divided by the separatrix passing through  $b$  into three disjoint regions. The yrast region (around  $a$ ) is phase separated from the excitations built at or, around the other fixed points. Thus there appear four distinct regimes starting from the lowest energies - the SHO (simple harmonic oscillator), AHO (anharmonic oscillator), QO (quartic oscillator) and DO (duffing oscillator). From the semiclassical quantisation procedures, we can quantise our system in all these regimes. Most significant point to note here is that the level sequences thus built up will not be easily connected to each other or, stated in other words, the transition probabilities to qualitatively different dynamical scenario are expected to be rather small.

## V. ALIGNED ANGULAR MOMENTUM

A quantity of great physical interest is the aligned angular momentum or, just alignment which quantifies the extent to which the particle angular momentum aligns with the direction of collective rotation. Alignment is defined as [16]

$$i = \frac{\langle (\vec{I} \cdot \vec{j}) \rangle}{\langle I_{\perp} \rangle} = \frac{\langle \vec{I} \cdot \vec{j} - j_3^2 \rangle}{\langle (I^2 - I_3^2)^{\frac{1}{2}} \rangle}. \quad (61)$$

It can be shown easily that at the fixed point  $a$ ,

$$(\vec{I} \cdot \vec{j} - j_3^2) = Ij - \frac{J\omega_{vib}}{2A} \left[ 1 - \frac{(Q - 2A)Ij}{QIj + A(I - J)^2} \cos^2(\omega_{vib}t + \nu_0) \right], \quad (62)$$

which implies that

$$\langle \vec{I} \cdot \vec{j} - j_3^2 \rangle = Ij - \frac{J}{\omega_{vib}} [(Q + A)Ij + A(2I - j)(I - j) + Aj^2]. \quad (63)$$

Taking  $\langle I_1^2 + I_2^2 \rangle^{\frac{1}{2}} \approx I$ , we get

$$i_a = j - \frac{J}{I\omega_{vib}} [(Q + A)Ij + A(2I - j)(I - j) + Aj^2]. \quad (64)$$

In the limit of  $Q \gg A$ ,

$$i_a \approx j - J\left(\frac{Qj}{4AI}\right)^{\frac{1}{2}}. \quad (65)$$

The alignment at  $c_{\pm}$  is obtained as

$$i_{c_{\pm}} = \left[ -\frac{\tilde{E}_{c_{\pm}} - 2AIj - Q\langle j_3^2(t) \rangle}{2A} - \langle j_3^2(t) \rangle \right] [\langle \sqrt{I^2 - j_3^2(t)} \rangle]^{-1}, \quad (66)$$

where  $\langle \rangle$  denotes the time average value of the quantity within the brackets. In order to find the value of  $\langle j_3^2(t) \rangle$  the averaging is to be done over the natural time period of the solutions of  $j_3$  which are elliptic functions [48]. Therefore,

$$\left(\frac{dj_3}{dt}\right)^2 = -Kj_3^2 - \frac{L}{2}j_3^4 + C, \quad (67)$$

which leads us to

$$\frac{dj_3}{dt} = \sqrt{\frac{L}{2}(e^2 - j_3^2)(j_3^2 - g^2)}, \quad (68)$$

where  $e^2 = -\frac{K}{L} + \sqrt{\left(\frac{K}{L}\right)^2 + \frac{2C}{L}}$  and  $g^2 = -\frac{K}{L} - \sqrt{\left(\frac{K}{L}\right)^2 + \frac{2C}{L}}$  and

$$\int_0^t dt' = \int_e^{j_3} \frac{dj_3}{\sqrt{\frac{L}{2}(e^2 - j_3^2)(j_3^2 - g^2)}}. \quad (69)$$

Here we have assumed that at time  $t = 0$  the particle is at point  $j_3 = e$  and at time  $t$ , it is at a point  $j_3$ . Note that for  $-1 \leq C < 0$ , the particle is confined to one of the wells while for  $0 < C \leq \infty$  the particle has enough energy to cross the barrier. The solution to equation (68) is given in terms of Jacobian Elliptic functions.

• For  $C < 0$ , we get [94]

$$j_3(t) = e \operatorname{dn}(et, s), \quad (70)$$

and the corresponding canonically conjugate momentum,

$$P_3(t) = -e^2 s^2 \operatorname{sn}(et, s) \operatorname{cn}(et, s), \quad (71)$$

where the modulus,  $s$ , is defined as

$$s^2 = \frac{e^2 - g^2}{e^2}. \quad (72)$$

Note that when  $C < 0$ ,  $s < 1$ , the natural time period of  $\operatorname{dn}(et, s)$  is  $2K(s)$  where  $K(s)$  is the complete elliptic function of first kind.

- The solutions to equation (68) for the case  $C > 0$ ,  $s > 1$  are

$$j^3(t) = e \operatorname{cn}(est, \frac{1}{s}), \quad (73)$$

and

$$P_3(t) = -se^2 \operatorname{sn}(est, \frac{1}{s}) \operatorname{dn}(est, \frac{1}{s}), \quad (74)$$

with the quantity  $\frac{1}{s}$  playing the role of the modulus. The time period of  $\operatorname{cn}(est, \frac{1}{s})$  is  $4K(s)$ .

- The phase space for the duffing oscillator is shown in FIG. 2.4. We see that phase space contains two stable (elliptic) fixed points ( $P = 0, j_3^2 = I_3^2 = j^2 - \frac{a(I^2 - j^2)}{4\sqrt{1+a}(\sqrt{1+a} + \sqrt{a})}$ ) and one unstable (hyperbolic) fixed point ( $P = 0, j_3 = 0$ ). The region of trapped motion ( $-1 \leq C < 0$ ) is separated from that of untrapped motion ( $0 < C \leq \infty$ ) by a separatrix  $C=0$ . The separatrix has the same energy as the hyperbolic fixed points however, they have different trajectories. A particle moving on a separatrix has infinite time period i.e. it takes an infinite time to reach the hyperbolic fixed point from any point on the separatrix.

The case  $C > 0$  corresponds to the superbarrier solutions ( $s > 1$ ) where  $\tilde{E}_b > \tilde{E}_c$ . For  $A=0.005$  MeV and  $j=7$ ,  $\tilde{E}_b$  becomes greater than  $\tilde{E}_c$  at  $I = 129.5\hbar$  as shown in FIG. 2.5(a). Since our interest lies in angular momentum  $I < 80\hbar$  we always remain in the region where  $C < 0$ . In other words the subbarrier solution need to be considered.

## VI. RESULTS AND DISCUSSION

We now present numerical results for the various fixed points and discuss the general nature of the solutions. As already pointed out, the fixed points  $c_{\pm}$  continue to exist until a

critical angular momentum  $I_c \approx 400\hbar$  for typical values of the parameters  $A= 0.005$  MeV,  $Q = \frac{14}{j^2}$  and  $j= 7$ , representative of superdeformed bands. Thus,  $c_{\pm}$  always remain within the domain of  $j$ -space. A plot of the energies of the various fixed points as a function of angular momentum  $I$  is shown in FIG. 2.5(a). We can see that the energy of fixed point  $c_{\pm}$ ,  $E_{c_{\pm}}$  becomes lower than  $E_b$  around  $I = 130\hbar$ . This is still a very large angular momentum. Thus for all practical purposes,  $E_b < E_{c_{\pm}}$ . If we choose  $I = 7$ , then  $\tilde{E}_b$  (the energy of  $b$  relative to  $a$ ) is about 1 MeV and  $\tilde{E}_{c_{\pm}}$  (the energy of  $c_{\pm}$  relative to  $a$ ) is about 14 MeV. In FIG. 2.5(b), we plot the gamma ray transition energies  $E_{\gamma}(I \rightarrow I - 2)$  as obtained from  $E_{c_{\pm}}$ . It is most remarkable that the  $I$  vs.  $E_{\gamma}$  plot is exactly linear, implying an exact rigid-rotor behaviour of levels built at  $E_{c_{\pm}}$ . Also the line has an intercept of -1.0 on the  $I$ -axis. The slope of the line gives a moment of inertia value of  $104\hbar^2 MeV^{-1}$ .

When exact solutions are obtained at fixed point  $c_{\pm}$ , we obtain bands corresponding to  $n=0,1,2,\dots, p=0$  and  $n=1,2,3,\dots,p=1$ . When solving the equations we ensure that action in  $j_3$  is quantized at least upto fourth decimal place. The resulting solutions of level energies for the standard set of parameters  $A=0.005$  MeV and  $j=7$  are shown in FIG. 2.6 and FIG. 2.7. We have plotted the alternate angular momentum  $I$  vs. the gamma ray energies  $E_{\gamma}(I \rightarrow I - 2)$ . It is remarkable to note that the transition energies obtained after SCQ begin to show very weak oscillations around an overall linear behaviour. The oscillations show up more clearly when we plot the energy difference  $E_{\gamma}(I \rightarrow I - 2) - E^{lin}(I \rightarrow I - 2)$  vs.  $I$  where  $E^{lin}(I \rightarrow I - 2)$  represents the linear fit to the calculated gamma ray energies. As is evident from the results in FIG. 2.8 and FIG. 2.9 the magnitude of the oscillations decreases rapidly as  $n$  is increased.

Another important feature resulting from our calculations is that these bands start with a finite angular momentum  $I_b$ . In other words the bandhead has a finite angular momentum which depends on  $A$ ,  $j$  and  $n$ . Effect of  $A$  and  $j$  on the starting angular momentum is shown in Table I. As  $j$  is increased the starting angular momentum comes down. We may point out at this stage that the many particle configurations assigned to the SD bands can give rise to a higher effective  $j$  value; the starting angular momentum therefore will depend in a

crucial manner on the SD band configuration.

Other quantities of physical interest are alignment  $i$  and dynamical moment of inertia  $\mathfrak{S}^{(2)}$ . The aligned angular momentum of a given band is numerically calculated by using the level energies of the band in equation (68). The time average of  $j_3(t)$  is obtained by using the procedure outlined in section V. The numerical results for  $n=1,2,3,4$ ,  $p=0$  and  $p=1$  are shown in FIG. 2.10 and FIG. 2.11 respectively. It is interesting to note that the alignments are negative near the bandhead, rise with increasing angular momentum and finally saturate. In FIG. 2.12 and FIG. 2.13 we show the behaviour of second moment of inertia  $\mathfrak{S}^{(2)}$  for  $n=1,2,3,4$ ,  $p=0$  and  $p=1$  respectively. We notice that the  $\mathfrak{S}^{(2)}$  value shows a sudden rise at certain angular momentum which is reminiscent of a similar discontinuity noticed in the behaviour of several SD bands [30]. Further  $\mathfrak{S}^{(2)}$  value appears to saturate at higher angular momenta for several  $n$  values. This saturation in  $\mathfrak{S}^{(2)}$  may be directly correlated with the saturation in the alignment observed at high angular momenta.

To conclude, we have carried out a complete analysis of the dynamics of the particle-rotor model in a single- $j$  configuration. The SCQ at the stable fixed points  $c_{\pm}$  leads to rotational bands with many unique features which resemble closely to those of the SD bands. The weak oscillations in gamma ray energies appears to be a direct consequence of the nonlinearity in the equation of motion of  $j_3$ . Also the calculated bands start at a finite angular momentum as is the case with the observed SD bands. The behaviour of the aligned angular momentum indicates that the alignment remains negative for a considerable portion of the band near the bandhead. The dynamical moment of inertia exhibits features similar to those noticed in the experimental data. A detailed comparison of these features and also some additional features like  $\Delta I = 2$  staggering with the experimental data will be presented in chapter III.

TABLES

TABLE I. Effect of Parameters  $A$  and  $j$  on Starting Angular Momentum  $I_b$

$A$	$j$	$I_b, n = 0, p = 0$	$I_b, n = 1, p = 0$	$I_b, n = 2, p = 0$	$I_b, n = 1, p = 1$	$I_b, n = 2, p = 1$
0.005	6	15.5	37.5	55.5	21.5	41.5
0.005	7	11.5	29.5	41.5	17.5	31.5
0.005	8	9.5	23.5	33.5	13.5	25.5
0.006	7	9.5	23.5	35.5	13.5	27.5
0.008	7	7.5	17.5	27.5	11.5	21.5



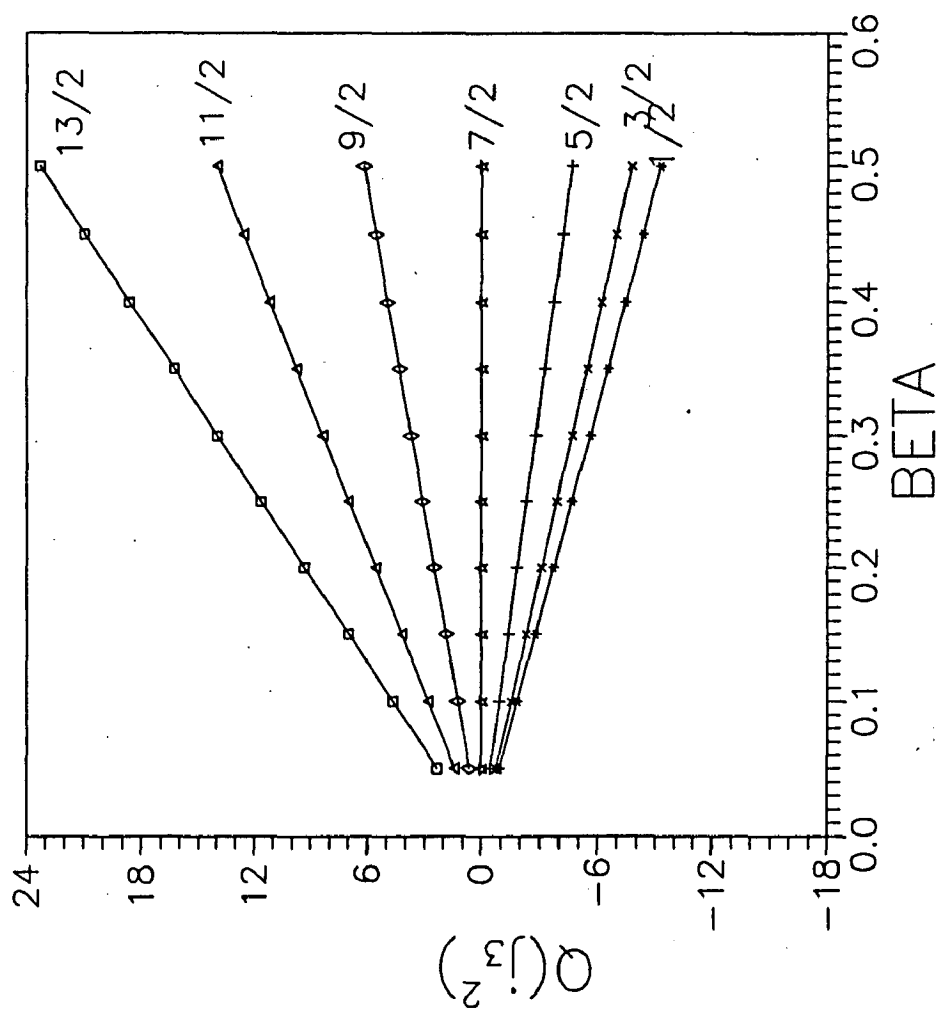


FIG. 2.1 Plot of  $Qj_3^2$  vs. the deformation  $\beta$  showing the fan-like splitting for  $j = \frac{13}{2}$ .

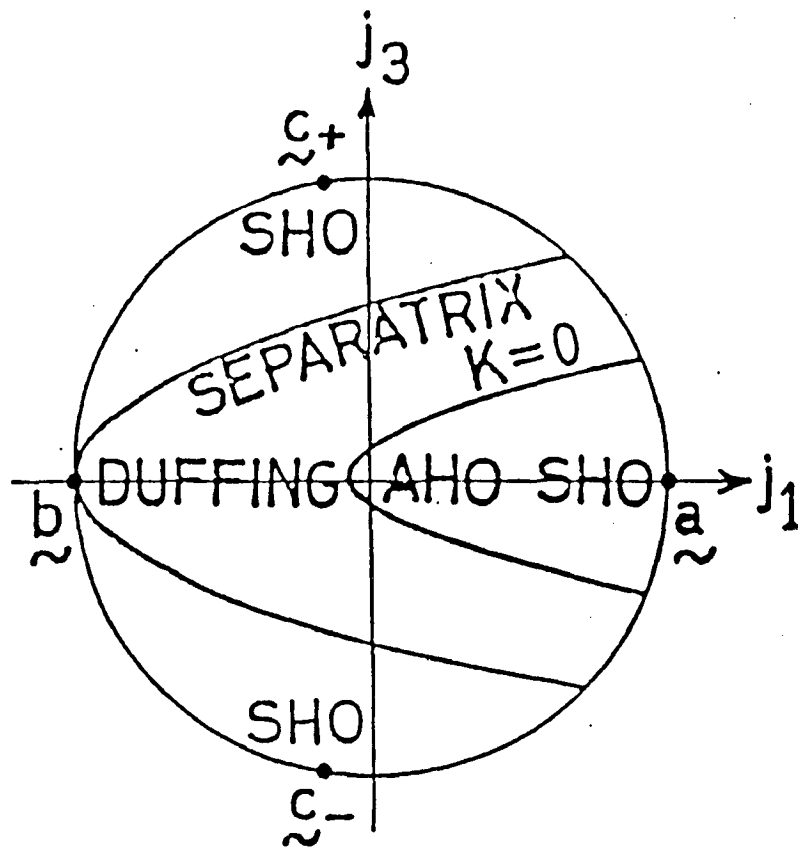


FIG. 2.2 Schematic diagram showing the division of the  $j$ -space into four distinct regions.

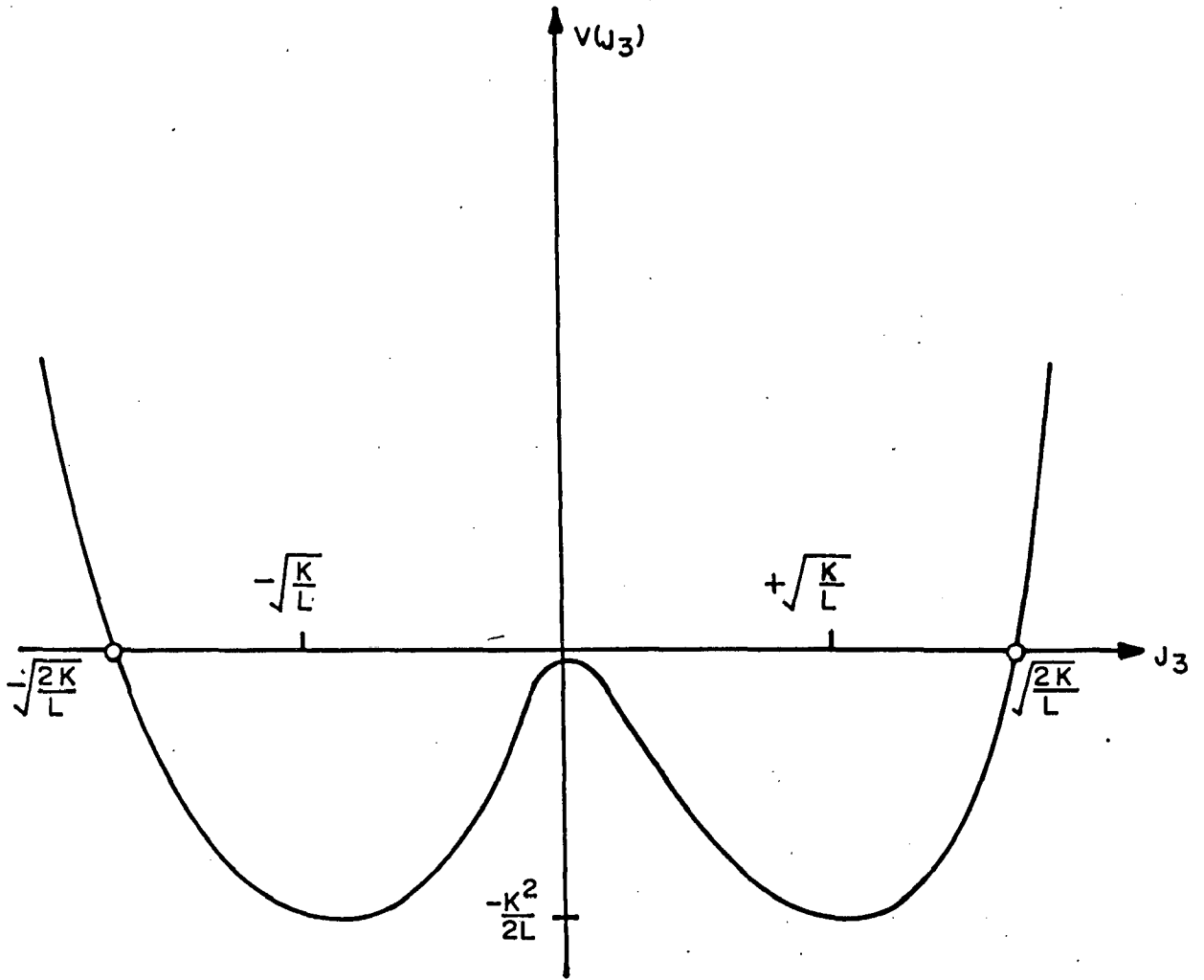


FIG. 2.3 Plot of  $V(j_3)$  vs.  $j_3$  showing the DWP when  $K < 0$ .

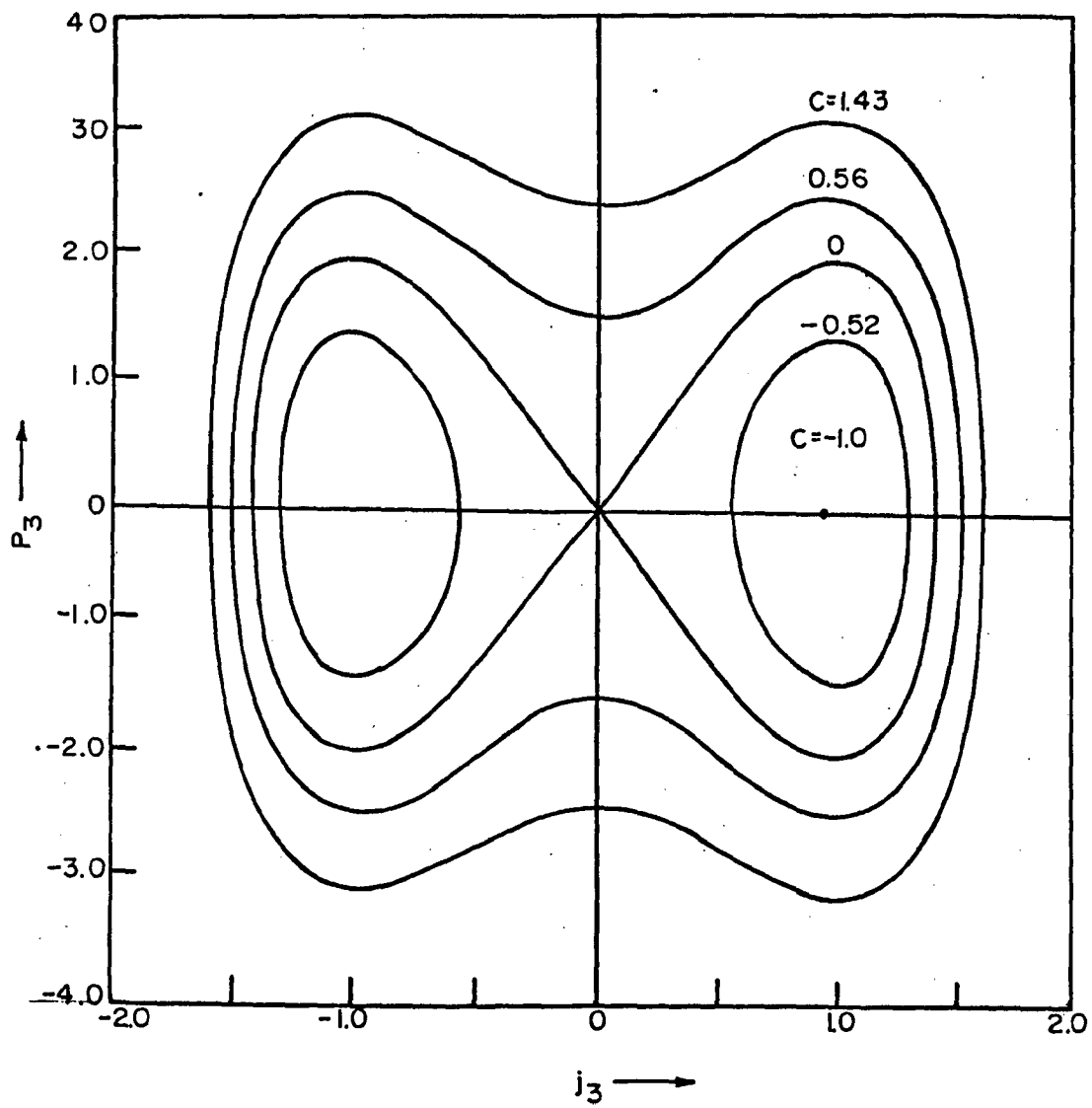


FIG. 2.4 Phase space diagram of duffing oscillator. From Ref. [94].

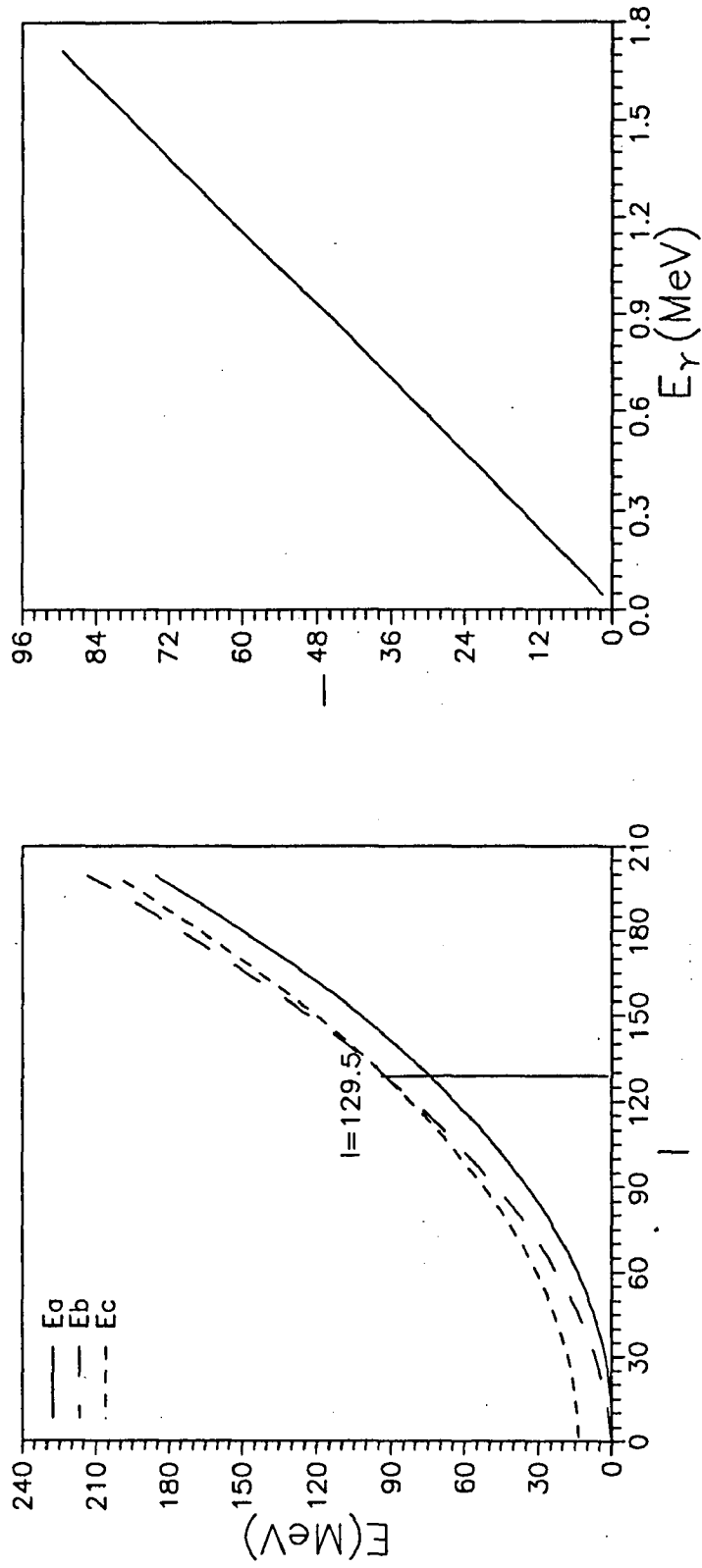


FIG. 2.5 (a) Plots of total energy at the fixed points  $a, b$  and  $c_{\pm}$  as a function of the total angular momentum  $I$  (without SCQ). (b) Plot of  $I$  vs.  $E_\gamma(I \rightarrow I - 2)$  for the fixed points  $c_{\pm}$ .

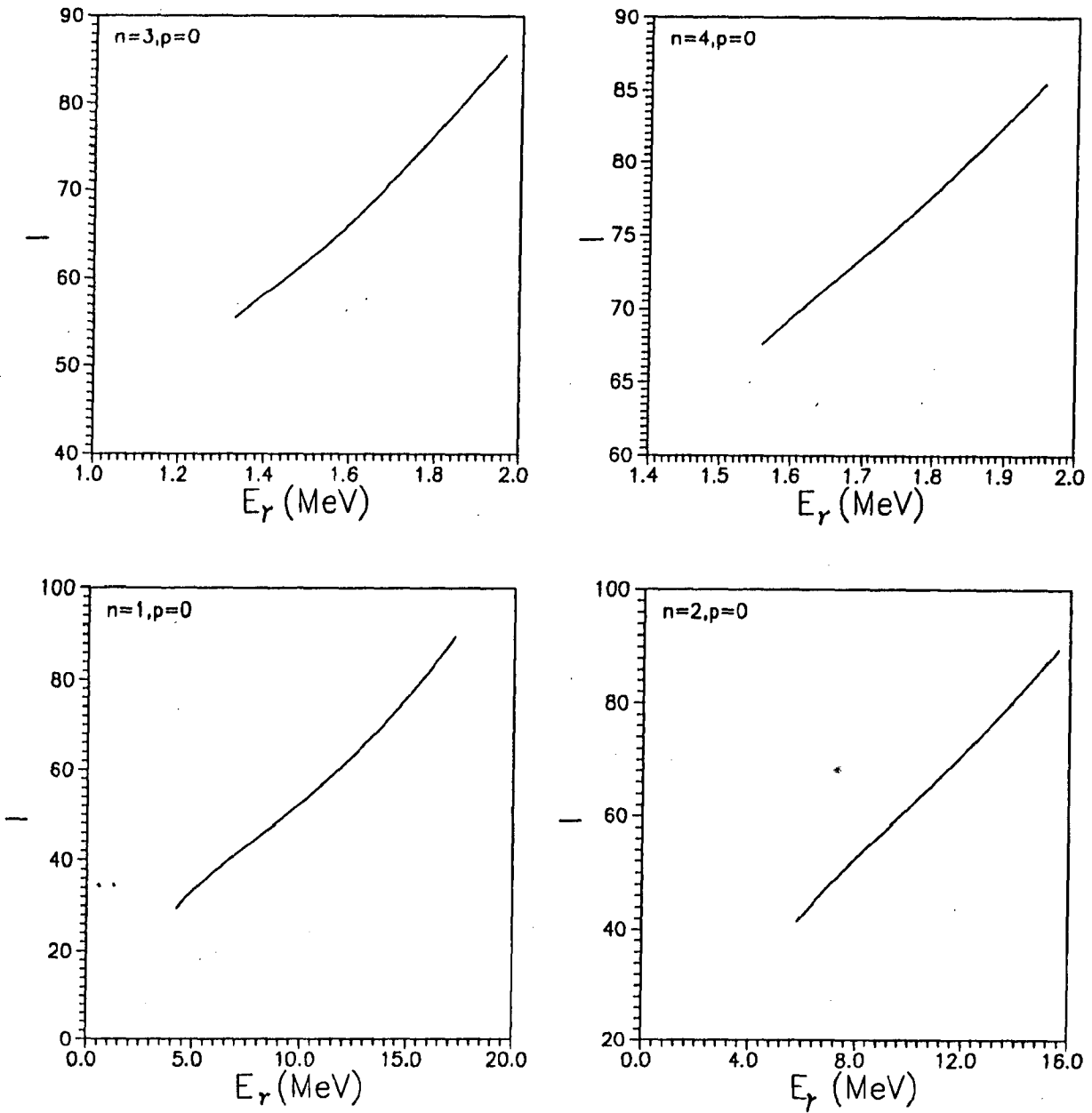


FIG. 2.6 Plots of  $I$  vs.  $E_\gamma(I \rightarrow I - 2)$  at fixed points  $c_\pm$  obtained after SCQ; for  $p=0$ .

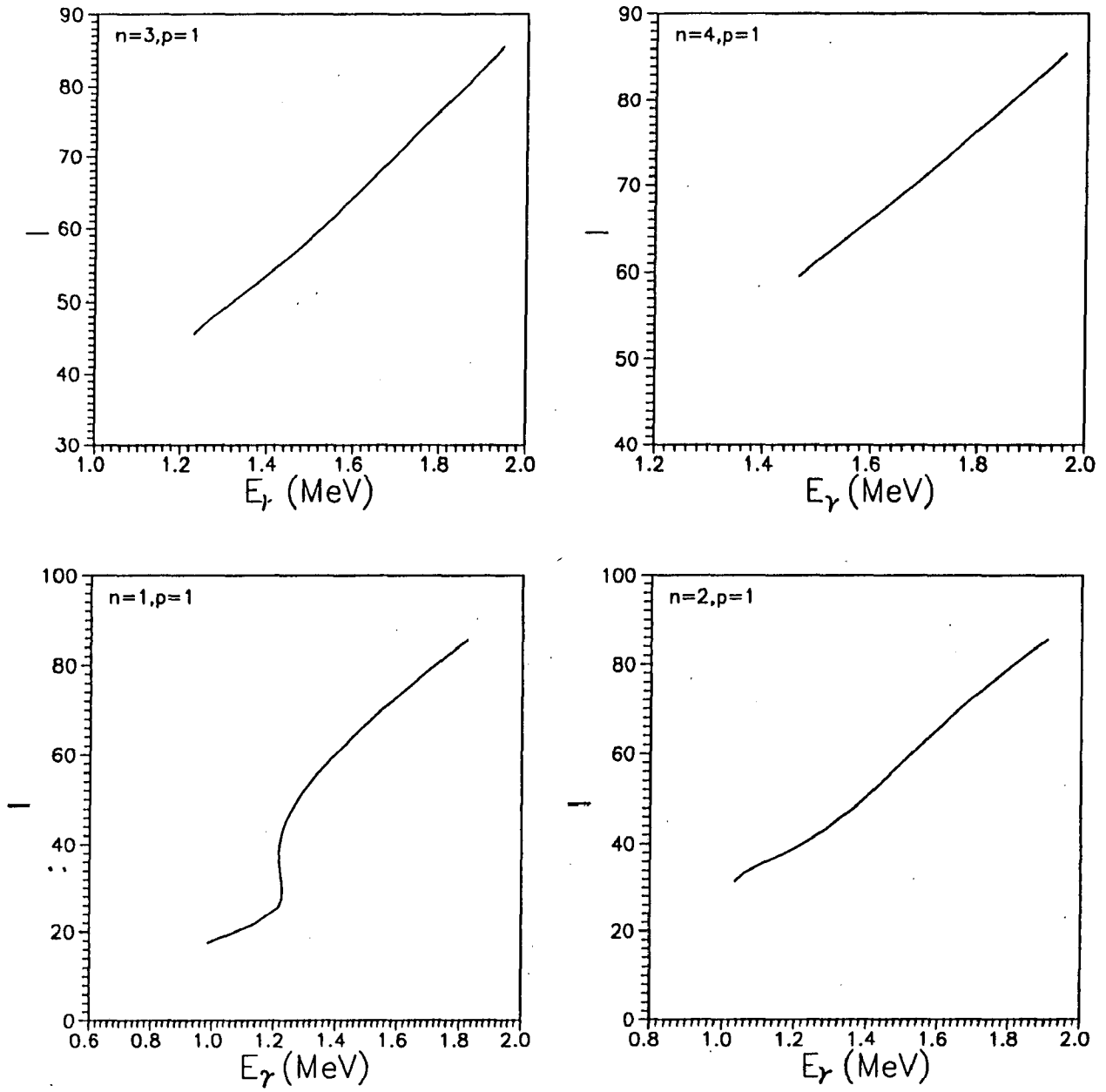


FIG. 2.7 Plots of  $I$  vs.  $E_\gamma(I \rightarrow I - 2)$  at fixed points  $c_\pm$  obtained after SCQ; for  $p=1$ .

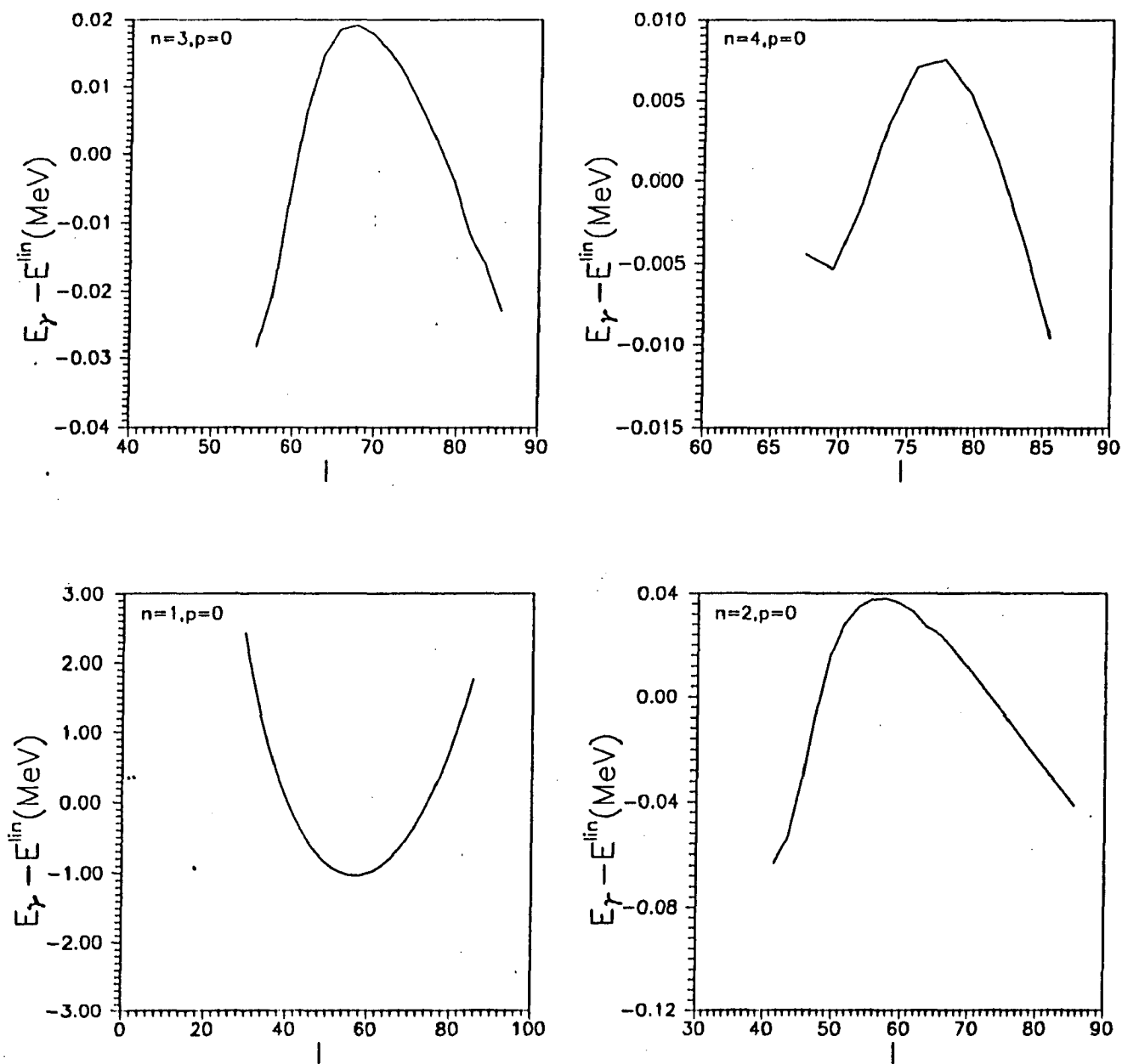


FIG. 2.8 Plots of  $E_\gamma(I \rightarrow I - 2) - E_\gamma^{\text{lin}}(I \rightarrow I - 2)$  vs.  $I$  showing weak oscillations in the gamma ray energies;  $p=0$ .



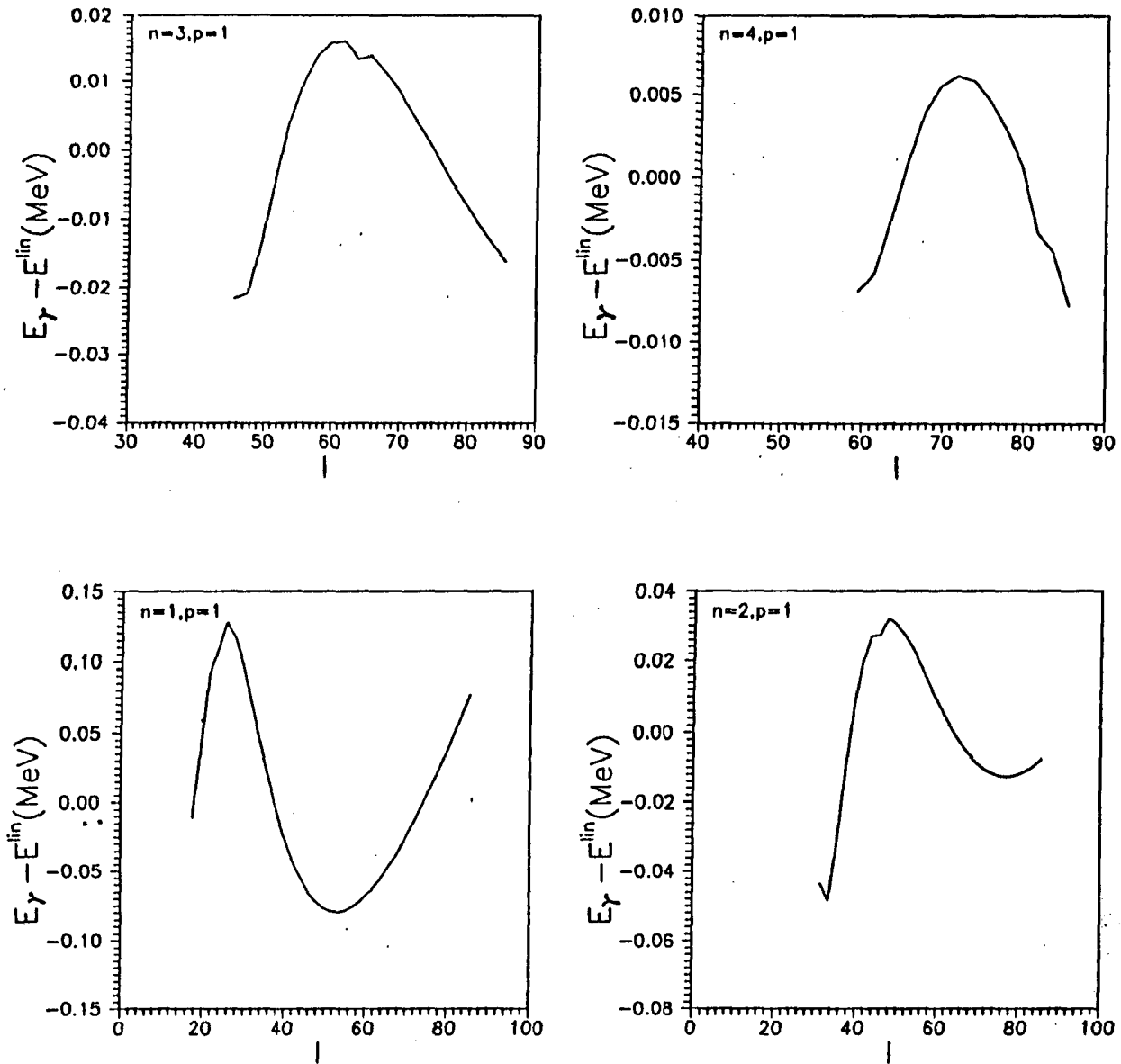


FIG. 2.9 Plots of  $E_\gamma(I \rightarrow I - 2) - E^{lin}(I \rightarrow I - 2)$  vs.  $I$  showing weak oscillations in the gamma ray energies;  $p=1$ .

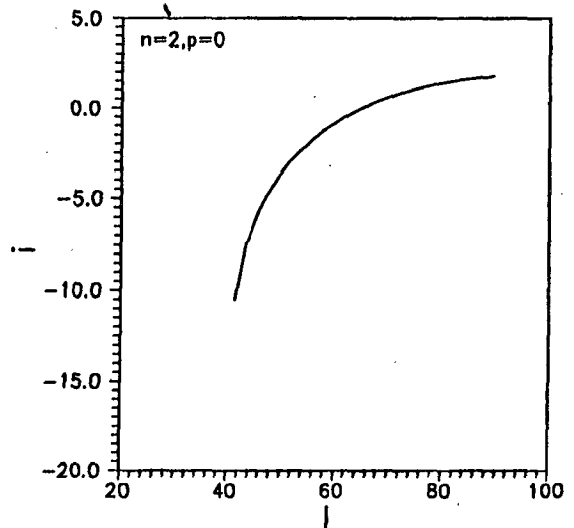
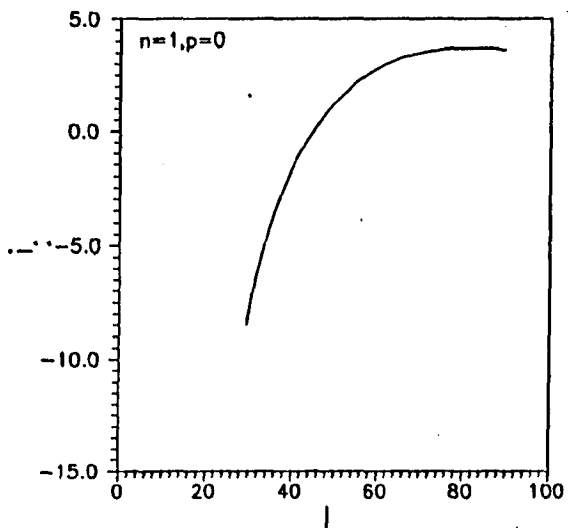
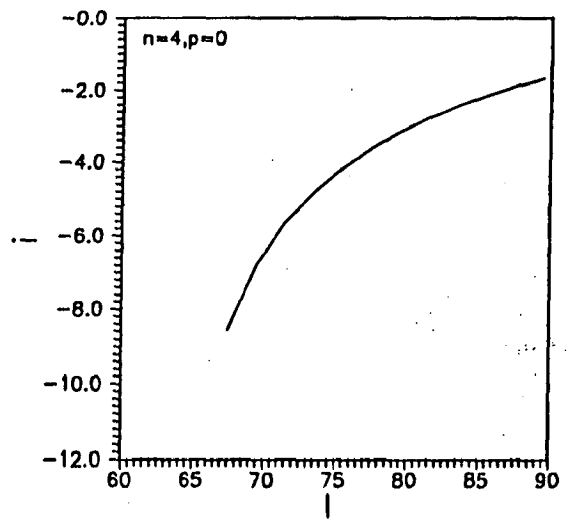
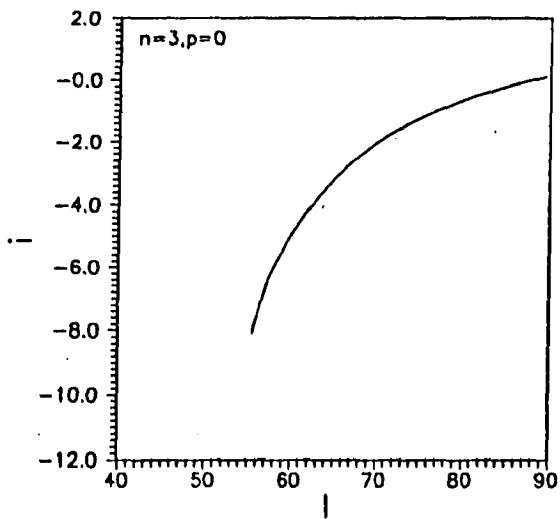


FIG. 2.10 Plots of aligned angular momentum  $i$  vs.  $I$ ;  $p=0$ .

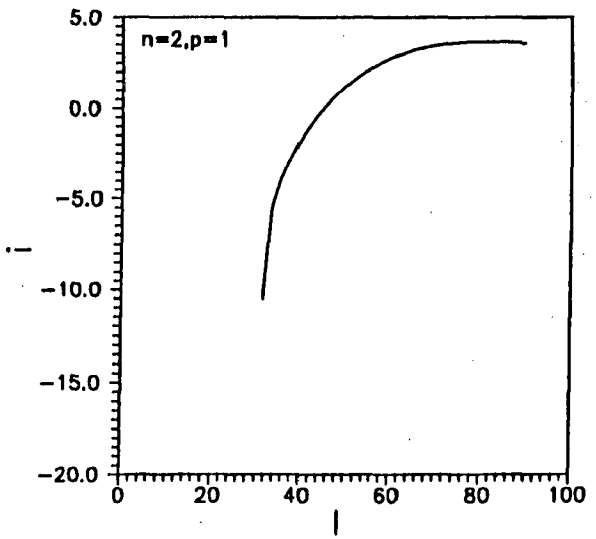
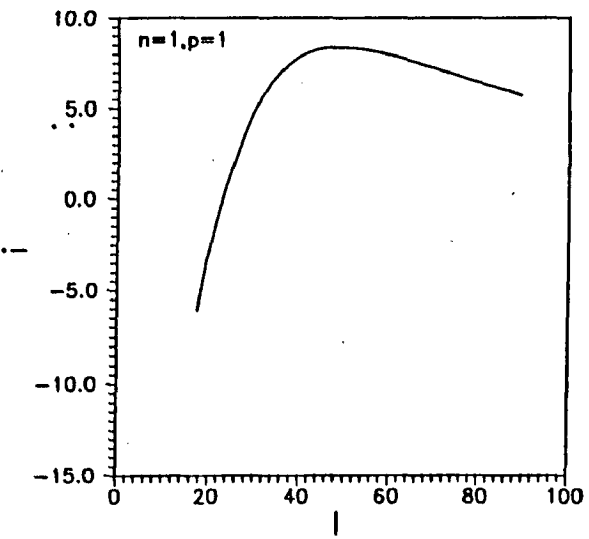
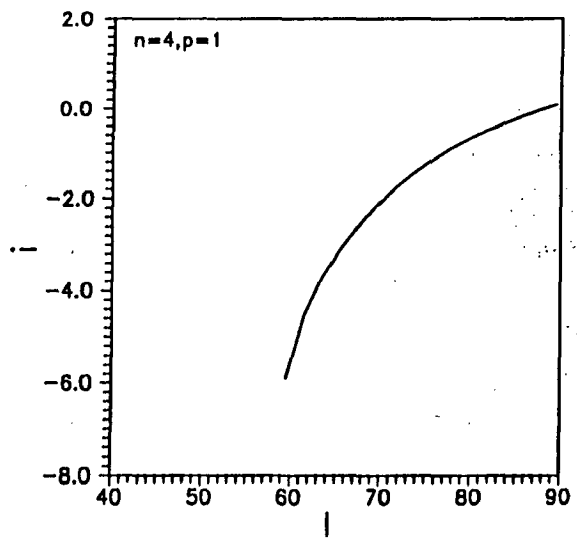
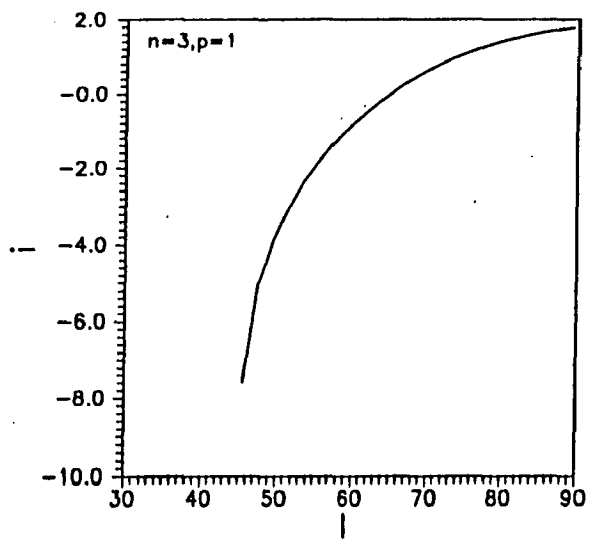


FIG. 2.11 Plots of aligned angular momentum  $i$  vs.  $I$ ;  $p=1$ .

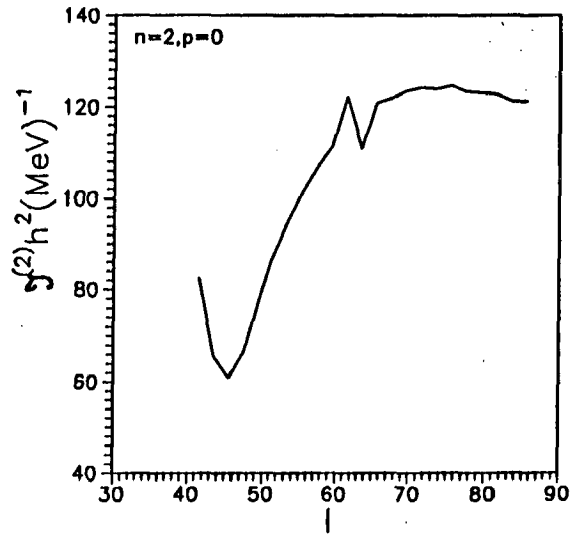
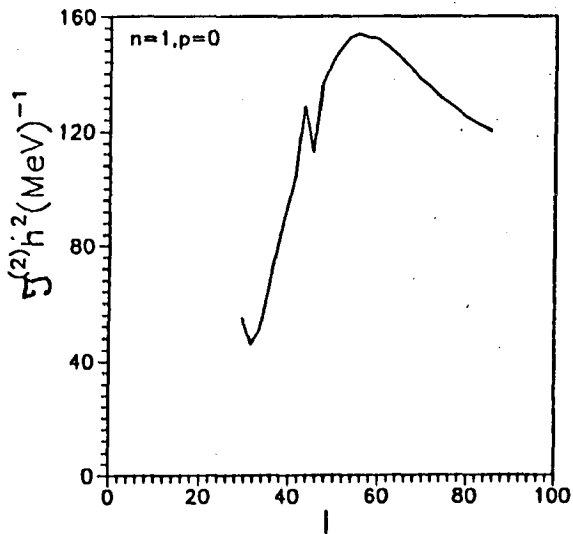
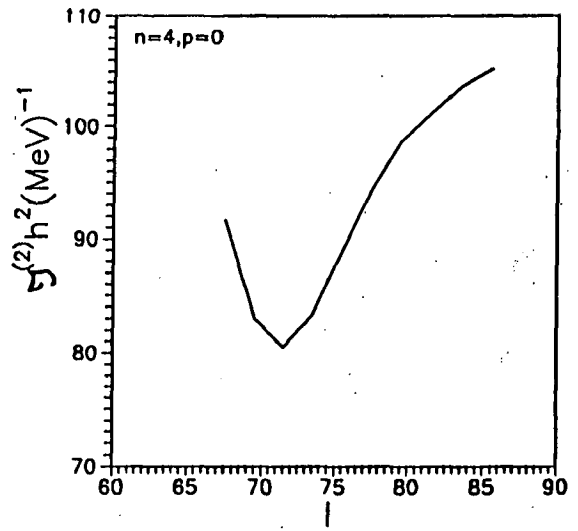
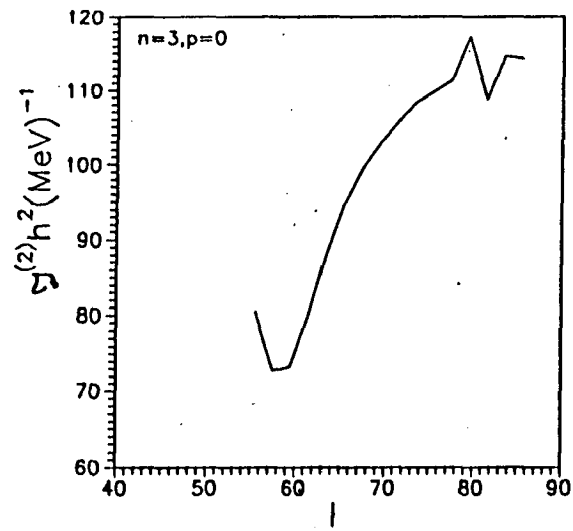


FIG. 2.12 Plots of second moment of inertia  $\mathfrak{I}$  vs.  $I$ ;  $p=0$ .

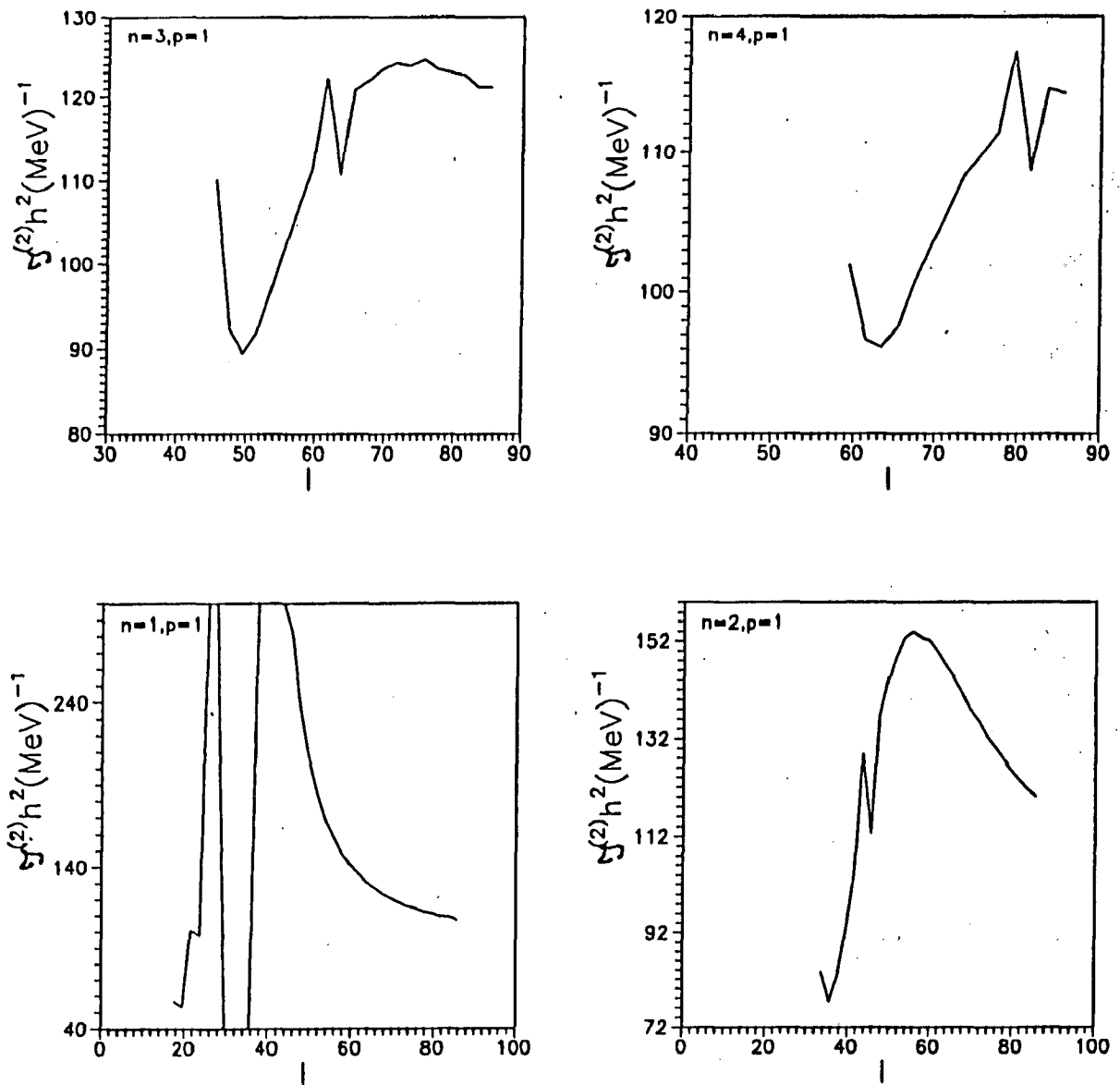


FIG. 2.13 Plots of second moment of inertia  $\mathfrak{I}$  vs.  $I$ ;  $p=1$ .

**CHAPTER III**

**SOME NEW UNIVERSAL**

**FEATURES OF SD BANDS AND**

**EMPIRICAL ANALYSIS OF SD**

**BAND DATA**

## I. INTRODUCTION

The phenomenon of superdeformed bands [110] and some well known features of these bands have already been introduced in chapter I. The aim of this chapter is to bring into light some additional new feature of SD bands pointed out more recently by us [61,62]. In particular, we would establish the following features on the basis of the data on SD bands.

- A weak oscillation in the angular momentum  $I$  vs. the gamma ray energies  $E_\gamma(I \rightarrow I - 2)$  plots.
- A negative intercept on the  $I$  axis of the linear fit through the  $I$  vs.  $E_\gamma$  plots in a large number of SD bands.
- A finite angular momentum for the bandhead of the SD band.
- The  $\Delta I = 2$  staggering is a third order effect compared to the weak oscillation which is a first order effect.
- A feature of general identical band. On the basis of the empirical analysis, we also show that a feature of general identical band (GIB) emerges in  $A = 190$  mass region. This phenomenon of GIB is also present in the other mass regions of SD bands but not as strongly as in the  $A=190$  mass region. The identical bands are therefore just an outcome of this more general feature.

An understanding of these features on the basis of particle-rotor model presented in chapter II will be attempted in this chapter. An empirical analysis of the SD band data based on our understanding clearly establishes the rigid rotor nature of the SD bands and also the negative aligned angular momentum. An explanation of the  $\Delta I = 2$  staggering follows in a most natural way.

## II. NEW EMPIRICAL FEATURES OF SD BANDS

### A. Weak oscillations in the $I$ vs. $E_\gamma$ plots

A very interesting general feature was noticed by us in the  $I$  vs.  $E_\gamma$  plots of the SD bands. We observe that the general nature of  $I$  vs.  $E_\gamma$  plots is almost linear as is evident from the examples shown in FIG. 3.1 for different mass regions [61,99]. It may be noticed that the gamma ray energy exhibits a systematic oscillation around the linear fit to the  $I$  vs.  $E_\gamma$  data. We have verified that such oscillations are present in almost all the SD bands [63]. These oscillations can be seen more clearly by plotting the energy difference  $E_\gamma^{Exp}(I \rightarrow I-2) - E_\gamma^{lin}(I \rightarrow I-2)$  vs.  $I$ . Here  $E_\gamma^{lin}(I \rightarrow I-2)$  represents the gamma ray energies obtained through a linear fit to the SD band data. These plots are shown in FIG. 3.2 (a), (b), (c) and (d) with examples from all the mass regions. It may be noticed that the amplitude of the oscillations is of the order of 10-20 keV. This universal feature of the SD bands gets further support from the observation of the weak oscillations in even-even, odd-A and odd-odd nuclei. For example as many as six SD bands are observed in  $^{194}\text{Tl}$ , which otherwise has very little spectroscopic information known at normal deformation. This suggests that a common mechanism must be operative which leads to the stabilization of the SD bands irrespective of these belonging to an even-even or an odd-odd nucleus. All the properties displayed by these SD bands are also common to other SD bands. It may also be emphasized that the data on SD bands in odd-odd nuclei do not display any new additional feature; it again brings into focus the universal nature of the properties of the SD bands [99].

### B. Negative intercept of the $I$ vs. $E_\gamma$ plots

The linear fit to the  $I$  vs.  $E_\gamma$  plots of the data on SD bands when extrapolated to the  $I$ -axis invariably leads to a negative intercept for the SD bands in  $A=190$  mass region [37]. This feature is also present in a large number of cases from the other mass regions. In the



first column of Table I we list the values of the alignment as obtained from the intercept; as will be shown in this chapter, an empirical analysis based on the particle-rotor model [37] allows us to interpret the values of these intercepts in terms of aligned angular momentum of SD bands. It immediately leads to the unusual conclusion that a large number of SD bands have negative alignment. This however appears to support the interpretation of SD bands built around the fixed points  $c_{\pm}$  located in a region of nonlinearity [63].

### C. Finite angular momentum of the SD bandheads

It is a general observation that the SD bands terminate at the lower end rather abruptly at an angular momentum which may lie anywhere between  $8\hbar$  to  $30\hbar$  [99]. The abrupt termination of the SD bands is explained in terms of the inability of the present day detection techniques. In other words it is believed that the gamma rays decaying out of the lowest observed band level have been fragmented into many weak gamma rays. This has been the biggest stumbling block to the experimental assignment of the angular momentum and parity as well as the excitation energy of the SD bands. Absence of linking transitions should not however be viewed as purely a deficiency of experimental techniques. Recent observation of linking transition in at least two cases [51,76] confirm this because the final level appears to decay out in to many-many paths and only few of the high energy gamma rays could be established.

These observations based on the experimental data suggest that the SD bands have a bandhead which always carries a finite angular momentum, we denote this by  $I_b$ . The empirical systematics of  $I_b$  [99] are shown in FIG. 3.3. It is clear from the FIG. 3.3 that SD bands in a given mass regions have their  $I_b$  values lying in a definite or fixed range of angular momenta. The SD1 bands, which are probably yrast, are plotted in the left block while the rest are plotted in the right. We find that the value of the  $I_b$ , in A=130 mass region, has the largest range extending from  $12.5\hbar$  to  $26.5\hbar$  except for  $^{133}\text{Nd}$  which has the lowest value of  $I_b=8.5\hbar$ . In the A=140-150 mass region, the value of  $I_b$  lies in the range of  $25\hbar - 32\hbar$ .

Finally for the A=190 mass region the value of  $I_b=8\hbar$  to  $12\hbar$ . It is thus clear that each mass region has its own characteristic range of values of  $I_b$ . It may be cautioned that all the angular momentum values listed here are tentative and their experimental determination still remains to be achieved.

#### D. $\Delta I = 2$ Staggering

We now establish that the  $\Delta I = 2$  staggering observed in few cases is a third order effect in gamma ray energies as compared to the weak oscillations which are first order effect and are much more general in nature. It may also be emphasized that a regular  $\Delta I = 2$  staggering has been observed in only three or four cases for example band 1 of  $^{149}\text{Gd}$  and band 1 of  $^{193}\text{Tl}$  [42,55]; it is therefore not a very general feature of all the SD bands. Most of the other SD bands display no such feature or, display an irregular staggering. It is therefore important that any explanation of this feature must therefore give a regular  $\Delta I = 2$  staggering only under special circumstances.

To establish that  $\Delta I = 2$  staggering is a third order effect we first calculate  $\Delta E_\gamma(I) = E_\gamma^{Exp.}(I \rightarrow I - 2) - E_\gamma^{lin}(I \rightarrow I - 2)$ . As an example we list the values  $\Delta E_\gamma(I)$  for  $^{149}\text{Gd}$  band 1 in the II column of Table II. We then define a second difference  $\Delta^2 E_\gamma(I) = \Delta E_\gamma(I) - \Delta E_\gamma(I - 2)$  also listed in column III of Table 2. A third difference defined as  $DD = \Delta^2 E_\gamma(I) - \Delta^2 E_\gamma(I - 2)$ , is given in the fourth column of Table II. Notice that the quantity DD begins to exhibit a small rise or fall in its values for  $I > 37.5\hbar$ , where  $\Delta I = 2$  staggering sets in. This rise and fall in DD is mostly less than 1 keV. It is this third order difference that shows up as  $\Delta I = 2$  staggering.

The weak oscillations in gamma ray energies as discussed above have a magnitude of the order of 10-20 keV [61,62], are observed in most of the SD bands and hence represent a more general feature than  $\Delta I = 2$  staggering.  $\Delta I = 2$  staggering must therefore follow naturally from any explanation that leads to the oscillatory behaviour of I vs.  $E_\gamma$  plots. We shall show that this is indeed the case.

### III. AN EMPIRICAL ANALYSIS OF SD BANDS

A complete discussion of the nonlinear dynamics of the Particle-Rotor model in association with semiclassical quantization (SCQ) procedure was presented in chapter II [63]. We have already shown that the motion around the twin fixed points  $c_{\pm}$  supports rotational bands which display several unusual features. We summarize some of these features as following.

1. The angular momentum  $I$  vs. the gamma ray energies  $E_{\gamma}(I \rightarrow I - 2)$  exhibits a linear behaviour signifying a constant moment of inertia.
2. Inclusion of the nonlinear term in  $j_3$  and subsequent semiclassical quantization (SCQ) introduces weak oscillations in the linear  $I$  vs.  $E_{\gamma}$  plots.
3. The aligned angular momentum of these bands is negative near the bandhead, increases with  $I$  and ultimately becomes positive at large angular momentum.
4. The rotational bands have a bandhead which always has a finite angular momentum which is around  $8\hbar$  or more.
5. The dynamical moment of inertia  $\mathfrak{S}^{(2)}$  is observed to saturate at large angular momentum and decreases slightly at the upper end.

We note that all the features mentioned above resemble very closely with those of the SD bands. A further confirmation of these features can be obtained only from an analysis of the experimental data on SD bands. Taking our cue from the theory, we propose a simple empirical model [37]. Here we assume that the total angular momentum  $I$  of the SD band consists of a rotational part  $\vec{R}$  and an aligned part  $\vec{i}$ ,

$$\vec{I} = \vec{R} + \vec{i}. \quad (1)$$

An almost linear behaviour of  $I$  vs.  $E_{\gamma}$  plots both in theory and experiment suggests that the SD bands can be treated as some kind of aligned bands. The spectrum of a classical rotor with rotational angular momentum  $\vec{R}$  and a decoupled particle with an aligned angular momentum  $\vec{i}$  may be written as

$$E_{rot}(I) = \frac{\hbar^2}{2\mathfrak{S}}[I(I+1) - 2iI + i(i+1)]. \quad (2)$$

The effect of alignment is thus to modify the rotational energy  $\frac{\hbar^2}{2\mathfrak{S}}I(I+1)$  by a term proportional to  $I$ . The gamma-ray transition energies are given by,

$$E_\gamma(I \rightarrow I-2) = \frac{\hbar^2}{2\mathfrak{S}}2[(2I-1) - 2i]. \quad (3)$$

Inverting this relation, we get

$$I = \frac{1}{4} \frac{2\mathfrak{S}}{\hbar^2} E_\gamma(I \rightarrow I-2) + (i + \frac{1}{2}). \quad (4)$$

On a plot of  $I$  vs.  $E_\gamma$ , the slope therefore gives the moment of inertia  $\mathfrak{S}$  and the intercept on the  $I$  axis gives the aligned angular momentum  $i$ . The extrapolation of the line to obtain the intercept is strictly valid only when the moment of inertia is constant. It is observed that the experimental data lie very close to this line. This method however cannot succeed in normal deformed (ND) bands.

It may be remarked that the usual method for extracting experimental alignment by comparing a given band with a reference band (for example the ground state band of an even-even nucleus as the reference band) cannot be used for SD bands for two reasons. First it is difficult to define a reference band for superdeformed nuclei and second the angular momenta are not known precisely. For this reason, only the incremental alignments are discussed in literature [101]. The procedure followed by us therefore promises to give some idea about the aligned angular momentum of SD bands. Our calculations based on the Particle-Rotor model presented in Chap. II are able to account for the weak oscillations around a general linear behaviour in  $I$  vs.  $E_\gamma$  plot. These oscillations are the result of taking into account the nonlinear term in the equation of motion of  $j_3$ . If we ignore the nonlinear term, an exact linear behaviour is obtained. The observed variation in the moment of inertia with angular momentum is therefore a direct result of these oscillations. That the variation is indeed small may be seen from the fact that the change in the moment of inertia of mass 190 SD bands, over a range of angular momentum of the order of  $10\hbar$ , is as little as

1-3 percent. On the other hand, the change in moment of inertia in ND bands is as much as a factor of 3 to 5 of the bandhead value over the same spin range [39]. Most of the SD bands being observed at high spins are thus expected to possess very weak pairing correlation [39]. In view of these discussions, a linear fit to the data of the SD bands by using the eq. (3) becomes meaningful. The moment of inertia obtained from such a linear fit can be taken as an average value of the moment of inertia over the whole band and are listed in column III of Table I. We show in FIG. 3.4, the moment of inertia obtained in this manner for all the yrast and nonyrast SD bands in all the four mass regions. These values are compared with rigid rotor value calculated from the well known relation  $\mathfrak{I}_{rig} = \frac{2}{5}AMR_0^2(1 + 0.31\beta)$ ;  $\beta$  is the deformation parameter obtained from the measured values of the quadrupole moment. The rigid body expression predicts a  $A^{\frac{5}{3}}$  dependence of the moment of inertia on the mass number  $A$ . FIG. 3.4 confirms such a dependence. Moreover the values extracted from the linear fit are always equal to or, slightly greater than the rigid body values. The analysis clearly establishes that the SD bands are rigid rotor in nature [37,69].

The aligned angular momentum or simply the alignment  $i$  is one of the most significant quantities which indicate the nature of the rotational bands. We have extracted this quantity from the intercept on the  $I$  axis and the values are tabulated in column II of Table I. We plot in FIG. 3.5 the alignments for the yrast and non-yrast SD bands. We notice that a negative value is obtained in a large number of cases. It may be recalled that our calculations based on the SCQ theory [63] predicts an alignment which is negative near the bandhead, increases with increasing angular momentum, becomes positive and then saturates. Sometimes a downturn at high angular momentum is also obtained. Alignment however remains negative for a considerable range of angular momentum in the beginning of the band. A constant value of alignment as obtained from the linear fit to the SD data can therefore at best be termed as some kind of averaged out value of the alignment. But the fact that a negative value is obtained in a large number of cases is a very significant result which appears to support the negative alignment predicted by our model. Since our model calculations relate to high- $j$  orbital, it would appear that high- $j$  configurations should be involved in those SD

bands which display a negative alignment behaviour.

#### IV. STARTING ANGULAR MOMENTUM FOR THE BANDHEAD

We have already emphasized that the existence of a finite angular momentum for the bandhead of SD bands is a new and general feature. It would be interesting to see if we can obtain an explanation for the systematics of  $I_b$  on the basis of our model calculations. It should be kept in mind that our model Hamiltonian is highly schematic in nature and has very few parameters. Moreover, the values of these parameters have to be fixed from the nuclear structure information on SD bands and therefore cannot be varied in an arbitrary manner. We present in Table III the set of parameters used to carry out the calculations in the four mass regions namely  $A=80,150,160,190$ . The value of  $j$  was chosen on the basis of the configuration assignments reported in the literature [33,41,8,74]. The deformation parameter was taken to represent the measured values. To keep the effect of parameters to a minimum, we decided to use a constant value of the radial matrix element  $k=40$  MeV [16]. For all the cases, the moment of inertia parameter  $A$  was estimated from the linear fits to the experimental data on SD band gamma ray energies. Using these sets of parameters we obtained the starting angular momentum as reported in Table III. We note that the predicted values for  $n=0, p=0$  case representing yrast SD bands as given in column V of Table III match with the observed values for  $A=130$  and  $190$  mass regions. However the observed values in  $A=80$  and  $150$  mass regions are much larger than the calculated values. There are two ways in which we can reconcile this discrepancy between the theory and experiment. One of the explanations may be given by assigning different  $n$  and  $p$  values [63] to the bands in these mass regions. In Table IV we list the values of  $I_b$  obtained for  $n=0, 1$  and  $2$  with the same set of parameters as listed in Table III. We note that starting angular momentum can lie anywhere between  $6\hbar$  and  $41\hbar$  depending on the  $n$  and  $p$  values. However another reasonable explanation is also possible in terms of the present understanding of SD bands from the Nilsson-Strutinsky calculations [103,104]. It is well known that the SD bands are

observed for the particle number and deformation which stabilise or develop a minimum in the potential energy surfaces (P.E.S) at a finite angular momentum [111]. It is this angular momentum with which a band may be expected to come into existence. Therefore even if lower angular momentum states for SD bands may be possible, they would not be observed if the second minimum develops at a higher angular momentum. Therefore if the second minimum develops at  $I \approx 20\hbar$  for  $A=80$  and  $150$  mass regions, we cannot expect to see states lying lower than  $I \approx 20\hbar$ .

Keeping the second explanation in mind we present in FIG. 3.6 the behaviour of gamma ray energies as calculated from our model and compare them with the behaviour of SD bands observed in  $^{82}\text{Y}$ ,  $^{133}\text{Nd}$ ,  $^{149}\text{Gd}$  and  $^{193}\text{Hg}$ . In plotting the calculated results we terminate the bands at the lower end at the same angular momentum as observed in experimental data [99]. We find that in doing so we automatically obtain the correct phase of the weak oscillatory behaviour of gamma ray energies. The similarity in the calculated results and the observed values is quite remarkable in view of the fact that we are basically changing only three parameters. The amplitude of the oscillations as obtained from our model is larger than the observed amplitudes. This is controlled by the coefficient  $L$  of the nonlinear term in our model. In FIG. 3.7 and FIG. 3.8 we plot the difference  $E_{\gamma}^{Exp.}(I \rightarrow I-2) - E_{\gamma}^{Lin}(I \rightarrow I-2)$  for experimental and theoretical bands respectively. The correspondence between the two figures can be seen clearly. In our model a finite value of the angular momentum  $I_b$  arises from the fact that no solutions at  $c_{\pm}$  are possible below this angular momentum. The quantity  $C(= (4AIj - \tilde{E})\tilde{E})$  becomes negative for  $I > I_b$  which gives rise to a double well in  $j_3$  whose minima are the fixed points  $c_{\pm}$  where the SD bands are supposedly being supported. The saddle point  $b$  is a maximum and corresponds to a completely antialigned state implying a net alignment which is negative. As we increase the energy beyond  $b$  we begin to move towards fixed points  $c_{\pm}$ . The negative alignment for lower angular momentum states at  $c_{\pm}$  is therefore reminiscent of the complete antialigned configuration at fixed point  $b$  [63].

## V. $\Delta I=2$ STAGGERING

The phenomenon of identical bands and  $\Delta I=2$  staggering have proved to be the most difficult to resolve [5,42] among the other unresolved features of SD bands. The SD bands are  $\Delta I=2$  structures with a nearly linear dependence of transition energies  $E_\gamma$  on the angular momentum  $I$ . It was observed that one set of states with  $\Delta I=4$  are slightly shifted in energy with respect to the complimentary set of states. While  $\Delta I=1$  staggering is quite common in rotational bands of odd-A [67] and odd-odd nuclei [68], a  $\Delta I=2$  shift is quite unexpected and puzzling.

This phenomenon has motivated many theoretical studies which have offered explanations in terms of a four-fold  $C_4$  symmetry [52,79,88], a g-boson in IBM [77], mixing of two bands [107], hexadecapole interaction [87] and an intrinsic vortical motion [83]. More recently, studies have attempted to look for similar feature in normal rotational bands and offer an explanation in terms of the sd-IBM [109].

It may be remarked that a regular  $\Delta I=2$  staggering has been observed in only two cases viz., band 1 of  $^{149}\text{Gd}$  and band 1 of  $^{193}\text{Tl}$ ; it is therefore not a general feature of all the SD bands. Most of the other SD bands display such feature over a limited range of angular momenta or, display an irregular staggering. Any explanation of this feature must therefore give a regular  $\Delta I=2$  staggering only occasionally.

Several kind of parameters have been used to quantify the  $\Delta I = 2$  staggering. One of the quantities widely used has been a five-point formula [29]. It has been shown [54] that the feature of staggering depends sensitively on the multi point formula used to analyze the data and may often give misleading conclusions; a one-point formula was therefore proposed which confirmed the presence of  $\Delta I=2$  staggering in only one case i.e.  $^{149}\text{Gd}$ . It is therefore indeed necessary that any conclusion regarding the presence of staggering is based on sound footings. In the present chapter, we have already shown that the  $\Delta I=2$  staggering is a third order effect in transition energies as compared to the weak oscillations superimposed on the linear  $I$  vs.  $E_\gamma$  plots, which are first order effect and have recently been shown to be much



more general in nature [61,62]. A very natural explanation for the weak oscillations in the  $I$  vs.  $E_\gamma(I \rightarrow I-2)$  plots has been provided in terms of the non-linear dynamics of the particle-rotor model [63]. The present section focuses upon the  $\Delta I=2$  staggering and offers a very reasonable explanation in terms of the tunneling effect in the double well potential (DWP) that comes into picture in the non-linear dynamical regime of the particle-rotor model [63]. Unlike the five point formula, the quantity DD introduced in section II.D is a reasonable measure of  $\Delta I=2$  staggering. The oscillations on the other hand have a magnitude of the order of 10-20 keV, are observed in most of the SD bands and hence represent a more general feature than the  $\Delta I=2$  staggering. The  $\Delta I=2$  staggering must therefore follow as a corollary to any explanation that leads to the oscillatory behavior of  $I$  vs.  $E_\gamma$  plots. We now proceed to show that this is indeed the case.

It is most interesting to note that the height of the DWP in  $j_3$  depends on  $n$  and  $I$  as shown in FIG. 3.9. Our DWP is thus energy dependent and the tunnelling between the DWP leads to a shift in the eigenvalues of  $C$  which ultimately results in a shift of the energy eigenvalues. The energies corresponding to different  $I$  for a given  $n$  are therefore shifted differently. Also, the various bands designated by different  $n$  are shifted differently.

We have already shown that these solutions display properties which match closely with the several observed properties of the SD bands [37,63]. We have thus been able to reproduce the weak oscillations in the  $I$  vs.  $E_\gamma$  plots; also the bands start with a finite angular momentum. We now show that the same model is also capable of explaining the  $\Delta I=2$  staggering.

To check the presence of the  $\Delta I=2$  staggering we calculate the quantity DD defined earlier; of course now we replace  $E_\gamma^{Exp.}$  by  $E_\gamma^{Theo.}$ . We plot this quantity DD vs.  $I$  in FIG. 3.10 for  $n=3$ ,  $p=1$  and four values of  $j=7,8,9$  and  $11$ ;  $A=0.005$  MeV in all the cases. We notice that a  $\Delta I=2$  staggering is present in the high spin region; the magnitude of staggering is of the right order and decreases as  $j$  increases. It is our general observation that the  $\Delta I=2$  staggering is more pronounced in  $p=1$  cases than in  $p=0$  cases. In the upper panels of FIG. 3.11 we show the results of  $j=7$ ,  $p=0$ ,  $A=0.006$  MeV and  $n=1$  and  $3$ . We find

that significant staggering is still present in  $n=3, p=0$  case. We also find that the staggering completely disappears when  $A$  is increased to 0.008. The staggering feature thus depends sensitively on  $A$  and  $j$ . In the lower panels of FIG. 3.11, we compare the observed feature of  $\Delta I=2$  staggering in  $^{149}\text{Gd}$  with the  $n=3, p=1$  solution for  $j=9$  and  $A=0.005$  MeV; a nice comparison can be made between the observed features although the calculated staggering starts at a higher angular momentum. The  $\Delta I=2$  staggering is thus directly related to the height of the DWP which in turn depends on  $A, j$  and  $n$ . It may also be stressed that a regular  $\Delta I=2$  staggering is only an occasional feature as obtained experimentally.

The unusual dependence of the depth of the DWP in  $j_3$  on  $I$  has another important consequence. Since the depth goes on increasing with  $I$ , the higher members of a SD band remain well entrenched inside the well and acquire extra stability. This explains the unusual stability of the long cascades of the SD bands.

In conclusion, we find that the observed phenomenon of  $\Delta I=2$  staggering may be understood in terms of the nonlinear features of the particle rotor model. It does not require any extra assumptions. The depth of the fictitious potential  $V(j_3)$  increases with  $I$  as shown in FIG. 3.9. It has a very interesting consequence in terms of the unusual stability of SD bands. As the angular momentum increases, the motion remain well-entrenched in the well.

## VI. IDENTICAL BAND FEATURE

The phenomenon of identical band (IB) is another puzzling feature of SD nuclei which probably remains least understood. It is observed that the SD bands in different nuclei have nearly identical gamma ray energies and therefore nearly identical moment of inertia. The first pair of identical band was discovered in  $^{151}\text{Tb}$  whose excited SD band exhibited gamma ray energies identical with the yrast SD band of  $^{152}\text{Dy}$  to within 1.5keV over 20 transitions [25]. After the discovery of IB in SD nuclei, attention was focused on discovering similar features in normal deformed (ND) nuclei also. Existence of twined bands among several even-even cores and their adjacent odd-N and odd-Z nuclei were shown for the first time

by Jain et al. [60,72]. Later on existence of such twined bands in widely dispersed nuclei was also pointed out by Jain and Sood [100] and later on interpreted in terms of F-spin multiplets by Jain and Casten [64]. In the present section we primarily concentrate upon the identical band feature of SD bands. For a detailed review of the IB phenomenon in deformed and superdeformed nuclei one may refer to reference [102].

The discovery of IB phenomenon implies that the valence particles beyond the SD shell closure do not influence the core as much as they do in ND nuclei. In other words the valence particles remain decoupled from the core and therefore a simple interpretation of the IB phenomenon may be sought in terms of an aligned or a decoupled structure. This premise forms the basis of several explanations including the one based on pseudo spin alignment [102]. The role of high-N intruder orbitals appears to be crucial in deciding the identity of the bands. The empirical model presented by us in this chapter is also based on the same assumptions. The aim of this subsection is to use the results of this empirical analysis along with a reasonable criterion for identical bands and to show that in this process we arrive at a new phenomenon termed as the general identical band (GIB). In other words we show that a substantial number of SD bands come very close to a reference band in each mass region and give rise to the GIB phenomenon.

A number of criteria have been used in the literature for defining two bands as identical bands. A detailed discussion of these criteria may be found in the review [5]. These criteria are based on the closeness of gamma ray energies in the two bands or a matching of dynamical or kinematic moment of inertia. It is important to note that ultimately all the criteria use the gamma ray energy as the basic input. However since the angular momenta of SD band levels are still not measured quantities, the dynamic moment of inertia is preferred by several authors.

To identify the identical bands, one tries to bring the transition energies of a SD band as close as possible to the transition energies of another SD band in a neighbouring nucleus; this is achieved by suitably displacing the angular momentum of one across the other. Let the gamma ray energies of band  $R$  and  $S$  be represented by  $E_\gamma(I_R)$  and  $E_\gamma(I_S)$  respectively,

where the transitions correspond to  $(I_R \rightarrow I_R - 2)$  and  $(I_S \rightarrow I_S - 2)$ . The two SD bands R and S which belong to different nuclei may be said to have an IB pattern if the difference in gamma ray energies  $\Delta E$  tends to vanish or, is small.

$$\Delta E = E_\gamma(I_R) - E_\gamma(I_S) \approx 0. \quad (5)$$

The criterion may be further extended to include half average,  $(1/4, 3/4)$  average or  $(3/4, 1/4)$  average of gamma ray energies becoming identical to the gamma ray energies of the reference band as defined below [40]:

$$\Delta E \equiv E_\gamma(I_R) - \frac{1}{2}[E_\gamma(I_{S+2}) + E_\gamma(I_S)], \quad (6)$$

$$\Delta E \equiv E_\gamma(I_R) - \frac{1}{4}[E_\gamma(I_{S+2}) + 3E_\gamma(I_S)], \quad (7)$$

$$\Delta E \equiv E_\gamma(I_R) - \frac{1}{4}[E_\gamma(3I_{S+2}) + E_\gamma(I_S)]. \quad (8)$$

These four criteria can in fact be generalised to write a general expression for the average gamma ray energies  $E'_\gamma(I_S)$  as follows [26],

$$E'_\gamma(I_S) = xE_\gamma(I_S) + (1 - x)E_\gamma(I_S + 2). \quad (9)$$

In this equation  $x$  is a parameter which may be continuously varied in the interval  $[0,1]$ . The gamma ray energies so obtained may be compared with the reference band to check the smallness of the quantity.

$$\Delta E = E_\gamma(I_R) - E'_\gamma(I_S). \quad (10)$$

There are two points to be further decided in making this comparison. One is the relative displacement of band S with respect to the band R (which is our reference band) by  $\Delta I$  in order to obtain the best matching. And second is to decide how small  $\Delta E$  should be so that bands R and S may be called identical. According to equation (3),

$$E_\gamma(I_R) = 2A[2(I_R - 1) - 2i_R], \quad (11)$$

$$E_\gamma(I_S) = 2A[2(I_S - 1) - 2i_S], \quad (12)$$

where we have chosen the rotational parameter approximately the same for both the nuclei. This immediately leads us to the following value for  $\Delta E$  (equation (10))

$$\Delta E = 4A[(I_R - I_S - 2(1 - x) - (i_R - i_S)], \quad (13)$$

$$= 4A[\Delta I - 2(1 - x) - \Delta i]. \quad (14)$$

In the ideal situation  $\Delta E \approx 0$  which implies that

$$\Delta I = 2(1 - x) + \Delta i. \quad (15)$$

From the least square fitting of data on SD bands we already know the quantities  $A$ ,  $i_R$  and  $i_S$ . The quantity  $x$  is obtained by a procedure of minimizing the difference  $\Delta E$  in equation (10). Using the value of  $x$ , we obtain  $\Delta I$  by which the band S should be shifted with respect to the band R in order to make them identical.

To obtain an upper limit on the value of  $\Delta E$ , we further define a quantity called fractional change (FC) [88] in the kinematic moment of inertia of two bands R and S.

$$FC = \frac{\mathfrak{S}_R^{(1)} - \mathfrak{S}_S^{(1)}}{\mathfrak{S}_R^{(1)}}. \quad (16)$$

If  $\mathfrak{S}_R^{(1)}$  and  $\mathfrak{S}_S^{(1)}$  are approximated by the respective rigid rotor value, the above FC will reduce to

$$FC = \frac{\Delta(A^{\frac{5}{3}})}{A^{\frac{5}{3}}}, \quad (17)$$

where  $A$  are the mass numbers of respective nuclei. Whether or not two bands are identical depends on the value of  $\epsilon_0$ , where

$$\epsilon_0 = (FC)(E_\gamma), \quad (18)$$

since the two bands are identical only if the energy difference  $\Delta E$  between the two is less than the allowed change in gamma ray energies  $\epsilon_0$  resulting from the difference in their

masses. The gamma ray energies in the four mass regions i.e.  $A=130, 150, 190$  are of the order of 1 MeV and in  $A=190$  mass region are of the order of 0.5 MeV. The values of  $\epsilon_0$  for various  $\Delta A$  (change in mass) are listed in Table V. The last column in Table V lists the largest RMSD that we come across in the  $A=190$  mass region while identifying the identical bands; it should be less than the corresponding limit of  $\epsilon_0$  for two bands to be identical.

#### A. $A=190$ Mass region

First we present an analysis of the SD bands in  $A=190$  mass region using the procedure outlined above. The quantity  $\Delta E$  which should vanish for the existence of identical bands was obtained on the assumption that the parameter  $A$  remains constant when going from band R to band S. However a change in the mass of nuclei is expected to give rise to a minimal change in gamma ray energies as listed in Table V. The observed change in  $\Delta E$  should therefore be less than this limit  $\epsilon_0$  in order that band R and S may be said to form an IB pair. In this analysis we choose SD band 1 of  $^{192}\text{Hg}$  as the reference band R and treat all other SD bands as band S. In Table VI we list the bands which could be identified as identical with band R. Out of a total number of 53 bands, 32 bands are found to be identical with band R. When we plot these bands on  $I$  vs.  $E_\gamma$  plots, properly displaced with respect to each other by  $\Delta I$  obtained from equation (15), all the SD bands appear to coalesce with the reference band giving rise to a General Identical Band (GIB). As is evident from FIG. 3.12 there is further scope to bring these bands still closer to the reference band R. This may be done by using a more refined expression for describing the SD bands rather than the simple linear equations (11) and (12) used by us. Emergence of the GIB feature substantiates the general observation that the SD bands appear to be rather insensitive to their configurations.

The SD bands which could not be identified with the SD1 band in  $^{192}\text{Hg}$  are listed in Table VII. We find that if we drop a few transitions from the top of these bands, it is possible to identify these bands also with the band R; the resulting RMSD (root mean

248233



square deviation) for these bands with the truncated cascade are also listed in Table VII. The RMSD values are certainly higher than those for bands in Table V. This indicates that these bands do not form as good GIB pattern as those listed in Table VI but within the limit  $\epsilon_0$ .

### B. A=130, 140 and 150 mass regions

Following the same procedure as outlined for A=190 mass region, we carried out an analysis for the SD bands A=130, 140 and 150 mass regions. We have chosen the SD band in  $^{133}\text{Nd}$ ,  $^{146}\text{Gd}$  and  $^{152}\text{Dy}1$  as the reference band R for our analysis in respective mass regions. The upper limit in the variation of gamma ray energies  $\Delta E$  are again found out. We find that in A=130 mass region 8 out of 11 SD bands satisfy the criteria of identical bands. The corresponding  $I$  vs.  $E_\gamma$  plot is shown in FIG. 3.13. In A=140 mass region only 7 out of 14 SD bands coalesce with the reference band; corresponding plot of  $I$  vs.  $E_\gamma$  is shown in FIG. 3.14. In mass 150 region, 17 out of 27 SD bands appear to form GIB pattern as shown in FIG. 3.15. It is clear from the figures that the GIB pattern or phenomenon is observed with the greatest accuracy in A=190 mass region. The deviations in the other mass regions are larger.

## VII. CONCLUSIONS

A detailed presentation of the results and their discussion has already been made in each section. We present here the highlights of this chapter and a summary of the results.

On the basis of the SD band data, we have shown that the SD bands exhibit weak oscillations in the  $I$  vs.  $E_\gamma$  plots, are more likely to have a negative intercept on the  $I$  axis in these plots and possess a finite angular momentum for bandhead which is greater than  $8\hbar$ . Also we have shown that  $\Delta I = 2$  staggering is a third order effect and probably an outcome of the weak oscillations which are first order effect.

An empirical analysis of the SD band, carried out on the basis of a simple expression for decoupled bands, leads us to moment of inertia values for SD bands which are close to the rigid rotor moment of inertia. Further the negative aligned angular momentum suggests that most of the SD bands are located near the fixed points  $c_{\pm}$  in a region of chaos.

We also present the systematics of the starting angular momentum,  $I_b$ , and show that it is possible to reconcile these systematics with the results of our schematic particle-rotor model results.

The  $\Delta I = 2$  is shown to be a feeble third order effect arising out of the first order weak oscillations. Since our model calculations reproduce the weak oscillations should also reproduce the  $\Delta I = 2$  staggering provided effect of tunneling in the DWP is taken into account. We have shown that this is indeed the case.

We also present an interesting analysis, where we show that the SD bands are quite similar to each other at least within a mass region. Their similar behaviour can be exploited to obtain a general identical band feature. We show that the SD bands in  $A=190$  mass region most easily form a GIB pattern. The SD bands from other mass regions are not so well behaved. This feature focusses our attention on the universality of the SD band phenomenon cutting across the various mass regions and various types of nuclei (even-even, odd-A and odd-odd). Although we cannot provide any explanation for such a wide scale similarity, we believe that the phenomenon is important enough to warrant a deeper study of the SD bands. It is our hope that more fundamental theories like the periodic orbit theory may be able to throw some light on the unusual scaling behaviour of the SD bands.



TABLES

TABLE I. Values of alignment  $i$  and moment of inertia  $\mathcal{I}$  from fitting of experimental data

SD Band	$i$	$\mathcal{I}$
$^{82}\text{Sr}1$	2.69	24.86
$^{82}\text{Sr}2$	1.27	26.19
$^{83}\text{Sr}$	4.21	27.06
$^{84}\text{Zr}$	3.13	25.75
$^{130}\text{La}$	-1.61	50.24
$^{131}\text{Ce}1$	-1.25	58.15
$^{132}\text{Ce}1$	0.45	51.22
$^{133}\text{Ce}1$	3.53	54.82
$^{133}\text{Ce}2$	1.25	54.35
$^{133}\text{Ce}3$	-7.58	68.58
$^{133}\text{Pr}1$	4.64	55.91
$^{133}\text{Pr}2$	5.09	55.04
$^{133}\text{Pr}3$	8.44	50.17
$^{133}\text{Pr}4$	7.87	52.27
$^{133}\text{Nd}$	-0.35	55.09
$^{135}\text{Nd}$	-1.71	58.38
$^{136}\text{Nd}$	-1.81	55.37
$^{137}\text{Nd}$	-4.01	64.63

Table I continued, for  $A \approx 140$

SD Band	$i$	$\mathfrak{S}$
$^{142}\text{Sm}$	4.72	64.74
$^{142}\text{Eu}$	5.22	66.18
$^{143}\text{Eu}$	1.48	67.12
$^{146}\text{Gd1}$	2.36	78.12
$^{146}\text{Gd2}$	5.08	71.37
$^{147}\text{Gd1}$	2.04	77.29
$^{147}\text{Gd2}$	6.39	71.96
$^{148}\text{Gd1}$	6.12	71.81
$^{148}\text{Gd2}$	1.86	80.24
$^{149}\text{Gd1}$	4.65	75.18
$^{149}\text{Gd2}$	0.62	80.49
$^{149}\text{Gd3}$	5.69	75.91
$^{149}\text{Gd3}$	5.70	75.91
$^{149}\text{Gd4}$	2.46	84.38
$^{149}\text{Gd5}$	6.70	71.06
$^{149}\text{Gd6}$	6.41	71.33

Table I continued, for  $A \approx 150$ 

SD Band	$i$	$g$
$^{150}\text{Gd}1$	-1.43	88.09
$^{150}\text{Gd}2$	0.66	83.90
$^{150}\text{Gd}3$	2.90	75.37
$^{150}\text{Gd}4$	3.49	74.37
$^{150}\text{Gd}5$	-3.25	89.97
$^{150}\text{Tb}1$	3.21	75.75
$^{151}\text{Tb}1$	0.27	83.80
$^{151}\text{Tb}2$	0.78	84.79
$^{151}\text{Tb}3$	1.27	82.15
$^{151}\text{Tb}4$	0.85	83.55
$^{151}\text{Tb}5$	1.19	76.05
$^{151}\text{Tb}6$	0.99	76.38
$^{151}\text{Tb}7$	0.19	76.52
$^{151}\text{Tb}8$	0.06	76.78
$^{152}\text{Tb}1$	-1.21	83.11
$^{152}\text{Tb}2$	-2.06	84.71
$^{151}\text{Dy}1$	2.13	78.65
$^{152}\text{Dy}1$	0.36	79.06
$^{153}\text{Dy}1$	1.78	87.03
$^{153}\text{Dy}2$	2.66	84.08
$^{153}\text{Dy}3$	2.63	84.29
$^{153}\text{Dy}4$	0.53	84.87
$^{153}\text{Dy}5$	2.71	84.56
$^{154}\text{Er}$	0.75	78.06

Table I continued, for  $A \approx 190$ 

SD Band	$i$	$Q$
$^{191}\text{Au}$	-1.68	106.81
$^{189}\text{Hg}$	-3.48	104.83
$^{190}\text{Hg}1$	-5.42	112.98
$^{190}\text{Hg}2$	-4.73	122.31
$^{191}\text{Hg}1$	-0.37	108.75
$^{191}\text{Hg}2$	-1.86	107.02
$^{191}\text{Hg}3$	-3.14	109.98
$^{191}\text{Hg}4$	-0.76	101.48
$^{192}\text{Hg}1$	-4.07	114.00
$^{192}\text{Hg}2$	-4.36	120.83
$^{193}\text{Hg}1$	-4.05	119.41
$^{193}\text{Hg}2$	-3.75	115.69
$^{193}\text{Hg}3$	-3.44	114.68
$^{193}\text{Hg}4$	-3.75	115.69
$^{193}\text{Hg}5$	-1.30	109.10
$^{193}\text{Hg}6$	-0.87	103.04
$^{194}\text{Hg}1$	-4.40	115.88
$^{194}\text{Hg}2$	-3.13	114.02
$^{194}\text{Hg}3$	-3.75	116.06
$^{193}\text{Tl}1$	-1.49	106.58
$^{193}\text{Tl}2$	-1.99	109.48
$^{194}\text{Tl}1$	-1.56	110.18

Table I continued, for  $A \approx 190$ 

SD Band	$i$	$Q$
$^{194}\text{Tl}2$	-1.22	108.97
$^{194}\text{Tl}3$	-1.89	108.42
$^{194}\text{Tl}4$	-1.66	107.41
$^{194}\text{Tl}5$	-0.91	108.96
$^{194}\text{Tl}6$	-0.82	108.08
$^{195}\text{Tl}1$	-1.56	107.34
$^{195}\text{Tl}2$	-2.19	111.16
$^{192}\text{Pb}$	-2.33	104.39
$^{193}\text{Pb}1$	0.94	101.066
$^{193}\text{Pb}2$	0.99	94.39
$^{193}\text{Pb}3$	-1.29	103.82
$^{193}\text{Pb}4$	-2.15	108.17
$^{193}\text{Pb}5$	-1.04	102.18
$^{193}\text{Pb}6$	-1.43	104.28
$^{194}\text{Pb}1$	-1.86	104.27
$^{195}\text{Pb}1$	-0.50	102.62
$^{195}\text{Pb}2$	-0.03	98.39
$^{195}\text{Pb}3$	-1.86	106.48
$^{195}\text{Pb}4$	-1.63	104.99
$^{196}\text{Pb}1$	-2.03	102.52
$^{196}\text{Pb}2$	-1.62	104.48
$^{196}\text{Pb}3$	-1.85	105.72
$^{198}\text{Pb}$	-2.49	101.88
$^{197}\text{Bi}1$	-0.32	98.51
$^{197}\text{Bi}2$	-0.53	100.47

TABLE II. A comparison of various quantities as obtained from the experimental data of SD

band 1 in  $^{149}\text{Gd}$

I	$\Delta E_\gamma$ (keV)	$\Delta^2 E_\gamma$ (keV)	DD (keV)
25.5	23.25	-6.81	1.21
27.5	16.44	-5.60	0.29
29.5	10.84	-5.31	0.50
31.5	5.53	-4.81	0.60
33.5	0.72	-4.21	0.61
35.5	-3.49	-3.60	0.79
37.5	-7.09	-2.81	1.2
39.5	-9.90	-1.61	0.4
41.5	-11.51	-1.21	1.11
43.5	-12.72	-0.10	0.29
45.5	-12.82	0.19	1.2
47.5	-12.63	1.39	0.1
49.5	-11.24	1.49	0.81
51.5	-9.75	2.30	0.09
53.5	-7.45	2.39	1.0
55.5	-5.06	3.39	-0.3
57.5	-1.67	3.09	1.01

TABLE III. Values of Parameters and Starting Angular Momentum  $I_b$ .

A	$j$	$\beta$	$A = \frac{\hbar^2}{2\mathcal{I}}(\text{MeV})$	$I_b(\text{Exp.})$	$I_b(\text{Theo.})$
80	4.5	0.55	0.02	20	6
130	5.5	0.4	0.009	8.5	8.5
150	7.5	0.6	0.0066	25.5	7.5
190	7.5	0.45	0.0042	9.5	9.5

TABLE IV. Value of Starting Angular Momentum  $I_b$  for various  $n$  and  $p$  values

A	$I_b$ for $n=0,p=0$	$I_b$ for $n=1,p=0$	$I_b$ for $n=1,p=1$	$I_b$ for $n=2,p=0$	$I_b$ for $n=2,p=2$
80	6	14	8	22	16
130	8.5	21.5	11.5	33.5	23.5
150	7.5	19.5	11.5	27.5	21.5
190	9.5	27.5	15.5	41.5	31.5

TABLE V. Values of Tolerance Limit( $\epsilon_0$ ) for mass 190 region

$\Delta A$	$\epsilon_0(\text{keV})$	Upper Limit of RMSD (keV)
$\pm 1$	4.3	3.4
$\pm 2$	8.5	4.9
$\pm 3$	12.7	3.7
$\pm 4$	16.9	2.0
$\pm 5$	20.9	1.9
$\pm 6$	24.9	1.9



TABLE VI. Values of  $x$ , RMSD and  $\Delta I$  for GIB feature in mass 190 region

SD Band	$x$	RMSD	$\Delta I$
$^{191}\text{Au}$	0.25	1.18	-0.89
$^{190}\text{Hg}2$	0.25	1.84	2.16
$^{191}\text{Hg}2$	0.85	3.44	-1.29
$^{191}\text{Hg}3$	0.25	1.13	0.57
$^{193}\text{Hg}2$	0.80	1.29	0.02
$^{193}\text{Hg}3$	0.30	1.56	0.77
$^{193}\text{Hg}4$	0.80	1.53	0.26
$^{194}\text{Hg}1$	0.85	3.75	0.60
$^{194}\text{Hg}2$	0.55	1.98	-0.07
$^{194}\text{Hg}3$	0.00	1.53	1.65
$^{191}\text{Tl}1$	0.50	2.55	-0.91
$^{191}\text{Tl}2$	0.95	1.14	-0.75
$^{193}\text{Tl}1$	0.25	4.67	-0.74
$^{193}\text{Tl}2$	0.60	2.97	-1.09
$^{194}\text{Tl}1$	0.05	2.56	-0.61
$^{194}\text{Tl}2$	0.55	4.95	-1.95
$^{194}\text{Tl}3$	0.45	2.28	-1.08
$^{194}\text{Tl}4$	0.00	3.29	-0.41
$^{195}\text{Tl}1$	0.30	2.89	-1.11
$^{195}\text{Tl}2$	0.65	3.79	-1.18
$^{192}\text{Pb}$	0.10	0.72	0.05
$^{193}\text{Pb}3$	0.85	4.24	-2.3
$^{193}\text{Pb}4$	0.25	1.05	0.22
$^{193}\text{Pb}5$	0.85	2.04	-2.1

Table VI continued,

SD Band	$x$	RMSD	$\Delta I$
$^{193}\text{Pb6}$	0.35	2.41	-0.71
$^{194}\text{Pb1}$	1.00	2.36	-1.88
$^{195}\text{Pb3}$	0.40	2.47	-1.01
$^{195}\text{Pb4}$	0.40	1.76	-2.34
$^{196}\text{Pb2}$	0.75	1.72	-1.95
$^{196}\text{Pb3}$	0.20	2.07	-0.62
$^{197}\text{Bi}$	0.30	1.95	-2.00
$^{198}\text{Po}$	0.20	1.91	-1.06

TABLE VII. Values of  $x$ , RMSD and Number of transitions taken into account for the bands

which could not be identified with reference band

SD Band	$x$	RMSD	No. of Transitions
$^{189}\text{Hg}$	0.80	4.77	7
$^{190}\text{Hg}1$	0.60	4.85	9
$^{191}\text{Hg}1$	0.35	4.28	11
$^{191}\text{Hg}4$	0.70	6.03	7
$^{192}\text{Hg}2$	0.45	3.88	11
$^{193}\text{Hg}1$	0.25	4.10	8
$^{193}\text{Hg}5$	0.75	4.95	9
$^{193}\text{Hg}6$	0.65	4.63	9
$^{195}\text{Hg}1$	0.60	4.98	15
$^{195}\text{Hg}2$	0.15	4.72	14
$^{195}\text{Hg}3$	0.70	4.74	10
$^{195}\text{Hg}4$	1.00	4.26	14
$^{194}\text{Tl}5$	0.05	6.68	7
$^{194}\text{Tl}6$	0.55	6.39	7
$^{193}\text{Pb}1$	0.50	4.14	9
$^{193}\text{Pb}2$	0.50	4.19	8
$^{195}\text{Pb}1$	0.10	4.11	12
$^{195}\text{Pb}2$	0.70	4.41	11
$^{196}\text{Pb}1$	0.15	4.92	10
$^{198}\text{Pb}$	0.35	5.92	7
$^{196}\text{Bi}$	0.85	3.75	6

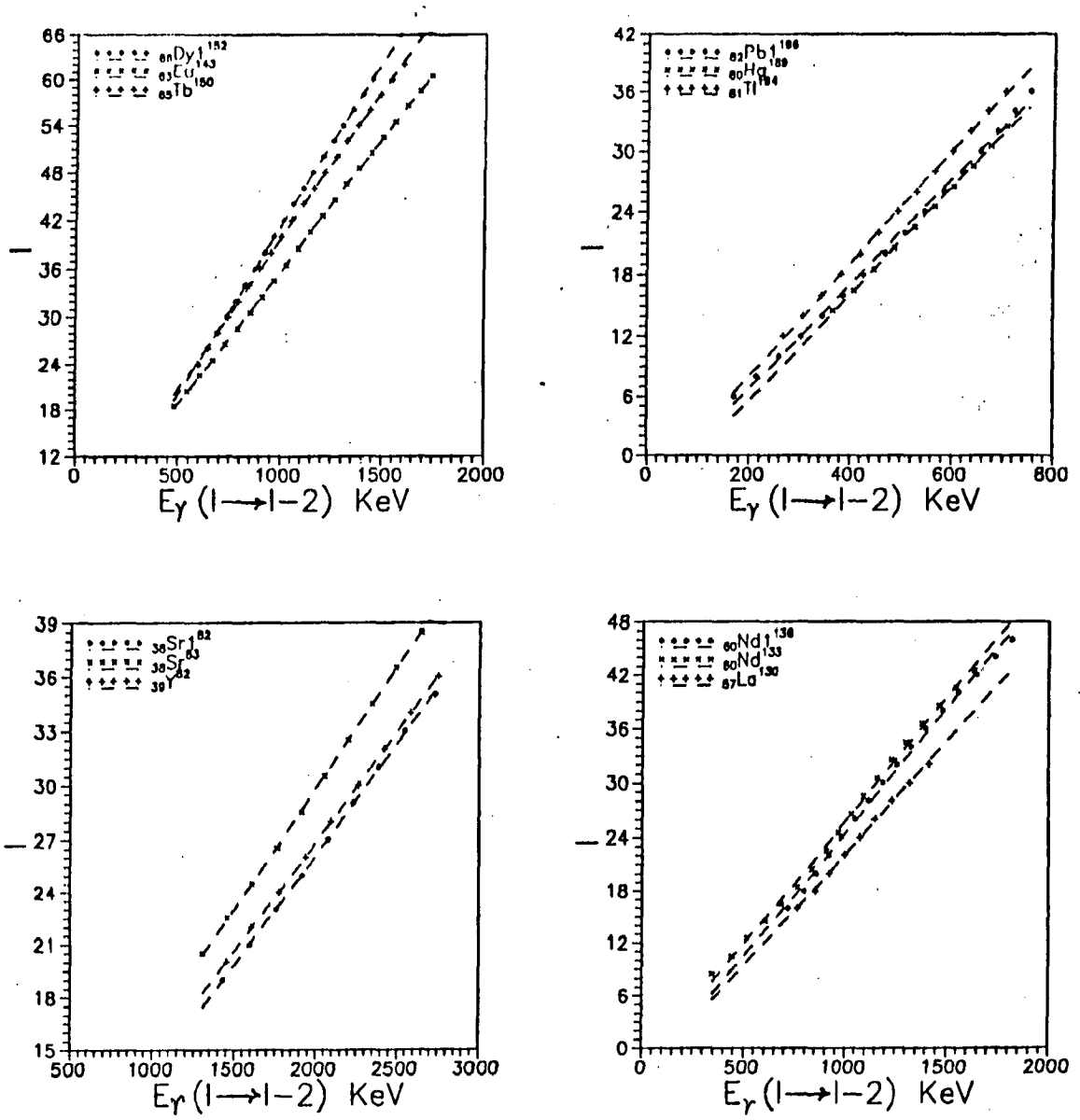


FIG. 3.1 Plots of  $I$  vs.  $E_\gamma(I \rightarrow I - 2)$  for nuclei from different mass regions.

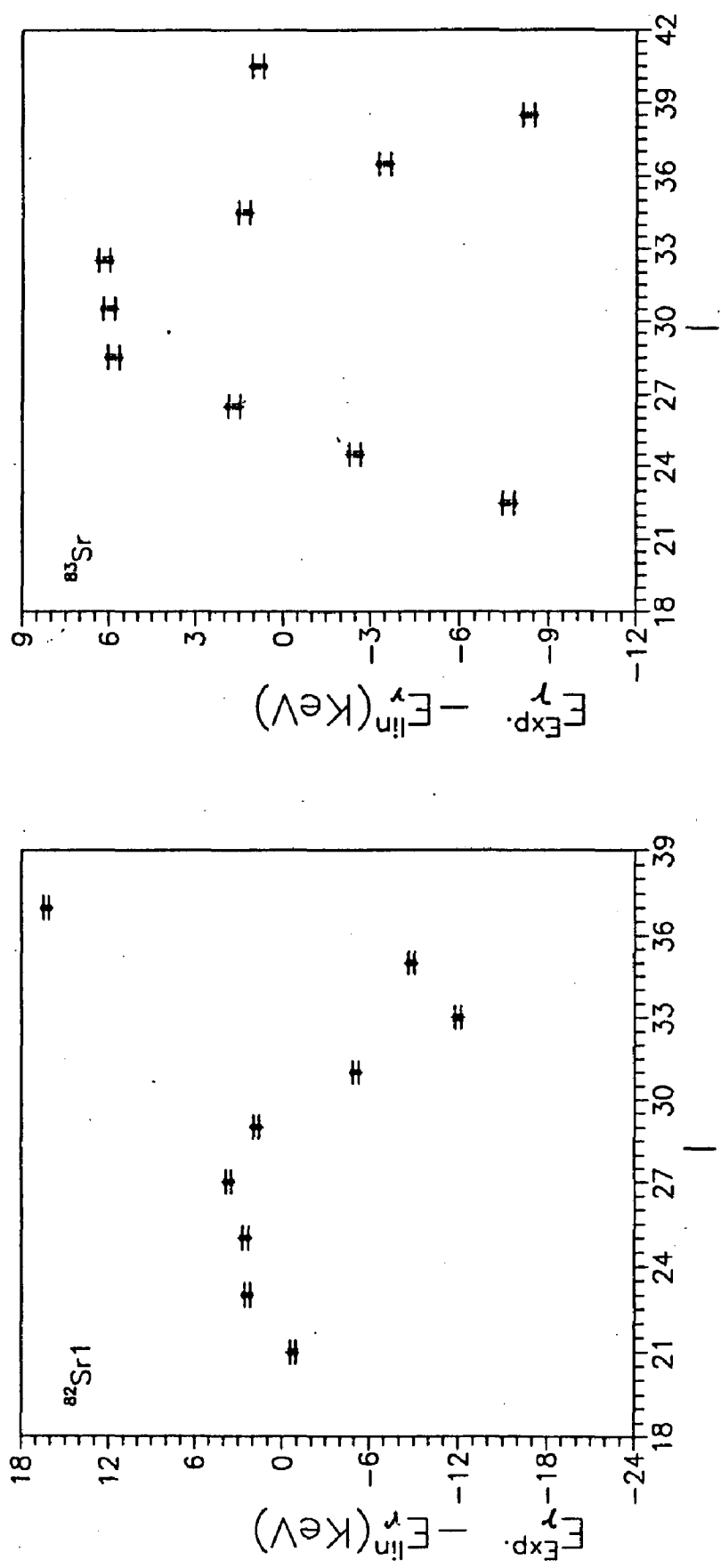


FIG. 3.2(a) Plots of  $E_{\gamma}^{\text{Exp}} - E_{\gamma}^{\text{Lin}}$  vs.  $I$  for nuclei from mass region 80.

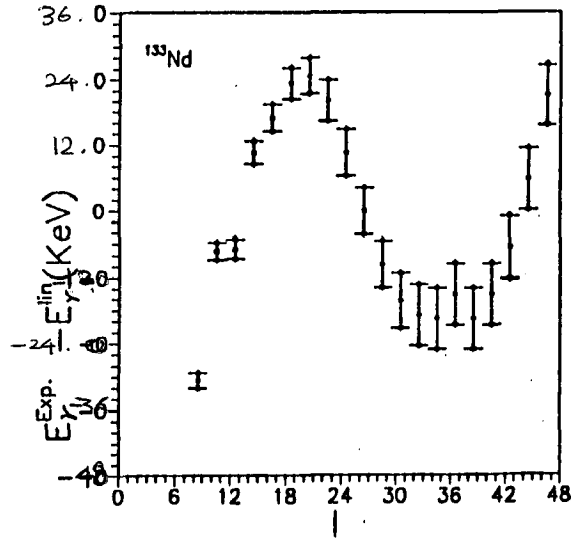
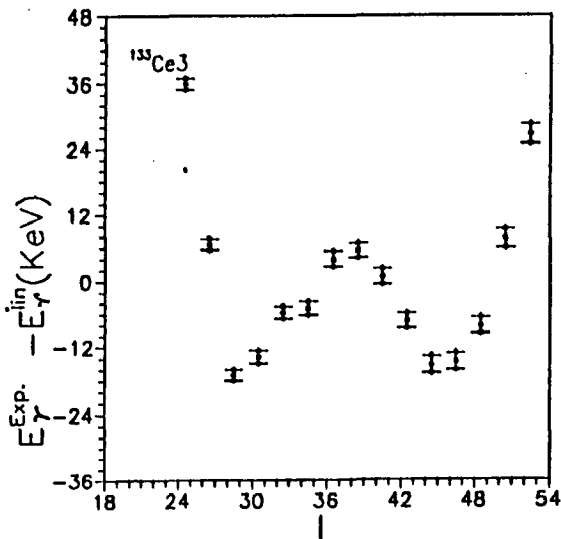
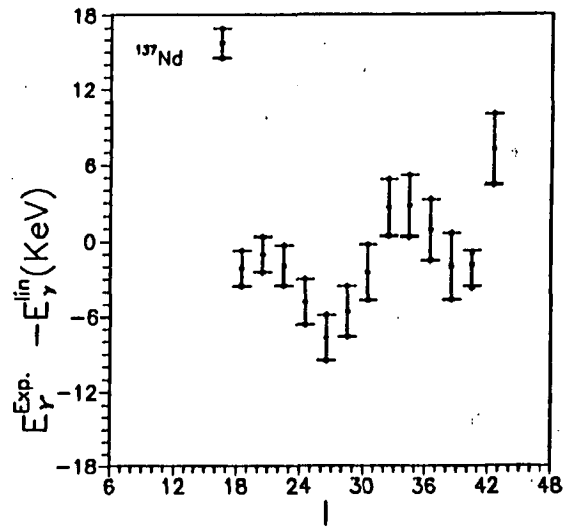
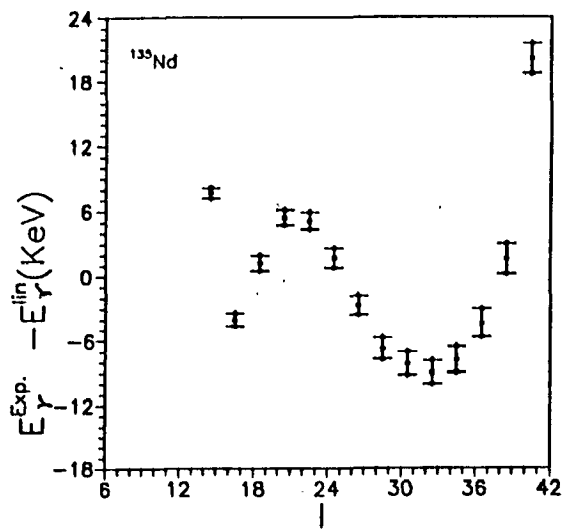


FIG. 3.2(b) Plots of  $E_{\gamma}^{\text{Exp.}} - E_{\gamma}^{\text{lin}}$  vs.  $I$  for nuclei from mass region 130.

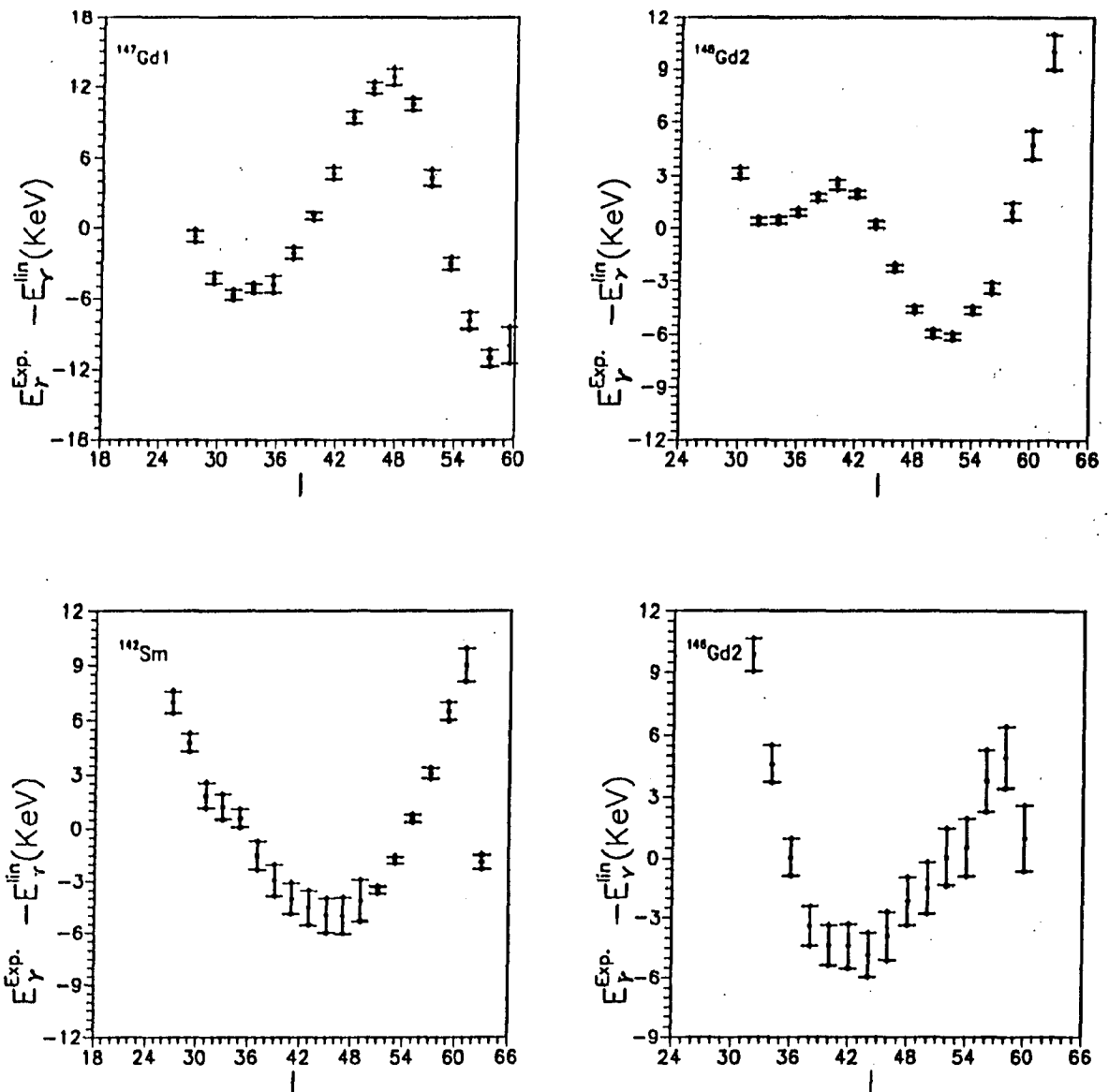


FIG. 3.2(c) Plots of  $E_{\gamma}^{Exp.} - E_{\gamma}^{lin}$  vs.  $I$  for nuclei from mass region 150.

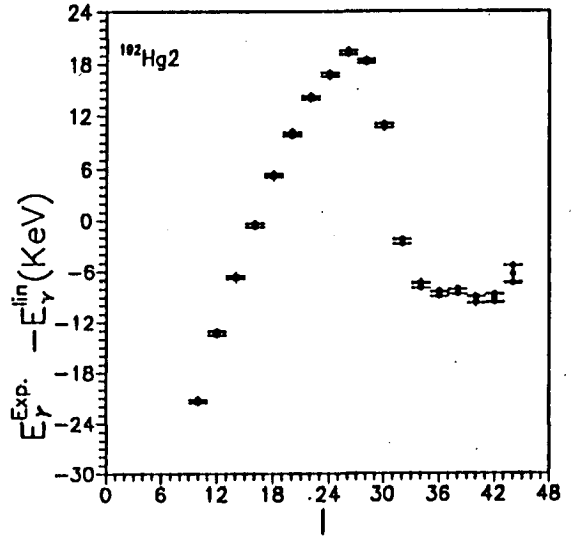
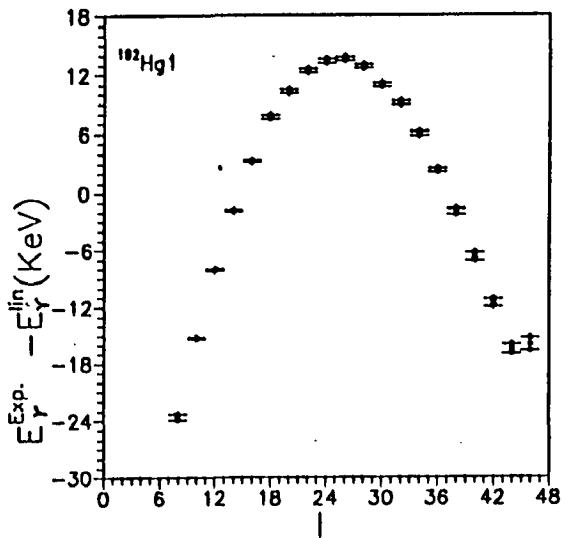
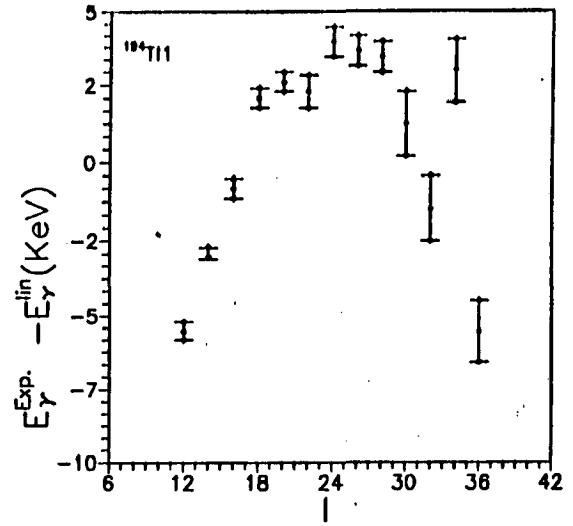
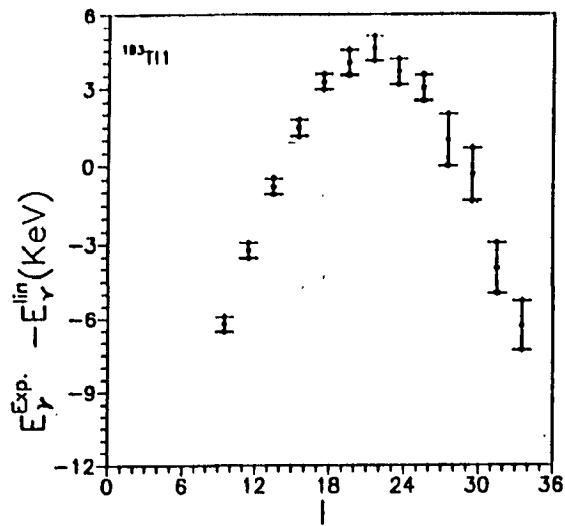


FIG. 3.2(d) Plots of  $E_{\gamma}^{Exp.} - E_{\gamma}^{lin}$  vs.  $I$  for nuclei from mass region 190.



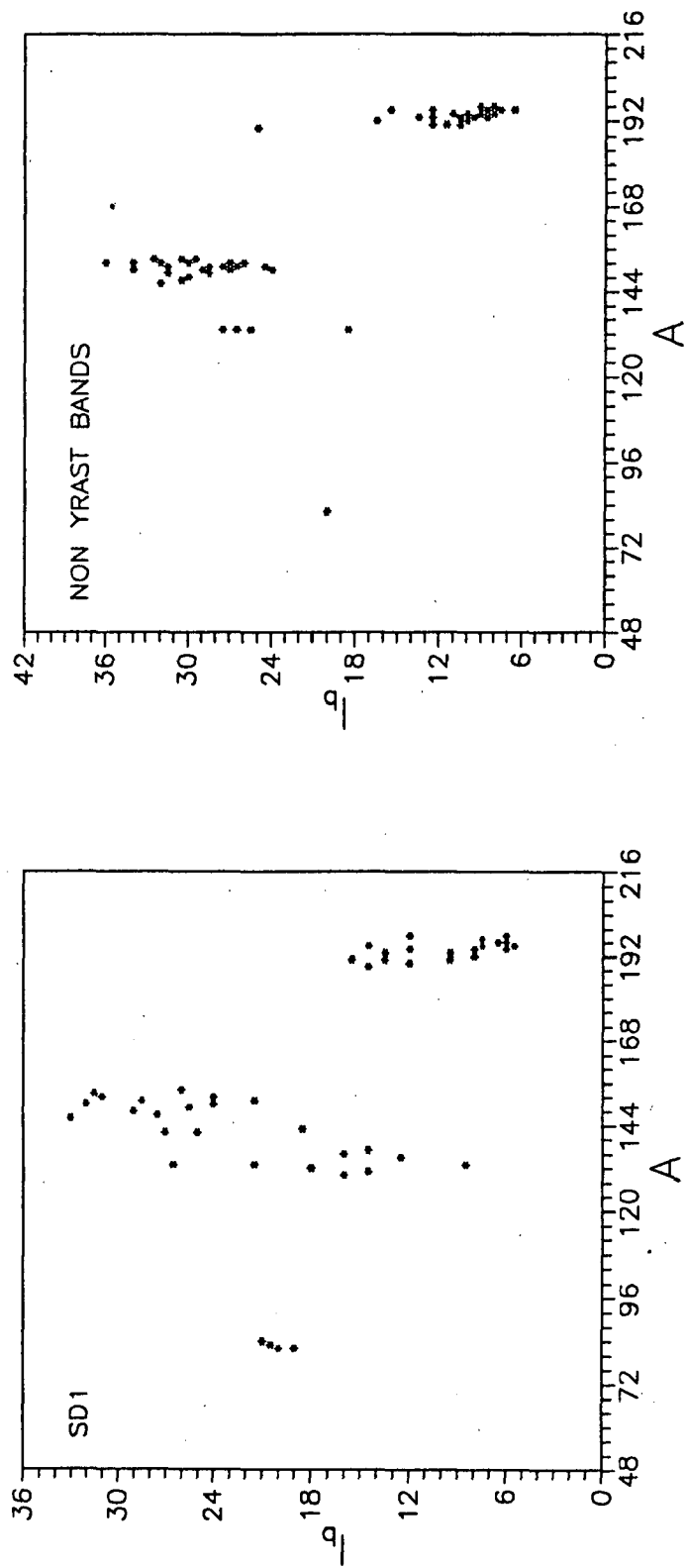


FIG. 3.3 (a) Plot of starting angular momentum  $I_b$  vs. the mass number  $A$  for yrast SD bands. (b) Non yrast SD bands .

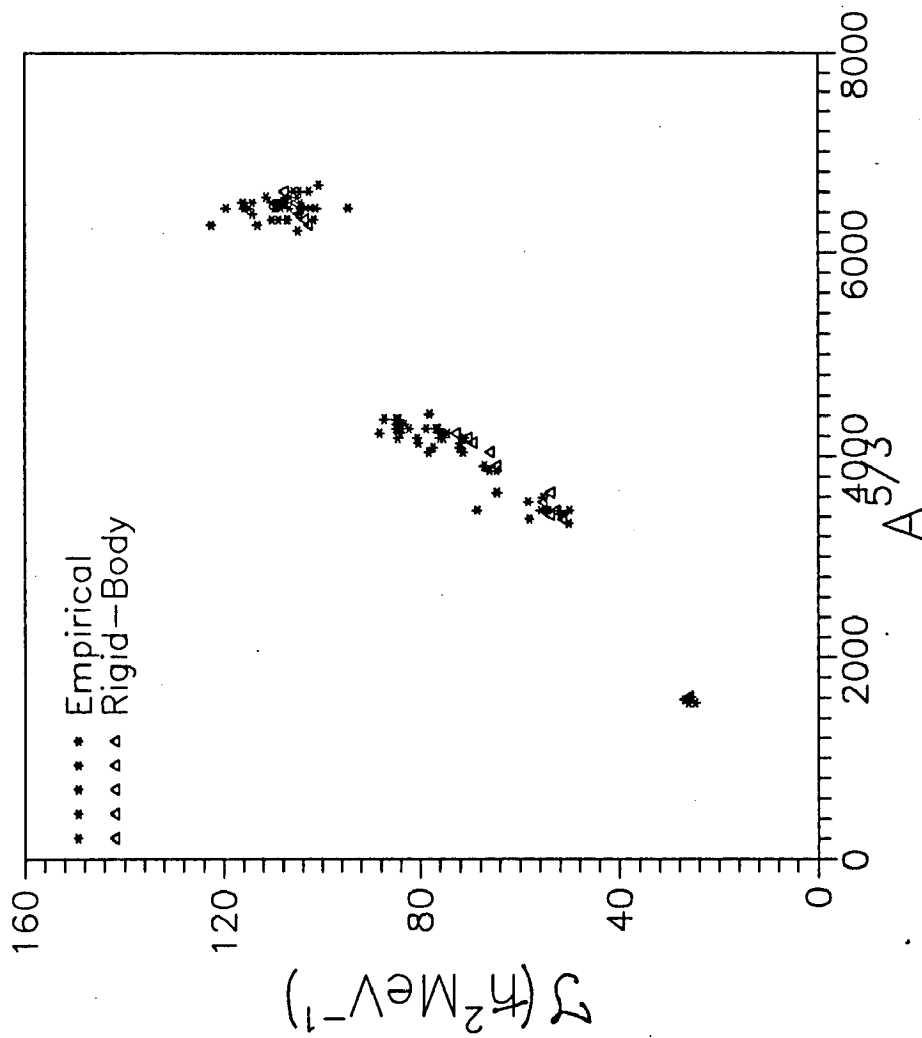


FIG. 3.4 Plot of kinematic moment of inertia  $\mathcal{J}$  vs. the mass number  $A$  as obtained from the empirical fitting and its comparison with rigid-rotor value.

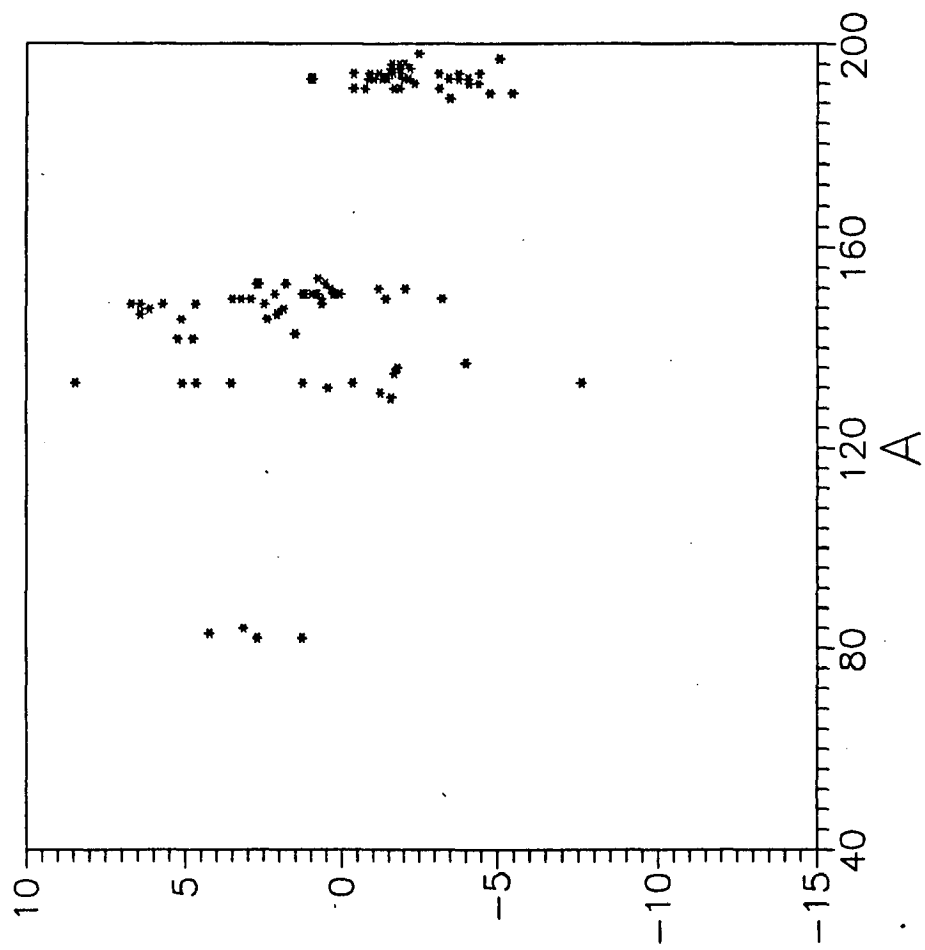


FIG. 3.5 Plot of aligned angular momentum  $i$  vs.  $A$  as obtained from the empirical fitting.

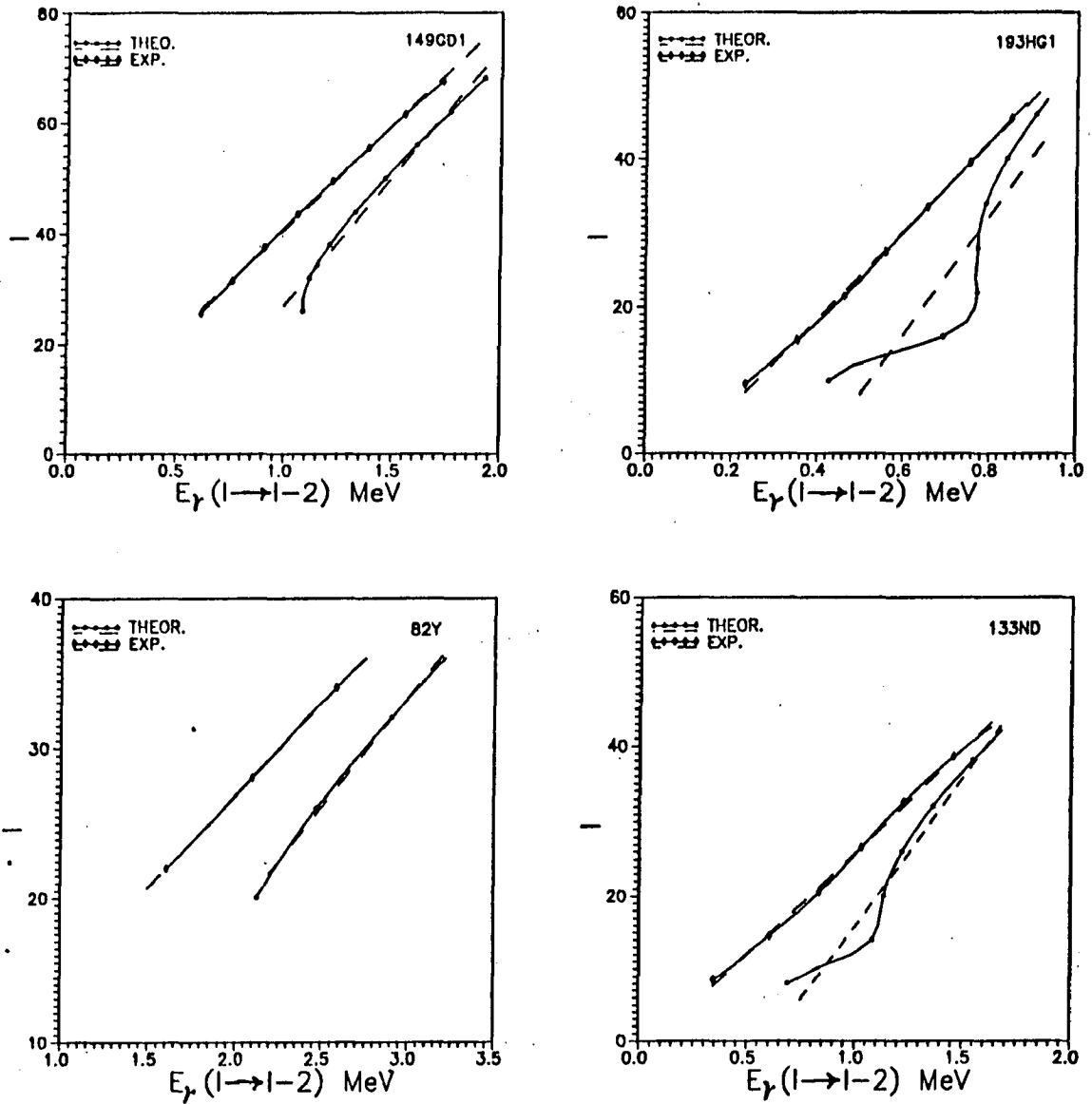


FIG. 3.6 Plots of theoretical  $I$  vs.  $E_\gamma(I \rightarrow I - 2)$  for the four mass regions and their comparison with typical nuclei from each mass region.

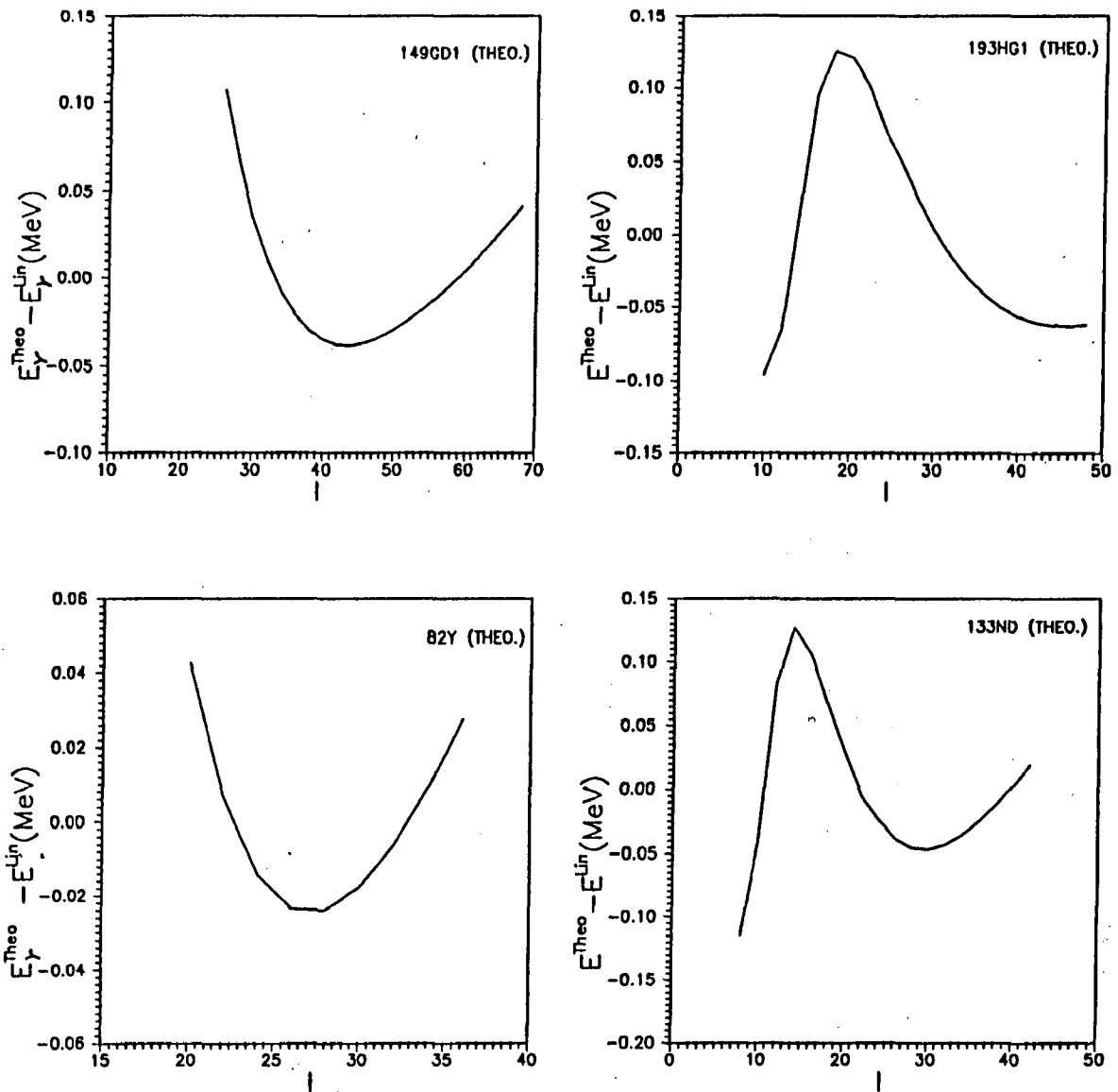


FIG. 3.7 Plots of theoretical  $E_{\gamma}^{Theo} - E_{\gamma}^{lin}$  vs.  $I$  for typical sets of parameters representing the four mass regions.

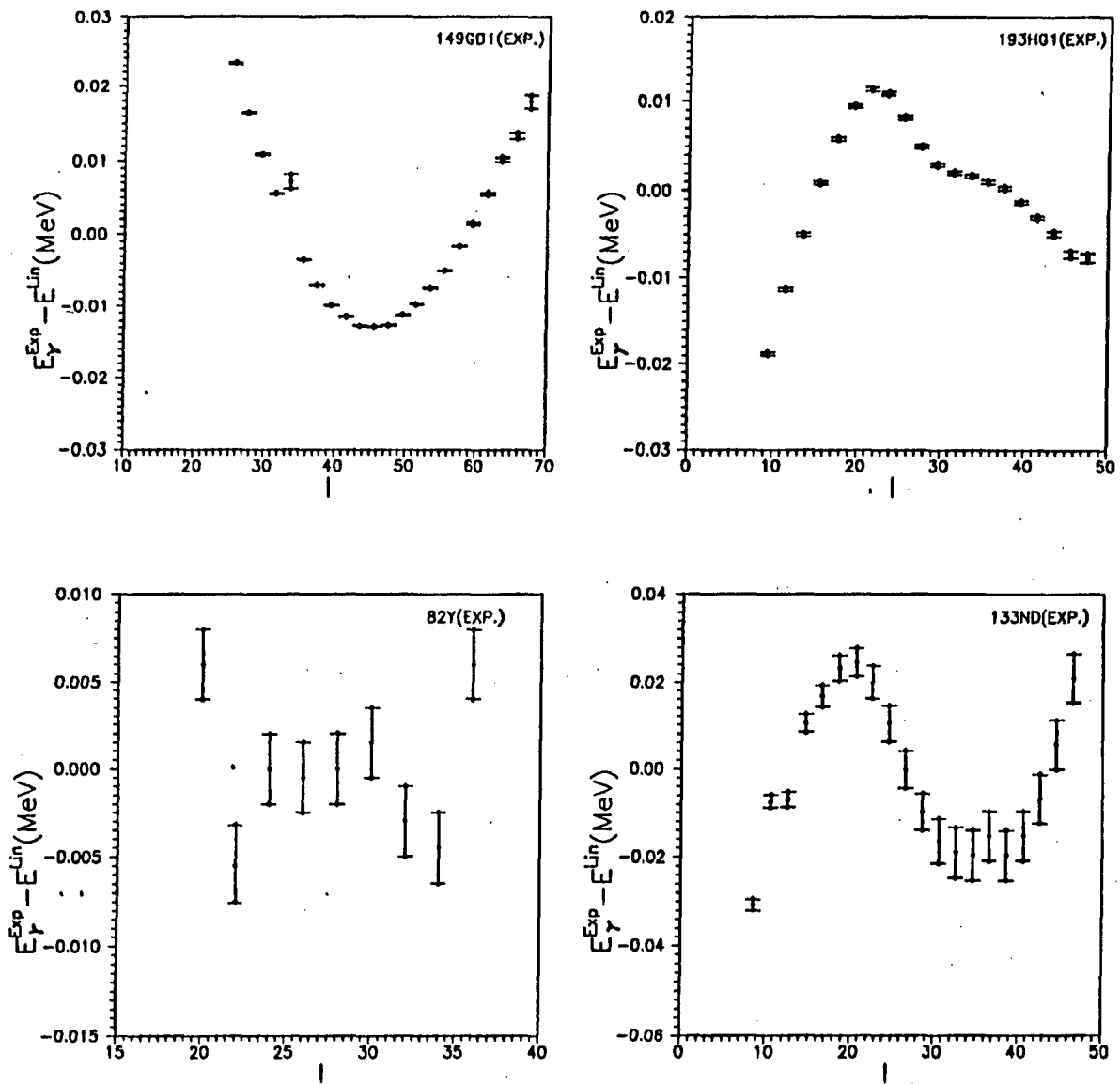


FIG. 3.8 Plots of experimental  $E_{\gamma}^{Exp.} - E_{\gamma}^{lin}$  vs.  $I$  for nuclei from the four mass regions.

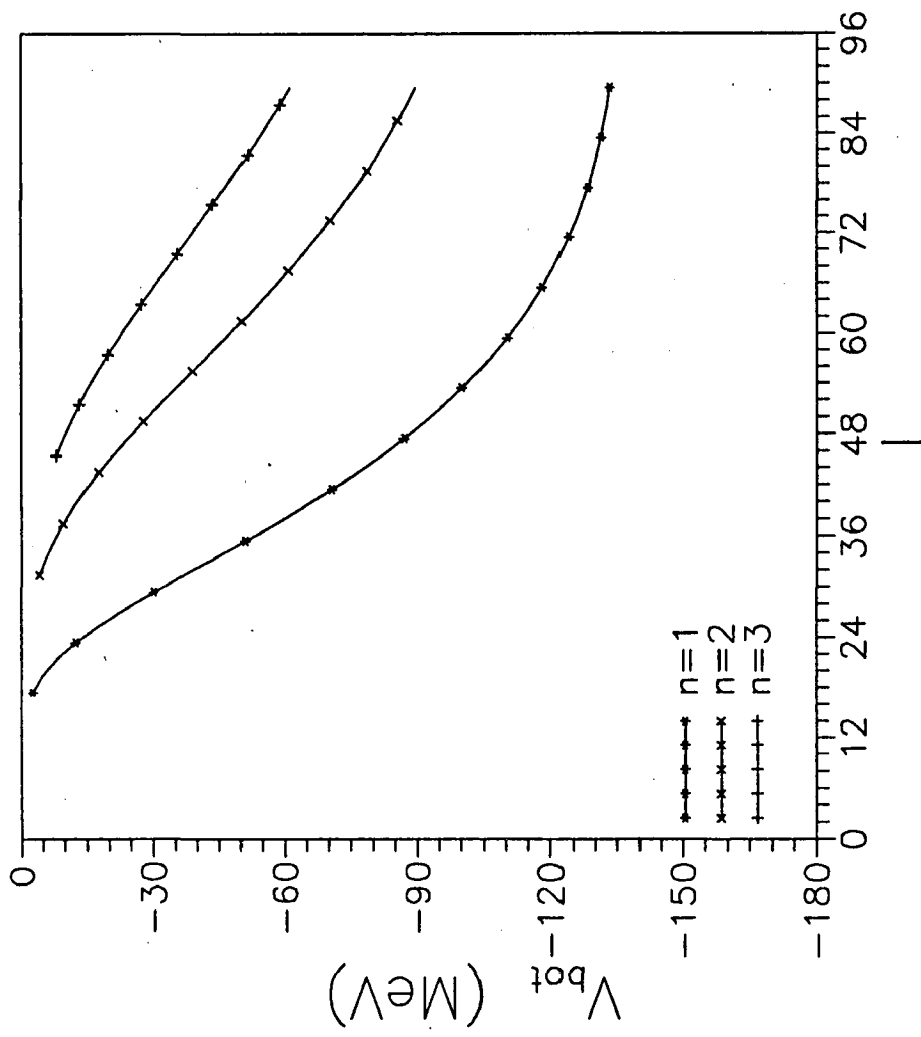


FIG. 3.9 Depth of the double well potential in  $j_3$  vs. angular momentum  $I$  for  $n=1, 2$  and 3.

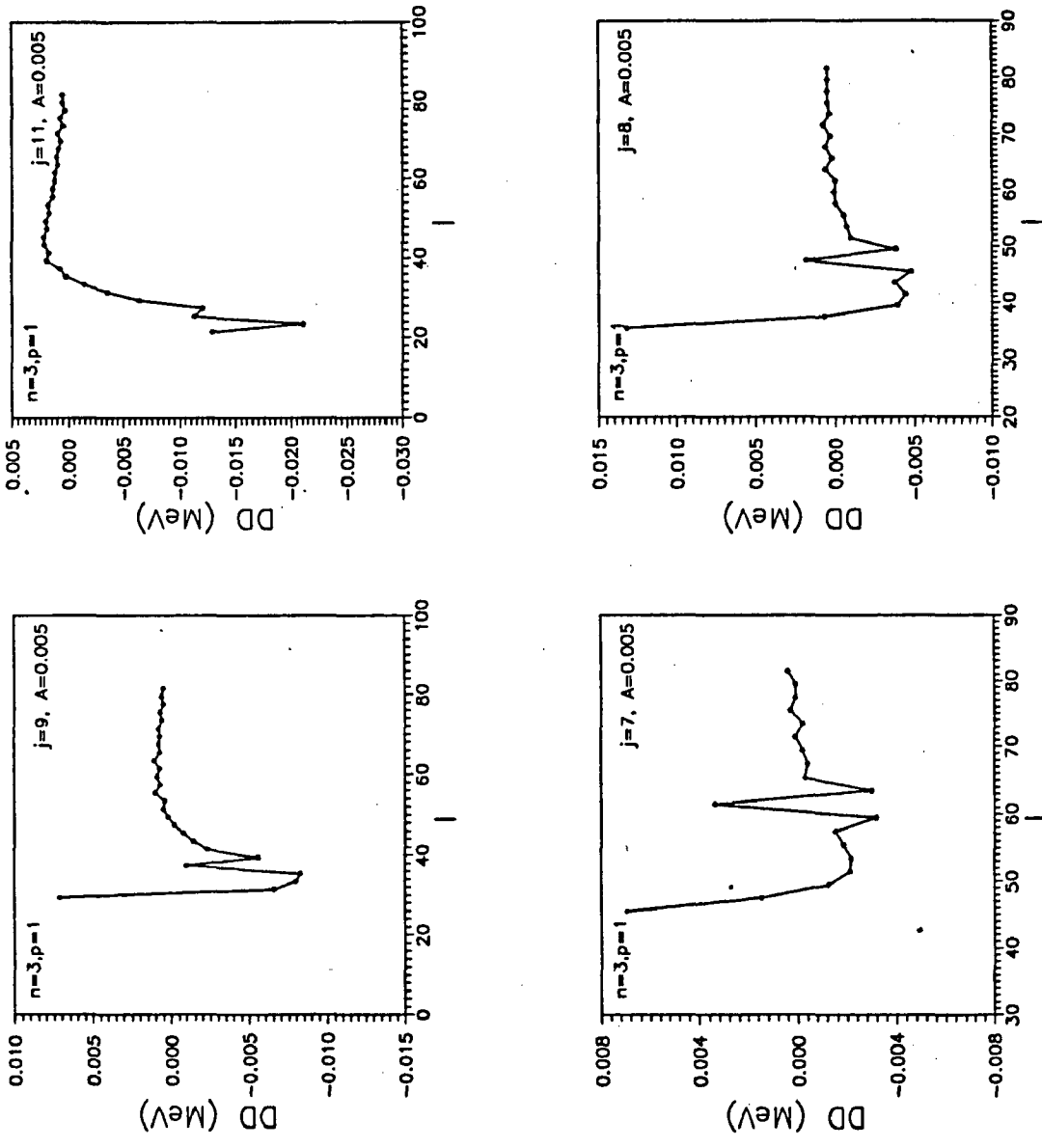


FIG. 3.10 Plots of the quantity DD obtained from the calculated gamma ray energies of SD bands as a function of  $I$  for  $n=3$ ,  $p=1$ ,  $j=7$ , 8, 9 and 11. The moment of inertia parameter  $A=0.005$  MeV in all the cases. A staggering is obtained in all the cases.



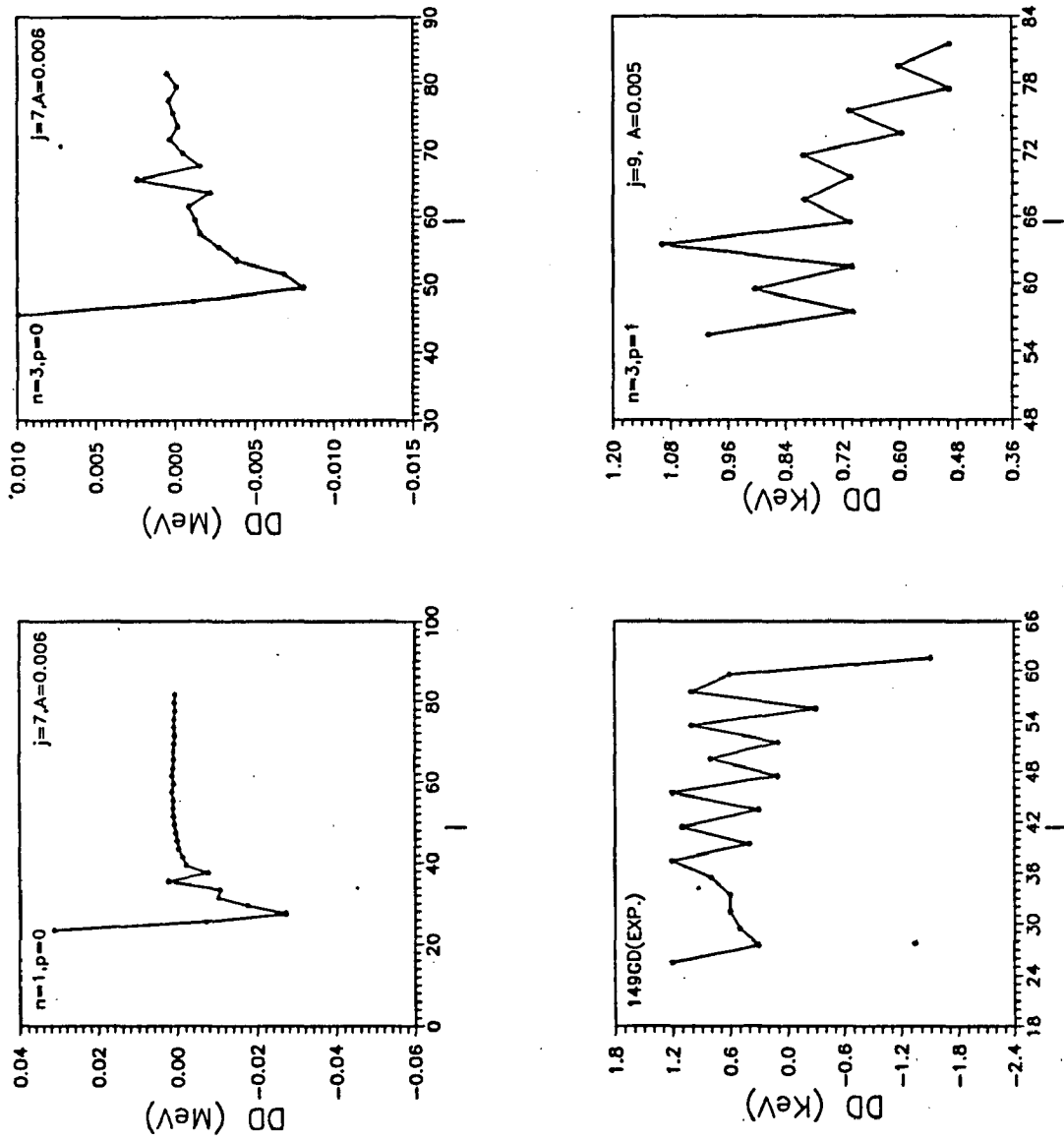


FIG. 3.11 Same as Figure 10 but for  $p=0$ ,  $n=1$  and  $n=3$  and  $A=0.006$  MeV (upper panels). In the lower panels, the  $\Delta I=2$  staggering in SD band 1 of  $^{149}\text{Gd}$  is compared with that obtained from our model for  $n=3$ ,  $p=1$  and  $j=9$ .

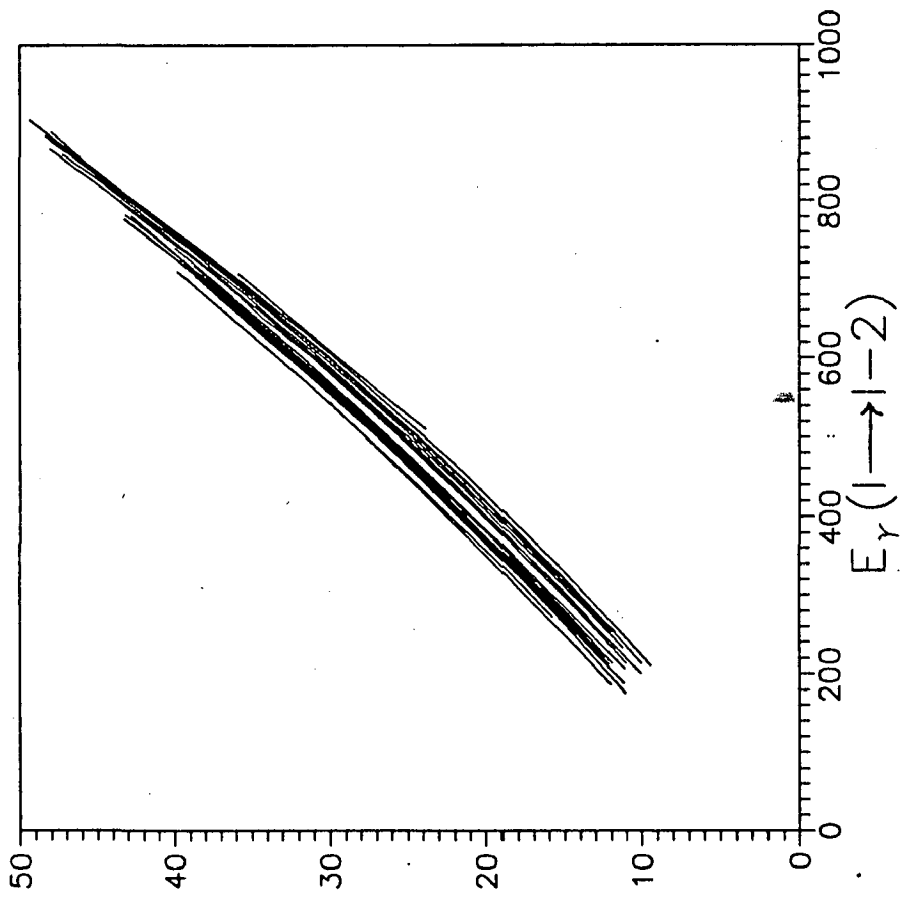


FIG. 3.12 Plot of  $I$  vs.  $E_\gamma(I \rightarrow I - 2)$  showing General Identical Band (GIB) feature in mass 190 region.

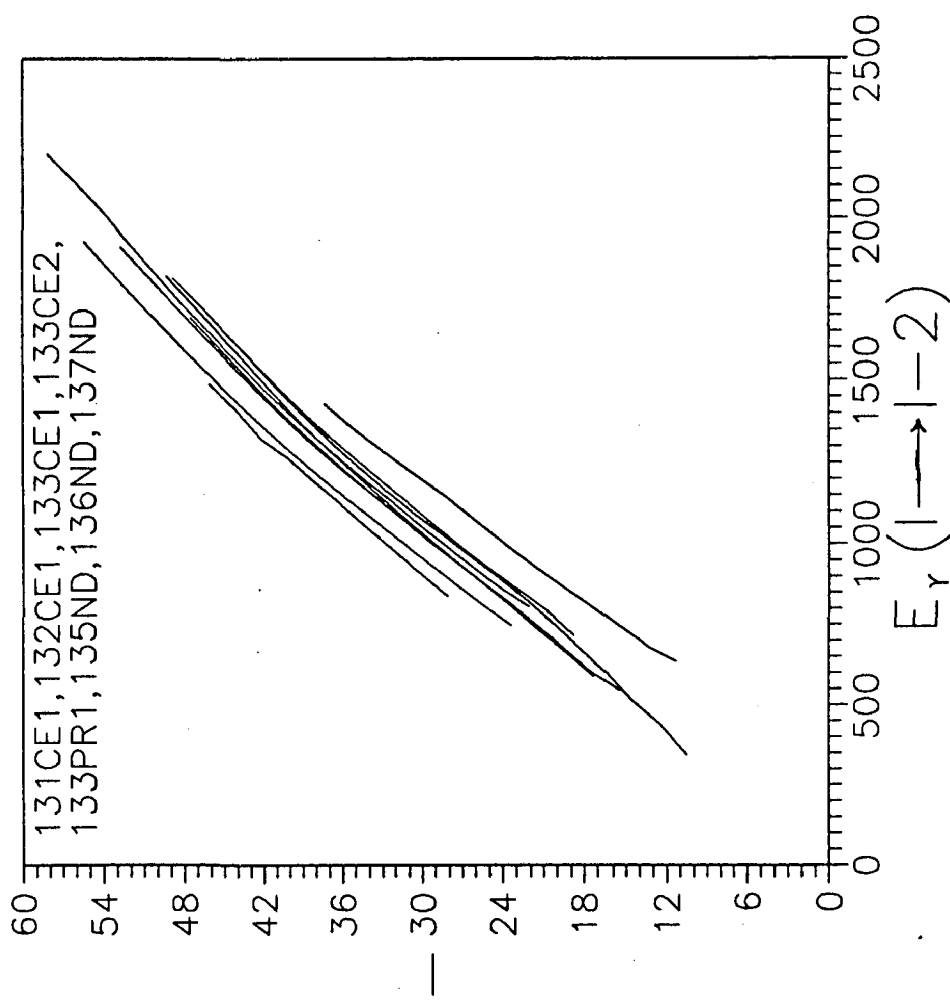


FIG. 3.13 Plot of  $I$  vs.  $E_\gamma(I \rightarrow I - 2)$  showing General Identical Band (GIB) feature in mass 130 region.

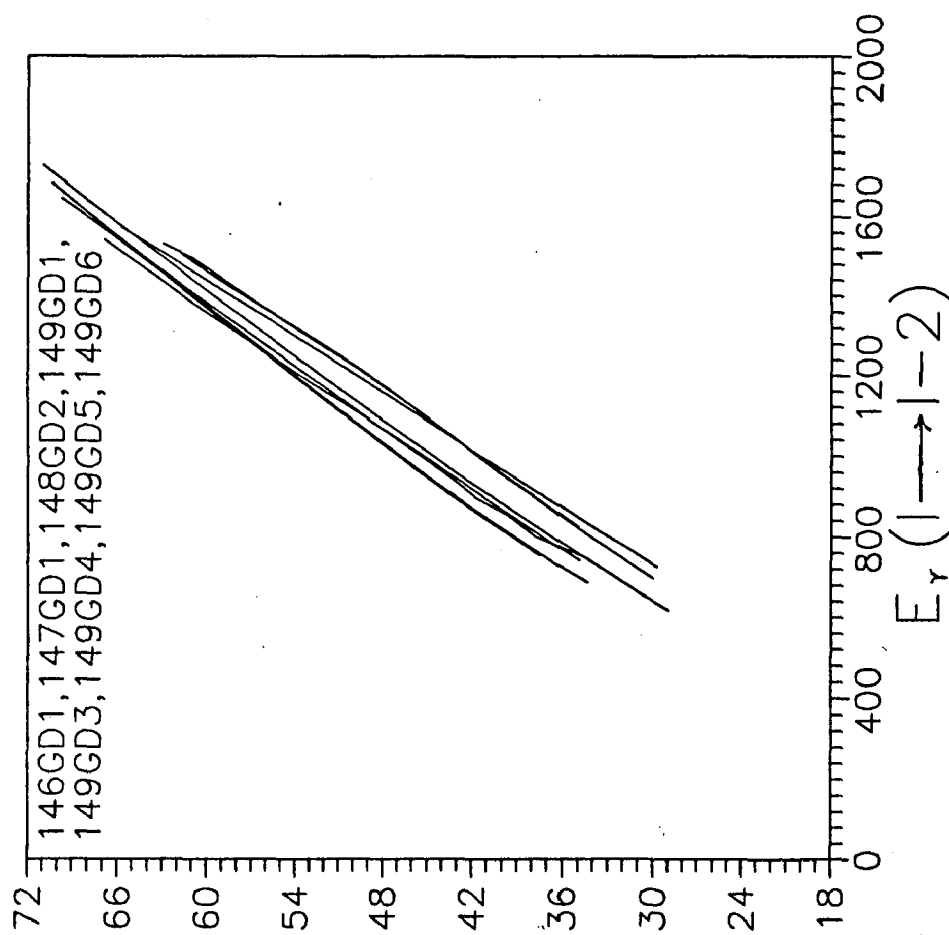


FIG. 3.14 Plot of  $I$  vs.  $E_\gamma(I \rightarrow I - 2)$  showing General Identical Band (GIB) feature in mass 140 region.

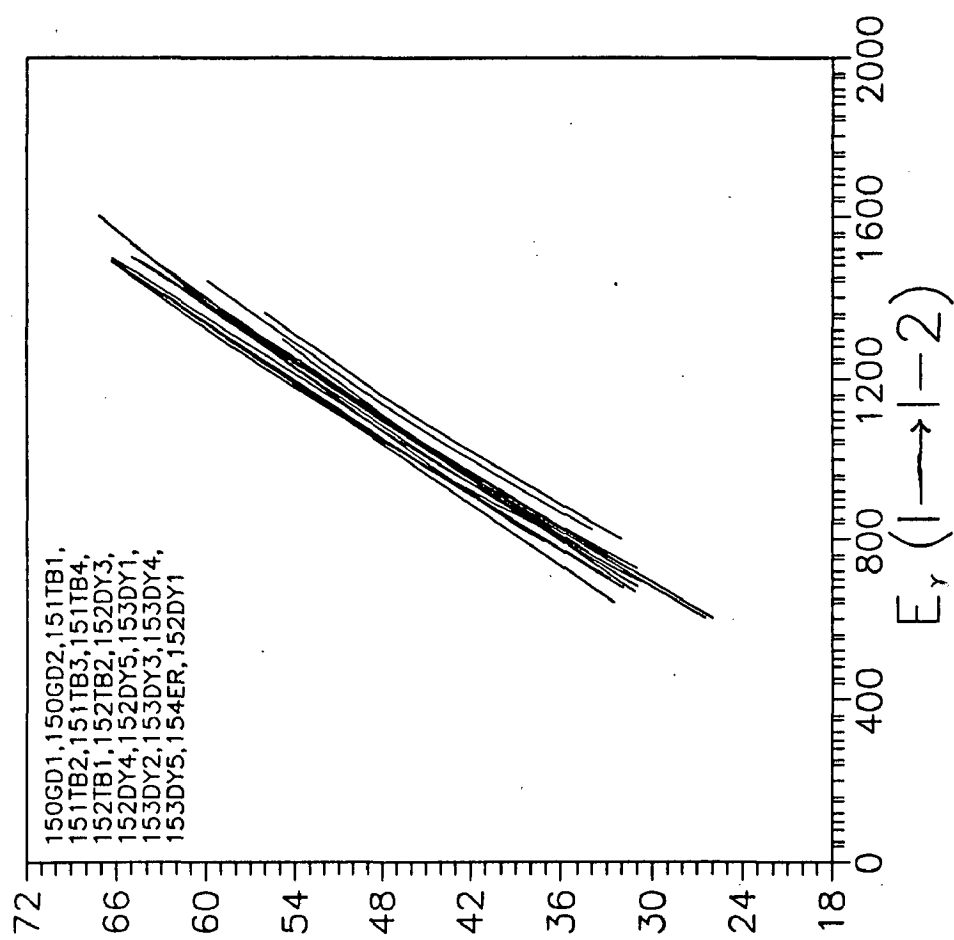


FIG. 3.15 Plot of  $I$  vs.  $E_\gamma(I \rightarrow I - 2)$  showing General Identical Band (GIB) feature in mass 150 region.

**CHAPTER IV**  
**CRANKING MODEL AND ITS**  
**SEMI-CLASSICAL**  
**QUANTIZATION**

## I. INTRODUCTION

In this chapter we present a complete discussion of the dynamical features of the cranking model hamiltonian as applicable to high- $j$  orbitals. The cranking model first introduced in 1954 by Inglis [58] has been used very extensively to study the rotational phenomena in nuclei [35]. It has now become a standard tool in nuclear physics to calculate a large number of properties such as the nuclear deformation, moment of inertia, aligned angular momentum etc. It has also been used in recent times to assign configurations to the superdeformed bands and calculate other properties based on these configurations [1]. In its simplest form, a single particle potential is cranked about one of the principal axes and then study the influence of this rotation on the properties of the nucleons.

Following the treatment presented for the particle-rotor model in chapter II and III, we present an analysis of the cranking hamiltonian on a similar line. Our emphasis will be on a detailed discussion of the nonlinear dynamical regime of the cranking model and its semiclassical quantisation. We show that the cranking model results support the findings of the Particle-Rotor model.

## II. MODEL HAMILTONIAN

Assuming that the deformation of the single-particle potential contains only a quadrupole axially symmetric component with respect to the 3-axis, the hamiltonian in the rotating frame may be written as [16]

$$H = Qj_3^2 - \omega_c j_1, \quad (1)$$

where

$$Q = k\beta \sqrt{\frac{5}{4\pi}} \frac{3}{4j(j+1)}, \quad (2)$$

and  $k$  is the radial matrix element given by  $\langle nljj_3 | r^2 Y_{20} | nljj_3 \rangle$ . The rotation axis is defined by axis 1 which is perpendicular to the symmetry axis denoted by 3-axis.

### A. Equations of motion and fixed point structure

Equations of motion can be obtained by using the properties of Poisson's bracket and were given by Bohr and Mottelson [16]:

$$\frac{dj_1}{dt} = -2Qj_2j_3, \quad (3)$$

$$\frac{dj_2}{dt} = 2Qj_1j_3 + \omega_c j_3, \quad (4)$$

$$\frac{dj_3}{dt} = -\omega_c j_2. \quad (5)$$

A fixed point analysis of the problem is very helpful in classifying the orbits. We obtain four fixed points denoted by  $a, b$  and  $c_{\pm}$  whose characteristic features are listed below

$$a = (j, 0, 0), \epsilon_a = -\omega_c j \quad (\text{minimum; stable and isolated}),$$

$$b = (-j, 0, 0), \epsilon_b = \omega_c j \quad (\text{maximum for } \omega_c > 2Qj$$

and saddle point for  $\omega_c < 2Qj$ ; unstable and isolated),

$$c_{\pm} = \left( \frac{-\omega_c}{2Q}, 0, \pm \sqrt{\left(j^2 - \frac{\omega_c^2}{4Q^2}\right)} \right), \epsilon_{c_{\pm}} = Qj_3^2 + \frac{\omega_c^2}{4Q} \quad (\text{maxima for } \omega_c < 2Qj; \text{ stable and isolated}) \quad (6)$$

The conservation of the angular momentum  $j$  restricts the motion in  $j$ -space to lie on a spherical surface given by  $j^2 = j_1^2 + j_2^2 + j_3^2$ . The energy conservation on the other hand restricts the motion to lie on a parabolic cylinder defined by the Hamiltonian; an intersection of the two gives the allowed orbits. For a critical cranking frequency  $\omega_c^* > 2Qj$ , the saddle point is pushed out of the invariant region FIG. 4.1 and there is only one minimum of stability corresponding the fixed point  $a$ , which represents maximum alignment. The critical frequency  $\omega_c^*$  plays the role of critical angular momentum  $I_c$  in the particle-rotor model. For SD nuclei  $\omega_c$  is of the order of 0.1 MeV and hence the ratio  $\frac{\omega_c}{2Qj} < 1$  a value that keeps the saddle point in the region of interest. The fixed point  $b$  corresponds to a configuration where particle angular momentum is completely anti-aligned to the rotation axis. We can see from



and  $j_3$  follows anharmonic oscillator equation. When  $\epsilon = \frac{\omega_c^2}{2Q}$  and  $K = 0$ ,  $j_3$  obeys the solutions of quartic oscillator. On increasing the energy further,  $K$  becomes negative and we enter the nonlinear dynamical regime dictated by the Duffing oscillator which persists for all higher energies. A detailed discussion of this has already been presented in chapter II.

### III. SMALL AMPLITUDE OSCILLATIONS

#### A. Fixed point $a$

Using the method of linearization of the equation of motion, at fixed point  $a(= j, 0, 0)$ , we obtain the linearised set of equations as

$$\frac{d(\delta j_1)}{dt} = 0, \quad (12)$$

$$\frac{d(\delta j_2)}{dt} = (2Qj + \omega_c)\delta j_3, \quad (13)$$

$$\frac{d(\delta j_3)}{dt} = -\omega_c\delta j_2, \quad (14)$$

where  $\delta j_i (i = 1, 2, 3)$  are infinitesimal deviations about the fixed point.

These equations give the solutions as

$$\delta j_1(t) = \delta j_1(0), \quad (15)$$

$$\delta j_2(t) = \delta j_2(0)\cos(\sqrt{\omega_c(\omega_c + 2Qj)}t) + \frac{\delta j_2''(0)}{\sqrt{\omega_c(\omega_c + 2Qj)}}\sin(\sqrt{\omega_c(\omega_c + 2Qj)}t), \quad (16)$$

$$\delta j_3(t) = \delta j_3(0)\cos(\sqrt{\omega_c(\omega_c + 2Qj)}t) + \frac{\delta j_3''(0)}{\sqrt{\omega_c(\omega_c + 2Qj)}}\sin(\sqrt{\omega_c(\omega_c + 2Qj)}t). \quad (17)$$

The action-angle variables were introduced by Bohr and Mottelson to facilitate semiclassical quantisation. The energy  $\epsilon$  depends only on the action  $J_a$  and for harmonic oscillations around the equilibrium, we have

$$\epsilon = \epsilon_a + J_a \omega_{vib,a}, \quad (18)$$

$$= -\omega_c j + J_a (\sqrt{\omega_c(\omega_c + 2Qj)}). \quad (19)$$

For a quantised system, the action takes the value

$$J_a = (n_a + \frac{1}{2})\hbar, \quad (20)$$

with  $n_a = 0, 1, 2, \dots$  etc.

The action  $J_a$  at the fixed point  $a$  in harmonic approximation is given by,

$$J_a = 4 \int_0^j [\omega_c^2 j^2 - \epsilon^2 - K j_3^2]^{\frac{1}{2}} dj_3. \quad (21)$$

The integral is exactly solvable and its semiclassical quantisation (SCQ) gives us the condition,

$$\frac{2(\omega_c^2 j^2 - \epsilon^2)}{\sqrt{\omega_c^2 - \frac{28\epsilon}{j^2}}} \sin^{-1} \left[ \sqrt{\frac{\omega_c^2 j^2 - 28\epsilon}{\omega_c^2 j^2 - \epsilon^2}} \right] + 2j \sqrt{28\epsilon - \epsilon^2} \approx (n + \frac{1}{2}). \quad (22)$$

When solved for a given  $n$ , we obtain the energy  $\epsilon$  as a function of  $\omega_c$ .

In a similar way one can show that the frequency of vibration at the fixed point  $b$  is given by

$$\omega_{vib,b} = (\sqrt{\omega_c(\omega_c - 2Qj)}). \quad (23)$$

The motion at  $b$  is however not of much interest to us. As in the Particle-Rotor model, we will concentrate upon the twin fixed points  $c_{\pm}$  where the solutions are more complex and interesting.

## B. Fixed points $c_{\pm}$

When  $K < 0$ ,  $j_3$  evolves as a duffing oscillator. We have already discussed the shape of the potential in  $j_3$ ,  $V(j_3) = K j_3^2 + \frac{L}{2} j_3^4$  which exhibits a sudden appearance of a double well. We have already shown that this spontaneous breakdown of symmetry is associated

with a second order phase transition. Assuming a simple harmonic motion at fixed points  $c_{\pm}$  linearization of the equations gives us a frequency of vibration

$$\omega_{vib} = \pm(\sqrt{4Q^2j^2 - \omega_c^2}), \quad (24)$$

and the corresponding energies are given by

$$\epsilon = \epsilon_{c_{\pm}} + J_c \omega_{vib} = \epsilon_{c_{\pm}} + (n_c + \frac{1}{2})\omega_{vib}, \quad (25)$$

where  $n_c=0,1,2,3,\dots$  etc. is introduced to obtain quantised energy levels.  $J_c$  is the action given by

$$J_c = 4 \int_0^{j^+} dj_3 (\omega_c^2 j^2 - \epsilon^2 - K j_3^2 - \frac{L}{2} j_3^4)^{1/2}, \quad (26)$$

$$= 4 \int_0^{j^+} dj_3 [C - K j_3^2 - \frac{L}{2} j_3^4]^{\frac{1}{2}}, \quad (27)$$

and,

$$j^+ = [\frac{1}{L}(\sqrt{K^2 + 2LC} - K)]^{\frac{1}{2}}. \quad (28)$$

The semiclassical quantization of this action provides us with the energy levels corresponding to  $n = 0,1,2,3 \dots$  as a function of  $\omega_c$ . As already pointed out, as  $K$  changes sign from positive to negative, a double well potential (DWP) appears from a single well in  $V(j_3)$  of the fictitious Hamiltonian of  $j_3$  given by

$$\left(\frac{dj_3}{dt}\right)^2 + V(j_3) = C, \quad (29)$$

where  $V(j_3) = K j_3^2 + (L/2)j_3^4$  and  $C = (\omega_c j - \epsilon)(\omega_c j + \epsilon)$ . The minima of the DWP correspond to the two isolated fixed points  $c_{\pm}$ ; these are located in a region of nonlinearity.

When tunnelling between the two wells of DWP is taken into account, the DWP is found to support two solutions which we denote by  $p=0$  and  $p=1$ ; these correspond to the usual even and odd solutions of a potential well. The appearance of the double well potential and tunnelling between the two wells modify the semiclassical quantization condition as follows,

$$\frac{1}{\pi} \int_{j_-}^{j_+} \sqrt{C - V(j_3)} dj_3 - \frac{\Phi(\epsilon) \mp \Delta\Phi(\epsilon)}{2\pi} = (n_{\pm} \pm \frac{1}{4}), \quad (30)$$

where

$$\epsilon(C) = \sqrt{\frac{1}{2V''(0)}}(C - V(0)) = \frac{C}{\sqrt{4K}}, \quad (31)$$

$$\Phi_{\pm}(\epsilon) = \frac{1}{2}[\arg\Gamma(\frac{1}{2} + i\epsilon) - \epsilon \ln |\epsilon| + \epsilon \pm \tan^{-1} e^{-\pi\epsilon}], \quad (32)$$

and,  $\Delta\Phi = \Phi_- - \Phi_+$  and  $\Phi = \Phi_- + \Phi_+$ . The limits on  $j_3$  are the four real turning points at sub barrier energies denoted by  $-j_+$ ,  $-j_-$ ,  $j_-$  and  $j_+$ . If we choose the upper sign in equation (28) and take  $n_+=0,1,2,3,\dots$ , we get the even solutions denoted by  $p=0$ . By taking the lower sign and  $n_-=1,2,3,\dots$  we get the odd solutions denoted by  $p=1$ . Fulfillment of the SCQ condition given by equation(29) yields a set of energies  $\epsilon$  for a given  $n$  and different  $\omega_c$ ; this constitutes a band which exhibits rotational features. The tunnelling between the DWP leads to a shift in the eigenvalues of  $C$  which ultimately results in a shift of the energy eigenvalues. Here the effect of tunneling between the two potential wells has also been included. Most of this discussion is parallel to that in chap II and similar details apply.

#### IV. ALIGNED ANGULAR MOMENTUM

A quantity of great physical interest is the aligned angular momentum or simply the alignment defined as

$$i = \langle j_1 \rangle. \quad (33)$$

From the Hamilton's principle we obtain

$$i = -\left(\frac{\partial \epsilon}{\partial \omega_c}\right)_J. \quad (34)$$

The alignment at the fixed point  $a$  was obtained by Bohr and Mottelson to be

$$i = j - J \frac{Qj + \omega_c}{\sqrt{(\omega_c(2Qj + \omega_c))}}. \quad (35)$$

We can see that for  $\omega_c \gg Qj$ , the alignment approaches the asymptotic limit  $i = j - J_a$ .

To obtain the alignment at fixed points  $c_{\pm}$  we note that energy of small oscillations around  $c_{\pm}$  is given by

$$\epsilon = Qj^2 + \frac{\omega_c^2}{4Q} + J\omega_{vib}. \quad (36)$$

To obtain the frequency of vibration of  $j_3$  we recall that (see chapter II, section V) the solutions of  $j_3$  are elliptic functions of the first kind where natural time period provides us with the values of  $\omega_{vib}$ . The alignment can be obtained by using equation (34).

## V. NUMERICAL RESULTS AND DISCUSSION

As pointed out by Bohr and Mottelson [16], the nature of the equation governing the motion of  $j_3$  in the cranking model is identical to that found in the Particle-Rotor model. The fixed point structure and the nature of orbits is also same.

In FIG. 4.3, we plot the energy  $\epsilon$  vs.  $\omega$  obtained by SCQ at fixed point  $a$  for  $n = 1$ . The behaviour of solution indicates a rotational band whose aligned angular momentum is  $(j - \frac{1}{2})\hbar$ . This is the rotation aligned band with maximum alignment.

In FIG. 4.4 and 4.5, we plot a similar quantity  $\epsilon$  obtained by SCQ procedure at fixed point  $c_{\pm}$ . FIG. 4.4 contains the results for  $p = 0$  and FIG. 4.5 contains the results for  $p = 1$ . The nature of solutions is similar to that obtained in the Particle-Rotor model where weak oscillations were observed to be superimposed on what would otherwise have been an ideal rotational band.

The alignment for the cases plotted in FIG. 4.4 and FIG. 4.5 are shown in FIG. 4.6 and FIG. 4.7 respectively. The behaviour of alignment with rotational frequency is similar to that observed in the Particle-Rotor model. The aligned angular momentum is negative at low  $\omega$ , rises with increasing  $\omega$  and then saturates. One important difference with the results of Particle-Rotor model is noticed. The alignment as obtained here, saturates at around  $-7\hbar$  whereas the alignment obtained in the Particle-Rotor model becomes positive

and then saturates. The saturation value reached in the case of cranking model seems to be limited by the alignment at the fixed point  $b$ . It is not clear why this difference in the numerical value of  $i$  should arise. However it is not surprising that the cranking and particle-rotor models should give different numerical results particularly when the solutions are coming from nonlinear equations. As pointed out by Bohr and Mottelson [16], important discrepancies in the cranking and particle-rotor model with the observed spectra still remain unresolved.

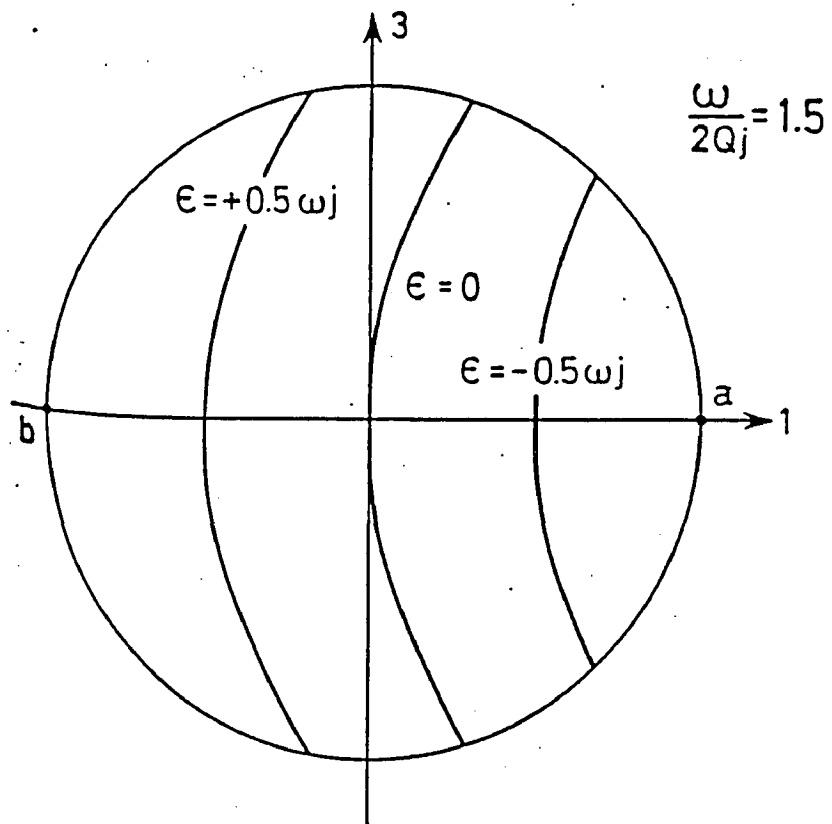


FIG. 4.1  $j$  space diagram depicting the exclusion of saddle point  $b$  for certain  $\omega_c > 2Qj$ .  
From Ref. [16].

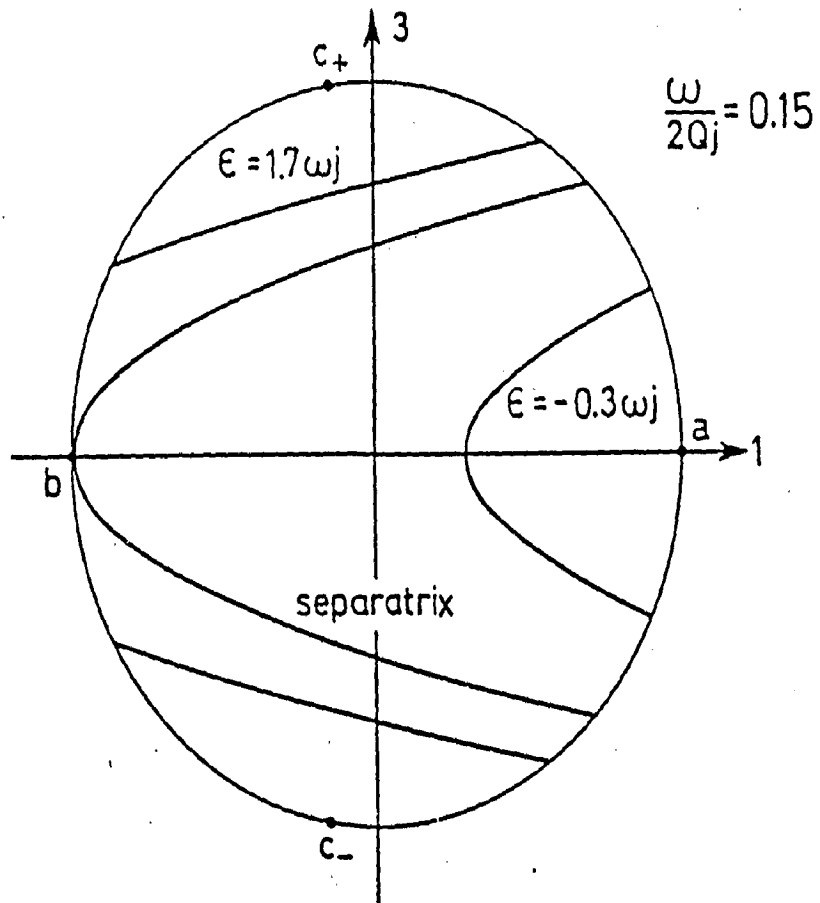


FIG. 4.2 Diagram showing  $j$  space being divided into four distinct regions. From Ref. [16].



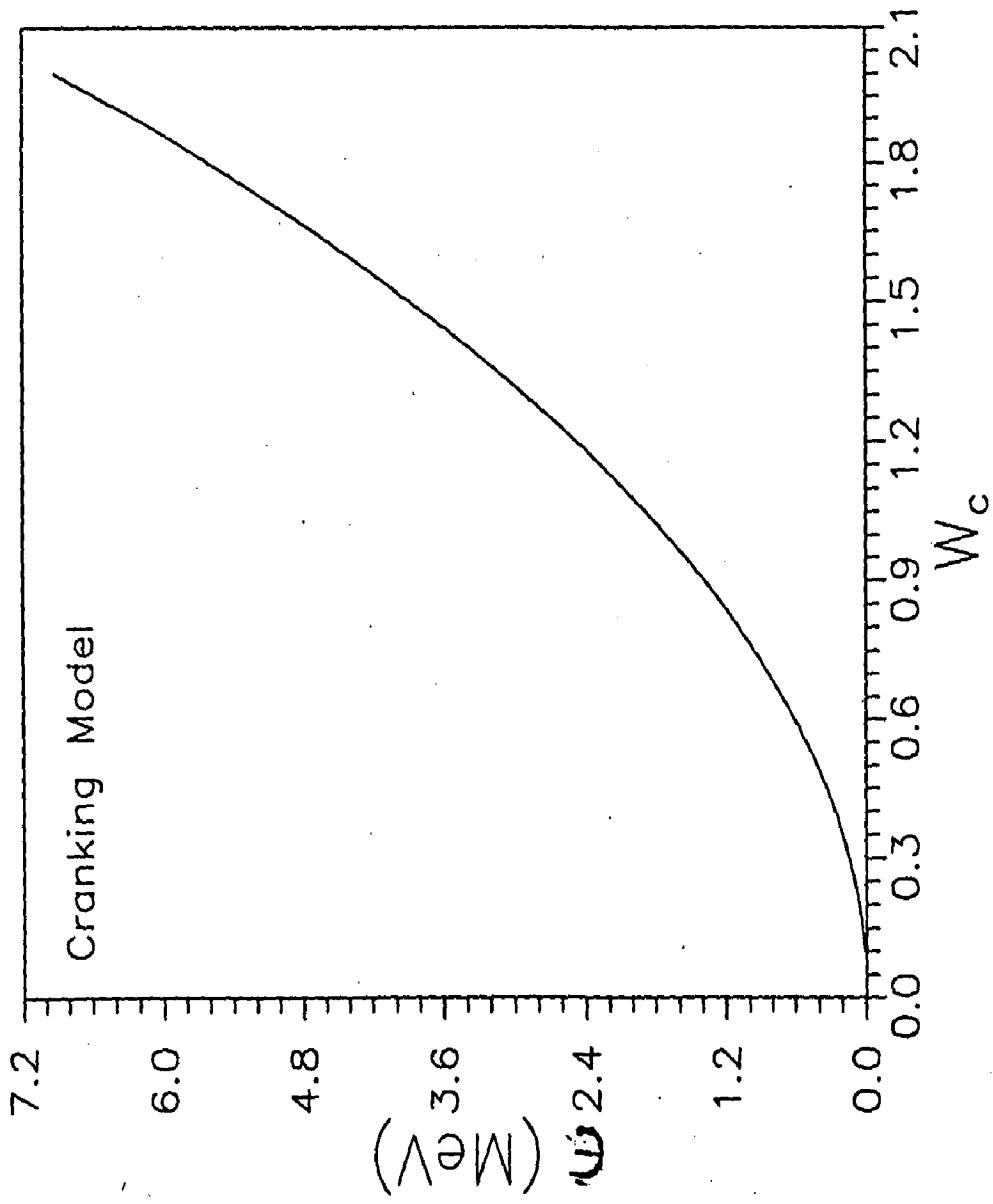


FIG. 4.3 Plot of energy  $\epsilon$  vs.  $\omega$  at fixed point  $a$  obtained after SCQ.

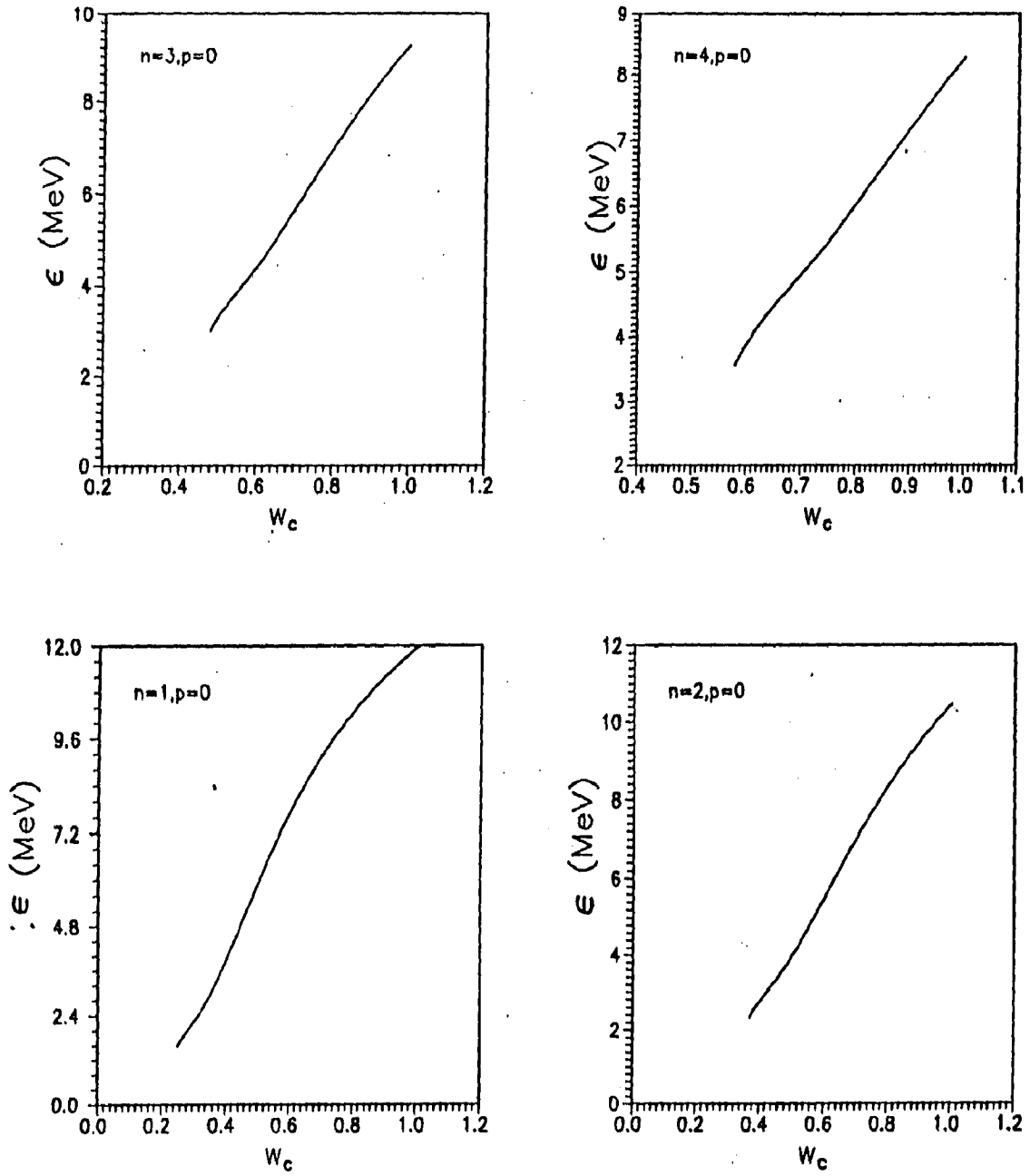


FIG. 4.4 Plots of energy  $\epsilon$  vs.  $\omega$  at fixed point  $c_{\pm}$  obtained after SCQ; for  $p=0$ .

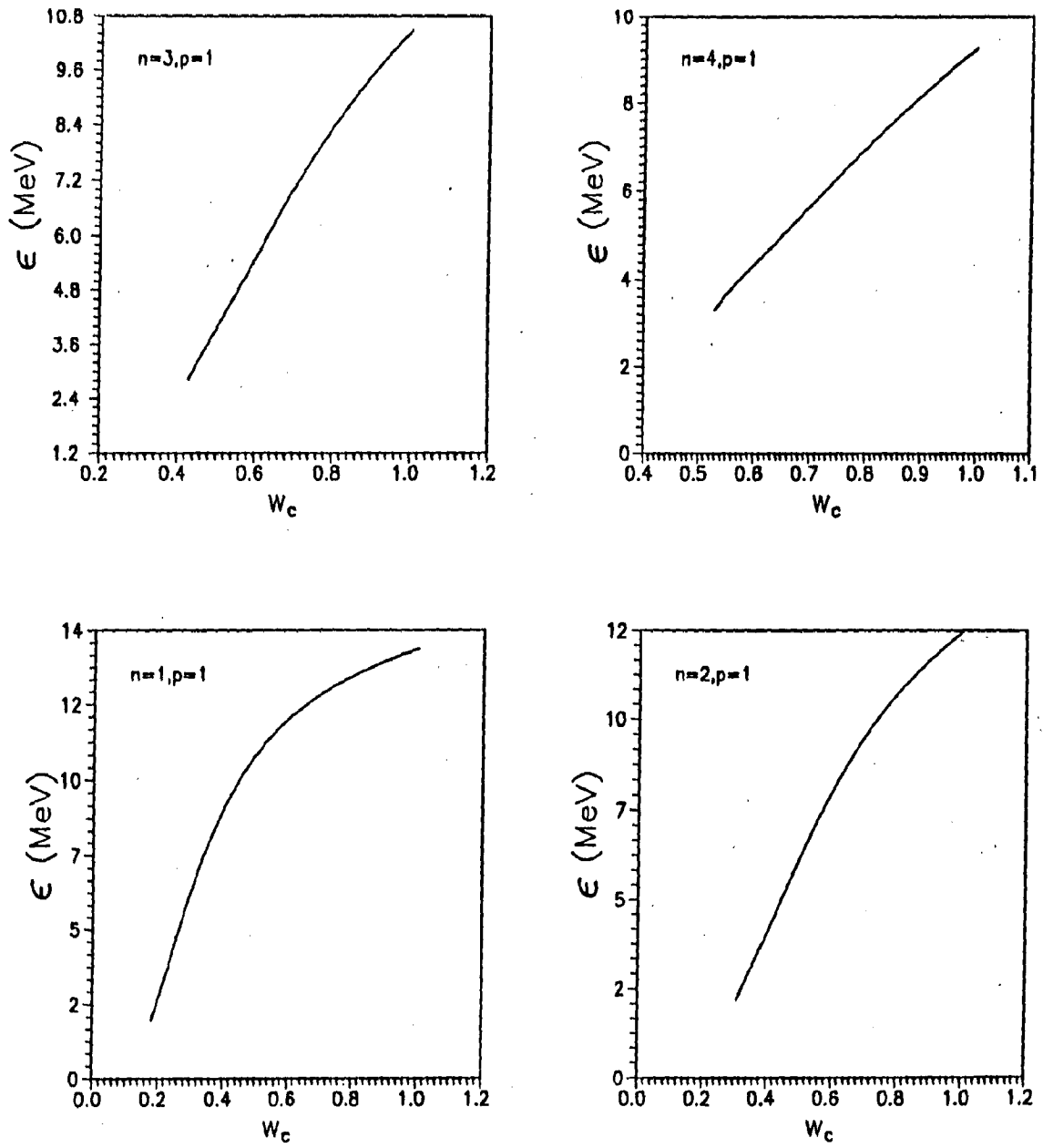


FIG. 4.5 Plots of energy  $\epsilon$  vs.  $\omega$  at fixed point  $c_{\pm}$  obtained after SCQ; for  $p=1$ .

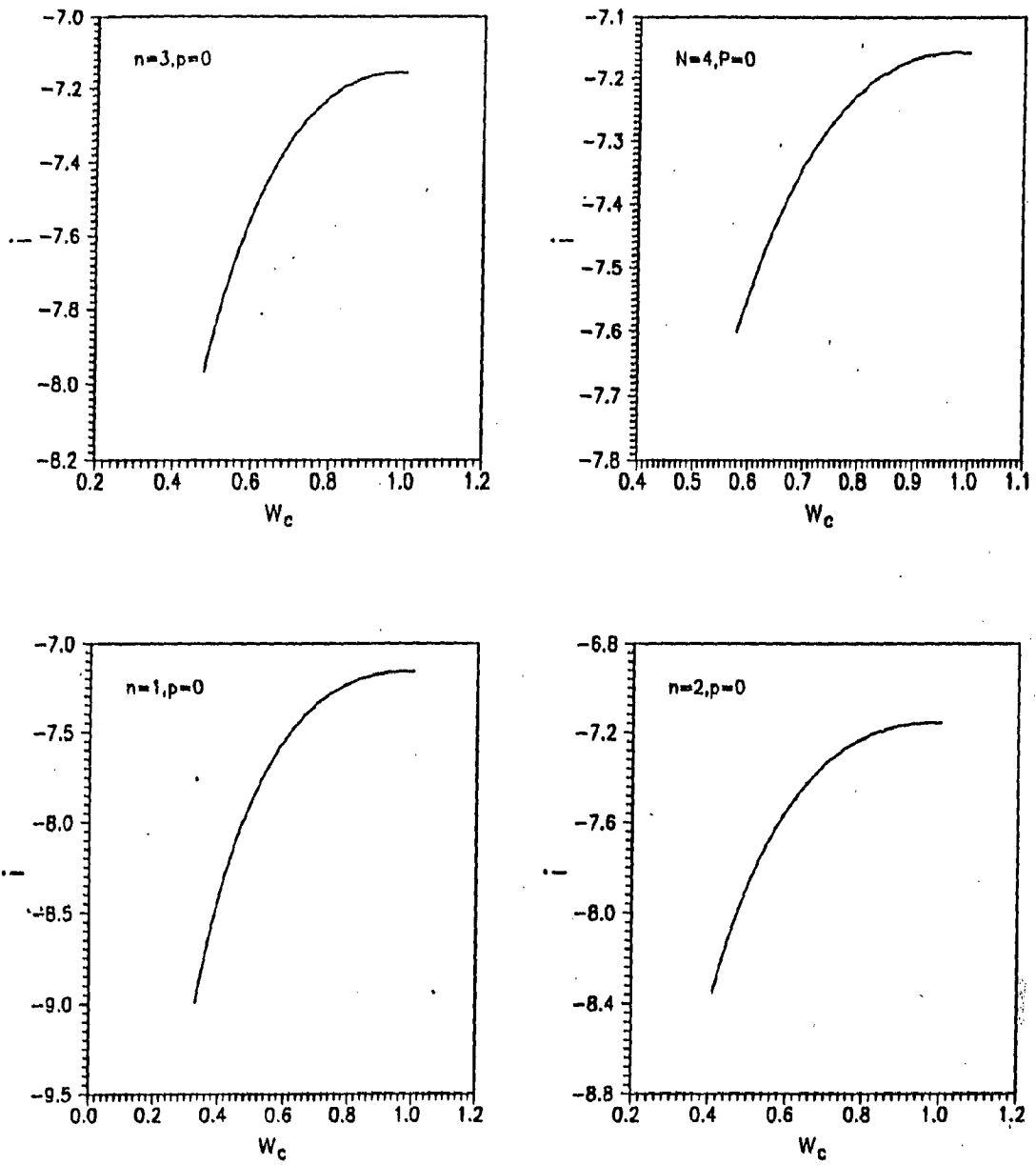


FIG. 4.6 Plots of alignment  $i$  vs.  $\omega$  at fixed point  $c_{\pm}$ ; for  $p=0$ .

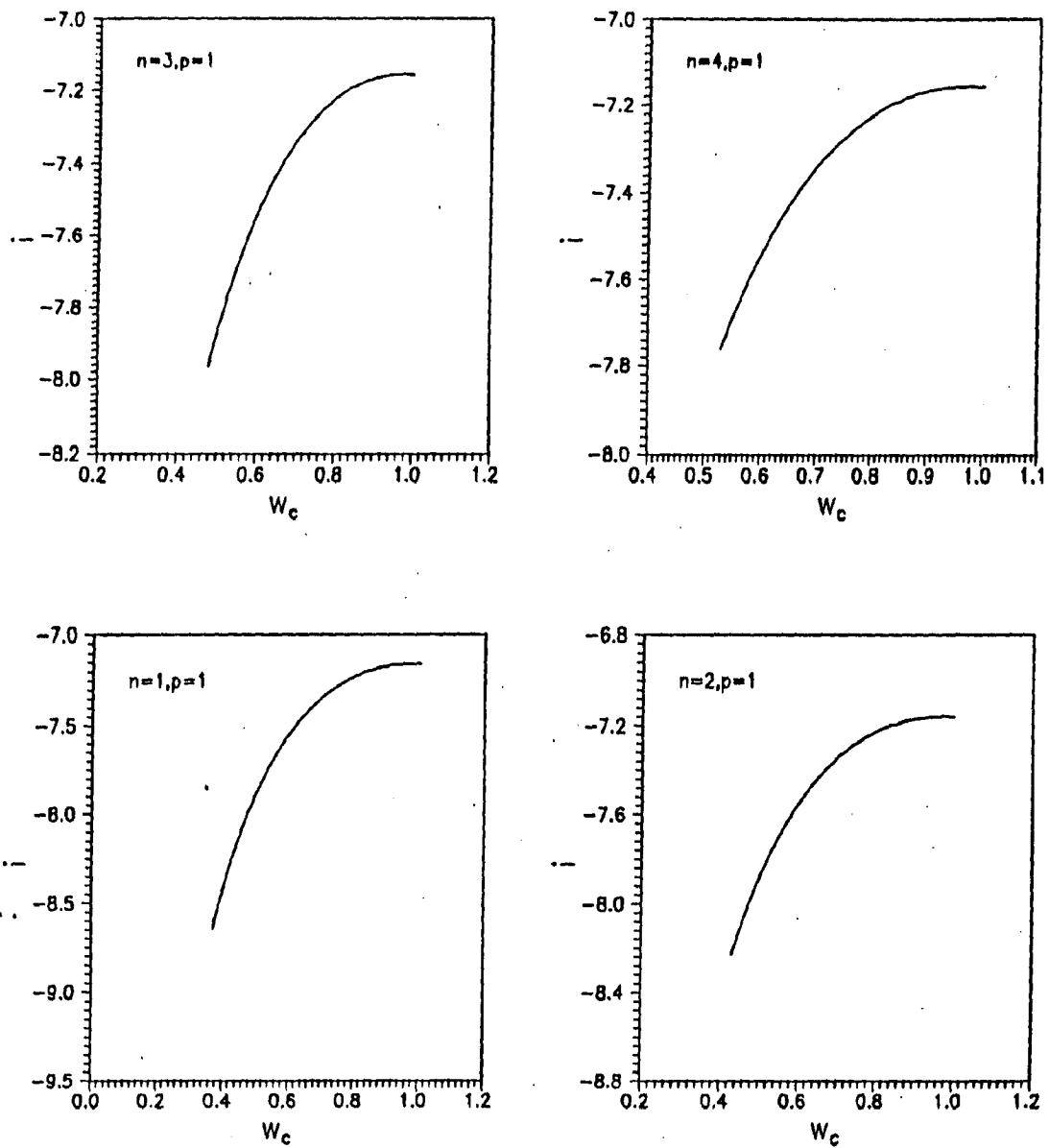


FIG. 4.7 Plots of alignment  $i$  vs.  $\omega$  at fixed point  $c_{\pm}$ ; for  $p=1$ .

**CHAPTER V**  
**PERIODIC ORBIT THEORY AND**  
**SPHERICAL CAVITY**

## I. INTRODUCTION

The current understanding of nuclear shapes as a function of angular momentum, nucleon number and excitation energies is based on the theory of shell structure developed over the last three decades. This understanding gained further ground with the introduction of the microscopic plus macroscopic approach put forward by Strutinsky [103]. A detailed exposition of the Strutinsky's approach and the relationship of shell structure to the underlying physical concepts like degeneracy in quantum systems may be found in the reviews of Brack et al. [22] and Bjorholm and Lynn [12]. It is now understood that shell structure is a general phenomena which pervades all quantum systems. The quantal nature of a system naturally leads to the emergence of shell structure. It has been found that quantal fluctuations tend to stabilise shapes having axes ratio 2:1, 3:1 etc. [15]. These ratios in turn can be directly linked to the frequency ratios as in the harmonic oscillator where the shape of the potential is defined in terms of frequencies. As we shall see, these axes ratios can also be linked to the frequencies of the periodic orbits in an appropriately deformed cavity.

Parallel to the Strutinsky method, a new and radically different understanding of shell structure has continued to evolve which is based on the closed periodic paths possible in a given cavity [6,50]. A semiclassical approach based on periodic orbits led Gutzwiller to propose a trace formula for level density of a quantum system in terms of quantities which are classical in nature [49]. Strutinsky and coworkers [105,106] used this approach to propose the first semiclassical interpretation of the gross shell structure in deformed nuclei. This seminal work constitutes the basis of much of what will be presented in this chapter and the next one.

In the present chapter we discuss very briefly the general conditions for the occurrence of shell structure with special reference to the harmonic oscillator potential. We then show that the level density for the harmonic oscillator can be naturally separated into a smooth and a fluctuating part. Explicit analytical expressions [20] can be easily obtained and serve as an easy text book example to illustrate the power of this technique. Next we introduce

some elementary ideas of the periodic orbit theory (POT) due to Gutzwiller and his famous trace formula for the fluctuating part of the level density. This formula was modified by Strutinsky to include the effect of systems with continuous symmetries such as a spherical or a spheroidal cavity [105]. Using this expression we obtain a simple formula for the level density of a spherical billiard and test the validity of the formula.

## II. CONDITIONS FOR SHELL STRUCTURE : ISOTROPIC HARMONIC OSCILLATOR

The harmonic oscillator potential serves as a paradigm to illustrate the underlying concepts of shell structure. The solutions of the isotropic harmonic oscillator are well known and are specified in terms of three quantum numbers  $[N, \ell, \Lambda]$  in polar coordinates. The energy eigenvalues are given by

$$E(N, \ell) = (N + 3/2)\hbar\omega_0 = [2(n_r - 1) + \ell + 3/2]\hbar\omega_0. \quad (1)$$

Here  $(n_r - 1)$  is the number of radial nodes. For each  $N$ ,  $\ell = N, N - 2, \dots, 1$  or  $0$ . For each  $N$ , there are  $(N + 1)(N + 2)$  orbitals including the two fold degeneracy of spin. The degeneracy ' $d$ ' of shells defined by  $N = 0, 1, 2, 3, \dots$  etc. are given by  $d = 0, 6, 12, 20, \dots$  etc. respectively; these are the magic numbers of harmonic oscillator. The energy  $E(n, \ell)$  is generally an increasing function of  $n$  and  $\ell$ . Same energy is obtained by increasing  $\ell$  and decreasing  $n$  by appropriate integer amounts; this leads to degeneracy and shell structure. Bohr and Mottelson [15] generalised this idea by expanding the  $E(n, \ell)$  around a given point  $(n_0, \ell_0)$

$$E(n, \ell) = E(n_0, \ell_0) + (n - n_0)(\partial E / \partial n)_{n=n_0} + (\ell - \ell_0)(\partial E / \partial \ell)_{\ell=\ell_0} + \text{second and higher order terms.} \quad (2)$$

Approximate degeneracy is obtained for mutual compensation of the two first order terms; it implies that



$$b(\partial E/\partial n)_0 = a(\partial E/\partial \ell)_0, \quad (3)$$

where  $a$  and  $b$  are small integers. We therefore obtain the condition  $an + b\ell = an_0 + b\ell_0$ . So the levels with a constant value of  $N = an + b\ell$  only slightly differ in energy (due to second and higher order derivatives). We may redefine  $N$  as  $N_{shell} = a(n-1) + b\ell$ , which now looks similar to the value obtained for H.O. with  $a = 2$  and  $b = 1$ . It is easy to show that two consecutive shells occur with an energy separation

$$\hbar\omega_{shell} = 1/a(\partial E/\partial n)_0 = 1/b(\partial E/\partial \ell)_0. \quad (4)$$

It is most revealing to realize that the derivatives  $(\partial E/\partial n)$  and  $(\partial E/\partial \ell)$  are the radial and angular frequencies of the orbits and the equation (4) corresponds to the condition that the classical orbits close upon themselves after  $a$  radial and  $b$  angular oscillations giving rise to periodic orbits with a frequency  $\omega_{shell}$ . The orbitals having the same value of  $N_{shell}$  bunch together. This shell structure is clearly visible in FIG. 5.1 what is now one of the most common figures on shell structure in harmonic oscillator [15]. If an axial symmetry is introduced in the system and if we choose  $\omega_x = \omega_y = \omega_{\perp}$ , then the harmonic oscillator potential can be written as,

$$V(x, y, z) = m/2(\omega_{\perp}^2(x^2 + y^2) + \omega_z^2 z^2), \quad (5)$$

or,

$$V(r, \theta) = \frac{1}{2}m\omega_0^2 r^2 \left(1 - \frac{4}{3}\delta P_2(\cos\theta)\right), \quad (6)$$

where  $\omega_z \approx \omega_0(1 - \frac{2}{3}\delta)$  and  $\omega_{\perp} \approx \omega_0(1 + \frac{1}{3}\delta)$  and  $\delta$  is a deformation parameter given by  $\delta = \frac{3(c/a-1)}{2(c/a+1)}$  where  $c$  and  $a$  are the semi major and semi minor axes respectively. The energy of this anisotropic oscillator is given by

$$E(n_{\perp}, n_z) = (n_z + \frac{1}{2})\hbar\omega_z + (n_{\perp} + 1)\hbar\omega_{\perp}, \quad (7)$$

where  $n_{\perp} = n_x + n_y$ . Denoting  $\eta = \frac{\omega_{\perp}}{\omega_z}$ , we obtain by using the condition of volume conservation,

$$E(n_{\perp}, n_z) = \eta^{-2/3} \hbar \omega_0 [\eta n_{\perp} + \eta_z + (\eta + \frac{1}{2})]. \quad (8)$$

For the special case of  $\omega_{\perp} = 2\omega_z$  which represents the 2:1 shape, we obtain

$$E(N, n_z) = 0.6 \hbar \omega_0 [2N - n_z + \frac{5}{2}]. \quad (9)$$

For a given  $N$ ,  $n_z = 0, 1, \dots, N$ . Thus, for the same value of  $(2N - n_z)$ , degenerate states arise. It is worth noticing that levels from several major shells (several  $N$ ) and therefore having both parities come together to form superdeformed shell structure as shown in FIG. 5.1. For the spherical shape, the energies are equally spaced at  $\hbar\omega_0$  and are highly degenerate; the degeneracy is partially lifted when deformation is introduced. A nearly uniform distribution appears to prevail at  $\delta \approx 0.15$ . The levels regroup in a very orderly way to form new sets of degenerate levels when the axes ratio of the spheroid is equal to the ratio of two integers. The regrouping is most pronounced at the axes ratio equal to 2 : 1. The energy of a system, for a given deformation, will be relatively lower if the number of particles is just sufficient to fill a group of degenerate levels; this represents a shell closure. For example, 168 particles completely fill a shell for the spherical shape and will have relatively lower energy than having only 140 particles. On the other hand, 140 particles completely fill a shell at 2 : 1 deformation and therefore lead to shell closure at the 2 : 1 shape. This leads to a generalisation of the concept of shells and shell closures.

### III. SOME BASIC TOOLS FOR SEMICLASSICAL PERIODIC ORBIT THEORY

In the next section we will present the periodic orbit theory (POT) which quite generally establishes a link between the density of states of a given quantum mechanical system with the periodic orbits of the corresponding classical system through the so called trace formula. As a preparation to this, we present in this section some basic quantum mechanical tools needed to calculate the density of states or the level density.

## A. Level Density

We start from the Hamiltonian for a particle with mass  $m$  in a local potential  $V(r)$  [20]

$$\hat{H} = \hat{T} + V(r), \quad (10)$$

$$\hat{T} = -\frac{\hbar^2}{2m}\nabla^2. \quad (11)$$

The stationary Schrodinger equation for bound states gives the spectrum  $E_n$  as,

$$\hat{H} |n\rangle = E_n |n\rangle, \quad E_n > 0. \quad (12)$$

The eigenstates  $|n\rangle$  form a complete, orthonormal basis set of wavefunctions.

$$\psi_n(r) = \langle r | n \rangle, \quad \langle n | m \rangle = \delta_{nm}; \quad \sum_n \psi_n^*(r') \psi(r) = \delta(r' - r). \quad (13)$$

The single-particle level density or density of states  $g(E)$  is defined as the sum of delta functions,

$$g(E) = \sum_n \delta(E - E_n). \quad (14)$$

## B. Separation Of $g(E)$ Into Smooth and Oscillatory Part

The level density  $g(E)$  contains information related to the stability of a quantum system. On the average, it has a smooth energy dependence which is determined by the number of degrees of freedom and the degeneracies of the single particle levels given by the symmetries of the hamiltonian. In general  $g(E)$  can be written as a sum of an average level density  $\tilde{g}(E)$  which has a smooth energy dependence and an oscillatory part  $\delta g(E)$

$$g(E) = \tilde{g}(E) + \delta g(E) \quad (15)$$

Both the parts can be obtained in a number of ways. In principle, for a given system both parts are determined uniquely.  $\tilde{g}(E)$ , the smooth part is most commonly obtained from the

extended Thomas Fermi model [73], the Weyl's formula [7] and the Strutinsky averaging procedure [103,104]. The oscillating part is the subject of various semiclassical methods including the periodic orbit theory. In the following, we present an example of harmonic oscillator where both the smooth and oscillating part of  $g(E)$  can be obtained analytically without using the trace formula. A detailed discussion of the various methods may be found in [20,23].

### C. Solvable Case of Harmonic Oscillator

Linked to section III.A the single-particle density matrix  $\rho(r, r')$  is defined as

$$\rho(r, r') = \sum_n \psi_n^*(r') \psi_n(r) = \sum_{E_n < \mu} \psi_n^*(r') \psi_n(r), \quad (16)$$

where  $\mu$  is the Fermi energy. Now  $\rho(r, r')$  depends on  $\mu$  and thus on statistics. A Laplace transform of  $g(E)$  yields the single-particle canonical partition function  $Z(\beta)$

$$Z(\beta) = L_\beta[g(E)] = \int_0^\infty e^{-\beta E} g(E) dE = \sum_i e^{-\beta E_n}, \quad (17)$$

where  $\beta$  is just a mathematical variable. Thus inverse Laplace transform of the partition function of the system yields the density of states  $g(E)$

$$g(E) = L_E^{-1}[Z(\beta)] = \frac{1}{2\pi i} \int_{\epsilon+i\infty}^{\epsilon-i\infty} e^{\beta E} Z(\beta) d\beta, \quad (18)$$

where the integral is to be taken in the complex  $\beta$ -plane along a contour  $C$ .

Examples:

- Schematic spectrum with one quantum number: Poisson formula

Let us choose the following schematic spectrum [20],

$$E_n = n, \quad d_n = 1, \quad n = 0, 1, 2, 3, \dots \quad (19)$$

Here  $d_n$  denotes the degeneracy of  $n^{\text{th}}$  level. The partition function for this system can be given as

$$Z(\beta) = \sum_n e^{-n\beta} = \frac{1}{1 - e^{-\beta}} = \frac{e^{\frac{\beta}{2}}}{2\sinh(\frac{\beta}{2})}. \quad (20)$$

Now by the calculus of residues we get the inverse Laplace transform,

$$g(E) = \sum_{n=0}^{\infty} \delta(E - n) = \sum_{k=-\infty}^{k=+\infty} e^{2\pi i k E}, \quad (21)$$

$$= [1 + 2 \sum_{k=1}^{\infty} \cos(2\pi k E)]. \quad (22)$$

Next we assume the energy spectrum  $E_n$  to be given by,

$$E_n = f(n), \quad d_n = D(n), \quad n = 0, 1, 2, 3, \dots, \quad (23)$$

where  $f(n)$  is an arbitrary monotonous function with differentiable inverse  $f^{-1}(E) = F(E)$  such that  $n = F(E_n)$  and  $D(E) = D(F(E))$  is another arbitrary function. The delta function may be written as,

$$\begin{aligned} \delta(E - E_n) &= \delta(E - f(n)), \\ &= \delta(\sum_n n f(n) - f(n)), \\ &= \delta(\sum_n F(E_n) F^{-1}(E_n) - F^{-1}(E_n)), \\ &= |F(E)| \delta(n - F(E)). \end{aligned} \quad (24)$$

$$(25)$$

Including the degeneracy  $D(n) = D(F(E)) = D(E)$ ,

$$\delta(E - E_n) = D(E) |F(E)| \delta(n - F(E)). \quad (26)$$

Comparing it with equation (22), we get

$$g(E) = D(E) |F(E)| [1 + 2 \sum_{k=1}^{\infty} \cos 2\pi k F(E)], \quad (27)$$

where the first term is smooth part  $\tilde{g}(E)$  and the second term is the fluctuating part  $\delta g(E)$ . This formula can be applied to any one-dimensional problem. Later on, in the periodic orbit theory,  $2\pi\hbar F(E)$  is identified with the classical action  $S$  along a primitive periodic orbit, where the number  $k$  represents the number of revolutions around the orbit. Note that the smoothed average level density separates out from the fluctuating part in a natural way. For 3-dimensional harmonic oscillator one obtains very easily,

$$g(E) = \frac{1}{2(\hbar\omega)^3} \left( E^2 - \frac{1}{4}(\hbar\omega)^2 \right) \left[ 1 + 2 \sum_{k=1}^{\infty} \cos\left( 2\pi k \frac{E}{\hbar\omega} - \frac{3}{2} \right) \right]. \quad (28)$$

In FIG. 5.2, we display the numerical results obtained by Brack and Bhaduri, to demonstrate the convergence of expression(27). The plot of  $g(E)$  vs.  $E$  (in units of  $\hbar\omega$ ) for different maximum values of  $k_{max}$  rapidly approaches the delta function peaks at the correct positions of the quantum energy spectrum as  $k_{max}$  becomes 50. On the other hand,  $k = 1$  already gives information about the gross shell structure.

#### IV. PERIODIC ORBIT THEORY

The periodic orbit theory (POT) received a boost with the proposal of a trace formula by Gutzwiller [50] which relates the oscillatory part in the level density  $\delta g$  to a sum over the actions, time periods and stability angles of all the periodic orbits. In its simplest form, the trace formula for a system with isolated orbits is given by

$$\delta g(E) = \frac{1}{\pi\hbar} \sum_{PO} \frac{T_{PPO}}{\sqrt{|\det(\tilde{M}_{PO} - I)|}} \cos \left[ \frac{S_{PO}(E)}{\hbar} - \frac{\sigma_{PO}\pi}{2} \right]. \quad (29)$$

Here  $T_{PPO}$  is the time period of the primitive periodic orbits. Each periodic orbit contributes an oscillating term whose phase is given by the action

$$S_{PPO} = \oint p \cdot dq. \quad (30)$$

$\sigma$  is the Maslov index which is an integer depending on the reflection points of the orbits. The matrix  $\tilde{M}_{PO}$  is a  $(2n - 2)$  dimensional stability matrix, where  $n$  is the number of degrees of

freedom. The determinant in the denominator is large for an unstable orbits, thus reducing their contribution. The POT as developed by Gutzwiller applies, only to systems with isolated orbits and thus is mostly of use for chaotic systems. For systems having high degree of symmetry, the periodic orbits exist in continuous families [105]. In such systems, the discrete sum over orbits in equation (28) cannot be carried out. It is necessary to first integrate over each family, and then sum over the various families. A detailed discussion of the general structure of trace formulae for systems with continuous symmetry was given by Creagh and Littlejohn [32]. In this thesis, we have adopted the trace formula given by Strutinsky et al. [106] with proper introduction of Maslov index.

Balian and Bloch [6] presented a similar formula which they developed for cavities with reflecting walls of arbitrary shape in two or more dimensions; their formula also applies to integrable systems, such as the spherical cavity. Berry and Tabor [10] derived a trace formula for integrable systems with arbitrary smooth potentials with EBK quantization as a basis. The formula proposed for isolated orbits, is mainly applicable to chaotic systems, although its clever usage for systems with families of degenerate periodic orbits has recently been demonstrated by Brack and Jain [19]. One of the main strengths of the periodic orbit theory is that it enables one to obtain gross-shell effects in the level density of a quantum system semiclassically, i.e. without solving the Schrodinger equation, independently of its integrability or the possibility of a full quantization, and to interpret shell effects in terms of the interplay of the most important short periodic orbits.

### A. Convergence of the Periodic Orbit Sum

Keeping in mind that equation (28) is a Fourier decomposition of the oscillating level density, it is clear that if one is interested in high resolution, one must include large number of Fourier components i.e. one has to sum up to higher number of orbits. Usually, the periodic orbit sum does not converge and the series has to be truncated. But if one is interested only in a low resolution of shell structure, only orbits with the smallest actions

and consequently the largest amplitude of Fourier component are enough. Many observable shell effects in real systems do not depend on the exact level density, but on a coarse-grained level density obtained by averaging over the finer details. Such an averaging, in practice, may arise due to finite temperature effects or, by uncertainties in the measurements. We therefore use Gaussian averaging of the level density [20] over an energy range  $\gamma$ , which should be less than the main shell spacings. This implies that  $\gamma$  should be chosen that

$$\gamma \leq \hbar\Omega \approx \frac{2\pi\hbar}{T_{PPO}^{min}}. \quad (31)$$

This leads to a damping factor  $\exp[-(\gamma\frac{T_{PPO}}{2\hbar})^2]$  in the trace formula. The fluctuating part of level density becomes,

$$\delta g(E) = \sum_{PO} e^{-(\gamma\frac{T_{PPO}}{2\hbar})^2} \delta g_{PO}(E). \quad (32)$$

Thus, each periodic orbit contribution is damped exponentially, whereby the orbits with longer periods are damped more strongly than the short ones. Therefore the problem of the convergence of the series is overcome by using the above averaging procedure. Since only shortest orbits contribute most significantly, this procedure allows us to retain the most important part of the information.

## B. Maslov Indices

The Maslov index plays a very crucial role in the periodic orbit sum as it decides the relative phase of the various terms in the summation. Creagh and Littlejohn [31] presented a much deeper understanding of the Maslov index showing that it is equal to twice the number of times the stable and unstable manifolds wind around the periodic orbit. They presented two practical methods for determining  $\sigma$ . One of the methods is useful for kinetic-plus-potential systems and its detailed application to harmonic oscillator has been discussed by Brack and Bhaduri [20]. The second method applies specifically to billiard systems and is a geometrical method. Specific rules in applying the geometrical method have been stressed by



Brack and collaborators [20,80]. Since we are specifically interested in billiards, we present the rules only for billiards. It may be remarked here that various authors do not seem to be consistent in using Maslov index. The resulting ambiguity has been difficult to resolve even in the simple case of a circular or a spherical billiard. The ultimate test of the success of a trace formula however is the reproduction of the exact quantum spectrum.

The Maslov index  $\sigma$  is given by  $\sigma = \mu + \nu$  where  $\mu$  is an index counting the number of conjugate points of a given orbit of fixed energy and  $\nu$  arises while taking the trace of the Green's function to obtain the level density  $g(E)$ . Following Creagh and Littlejohn [31], Balian and Bloch [6] and Magner et al. [80] a set of rules were presented by Brack and Bhaduri [20] to obtain the Maslov index for billiards. We present these rules in a more explicit form for an axially symmetric deformed cavity.

1.  $\mu$  is determined by number of conjugate points i.e. turning and caustic points.
2. A simple conjugate point gives a phase shift of  $-\frac{\pi}{2}$  corresponding to change in  $\mu$  by 1.
3. Each reflection from the boundary produces a simple turning point (sign change of the normal component of the particle momentum) and a caustic point in the tangential direction. This gives a change  $\Delta\mu = 2$  per reflection and a change in phase by  $-\pi$ .
4. Inside the billiard, there is a conjugate point along the caustic for each reflection, giving rise to  $\Delta\mu = 1$  and a phase change of  $-\frac{\pi}{2}$ . Thus the total contribution to  $\mu$  is  $-mn_r\frac{3\pi}{2}$ , where  $m$  is the number of repetitions.
5. There is a phase shift of  $-(mn_\theta - 1)\pi$  for 2- dimensional periodic orbits which is related to phase change in  $\pi$  due to rotation around the centre.
6. While  $\Delta\mu = 2$  for each reflection satisfying Dirichlet boundary condition,  $\Delta\mu = 0$  for Neumann boundary condition.
7. The contribution due to  $\nu$  depends on the sign of the quantity  $\omega$  defined by

$$\omega = \frac{\text{tr}\tilde{M} - 2}{b}, \quad (33)$$

where  $b$  is the upper right element of the stability matrix

$$\tilde{M} = \begin{pmatrix} a & b \\ c & d \end{pmatrix}, \quad (34)$$

which is also given by

$$b = \frac{\partial r_{\perp}(t = T)}{\partial p_{\perp}(t = 0)}. \quad (35)$$

If  $\omega$  is positive,  $\nu = 0$  and if  $\omega$  is negative, then  $\nu = 1$ .

8. For the diameters along the symmetry axis, 1- dimensional periodic orbits, there are two simple caustic points presented by two focal points.

9. Rule number (3) is also applicable to orbits in the equatorial plane.

### C. Smooth Part of the Level Density

For the smooth part of the level density  $\tilde{g}(E)$ , Weyl devised a formula which was later extended and generalised by Balian and Bloch [7]. This generalised Weyl formula for a cavity with an arbitrary smooth convex boundary is given by

$$\tilde{g}(E) = \frac{1}{4\pi^2} \left(\frac{2m}{\hbar^2}\right)^{\frac{3}{2}} \sqrt{E} V - \frac{1}{16\pi} \left(\frac{2m}{\hbar^2}\right) S + \frac{1}{12\pi^2} \left(\frac{2m}{\hbar^2}\right)^{\frac{1}{2}} \frac{1}{\sqrt{E}} C, \quad (36)$$

where  $V$  is the volume and  $S$  the surface area of the cavity.  $C$  is the mean curvature of the cavity, which is defined as the surface integral over the algebraic mean of the two principal curvatures  $\kappa_1, \kappa_2$ :

$$C = \oint d\sigma \frac{1}{2} (\kappa_1 + \kappa_2). \quad (37)$$

## V. SPHERICAL CAVITY

In this section, we use the POT presented in earlier sections to obtain the shell structure of a spherical cavity. There are number of reasons for choosing this cavity. First, it is the simplest and most elegant example where the basic ideas can be seen to work. Second, the exact results are known from quantum mechanics so that a direct comparison can be made.

Finally, the results of a spherical cavity have found applications in a number of situations. It is our hope that spherical nuclei must also display some basic characteristics of a spherical cavity leading to a deeper insight in the structure of these nuclei. First we present the exact quantum mechanical solution.

### A. Quantum Mechanical Results

The usual Schrodinger equation is solved to get the energy levels of a particle enclosed in a sphere of zero potential with infinitely high potential walls defining its surface of radius  $R$  [43]. Choosing  $\chi_\ell(r)$  as the radial eigen function, the radial Schrodinger equation can be written as

$$\begin{aligned} \chi_\ell'' + \left[ k^2 - \frac{\ell(\ell+1)}{r^2} \right] \chi_\ell &= 0 & 0 \leq r \leq R, \\ \chi_\ell &= 0 & r \geq R \end{aligned} \quad (38)$$

The solutions of the above equation are well known spherical Bessel functions given by

$$\chi_\ell(r) = C j_\ell(kr), \quad (39)$$

where  $C$  is a constant. The boundary condition gives us,

$$j_\ell(kR) = 0. \quad (40)$$

Since, for each given value of  $\ell$ , the Bessel function has an infinite number of zeros, we find an infinite number of values of  $k_{n_r, \ell}$  and of energy levels

$$E_{n_r, \ell} = \frac{\hbar^2}{2m} k_{n_r, \ell}^2. \quad (41)$$

For each  $\ell$ ,  $n_r=1,2,3,\dots$  etc., where  $n_r$  is the radial quantum number counting the zeros. The zeros of Bessel functions tend towards either  $n\pi$  for even, or  $(n+1/2)\pi$  for odd  $\ell$ . In FIG. 5.3 are plotted energy eigenvalues on y-axis and  $\ell$  on the x-axis. It is clear from the figure that many energy levels bunch together (for different  $n_r, \ell$ ) giving rise to fluctuation in the level density and hence a shell structure arises.

## B. Results Using POT

A spherical billiard is a system with continuous symmetries and therefore contains families of degenerate periodic orbits [6]. These results were recently used to explain the super-shell structure observed in sodium atom cluster [90]. The circular billiard has recently been applied to study atomic clusters [24,81], quantum dots [95] and nuclei by Frisk [44] and by Brack [21].

The starting point of our formulation is the trace formula presented by Strutinsky et al. [106], which takes care of degenerate family of periodic orbits. According to this, the oscillating component of single particle level density in cylindrical coordinate  $(\rho, \phi, z)$  is given by,

$$\delta g(E) = \frac{1}{\pi \hbar^2} \sum_{\beta, m} f_{\beta, m} \sin\left(\frac{S_{\beta, m}}{\hbar} + \sigma_{\beta, m}\right) \int \int d\rho dz \sqrt{|p_\rho p_z J(p_\rho p_z t_{\beta, m}; \rho' z' E)|_{\rho' z' \rightarrow \rho z}} \quad (42)$$

The factor  $f_{\beta, m}$  equals to 1 for the diametric orbits and 2 for other orbits like triangles, squares etc. The time period for the path from the initial point  $\vec{r}$  to final point  $\vec{r}'$  for energy  $E$  is defined as

$$t_\beta = \frac{\partial S_\beta(\vec{r}, \vec{r}', E)}{\partial E}. \quad (43)$$

The quantity  $J$  in equation (42) is the Jacobian of transformation between two sets of classical quantities  $(p_\rho, p_z, t_{\beta, m})$  and  $(\rho', z', E)$ , which are related by the classical equations of motion.

The maximum contribution to the gross-shell structure comes from the shortest periodic orbits. As pointed out, it has now become customary to carry out a smooth truncation of the contributions of longer periodic orbits by folding the level density with a Gaussian function of width  $\gamma/R$  [24],

$$\delta g_{av}(E) = \sum_{\beta, m} \delta g(E) e^{-\left(\frac{\gamma L_{\beta, m}}{2R}\right)^2}. \quad (44)$$

Here,  $L_{\beta, m}$  is the length of periodic orbit. The averaging width  $\gamma$  is chosen to be larger than the mean spacing between the energy levels within a shell, but much smaller than the

distance between the gross shells. This averaging ensures that all longer paths are strongly damped and only the shortest periodic orbits contribute to the oscillating part of the level density.

### 1. Spherical Billiard in Spherical Polar coordinates

We characterize the spherical cavity by using the spherical polar coordinates  $(r, \theta, \phi)$  which are related to the cartesian coordinates as

$$\begin{aligned} x &= r \sin \theta \cos \phi & 0 \leq r \leq \infty; \\ y &= r \sin \theta \sin \phi & 0 \leq \theta \leq \pi; \\ z &= r \cos \theta & 0 \leq \phi \leq 2\pi. \end{aligned} \quad (45)$$

The hamiltonian  $H$  is expressed in terms of  $(r, \theta, \phi)$  and the canonically conjugate momenta  $(p_r, p_\theta, p_\phi)$  as

$$H = \frac{1}{2M} \left( p_r^2 + \frac{1}{r^2} p_\theta^2 + \frac{1}{r^2 \sin^2 \theta} p_\phi^2 \right) + V(r), \quad (46)$$

where  $M$  is the mass of the particle and

$$\begin{aligned} V(r) &= 0 & r < R_0 \\ &= \infty & r \geq R_0. \end{aligned} \quad (47)$$

$R_0$  being the radius of the spherical cavity.

The time dependent Hamilton-Jacobi equation leads to the time independent equation given by,

$$\frac{1}{2M} \left[ \left( \frac{\partial S_\beta}{\partial r} \right)^2 + \frac{1}{r^2} \left( \frac{\partial S_\beta}{\partial \theta} \right)^2 + \frac{1}{r^2 \sin^2 \theta} \left( \frac{\partial S_\beta}{\partial \phi} \right)^2 \right] = E. \quad (48)$$

The three partial actions  $(s_r, s_\theta, s_\phi)$ , obtained by using the separation of variable technique, are

$$s_\phi = \oint p_\phi d\phi = 2\pi l_z, \quad (49)$$

$$s_\theta = \oint p_\theta d\theta = \oint \sqrt{\epsilon^2 - \frac{l_z^2}{\sin^2\theta}} d\theta = 2\pi(\epsilon - l_z), \quad (50)$$

$$s_r = \oint p_r dr = \oint \sqrt{2ME - \frac{\epsilon^2}{r^2}} dr, \quad (51)$$

where  $l_z$  and  $\epsilon$  are the separation constants in equation (49), (50) and (51). The limits of integration in (51) are determined by noting that the particle motion is bounded between an upper limit provided by the radius of the sphere  $r = R_0$  and a lower limit obtained from  $p_r^2 = 0$ ,

$$r_{min} = \frac{\epsilon}{\sqrt{2ME}}, \quad (52)$$

where,

$$\epsilon = \sqrt{(2ME)R_0} \cos\chi. \quad (53)$$

Solving the equation (51), we get

$$s_r = 2\sqrt{(2ME)R_0}(\sin\chi - \chi\cos\chi). \quad (54)$$

The constant  $\epsilon$  is fixed by using the periodicity condition i.e.

$$\frac{\omega_r}{\omega_\theta} = -\frac{\frac{\partial S_\theta}{\partial \epsilon}}{\frac{\partial S_r}{\partial \epsilon}} = \frac{n_r}{n_\theta}, \quad (55)$$

where  $n_r$  and  $n_\theta$  are relatively prime integers. This implies that  $\chi = \pi \frac{n_\theta}{n_r}$ . The frequency of rotation for a three dimensional orbit is

$$\begin{aligned} \Omega_\beta &= \frac{2\pi}{T_\beta} = \frac{\omega_r}{n_r} \\ &= \frac{\sqrt{2ME}}{MR_0} \frac{\pi}{n_r \sin\chi}, \end{aligned} \quad (56)$$

and,

$$T_\beta = \frac{M}{\sqrt{2ME}} L_\beta, \quad (57)$$

where  $L_\beta = 2R_0 n_r \sin\chi$ . It may be noted that the equation (56) for the rotational frequency is exactly the same as obtained in the quantum treatment [15].

The action  $S_\beta = \sqrt{2ME}L_\beta$  in equation (42) is determined by the length  $L_\beta(n_r, n_\theta)$ , which can easily be found from the time period in equation (57). This length comes out to be exactly the same as obtained from the geometrical considerations viz.  $L_\beta = 2n_r R_0 \sin \frac{n_\theta \pi}{n_r}$ . A good description of the periodic orbits in a circle may be found in [24].

The Jacobian is obtained by using the Hamilton-Jacobi equation and is given by

$$J = -\frac{2M^2}{\sqrt{2ME}} \frac{1}{\sqrt{r^2 - a^2}} \left(\frac{1}{m}\right). \quad (58)$$

with  $a = R_0 \cos\chi$ . The quantity  $\rho p_\rho$  appearing in equation (42) is given by

$$\rho p_\rho = \sqrt{2ME}[\sqrt{r^2 - a^2} \sin\theta + a \cos\theta] \sin\theta. \quad (59)$$

Using equations (58) and (59) in equation (42), the oscillating component of the level density is given by

$$\begin{aligned} \delta g(E) = & \frac{1}{\pi \epsilon_0} \sqrt{kR_0} \sum_{\tau_{n_\theta}} \sum_{\tau_{n_r} > 2\tau_{n_\theta}} \sin[kL(\tau_{n_r}, \tau_{n_\theta}) + \sigma(\tau_{n_r}, \tau_{n_\theta})] \times \\ & \int_{r=a}^{R_0} \int_{\theta=0}^{\pi} -r dr d\theta \left( \left| \frac{2}{m} \left[ \sin^2\theta + \frac{\cos\phi}{\sqrt{r^2 - \cos^2\phi}} \sin\theta \cos\theta \right] \right|^{\frac{1}{2}} \right). \end{aligned} \quad (60)$$

where  $\tau_{n_r} = mn_r$ ,  $\tau_{n_\theta} = mn_\theta$ ,  $m$  is the number of repeated cycles of a given type of orbit and  $\epsilon_0 = \frac{\hbar^2}{2MR_0^2}$ . We also multiply equation (60) by a factor  $\sqrt{kR_0}$  to compensate for the higher degeneracy of the spherical cavity. The Maslov index  $\sigma(\tau_{n_r}, \tau_{n_\theta})$  can be worked out by using the rules stated earlier. It may be pointed out that whereas the action  $S_\beta$  is identical for repeated cycles of a periodic orbit and therefore can be multiplied by the number of repetitions to obtain the total action, the same is not true, in general, for the Maslov index. It was recently demonstrated explicitly by Brack and Jain [19] that for stable isolated orbits in a harmonic oscillator potential, the Maslov index does not repeat itself in successive cycles. The Maslov index used here is taken from Balian and Bloch [6]:

$$\sigma(\tau_{n_r}, \tau_{n_\theta}) = -\frac{3\pi}{2}\tau_{n_r} - (\tau_{n_\theta} - 1)\pi + \frac{3\pi}{4}. \quad (61)$$

For diametric orbits, the equation (60) simplifies to

$$\delta g_{dia}(E) = -\frac{1}{\pi\epsilon_0} \sum_m \frac{1}{\sqrt{2m}} \sin(kL(m) + \sigma(m)). \quad (62)$$

The Maslov index  $\sigma(m)$  in this case is taken as,

$$\sigma(m) = -\frac{3\pi}{2}m + \frac{3\pi}{4}. \quad (63)$$

Using Weyl's formula for smooth part of level density, we obtain for a spherical cavity,

$$\tilde{g}(E) = \frac{1}{3\pi\epsilon_0 k R_0} [(kR_0)^2 - \frac{3\pi}{4}kR_0 + 1]. \quad (64)$$

The total level density  $g(E)$ , therefore becomes,

$$g(E) = \tilde{g}(E) + \delta g(E) + \delta g_{dia}(E). \quad (65)$$

## VI. RESULTS AND DISCUSSION

We have used the formula (60) to calculate the oscillating part of the level density and the results are shown in figures 5.4(a) and (b). In FIG. 5.4(a), we show the variation of  $\delta g$  as a function of  $kR$  where the 3:1, 4:1, 5:1 and 6:1 orbits have been taken into account; the diametric orbits were not included and no sum was carried out over repeated cycles. The plot reveals the well known beating pattern or the supershell structure that arises out of the interference of mainly the triangular (3:1) and the rhomboidal (4:1) orbits. It may be noticed that  $\delta g$  oscillates at a higher frequency where  $\Delta kR \approx 1.1$  units and a supershell structure appears which oscillates with a slow frequency where  $\Delta kR \approx 12$  units. When the diametric orbits are included in the sum, the picture modifies to what is shown in FIG. 5.4(b) with a little change. Although the diametric orbits have a significantly smaller length than the 3:1 and other higher orbits included in the sum, but they have a degeneracy factor lower by one unit than other orbits so they do not lead to any significant modification in the supershell structure; in both the cases  $\gamma = 0.6$ . As pointed out earlier, the ultimate test of the trace formula is its ability to reproduce the exact quantum mechanical eigenvalues if sufficient



number of orbits are included in the periodic orbit sum. In figures 5.5 and 5.6 we show the results for orbits upto  $n_r = 100$  and  $n_\theta = 100$  included in the sum. FIG. 5.5 exhibits the results without smoothing while a smoothing width  $\gamma = 0.02$  is taken in FIG. 5.6. The effect of smoothing is visible in terms of a cleaning up of many spurious peaks and also the negative amplitude decreases appreciably. In figures 5.7 and 5.8, we show similar results when the number of orbits included in the sum is increased to  $n_r = 500$  and  $n_\theta = 500$ . A much better eigenvalue spectrum is obtained both with and without smoothing. The exact quantum eigenvalues are also shown in the graphs at the bottom for a direct comparison. It is satisfying to note that the observed peaks have a one-to-one correspondence with the quantum results. the formula for level density therefore appears to be reasonably successful.

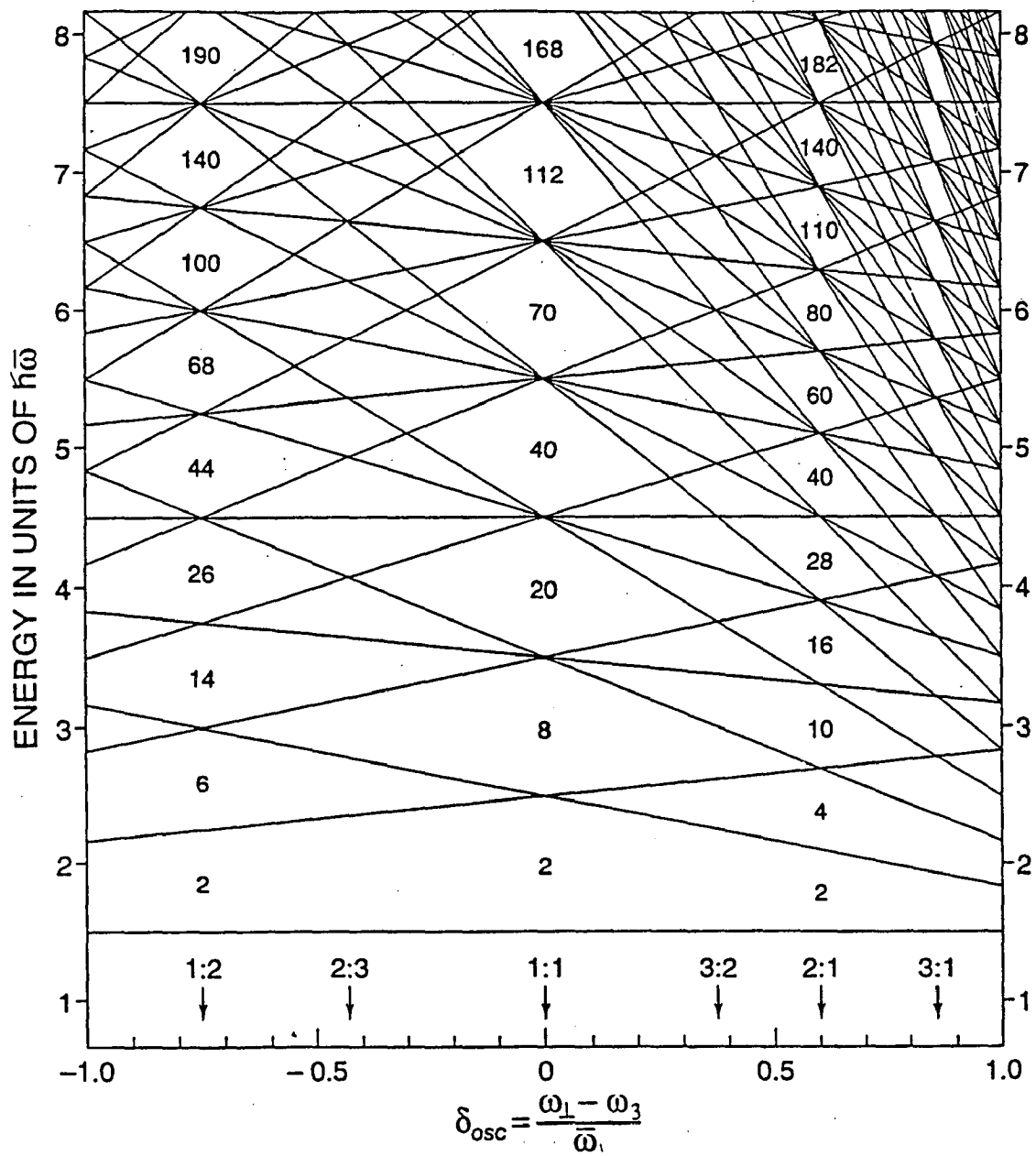


FIG. 5.1 Plot of single-particle level energies vs. the deformation showing shell structure for an axially symmetric harmonic oscillator. From Ref. [15].

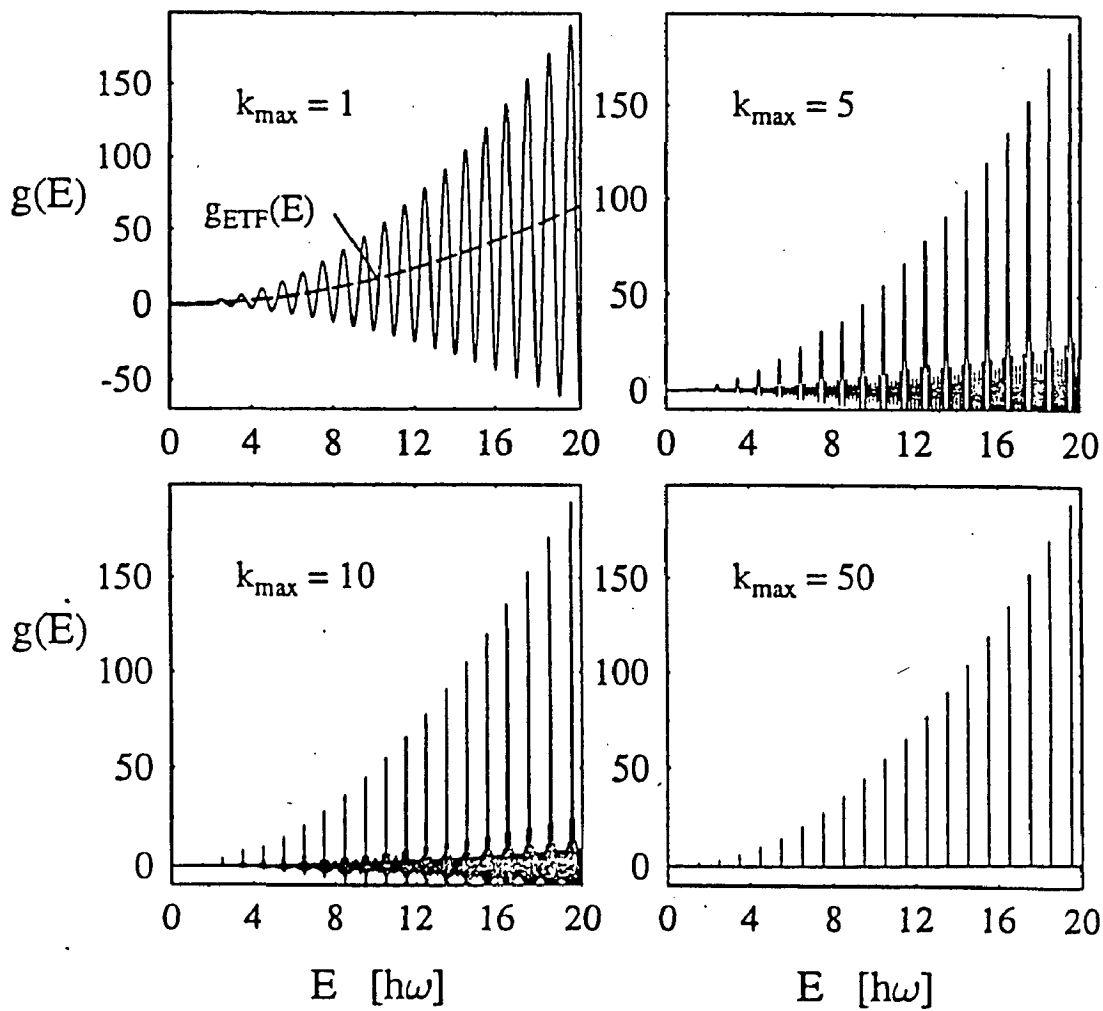


FIG. 5.2 Level density of the three-dimensional isotropic harmonic oscillator with different numbers  $k_{\max}$  of harmonics  $k$  included. From Ref. [20].

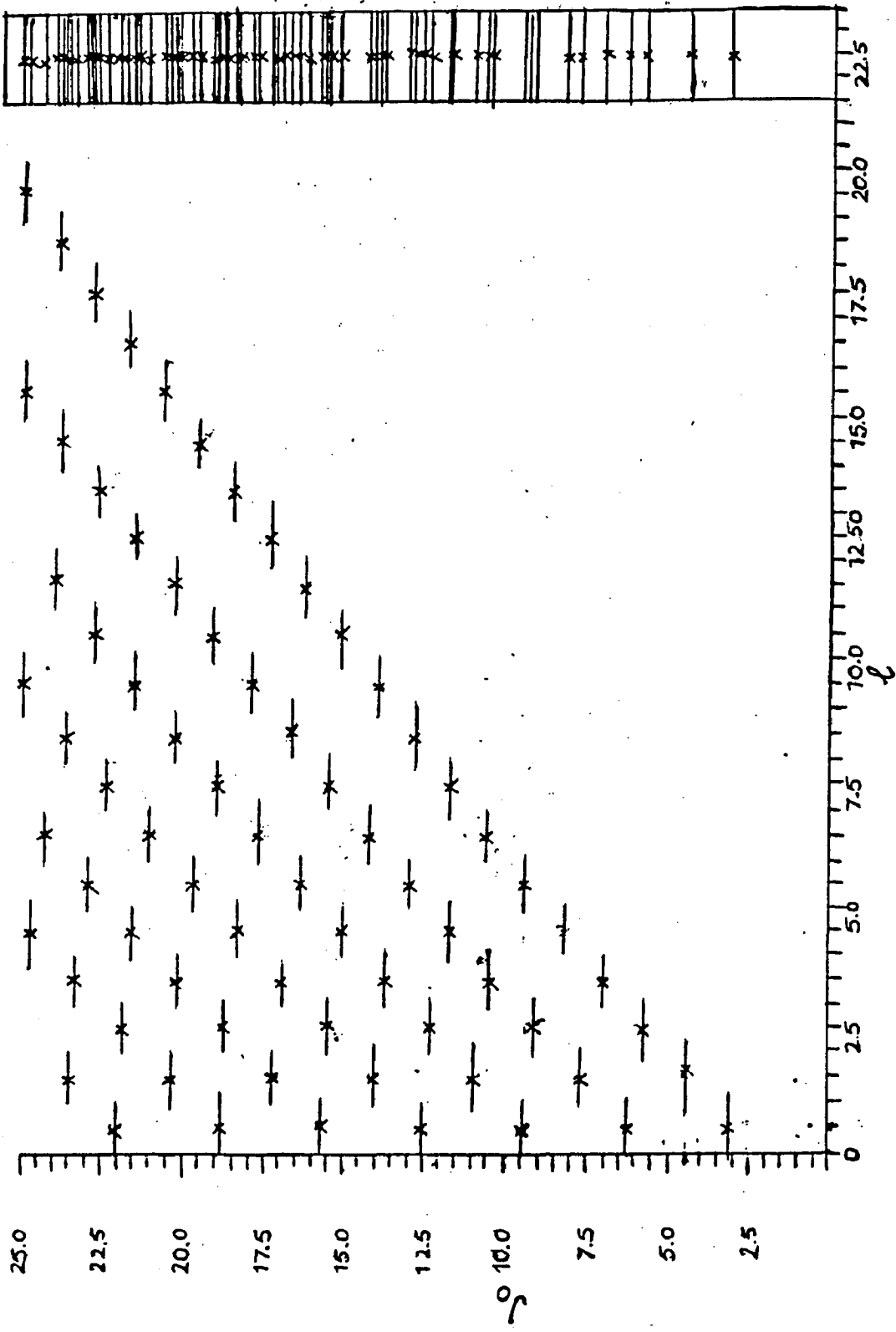


FIG. 5.3 Quantum mechanical energy spectrum for a particle in a spherical cavity. The levels are grouped in columns according to  $l$  values. On the right we show the total spectrum with a clearly visible shell structure.

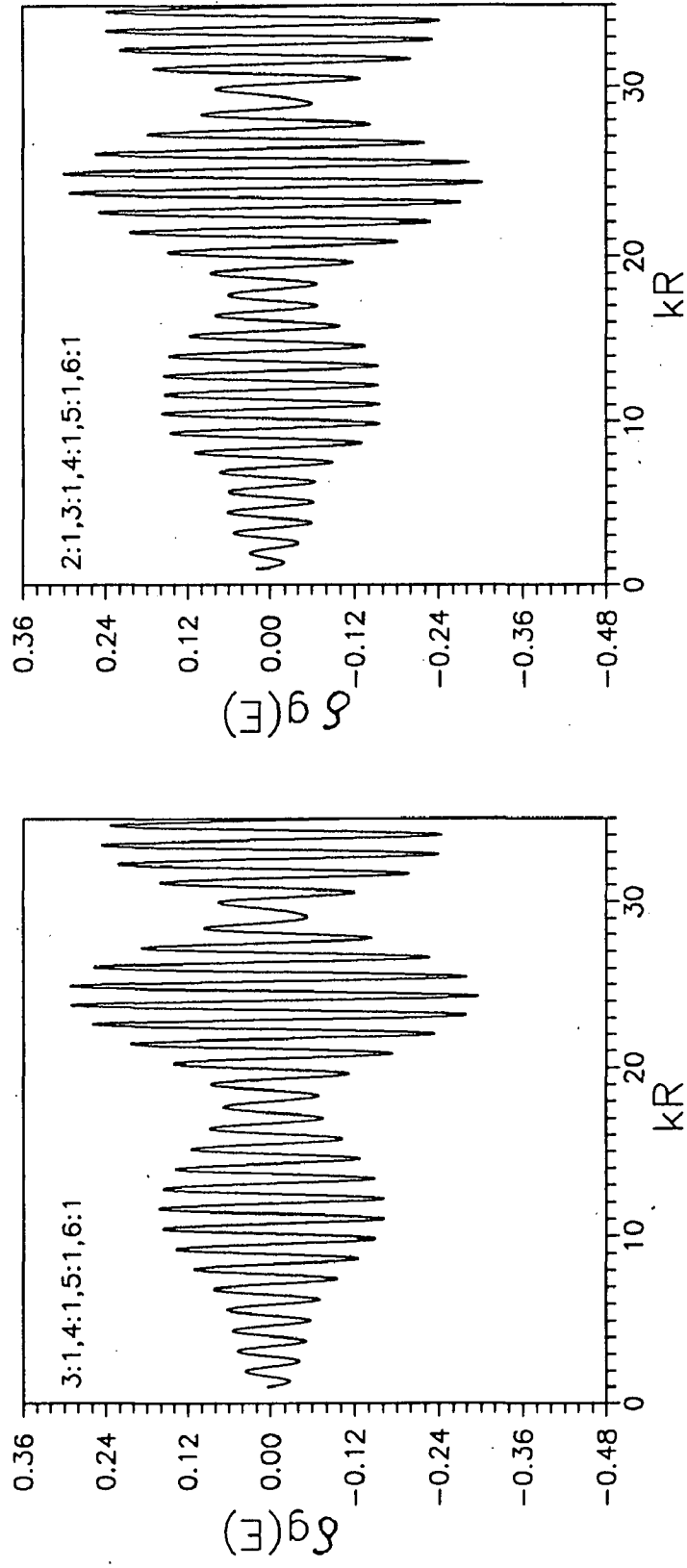


FIG. 5.4 Plots of  $\delta g(E)$  vs.  $kR$  for spherical cavity (a) taking four shortest periodic orbits except diametric orbit. (b) taking five shortest periodic orbits including diametric orbits using POT;  $\gamma = 0.6$ .

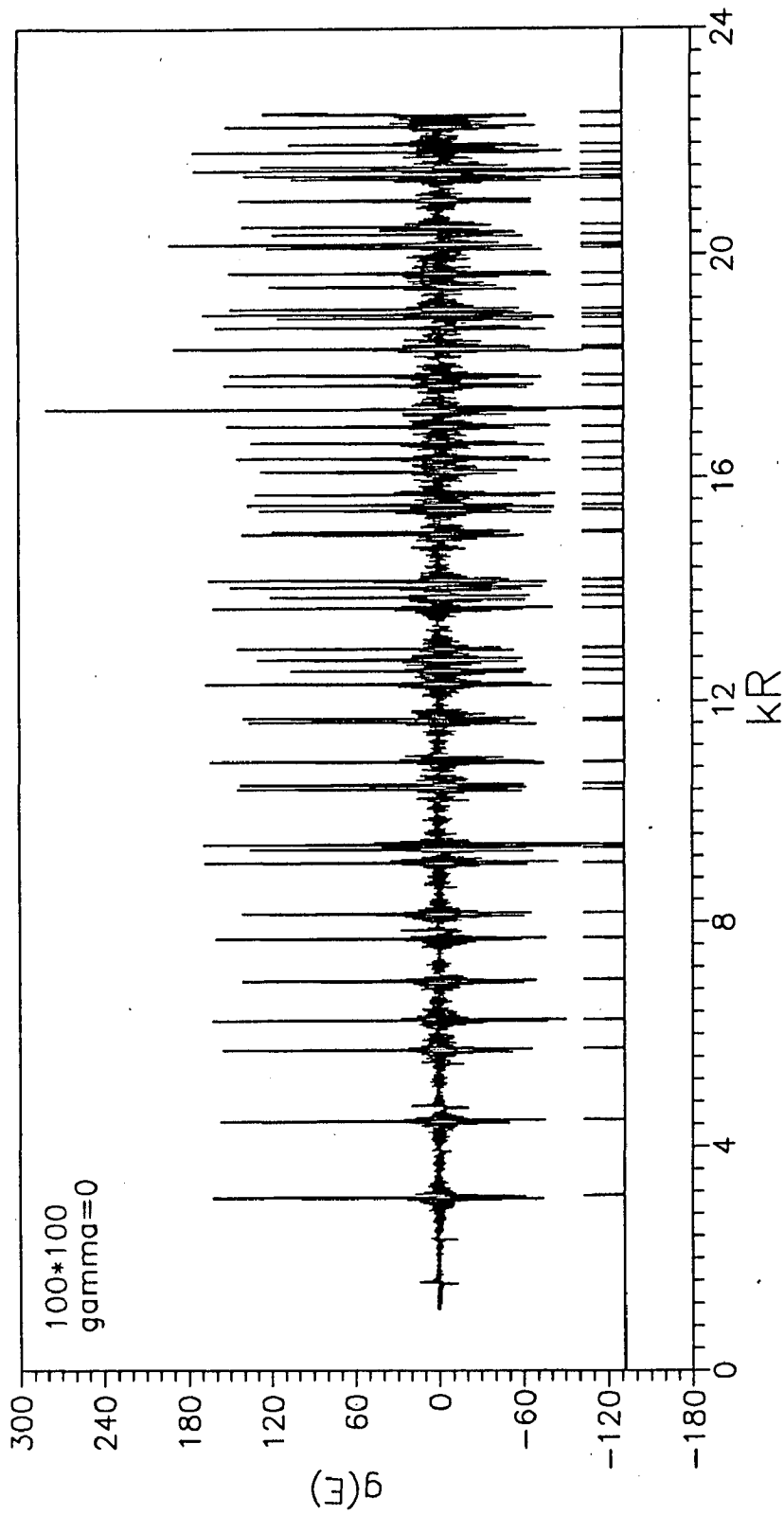


FIG. 5.5 Plot of  $g(E)$  vs.  $kR$  taking  $100 \times 100$  shortest periodic orbits with  $\gamma = 0$ ; also shown at the bottom are the quantum mechanical results.

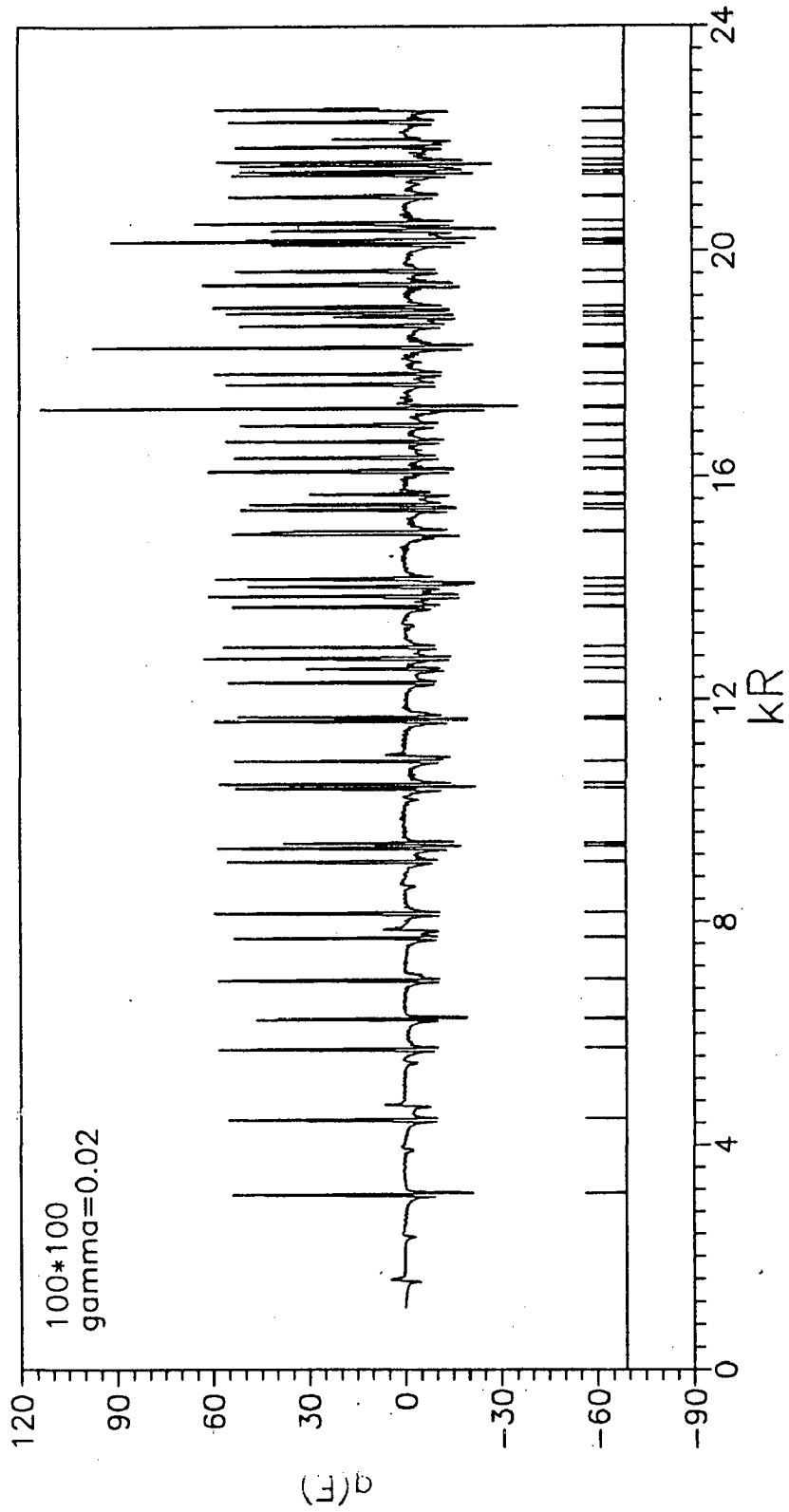


FIG. 5.6 Plot of  $g(E)$  vs.  $kR$  taking  $100 \times 100$  shortest periodic orbits with  $\gamma = 0.02$ ; also shown at the bottom are the quantum mechanical results.

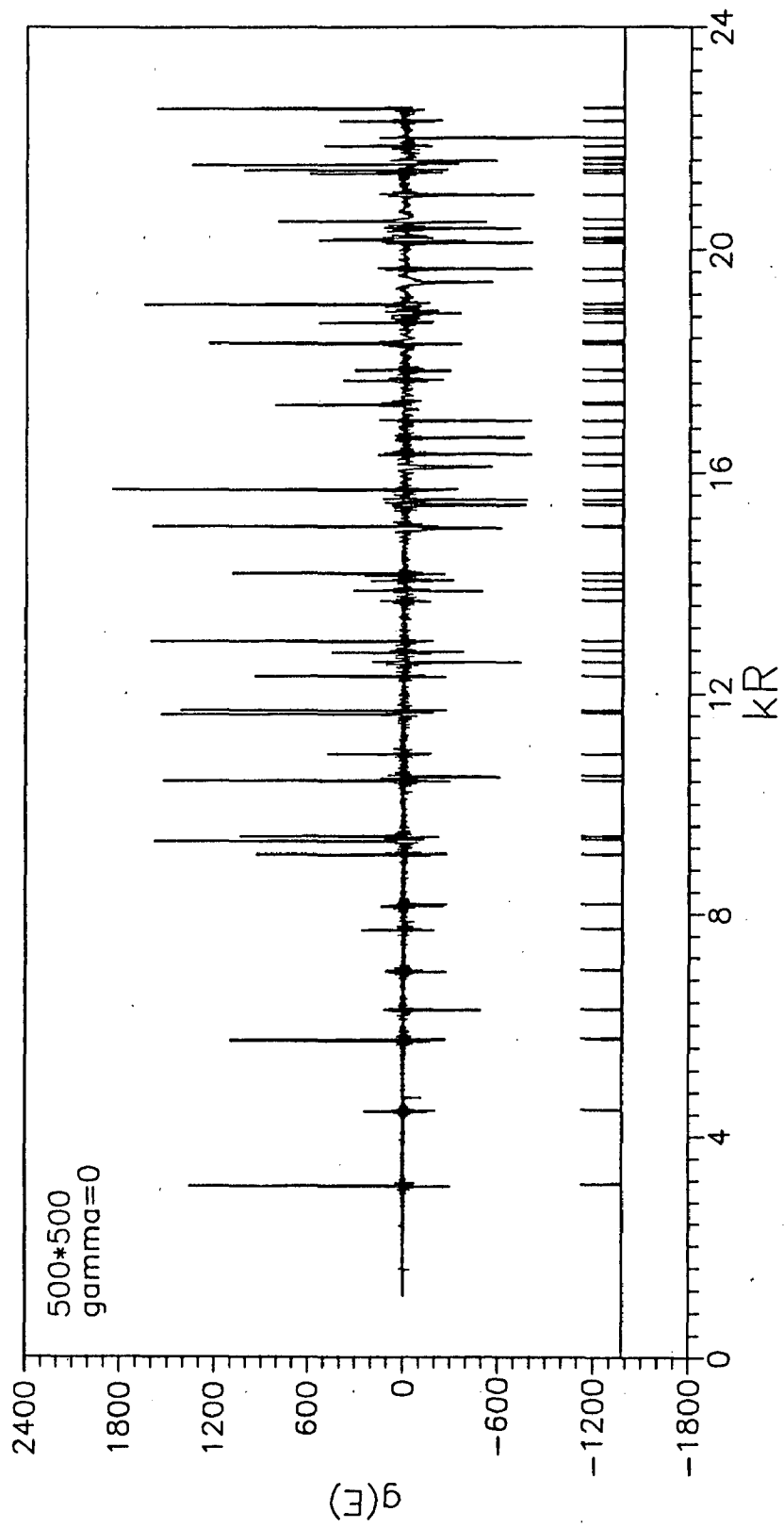


FIG. 5.7 Plot of  $g(E)$  vs.  $kR$  taking  $500 \times 500$  shortest periodic orbits with  $\gamma = 0$ ; also shown at the bottom are the quantum mechanical results.



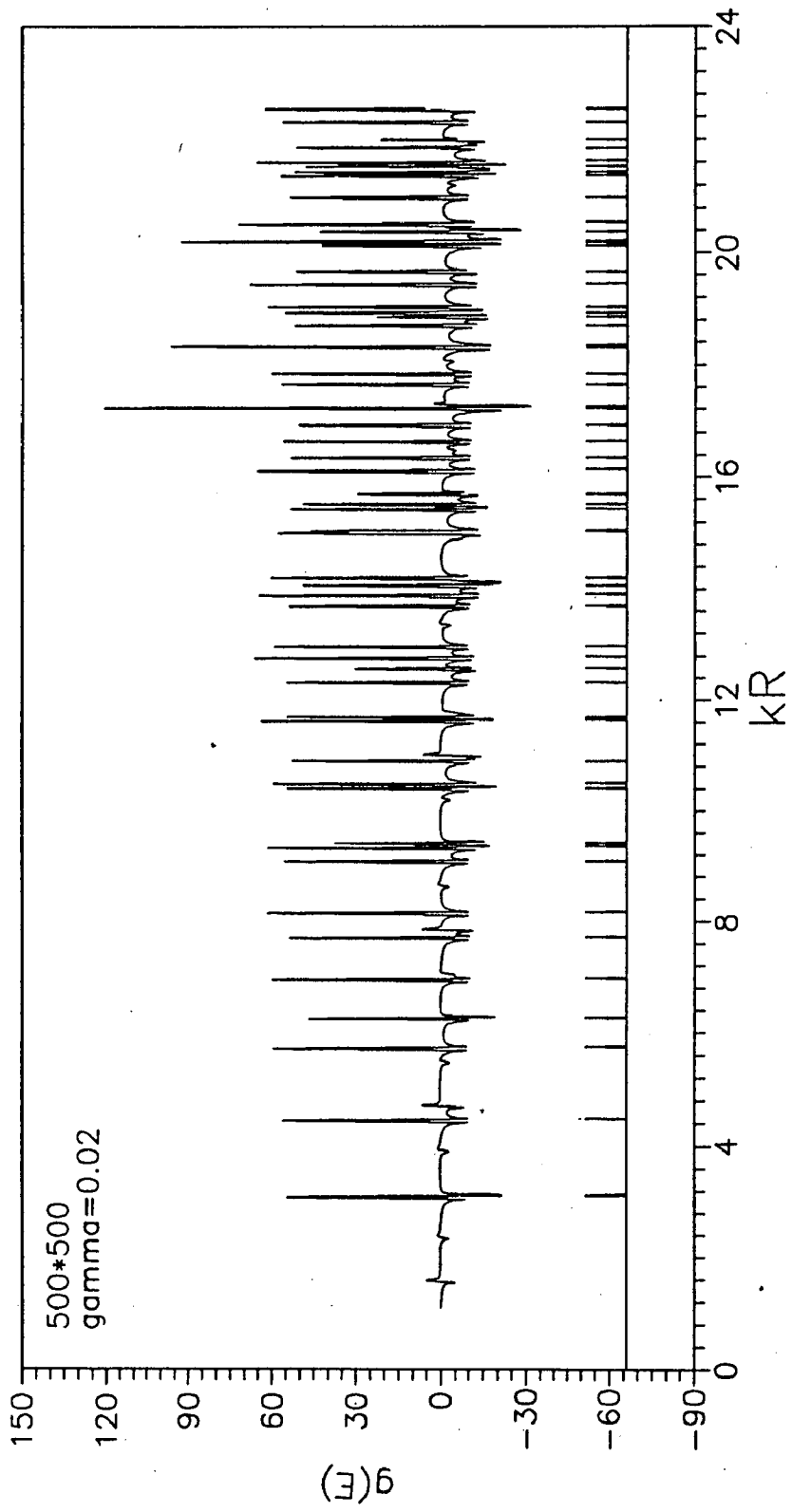


FIG. 5.8 Plot of  $g(E)$  vs.  $kR$  taking 500×500 shortest periodic orbits with  $\gamma = 0.02$ ; also shown at the bottom are the quantum mechanical results.

**CHAPTER VI**  
**PERIODIC ORBIT THEORY OF**  
**SPHEROIDAL CAVITY**

## I. INTRODUCTION

We have presented in chapter V, a limited exposition of the powerful semiclassical theory of the periodic orbits followed by its application to spherical billiard. It is now our general understanding that most of the nuclei are deformed rather than spherical. Moving few nucleons away from a closed shell, or changing the configuration of a nucleus is enough to introduce deformation or, shape change. Much of the nuclear structure over last three decades has remained centered around deformation in nuclei. A deformed cavity containing a particle provides a simple example of a deformed nucleus. An important connection in these studies is provided by the success of the single particle models of nuclei. It is now well known that the mean field approximations for the nuclear potential has proved to be the single most simplifying factor in much of the nuclear structure studies. It provides the basis for the single particle models which assume that nucleons move almost independently in a common potential. It also provides us the starting point for an alternate view of the questions related to nuclear shapes, the shell structure and their inter-relationships as a function of the particle number, excitation energy and the angular momentum. The alternate view arises from the realisation that the common potential in which nucleons move, does resemble a cavity. An early and lucid description of semiclassical theory of bound states was given may be found in Percival [93].

In the present chapter, we extend the studies presented in the preceding chapter and take up the problem of a particle in an infinitely deep ellipsoidal well. Such a system resembles a deformed nucleus and an application of the POT allows us to study the gross shell structure as well as the energy spectrum and their relationship with periodic orbits can be explored. Since most of the nuclei are prolate deformed we concentrate on a cavity with prolate spheroidal shape. The periodic orbits of such a system with continuous symmetry, exist in degenerate families. We therefore use the trace formula presented by Strutinsky et al. [106] which is applicable to non-isolated orbits. A similar study for prolate cavity was also carried out by Frisk [44] by using the formula of Berry and Tabor [10,11] and also

more recently by Magner et al. [80] by using the extended Gutzwiller theory. Arvieu and coworkers [3,4,27] have studied spherical as well as elliptical boxes by using semiclassical EBK quantisation techniques.

The outline of this chapter is as follows. First we present the details of the classical dynamics of a particle in a spheroidal cavity; this presentation closely follows the work of Strutinsky et al. [106] where we obtain the detailed conditions for the existence of periodic orbits in an ellipsoidal well. Three kinds of periodic orbits are possible in a spheroidal cavity; planar orbits in the axis of symmetry plane, planar orbits in the equatorial plane and 3-dimensional orbits. The actions, frequencies and periodicity conditions are derived for these orbits. We then use the trace formula to obtain the fluctuating part of level density for the three kinds of orbits. A brief discussion of the gross-shell structure is then presented.

## II. PERIODIC ORBITS IN A SPHEROIDAL CAVITY

Let us consider an ellipsoidal cavity with an infinitely high boundary so that a particle makes a perfect reflection on striking the walls. The potential inside the well is assumed to be zero. Spheroidal system of coordinates  $(u, v, \phi)$  is a natural choice to describe an ellipsoidal well; these are related to the cartesian coordinates  $(x, y, z)$  [106] by

$$\begin{aligned} x &= \xi \cos u \sinh v \cos \phi & -\frac{\pi}{2} \leq u \leq \frac{\pi}{2}; \\ y &= \xi \cos u \sinh v \sin \phi & 0 \leq v \leq \infty ; \\ z &= \xi \sin u \cosh v & 0 \leq \phi \leq 2\pi \end{aligned} \quad (1)$$

For the special case of spheroid, where the two smaller semi-axes are equal  $a = b$  and the third one,  $c$ , is longer,

$$\xi = (c^2 - a^2)^{\frac{1}{2}} = R_0 \eta^{-1/3} (n^2 - 1)^{\frac{1}{2}}. \quad (2)$$

where the volume conservation condition

$$\frac{4}{3}\pi R_0^3 = \frac{4}{3}\pi a^2 c, \quad (3)$$

Inside the ellipsoidal well and using the definition  $p_i = \frac{\partial S}{\partial q_i}$  where  $S$  is the total action,

$$\left(\frac{\partial S}{\partial u}\right)^2 + \left(\frac{\partial S}{\partial v}\right)^2 + \left(\frac{1}{\cos^2 u} + \frac{1}{\sinh^2 v}\right)\left(\frac{\partial S}{\partial \phi}\right)^2 = 2M\xi^2 e(\cosh^2 v - \sin^2 u). \quad (10)$$

Since  $\phi$  is cyclic, we obtain by using the technique of separation of variables,

$$\frac{\partial s_\phi}{\partial \phi} = \ell_z, \quad (11)$$

where  $\ell_z$  is a constant to be interpreted as the component of the orbital angular momentum along the symmetry axis. Hence,

$$s_\phi = 2\pi\ell_z. \quad (12)$$

Similarly, we obtain

$$s_u = \oint du \left[ 2M\xi^2 \left( \epsilon - e\sin^2 u - \frac{\ell_z^2}{2M\xi^2 \cos^2 u} \right) \right]^{\frac{1}{2}}, \quad (13)$$

and

$$s_v = \oint dv \left[ 2M\xi^2 \left( e\cosh^2 v - \epsilon - \frac{\ell_z^2}{2M\xi^2 \sinh^2 v} \right) \right]^{\frac{1}{2}}. \quad (14)$$

where  $\epsilon$  is the constant of separation. The limits of integration are decided by the classical turning points where momenta,

$$p_u^2 = 2M\xi^2 \left( \epsilon - e\sin^2 u - \frac{\ell_z^2}{2M\xi^2 \cos^2 u} \right), \quad (15)$$

$$p_v^2 = 2M\xi^2 \left( e\cosh^2 v - \epsilon - \frac{\ell_z^2}{2M\xi^2 \sinh^2 v} \right), \quad (16)$$

become zero. The second of these equations can be solved to give

$$\cosh^2 v = \frac{1}{2} \left( 1 + \frac{\epsilon}{e} \right) \pm \left[ \frac{1}{4} \left( 1 - \frac{\epsilon}{e} \right)^2 + \frac{\ell_z^2}{2m\xi^2 e} \right]^{\frac{1}{2}}. \quad (17)$$

Let  $\sigma_1 = \frac{\epsilon}{e}$  and  $\sigma_2 = \frac{\ell_z^2}{2M\xi^2 e}$ , where  $\sigma_1$  and  $\sigma_2$  are dimensionless quantities, so that

$$\cosh^2 v = \frac{1}{2} (1 + \sigma_1) \pm \left[ \frac{1}{4} (1 - \sigma_1)^2 + \sigma_2 \right]^{\frac{1}{2}}. \quad (18)$$

The particle moves in 2-dimensional elliptical periodic orbits between two confocal ellipsoids with  $v = v_0$  and  $v = v_{min}$  where  $v_{min}$  is given by

$$\cosh^2 v_{min} = \frac{1}{2}(1 + \sigma_1) + \left[\frac{1}{4}(1 - \sigma_1)^2 + \sigma_2\right]^{\frac{1}{2}}. \quad (19)$$

The 2-dimensional hyperbolic butterfly orbits are limited by two confocal hyperboloids with  $u = u_{max}$  and  $u = -u_{max}$  which are governed by the equation (15). We obtain

$$\sin^2 u = \frac{1}{2}(1 + \sigma_1) \pm \left[\frac{1}{4}(1 - \sigma_1)^2 + \sigma_2\right]^{\frac{1}{2}}, \quad (20)$$

which gives for a hyperboloid,

$$\sin^2 u_{max} = \frac{1}{2}(1 + \sigma_1) - \left[\frac{1}{4}(1 - \sigma_1)^2 + \sigma_2\right]^{\frac{1}{2}}. \quad (21)$$

We have thus expressed  $v_{min}$  and  $u_{max}$  in terms of the variables  $\sigma_1$  and  $\sigma_2$ . Further limits on  $\sigma_1$  and  $\sigma_2$  are set by the requirement that the kinetic energy be positive. This implies that  $p_u^2 \geq 0$  or,

$$\frac{\epsilon}{e} \geq \sin^2 u + \frac{\sigma_2}{\cos^2 u}. \quad (22)$$

It implies that  $\sigma_1 \geq \sigma_2$  and  $\sigma_2 \geq 0$ . Similarly, setting  $p_v^2 \geq 0$ , we obtain

$$\cosh^2 v - \frac{\sigma}{\sinh^2 v} \geq \sigma_1. \quad (23)$$

Combining these, we get

$$0 \leq \sigma_2 \leq \sigma_1 \leq \cosh^2 v_0 - \frac{\sigma_2}{\sinh^2 v_0}. \quad (24)$$

Hence,

$$\sigma_2 \leq \cosh^2 v_0 - \frac{\sigma_2}{\sinh^2 v_0}, \quad (25)$$

which also implies that

$$\sigma_2 \leq \frac{1}{\eta^2 - 1}. \quad (26)$$

It is also clear from the above equations that

$$\max(1, \sigma_1^{\frac{1}{2}}) \leq \cosh v_{min} \leq (1 + \sigma_1)^{\frac{1}{2}} < \cosh v_0, \quad (27)$$

and

$$\sin u_{max} \leq \min(1, \sigma_1^{\frac{1}{2}}). \quad (28)$$

The two dimensional elliptical orbits in the axis of symmetry plane reflect from the outer boundary at  $v = v_0$  and pass tangentially to the internal caustic defined by  $v = v_{min}$ . Similarly, the two dimensional hyperbolic butterfly orbits touch the internal caustics defined by the hyperbolae at  $u = -u_{max}$  and  $u = u_{max}$ . The diametric orbits are defined by  $v_{min} = 0$ . In the spheroid, there is only one (isolated) diametric orbit along the axis of symmetry. In addition to these, we have planar orbits in the equatorial plane defined by  $z = 0$ ; these are similar to the orbits of a circular billiard and will be treated by using the results of the earlier chapter V (spherical billiard). The hyperbolic butterfly orbits appear for deformations  $\eta > \eta_{min}$  and their effect will not be considered in the present calculations. Magner et al. [80] discuss these orbits.

Finally, we have the three-dimensional periodic orbits which exist for only large deformations. These satisfy the conditions,

$$v_0 > v_{min} > 0, \quad 0 < u_{max} < \frac{\pi}{2}. \quad (29)$$

These appear at a specific deformation for specific values of  $n_u, n_v$  and  $n_\phi$  and will be considered in the present work.

### III. PARTIAL FREQUENCIES AND PERIODICITY CONDITIONS

We note that the partial actions

$$\begin{aligned} s_u &= s_u(e, \epsilon, l_z), \\ s_v &= s_v(e, \epsilon, l_z), \\ s_\phi &= s_\phi(e, \epsilon, l_z), \end{aligned} \quad (30)$$

may be used to obtain the partial frequencies

$$\omega_u = 2\pi \left( \frac{\partial e}{\partial s_u} \right) = -2\pi \frac{\left( \frac{\partial s_u}{\partial \epsilon} \right)}{J(s_v s_u; e\epsilon)}, \quad (31)$$

$$\omega_v = 2\pi \left( \frac{\partial e}{\partial s_v} \right) = -2\pi \frac{\left( \frac{\partial s_v}{\partial \epsilon} \right)}{J(s_v s_u; e\epsilon)}, \quad (32)$$

$$\omega_\phi = 2\pi \left( \frac{\partial e}{\partial s_\phi} \right) = -\frac{J(s_v s_u; \ell_z \epsilon)}{J(s_v s_u; e\epsilon)}, \quad (33)$$

in the angular, radial and azimuthal directions. Here  $J$  represent the respective Jacobians of transformation. The periodicity condition may now be written as

$$\frac{\omega_u}{\omega_v} = -\frac{\left( \frac{\partial s_u}{\partial \epsilon} \right)}{\left( \frac{\partial s_v}{\partial \epsilon} \right)}, \quad (34)$$

where

$$\left( \frac{\partial s_v}{\partial \epsilon} \right) = -\sqrt{2M\xi^2} \oint \frac{dv}{2e^{\frac{1}{2}} [\cosh^2 v - \sigma_1 - \frac{\sigma_2}{\sinh^2 v}]^{\frac{1}{2}}}, \quad (35)$$

$$\left( \frac{\partial s_u}{\partial \epsilon} \right) = -\sqrt{2M\xi^2} \oint \frac{dv}{2e^{\frac{1}{2}} [\sigma_1 - \sin^2 u - \frac{\sigma_2}{\cos^2 v}]^{\frac{1}{2}}}. \quad (36)$$

Solving these integrals, we obtain

$$\frac{\omega_u}{\omega_v} = \frac{1}{2} \left[ 1 - \frac{F(\theta, \kappa)}{F(\frac{\pi}{2}, \kappa)} \right] = \frac{n_u}{n_v}, \quad (37)$$

where  $n_u$  and  $n_v$  are relatively prime integers. Also,  $F(\theta, \kappa)$  are elliptic functions of first kind with,

$$\kappa = \frac{\sin u_{max}}{\cosh v_{min}}, \quad \theta = \sin^{-1} \left( \frac{\cosh v_{min}}{\cosh v_0} \right). \quad (38)$$

Similarly, the ratio of frequencies in  $\phi$  and  $u$  is given by

$$\frac{\omega_\phi}{\omega_u} = -\frac{1}{2\pi} \left[ \frac{\partial s_u}{\partial \ell_z} + \frac{\frac{\partial s_u}{\partial \ell_z}}{\frac{\omega_u}{\omega_v}} \right], \quad (39)$$

which may be solved to give



$$\frac{\omega_\phi}{\omega_u} = \frac{2}{\pi} \left[ \left( 1 - \left( \frac{\kappa}{\bar{\kappa}} \right)^2 \right) (1 - \bar{\kappa}^2) \right]^{\frac{1}{2}} \times \left[ \Pi\left(\frac{\pi}{2}, \left(\frac{\kappa}{\bar{\kappa}}\right)^2, \kappa\right) - F\left(\frac{\pi}{2}, \kappa\right) + \frac{\left( \Pi\left(\frac{\pi}{2}, \bar{\kappa}^2, \kappa\right) - \Pi(\theta, \bar{\kappa}^2, \kappa) \right)}{\frac{1}{2} \left( 1 - \frac{F(\theta, \kappa)}{F\left(\frac{\pi}{2}, \kappa\right)} \right)} \right] = \frac{n_\phi}{n_u}, \quad (40)$$

where  $n_\phi$  and  $n_u$  are also relatively prime integers, and

$$\bar{\kappa} = \frac{1}{\sin\theta \cosh v_0} = \frac{\sqrt{\eta^2 - 1}}{\eta \sin\theta}. \quad (41)$$

Here  $\Pi(\theta, \bar{\kappa}^2, \kappa)$  are the elliptic functions of the third kind.

For systems with continuous symmetries such as a sphere or a spheroid, the periodic orbits fall into families of orbits, each family  $\beta$  having a constant action  $S_\beta$  at a fixed energy. Each member of a family is defined by a fixed number of parameters  $K$ , which is the degeneracy of the family. A given periodic orbit, or family of orbit  $\beta$  is defined by the three relative prime integers  $n_u, n_v, n_\phi$  and also the repetition number  $m$  so that an orbit is labelled as  $\beta(n_u, n_v, n_\phi, m)$ . Equations (38) provide the range of values for  $\kappa$  and  $\theta$  for a given  $\beta$ .

### A. Three-Dimensional Orbits

For three-dimensional orbits, the solutions to  $\kappa(n_u, n_v, n_\phi)$  and  $\theta(n_u, n_v, n_\phi)$  exist for deformation  $\eta \geq \eta_{min}$ , where

$$\eta_{min} = \frac{\sin\left(\frac{\pi n_\phi}{n_v}\right)}{\sin\left(\frac{\pi n_u}{n_v}\right)}, \quad (42)$$

at which point  $\kappa = 0$ ,  $\theta = \frac{\pi}{2} \left( 1 - \frac{2n_u}{n_v} \right)$ . The 3-dimensional orbits are close to the equatorial plane  $z = 0$  at or, near  $\eta_{min}$ . They occupy increasingly larger volumes as  $\eta$  increases. It can be shown that  $\frac{n_u}{n_v} < \frac{1}{2}$  for the 3-dimensional orbits. Also  $n_v > 2n_\phi$  and  $n_\phi \geq 2$ . Thus for the nonplanar orbits, the minimal value of  $n_v$  is 5 i.e. there must be at least five reflection points from the potential well. For example the 3-dimensional orbits  $(n_u : n_v : n_\phi) = 1 : 5 : 2$  appear at rather large deformations with  $\eta_{min} = 1.62$ . The orbits with  $n_\phi : n_u = 2 : 1$  are the shortest nonplanar orbits and resemble the Lissajous figures of the harmonic oscillator with

the deformation corresponding to  $\omega_x : \omega_z = 2 : 1$ . It is well known that the 2 : 1 frequency ratio of harmonic oscillator corresponds to a shape where new shell gaps corresponding to superdeformation arise. For 3-dimensional orbits,  $K=2$ .

## B. Frequency Of Rotation

The frequency of rotation for 3-dimensional orbits is given by

$$\Omega_\beta = \frac{2\pi}{T_\beta} = \frac{\omega_u}{n_u} = \frac{\omega_v}{n_v} = \frac{\omega_\phi}{n_\phi}. \quad (43)$$

To calculate  $\Omega_\beta$ , we note that

$$\Omega_\beta = \frac{\omega_v}{n_v} = 2\pi \left( \frac{1}{\frac{\partial s_v}{\partial e} - \frac{n_u}{n_v} \frac{\partial s_u}{\partial e}} \right). \quad (44)$$

Now,

$$\frac{\partial s_v}{\partial e} = \frac{pR\eta^{\frac{2}{3}} \sin\theta}{e} \int_0^{\frac{\pi}{2}} \frac{d\theta}{\sin^2\theta [1 - \kappa^2 \sin^2\theta]^{\frac{1}{2}}}, \quad (45)$$

and

$$\frac{\partial s_u}{\partial e} = \frac{2pR\eta^{\frac{2}{3}} \sin\theta}{e} \kappa^2 D\left(\frac{\pi}{2}, \kappa\right). \quad (46)$$

Here  $p = \sqrt{2Me}$ . Using these results in equation (44), we obtain

$$\Omega_\beta = \frac{3^{\frac{3}{2}} \Omega_{sph}}{2n_v \eta^{\frac{2}{3}} \sin\theta} \left[ \frac{1}{\kappa^2 \left[ \left(1 - 2\frac{n_u}{n_v}\right) D\left(\frac{\pi}{2}, \kappa\right) - D(\theta, \kappa) \right] + \cot\theta (1 - \kappa^2 \sin^2\theta)^{\frac{1}{2}}} \right], \quad (47)$$

where  $\Omega_{sph} = \frac{4\pi e}{3^{\frac{3}{2}} pR}$ , is the frequency for triangular orbits in a sphere as shown in equation (55) of chapter V. The function  $D(\theta, \kappa)$  is given by

$$D(\theta, \kappa) = \int_0^\theta \frac{d\phi}{\sqrt{1 - \kappa^2 \sin^2\phi}}. \quad (48)$$

For rhomboidal orbits in the axis of symmetry plane  $n_u = 1, n_v = 4$  and  $\kappa \rightarrow 1$ . It can be shown that

$$\Omega_\beta(1 : 4) = \frac{3^{\frac{3}{2}}}{4} \Omega_{sph} \eta^{\frac{1}{3}} \frac{1}{\left[ 5\eta^2 - 1 - 4\eta^2 \left(1 - \frac{1}{2\eta^2}\right) \right]^{\frac{1}{2}}}. \quad (49)$$

For  $\eta > 1$ , it reduces to

$$\Omega_\beta(1 : 4) = \frac{3^{\frac{3}{2}} \Omega_{sph} \eta^{\frac{1}{3}}}{4(\eta^2 + 1)^{\frac{1}{2}}}, \quad (50)$$

a result used by Strutinsky et al [106].

### C. Planar Orbits

The 2-dimensional planar orbits exist in the axis-of-symmetry plane and also in the plane perpendicular to the axis of symmetry or, equatorial plane at  $z = 0$ . The orbits in the equatorial plane correspond to the periodic orbits in a circular billiard and are polygons satisfying the condition

$$\omega_\nu : \omega_\phi = n_\nu : n_\phi. \quad (51)$$

A family of orbits with constant action can be generated by continuously varying one angle parameter and therefore the classical degeneracy  $K = 1$ .

Periodic orbits in the axis of symmetry plane are more important and as pointed out earlier, fall into two categories, the elliptical periodic orbits and the hyperbolic periodic orbits, the latter making appearances at

$$\eta_{min} = \frac{1}{\sin\left(\frac{\pi n_u}{n_\nu}\right)}. \quad (52)$$

The degeneracy parameter  $K$  for these orbits is 2. Due to higher degeneracy, these orbits are a major contributor to the shell structure. The diametric orbit along the axis of symmetry is however isolated and has a degeneracy parameter  $K = 0$ .

## IV. RELATIONSHIP OF PLANAR ORBITS WITH THE GROSS-SHELL STRUCTURE

In the first application of the periodic orbits to the gross shell structure in nuclei and the evolution of nuclear deformation as a function of particle number, Strutinsky et al. [106] were quite successful in relating the rhomboidal orbits to the change in nuclear deformation near shell closure.

It is now a well established procedure to locate the minima (or, valleys) in the level density vs. deformation plots and identify the corresponding particle numbers as the most stable shapes. Instead of level density, one usually considers the energy  $e$  vs. deformation

$\eta$  plots. The minimum of the level density then corresponds to a minimum in the energy  $e_m(\eta)$ . Such minima are well recognised at the usual magic numbers for the spherical shape. As the shape changes, these points of minima turn into distinct prolonged valleys as shown in Figures 6.1 and 6.2 [106]. One may now calculate the nucleon numbers  $N_m(\eta)$  along these valleys which then represent the magic numbers at non-zero deformations. The characteristic quantities of these minima valleys are the slopes  $\frac{de_m}{d\eta}$  and  $\frac{dN_m}{d\eta}$  which decide the positions of the minima valleys in the contour plots of the shell corrections in density of states,  $\delta g(e, \eta)$  and the shell corrections in energy,  $\delta E(e, \eta)$ .

In an interesting application, that provides much insight into the relationship of periodic orbits with the most preferred nuclear shape at a given nucleon number, Strutinsky et al. [106] presented a simple relationship based on just one family of orbits  $n_u : n_v = 1 : 4$  that fortunately explained the fall in nuclear deformation as the magic number  $A = 208$  is approached. The basic argument is the constancy of the action integral  $S_\beta(e_m, \eta)$  along the minima valley. Thus,

$$S_\beta(e_m, \eta) = \text{constant}, \quad (53)$$

which leads to

$$\frac{de_m}{d\eta} = -\frac{(\frac{\partial S_\beta}{\partial \eta})}{T_\beta}, \quad (54)$$

where  $T_\beta = \frac{2\pi}{\Omega_\beta}$ . The slopes of the valleys are then given by

$$\frac{dN_m}{d\eta} = g(e_m)\left(\frac{de_m}{d\eta}\right), \quad (55)$$

where  $g(e_m)$  is the level density at the Fermi energy  $e_m$ . It can be shown that

$$\frac{\partial S_\beta}{\partial \eta} = 4\sqrt{2MeR} \frac{(2\eta^2 - 1)}{3\eta^{\frac{4}{3}}\sqrt{\eta^2 + 1}}. \quad (56)$$

For the rhomboidal orbits, where  $n_u = 1, n_v = 4$ ,

$$\frac{de_m}{d\eta} = -\frac{2e(2\eta^2 - 1)}{3\eta(\eta^2 + 1)}, \quad (57)$$

which is a negative quantity. Using the Thomas-Fermi relationship between the nucleon number  $N$  and the average level density  $\tilde{g}(e)$ ,

$$\tilde{g}(e) = \frac{3N}{2e}, \quad (58)$$

we obtain,

$$\frac{dN_m}{d\eta} \approx -\frac{N}{2}, \quad (59)$$

for  $\eta$  close to unity. At  $\eta = 1$ ,  $N = N_{magic}$  and at  $\eta > 1$ , the nucleus acquires the most preferred equilibrium shape  $\eta_{eq}$  at a given  $N$ . Integrating, we obtain

$$\eta_{eq} = 1 + \frac{2(N_{magic} - N)}{N}. \quad (60)$$

Here  $N_{magic}$  is the magic number at spherical shape. Strutinsky et al. [106] used this relation to reproduce the nearly linear trend of nuclear deformation prior to the magic number 208. The same cannot however be said to be true for the onset of nuclear deformation after a shell closure. Recently, Brack et al. [18] adapted this formula to the magic numbers of metal clusters and obtained straight lines that fit perfectly to the average deformations found numerically from the quantum spectra using the shell-correction method. Although this formula was worked out for prolate deformations, it also fits the oblate deformations in metallic clusters.

It is indeed amazing that the predictions based only on the rhomboidal orbits can explain qualitatively the features of nuclear deformation. Particularly so when the triangular orbit, which is shorter, has not been considered. Using the exact expression for  $(\frac{de_m}{d\eta})$  and solving it numerically for the  $(n_u : n_v) = 1 : 3, 1 : 4, 1 : 5$  and  $1 : 6$  families of orbits, we obtain the variation in shape with particle number as shown in FIG. 6.3, where we have also used  $N_{magic} = 208$ . It is clear from the exact results that the dependence from any one family of orbits is not exactly linear. Even then, the tangent drawn to the curve corresponding to  $1 : 4$  comes quite close to the observed deformations. It may be mentioned that our solutions are not valid near magic number. Therefore the large deviation near  $N_{magic}$  should be ignored.

It is also remarkable to note that all these curves for the four leading families of orbits tend towards each other near nucleon number 176 giving a deformation  $\delta = 0.3$ .

## V. TRACE FORMULA FOR SPHEROIDAL CAVITY

To calculate the oscillating component of level density for spheroidal cavity, we use the formula proposed by Strutinsky (taking degenerate families of orbits into account) as done in the case of spherical billiard in chap V:

$$\delta g(E) = \frac{2}{\pi \hbar^2} \sum_{\beta, m} f_{\beta, m} \sin\left(\frac{S_{\beta, m}}{\hbar} + \sigma_{\beta, m}\right) \int \int d\rho dz \sqrt{|p_\rho p_z J(p_\rho p_z t_{\beta, m}; \rho' z' E)|}_{\rho' z' \rightarrow \rho z}. \quad (61)$$

where the various terms have already been explained. Since this formula is in cylindrical coordinates and we have described our system in spheroidal coordinates, we make a transformation between the two sets of coordinates by using the relations,

$$\rho = \xi \cos u \sinh v, \quad (62)$$

$$z = \xi \sin u \cosh v, \quad (63)$$

$$p_\rho = M \frac{d\rho}{dt} = \sqrt{2Me} \left[ \frac{-\sin u \sinh v \left(\sigma_1 - \sin^2 u - \frac{\sigma_2}{\cos^2 u}\right)^{\frac{1}{2}} + \cos u \cosh v \left(\cosh^2 v - \sigma_1 - \frac{\sigma_2}{\sinh^2 v}\right)^{\frac{1}{2}}}{\sin^2 u \sinh^2 v + \cos^2 u \cosh^2 v} \right], \quad (64)$$

$$\rho p_\rho = kR\eta^{\frac{-1}{3}} \sqrt{\eta^2 - 1} \cos u \sinh v \times \left[ \frac{-\sin u \sinh v \left(\sigma_1 - \sin^2 u - \frac{\sigma_2}{\cos^2 u}\right)^{\frac{1}{2}} + \cos u \cosh v \left(\cosh^2 v - \sigma_1 - \frac{\sigma_2}{\sinh^2 v}\right)^{\frac{1}{2}}}{\sin^2 u \sinh^2 v + \cos^2 u \cosh^2 v} \right], \quad (65)$$

$$p_z = \sqrt{2me} \left[ \frac{\cos u \cosh v \left(\sigma_1 - \sin^2 u - \frac{\sigma_2}{\cos^2 u}\right)^{\frac{1}{2}} + \sin u \sinh v \left(\cosh^2 v - \sigma_1 - \frac{\sigma_2}{\sinh^2 v}\right)^{\frac{1}{2}}}{\sin^2 u \sinh^2 v + \cos^2 u \cosh^2 v} \right]. \quad (66)$$

Here  $\rho$  and  $z$  are the radial and axial coordinates in the cylindrical system;  $p_\rho$  and  $p_z$  are the corresponding canonically conjugate momenta. Also  $k = p/\hbar = \sqrt{2Me}/\hbar$ .

The total action may be given in the terms of the partial actions as

$$\begin{aligned}
S &= n_u s_u + n_v s_v + n_\phi s_\phi, \\
&= kR\eta^{-1/3} \sqrt{\eta^2 - 1} \left[ 4n_u \int_0^{u_{\max}} du \sqrt{\sigma_1 - \sin^2 u - \frac{\sigma_2}{\cos^2 u}} \right. \\
&\quad \left. + 2n_v \int_{v_{\min}}^{v_0} dv \sqrt{\cosh^2 v - \sigma_1 - \frac{\sigma_2}{\sinh^2 v}} + 2\pi n_\phi \sqrt{\sigma_2} \right].
\end{aligned} \tag{67}$$

The action can also be written in terms of the length of the orbit

$$S = kL_\beta = \sqrt{2Me}L_\beta, \tag{68}$$

where  $L_\beta$  in turn can be found out by using the time period.

Now the Jacobian of transformation is given by the determinant,

$$\begin{pmatrix} \frac{\partial p_\rho}{\partial \rho} & \frac{\partial p_\rho}{\partial z} & \frac{\partial p_\rho}{\partial e} \\ \frac{\partial p_z}{\partial \rho} & \frac{\partial p_z}{\partial z} & \frac{\partial p_z}{\partial e} \\ \frac{\partial t}{\partial \rho} & \frac{\partial t}{\partial z} & \frac{\partial t}{\partial e} \end{pmatrix}$$

The various terms of the Jacobian can be written down by using the following relations:

$$\frac{\partial p_\rho}{\partial \rho} = \frac{\sqrt{2Me}}{\xi} K_1 = \frac{\sqrt{2Me}}{\xi} \left[ -\frac{T_1}{\sin u \sinh v} + \frac{T_2}{\cos u \cosh v} \right], \tag{69}$$

where  $T_1$  and  $T_2$  are given by

$$\begin{aligned}
T_1 &= \frac{1}{(\sin^2 u \sinh^2 v + \cos^2 u \cosh^2 v)} \left[ -\cos u \sinh v \sqrt{\sigma_1 - \sin^2 u - \frac{\sigma_2}{\cos^2 u}} \right. \\
&\quad \left. + \frac{\sin u \sinh v \sin 2u (1 + \frac{\sigma_2}{\cos^4 u})}{2\sqrt{\sigma_1 - \sin^2 u - \frac{\sigma_2}{\cos^2 u}}} - \sin u \cosh v \sqrt{\cosh^2 v - \sigma_1 - \frac{\sigma_2}{\sinh^2 v}} \right] \\
&\quad + \frac{\sin 2u}{(\sin^2 u \sinh^2 v + \cos^2 u \cosh^2 v)^2} \left[ -\sin u \sinh v \sqrt{\sigma_1 - \sin^2 u - \frac{\sigma_2}{\cos^2 u}} \right. \\
&\quad \left. + \cos u \cosh v \sqrt{\cosh^2 v - \sigma_1 - \frac{\sigma_2}{\sinh^2 v}} \right],
\end{aligned}$$

and,

$$T_2 = \frac{1}{(\sin^2 u \sinh^2 v + \cos^2 u \cosh^2 v)} \left[ -\sin u \cosh v \sqrt{\sigma_1 - \sin^2 u - \frac{\sigma_2}{\cos^2 u}} \right]$$

$$\begin{aligned}
& + \frac{\cos u \cosh v \sinh 2v \left(1 + \frac{\sigma_2}{\sinh^4 v}\right)}{2\sqrt{\cosh^2 v - \sigma_1 - \frac{\sigma_2}{\sinh^2 v}}} + \cos u \sinh v \sqrt{\cosh^2 v - \sigma_1 - \frac{\sigma_2}{\sinh^2 v}} \\
& - \frac{\sinh 2v}{(\sin^2 u \sinh^2 v + \cos^2 u \cosh^2 v)^2} \left[ -\sin u \sinh v \sqrt{\sigma_1 - \sin^2 u - \frac{\sigma_2}{\cos^2 u}} \right. \\
& \quad \left. + \cos u \cosh v \sqrt{\cosh^2 v - \sigma_1 - \frac{\sigma_2}{\sinh^2 v}} \right].
\end{aligned}$$

Similarly,

$$\frac{\partial p_\rho}{\partial z} = \frac{\sqrt{2Me}}{\xi} K_2 = \frac{\sqrt{2Me}}{\xi} \left[ \frac{T_1}{\cos u \cosh v} + \frac{T_2}{\sin u \sinh v} \right], \quad (72)$$

$$\frac{\partial p_\rho}{\partial e} = \frac{2M}{\sqrt{2Mep_3}}, \quad (73)$$

where

$$\frac{1}{p_3} = \left[ \frac{-\sin u \sinh v \left(\sigma_1 - \sin^2 u - \frac{\sigma_2}{\cos^2 u}\right)^{\frac{1}{2}} + \cos u \cosh v \left(\cosh^2 v - \sigma_1 - \frac{\sigma_2}{\sinh^2 v}\right)^{\frac{1}{2}}}{\sin^2 u \sinh^2 v + \cos^2 u \cosh^2 v} \right]. \quad (74)$$

Also,

$$\frac{\partial p_z}{\partial \rho} = \frac{\sqrt{2Me}}{\xi} K_3 = \frac{\sqrt{2Me}}{\xi} \left[ -\frac{T_3}{\sin u \sinh v} + \frac{T_4}{\cos u \cosh v} \right], \quad (75)$$

and,

$$\frac{\partial p_z}{\partial z} = \frac{\sqrt{2Me}}{\xi} K_4 = \frac{\sqrt{2Me}}{\xi} \left[ \frac{T_3}{\cos u \cosh v} + \frac{T_4}{\sin u \sinh v} \right], \quad (76)$$

where  $T_3$  and  $T_4$  are given by,

$$\begin{aligned}
T_3 = & \frac{1}{(\sin^2 u \sinh^2 v + \cos^2 u \cosh^2 v)} \left[ -\sin u \cosh v \sqrt{\sigma_1 - \sin^2 u - \frac{\sigma_2}{\cos^2 u}} \right. \\
& - \frac{\cos u \cosh v \sinh 2u \left(1 + \frac{\sigma_2}{\cos^4 u}\right)}{2\sqrt{\sigma_1 - \sin^2 u - \frac{\sigma_2}{\cos^2 u}}} + \cos u \sinh v \sqrt{\cosh^2 v - \sigma_1 - \frac{\sigma_2}{\sinh^2 v}} \\
& + \frac{\sin 2u}{(\sin^2 u \sinh^2 v + \cos^2 u \cosh^2 v)^2} \left[ \cos u \cosh v \sqrt{\sigma_1 - \sin^2 u - \frac{\sigma_2}{\cos^2 u}} \right. \\
& \quad \left. + \sin u \sinh v \sqrt{\cosh^2 v - \sigma_1 - \frac{\sigma_2}{\sinh^2 v}} \right],
\end{aligned}$$



$$T_4 = \frac{1}{(\sin^2 u \sinh^2 v + \cos^2 u \cosh^2 v)} \left[ \cos u \sinh v \sqrt{\sigma_1 - \sin^2 u - \frac{\sigma_2}{\cos^2 u}} \right. \\ \left. + \frac{\sin u \sinh v \sinh 2v (1 + \frac{\sigma_2}{\sinh^2 u})}{2 \sqrt{\cosh^2 v - \sigma_1 - \frac{\sigma_2}{\sinh^2 v}}} + \cos u \sinh v \sqrt{\cosh^2 v - \sigma_1 - \frac{\sigma_2}{\sinh^2 v}} \right] \\ - \frac{\sinh 2v}{(\sin^2 u \sinh^2 v + \cos^2 u \cosh^2 v)^2} \left[ \cos u \cosh v \sqrt{\sigma_1 - \sin^2 u - \frac{\sigma_2}{\cos^2 u}} \right. \\ \left. + \sin u \sinh v \sqrt{\cosh^2 v - \sigma_1 - \frac{\sigma_2}{\sinh^2 v}} \right].$$

Further,

$$\frac{\partial p_z}{\partial e} = \frac{2M}{\sqrt{2Me} p_4}, \quad (79)$$

where,

$$\frac{1}{p_4} = \left[ \frac{\cos u \cosh v (\sigma_1 - \sin^2 u - \frac{\sigma_2}{\cos^2 u})^{\frac{1}{2}} + \sin u \sinh v (\cosh^2 v - \sigma_1 - \frac{\sigma_2}{\sinh^2 v})^{\frac{1}{2}}}{\sin^2 u \sinh^2 v + \cos^2 u \cosh^2 v} \right]. \quad (80)$$

To obtain  $\frac{\partial t}{\partial e}$ , we note that

$$t_\beta = \frac{\partial S_\beta}{\partial e}, \quad (81)$$

$$\frac{\partial t_\beta}{\partial e} = -\frac{S}{4e^2}. \quad (82)$$

Finally the Jacobian takes the following form,

$$\begin{pmatrix} \frac{\sqrt{2Me}}{\xi} K_1 & \frac{\sqrt{2Me}}{\xi} K_2 & \frac{2M}{\sqrt{2Me} p_3} \\ \frac{\sqrt{2Me}}{\xi} K_3 & \frac{\sqrt{2Me}}{\xi} K_4 & \frac{2M}{\sqrt{2Me} p_4} \\ \frac{2M}{\sqrt{2Me} p_3} & \frac{2M}{\sqrt{2Me} p_4} & -\frac{S}{4e^2} \end{pmatrix}$$

The fluctuating part of level density  $\delta g$  is finally obtained by using these terms in the trace formula and numerical computation. These are general expressions valid for 3-dimensional orbits in the spheroidal cavity. Results for the planar orbits can be simply obtained by putting  $\sigma_2 = 0$ .

The contribution to  $\delta g$  from the isolated diametric orbit along the symmetry axis is obtained by using the expressions for planar orbits. We take the effect of the lower degeneracy ( $K = 0$ ) for diametric orbits into account by dividing by a factor  $kR_0$ .

There now remains the contribution of orbits in the equatorial plane. We note that these orbits are simply those corresponding to a circular billiard at  $z = 0$  having a radius  $R = R_0 \eta^{-\frac{1}{3}}$ . We use the results presented in chapter V for the spherical billiard to calculate the  $\delta g_{eq}$  by properly taking into account the effect of classical degeneracy which in this case is  $K = 1$ . The total level density  $\delta g(e)$  therefore is obtained as,

$$\delta g(e) = \delta g^{K=2} + \delta g^{K=0} + \delta g^{K=1} \quad (83)$$

The effect of 3-dimensional orbits, which begin at higher deformations, will be discussed separately. We have not included the contribution of the hyperbolic butterfly orbits in our results. The damping factor for the convergence of the periodic orbit sum has been taken as the same as discussed in the previous chapter.

The Maslov indices have been discussed in chapter V. We have used the following values in accordance with Magner et al. [80]. For planar orbits (except diametric) in the plane of axis of symmetry the Maslov index has been taken as

$$\sigma_{sym} = -\frac{3mn_v\pi}{2} - (mn_u - 1)\pi - \frac{\pi}{2}. \quad (84)$$

For diametric orbits in the same plane the Maslov index is given by

$$\sigma_D = -\frac{3mn_v\pi}{2} - \frac{\pi}{2}. \quad (85)$$

The Maslov index for the orbits in the plane perpendicular to the plane of axis of symmetry is given by

$$\sigma_{eq} = -\frac{3mn_v\pi}{2} + \frac{\pi}{4}. \quad (86)$$

For 3-Dimensional orbits we have taken the Maslov index as,

$$\sigma_{3d} = -\frac{3mn_v\pi}{2} - (mn_u - 1)\pi - mn_\phi\pi - \frac{\pi}{2}. \quad (87)$$

## VI. NUMERICAL RESULTS AND DISCUSSION

We have presented in this chapter a detailed discussion of the periodic orbits in spheroidal deformed cavity. We have used the trace formula due to Strutinsky et al. to obtain a general formulation for the oscillating part of the level density  $\delta g(e)$ . This trace formula, valid for 3-dimensional non-planar orbits, can be reduced to that of planar orbits by putting  $\sigma_2 = 0$  and also to that of diametric orbits. In order to calculate the contribution to  $\delta g(e)$  from the orbits in the equatorial plane, we have adapted the expression obtained for spherical billiard (Chapter V) which was also derived by using the trace formula of Strutinsky et al. We now present some numerical results based on these expressions.

We consider the application of these formula to gross shell structure, a topic of great interest in nuclear and atomic cluster physics. We show in FIG. 6.4 four numerical results for  $\delta g(e)$  as a function of  $kR_0$  at  $\eta = 1.2$ . The quantity  $\delta g(e)$  has been evaluated here in units independent of energy by putting  $\epsilon = 1$ . The bottom panels exhibit the results of summing over  $n_u : n_v = 1 : 3, 1 : 4, 1 : 5$  and  $1 : 6$  orbits. Besides the fast oscillations, we also see the familiar beat pattern. The right panel exhibits results with  $\gamma = 0.6$  and the left panel exhibits results with  $\gamma = 0$ . In the top panels, we have also included the contribution of the shortest pendular orbit ( $1 : 2$ ). It modifies the magnitude of the oscillations but only at small  $kR$ ; most of the pattern remains unchanged. The  $1 : 2$  orbit is in fact shorter in length but does not affect the  $\delta g(e)$  significantly. As in the spherical case, the most important leading orbits are the  $3 : 1$  and  $4 : 1$  orbits. On looking back, it therefore does not seem to be so surprising that Strutinsky et al. succeeded in explaining the main trends of nuclear ground-state deformations by considering only the rhomboidal periodic orbits.

The four panels in FIG. 6.5 contain similar results for the orbits in the equatorial plane. The contribution of the equatorial orbits is significant but not more than that of the planar orbits. Although the degeneracy of the equatorial orbits is lower, they are shorter and this seems to enhance their contribution. Further, we observe that the number of beats has increased as compared to the planar orbits alone.

In FIG. 6.6, we show the results for the total  $\delta g$  at  $\eta=1.2$  where contributions of planar and equatorial orbits have been added. The upper right panel, which contains the results for  $\gamma = 0.6$ , is almost same as that obtained by Magner et al. [80] except for a small difference near  $kR = 0$ . Figures 6.7, 6.8, and 6.9 are similar to Figures 6.4, 6.5, and 6.6 but are now plotted for a deformation  $\eta = 1.53$ . Two distinct changes are evident. First is the decreasing contribution of the planar orbits. Second is the relatively enhanced contribution from the orbits in the equatorial plane; effectively the role of equatorial planar orbits has gone up with increase in deformation. This is as expected because the orbits in the equatorial plane continue to become shorter with increase in prolate deformation. Figures 6.10, 6.11 and 6.12 contain similar results for the important deformation  $\eta = 2$  where most of the non-planar orbits begin to play an important role. We notice the decreasing role of the planar orbits at  $\eta = 2$  from FIG. 6.10. The equatorial orbits, on the other hand, remain as important as shown in FIG. 6.11. The total  $\delta g(e)$  is shown in FIG. 6.12.

It is important to point out that the planar butterfly hyperbolic orbits (such as  $n_u : n_v = 1 : 4$ ) appear at  $\eta = \sqrt{2}$  and contribute at larger deformations. Magner et al. have included the effect of these orbits, which we have not done so far. This may explain some differences in our results with those of Magner et al. As pointed out by Magner et al.  $\eta = 2$  is the bifurcation point where the hyperbolic orbit  $n_u : n_v = 1 : 6$  appears.

Besides the hyperbolic butterfly orbits, the 3-dimensional non-planar orbits also begin to play a role for  $\eta > \eta_{min}$ . For example, the shortest 3-dimensional orbits correspond to  $n_u : n_v : n_\phi = 1 : 5 : 2$  which appear at  $\eta_{min} = 1.62$ . We therefore have chosen  $\eta = 2$  as the deformation to study the role of the 3-dimensional orbits. The deformation  $\eta = 2$  is also significant because at  $\eta = \frac{\omega_\perp}{\omega_z} = 2$ , the harmonic oscillator exhibits a large degeneracy and occurrence of shell closure. In FIG. 6.13 we display the results of  $\delta g$  obtained from six non-planar orbits  $n_u : n_v : n_\phi = 1 : 5 : 2 + 1 : 6 : 2 + 1 : 7 : 2 + 1 : 8 : 2 + 1 : 9 : 2 + 1 : 10 : 2$ . Most striking is a remarkable beating pattern with several beats occurring upto  $kR = 35$ . In contrast to the planar and equatorial orbits, where only one to three beats were seen upto  $kR = 35$ , we find almost five beats for non-planar orbits. Also the amplitude of the 3-

dimensional orbits is slightly greater than that of equatorial orbits. This brings an important point into focus, that the 3-dimensional orbits are as important or even more important than any other orbits particularly for superdeformed (SD) shapes. This conclusion therefore opens up a new dimension to the study of superdeformed nuclei. It appears that the 3-dimensional orbits stabilise the superdeformed shapes and are not perturbed by rotation as much as the planar orbits would be.

The role of 3-dimensional orbits is conjectured to assume more important role in SD nuclei in view of the following discussion. We note that we have approximated deformed nucleus by a spheroidal cavity. We also note that the SD bands are observed at high spins. Even otherwise, a deformed nucleus always has a rotational motion. Thus a proper understanding of these bands would require the inclusion of rotation which leads us to a rotating billiard. Significant modifications are expected in the periodic orbits, when we include rotation, because of the inertial forces.

In a simple yet significant work, Arvieu and Frisk [45] explored the classical dynamics of a particle in rotating ellipse and stadium billiard and discussed the organisation of the phase space which highlights the regions of order and chaos. While ellipse is an integrable system, the stadium is a non-integrable system. Yet at large rotational frequencies, both the billiards display very similar phase-space structure. It was found that rotation of stadium billiard (which is chaotic) leads to ordered motion which is very similar to that of an ellipse. The phase-space exhibits two confined regions in which only order is seen in both the cases. From our discussion of the dynamics of cranking model (and also the particle-rotor model), which is a rotating system, we are tempted to identify these two confined regions of order at large rotation with the two fixed points  $c_{\pm}$  where we suppose that the SD bands may exist. The SD bands thus appear to present a nice example of ordered motion in a sea of chaos; the stabilising effect is provided by large rotation.

It is our belief that the planar orbits of the spheroidal cavity will get more disturbed when rotation is introduced. The 3-dimensional orbits must therefore be considered at large rotational frequencies which are expected to play a significant role in SD nuclei.

The results presented in this chapter are only indicative of the direction in which more detailed studies are required. We have not carried out any detailed tests of convergence largely due to the considerable computational effort involved in it. We have therefore relied on the information on convergence provided by Magner et al. Yet this is proposed to be done in future as also the calculations of shell corrections to energy and comparison with the quantum results.

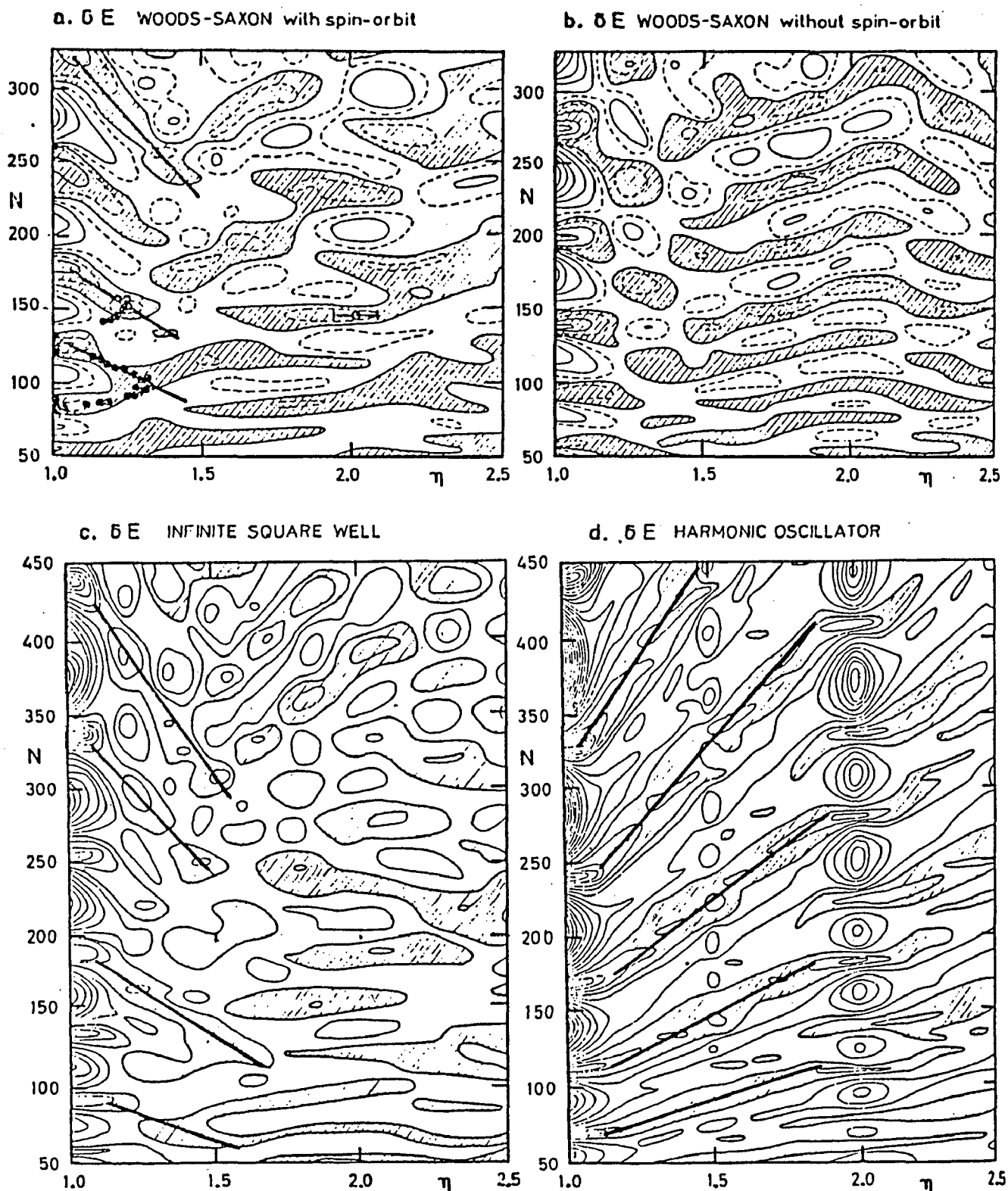


FIG. 6.1 Contour plots of shell energy corrections  $\delta E(N, \eta)$  obtained by shell correction method as a function of particle number and deformation for different potentials; The regions of negative  $\delta E$  are shaded. Solid contour lines correspond to 2.5 MeV intervals. The fat solid lines represent the position of the minima valleys for the rhomboidal planar orbits. From Ref. [106].

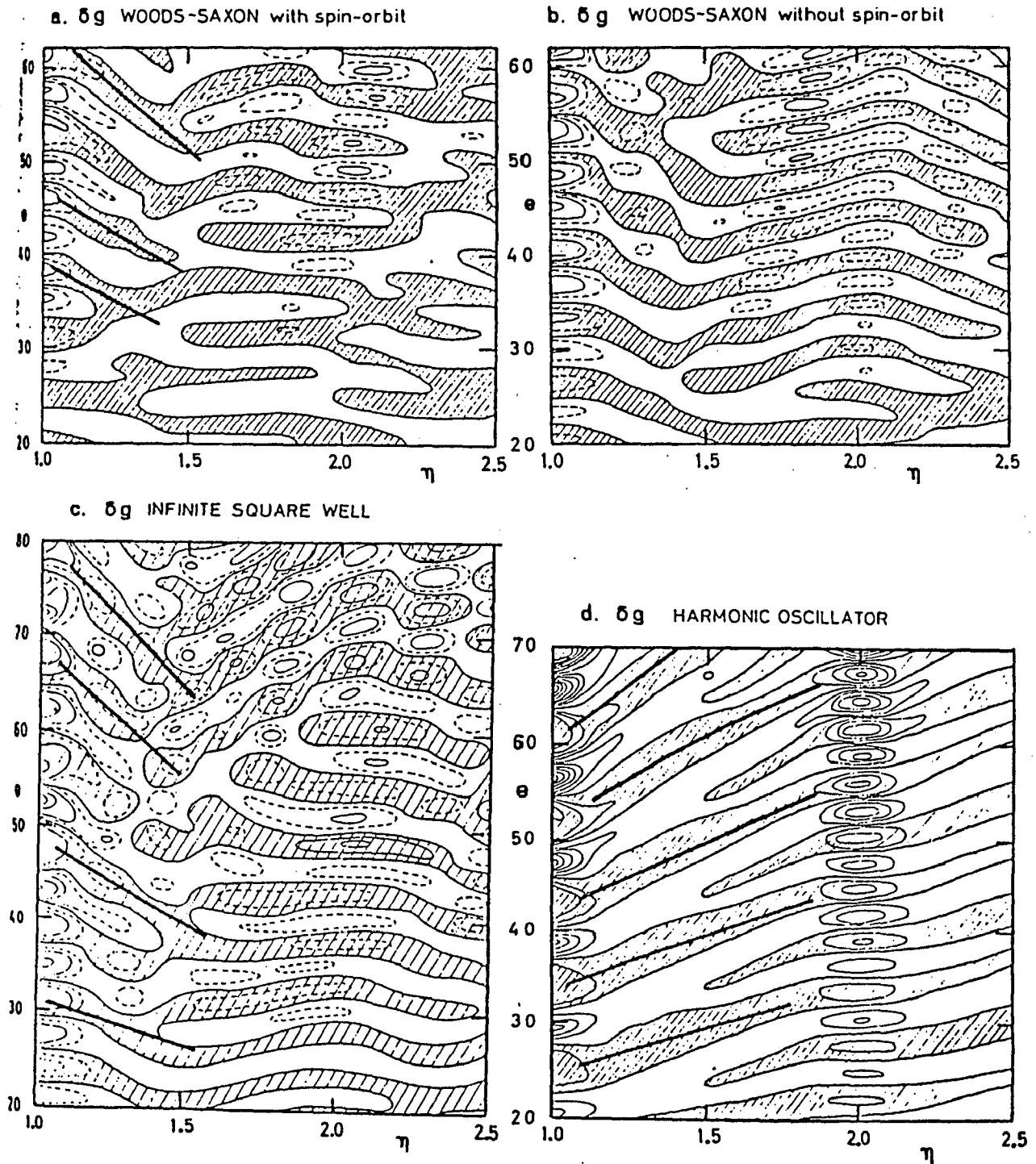


FIG. 6.2 Contour plots of oscillating component  $\delta g(e, \eta)$  as a function of energy and deformation for the same potentials as in FIG. 6.1. The increment per line is 1/MeV, the regions of negative  $\delta g$  are shaded. Fat solid lines represent the minima valleys due to rhomboidal planar orbits as explained in the text. From Ref. [106].



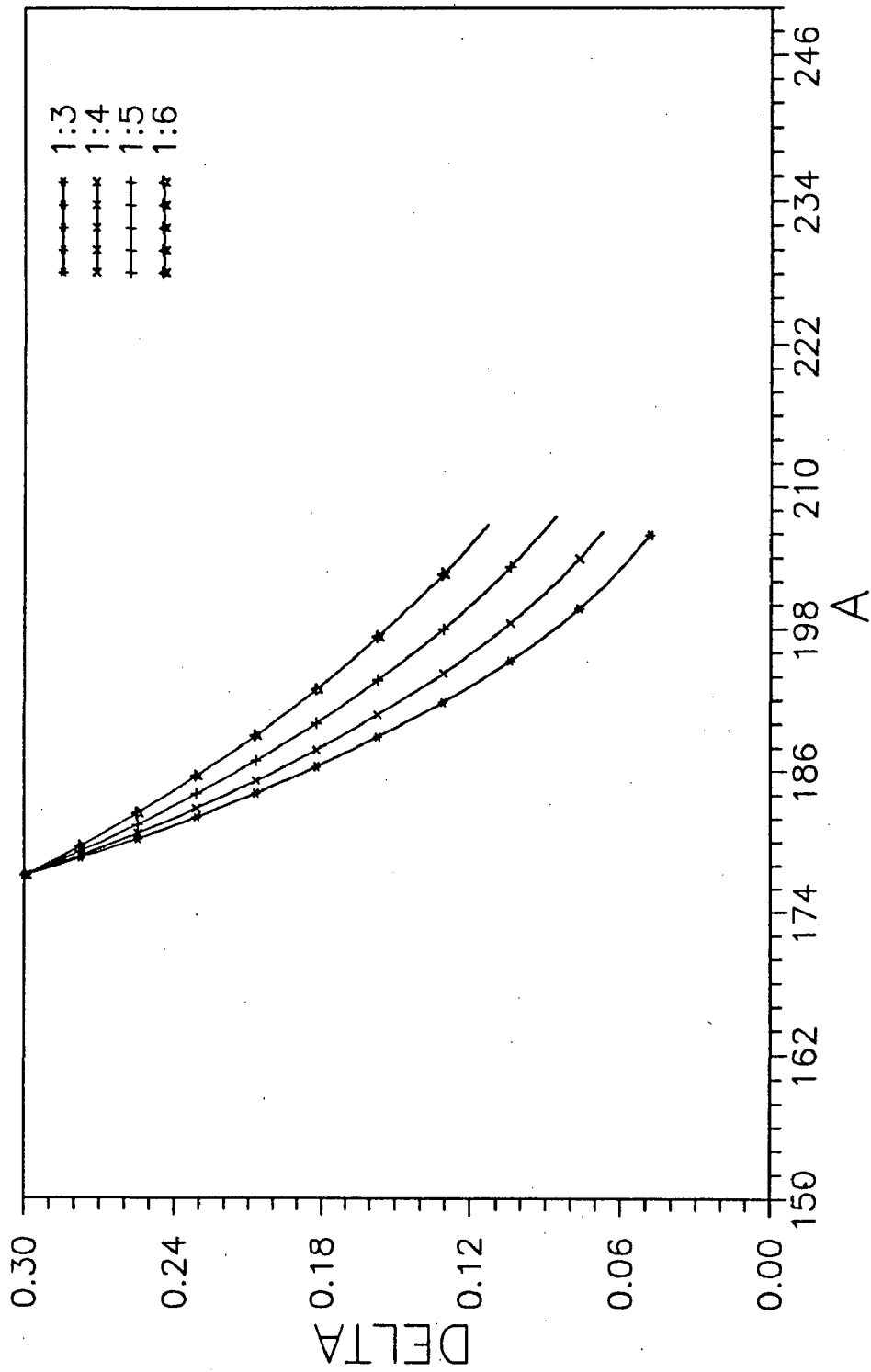


FIG. 6.3 Plot of quadrupole ground state deformation  $\delta$  vs. the mass number  $A$ , calculated for different families of planar orbits.

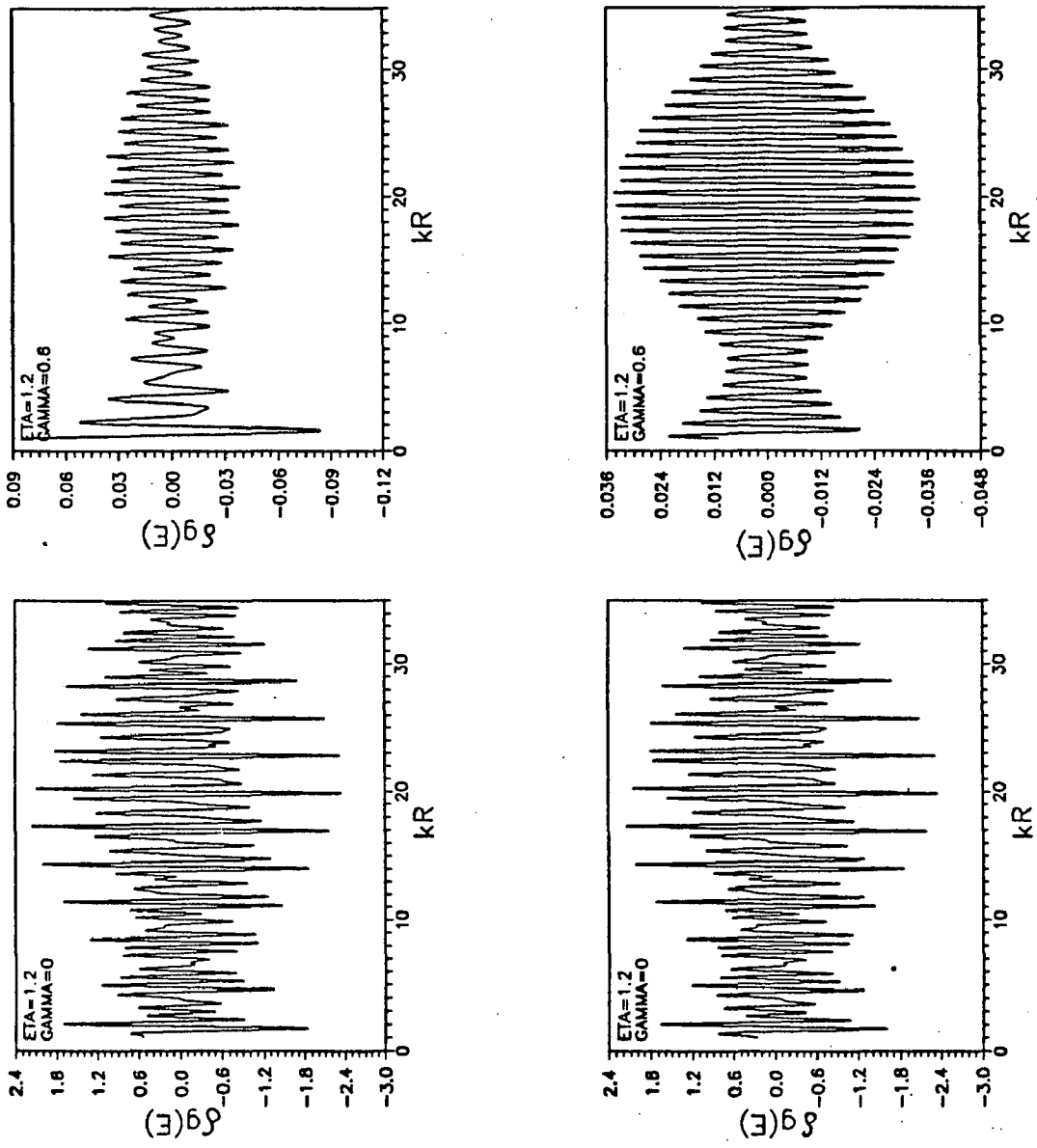


FIG. 6.4 Plots of  $\delta g(E)$  vs.  $kR$  for the orbits in the plane of axis of symmetry in spheroidal cavity with and without smoothing at  $\eta = 1.2$  obtained by summing over  $n_u = n_s = 1:3, 1:4, 1:5, 1:6$  orbits in the lower panels and  $1:2, 1:3, 1:4, 1:5, 1:6$  orbits in the upper panels.

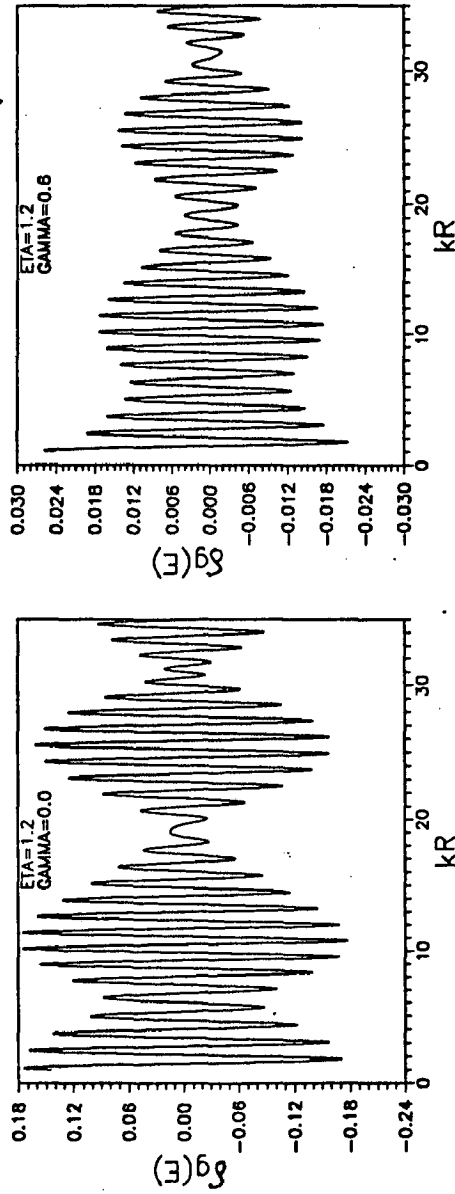
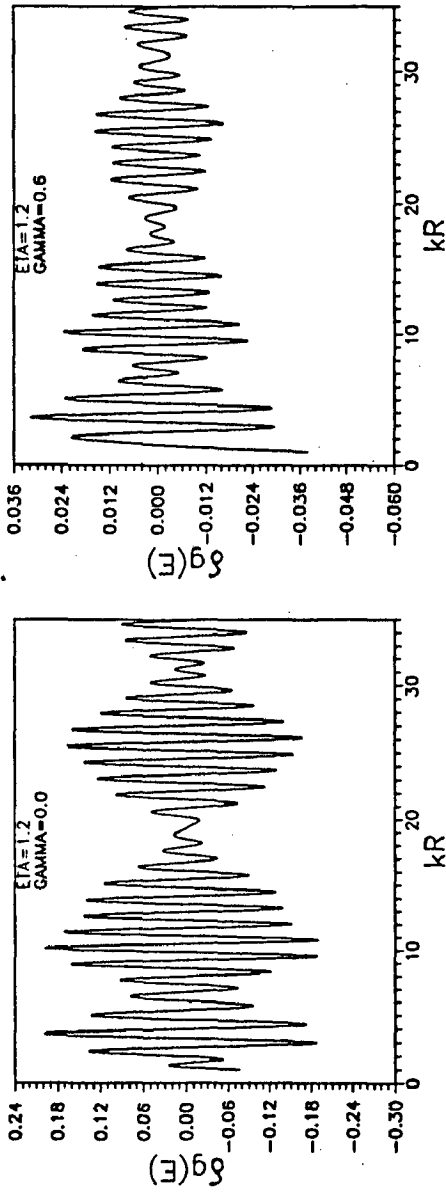


FIG. 6.5 Plots of  $\delta g(E)$  vs.  $kR$  for the orbits in the equatorial plane in spheroidal cavity with and without smoothing at  $\eta = 1.2$  obtained by summing over  $n_u = 1:3, 1:4, 1:5, 1:6$  orbits in the lower panels and  $1:2, 1:3, 1:4, 1:5, 1:6$  orbits in the upper panels.

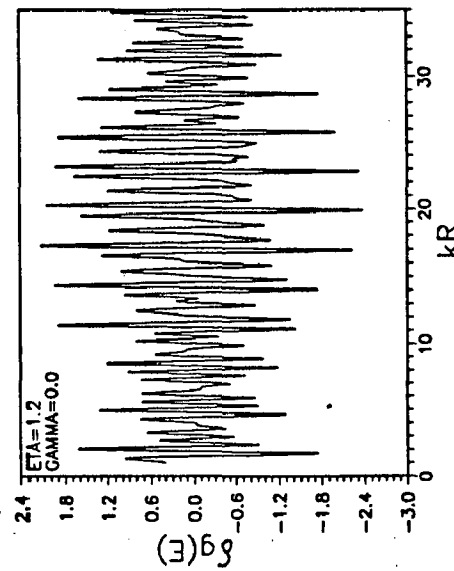
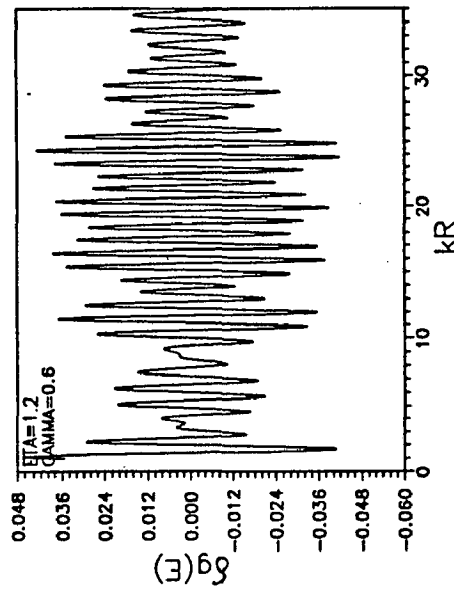
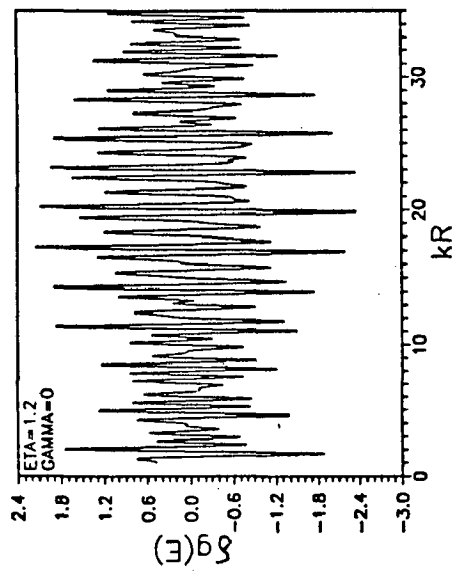
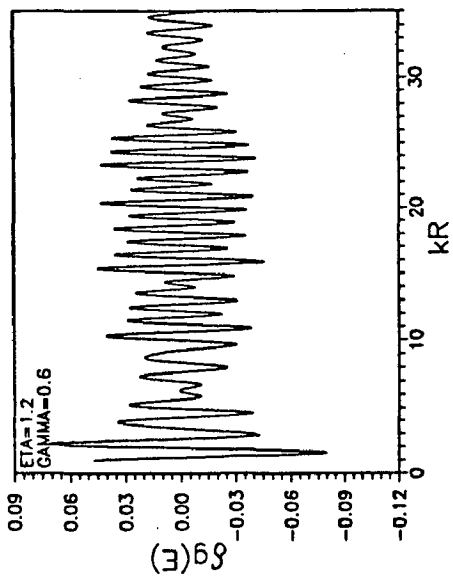


FIG. 6.6 Plots of total  $\delta g(E)$  vs.  $kR$  due to the orbits in the plane of axis of symmetry and the orbits in the equatorial plane in spheroidal cavity with and without smoothing at  $\eta = 1.2$  by summing over  $n_u : n_v = 1:3, 1:4, 1:5, 1:6$  orbits for lower panels and 1:2, 1:3, 1:4, 1:5, 1:6 orbits for upper panels.

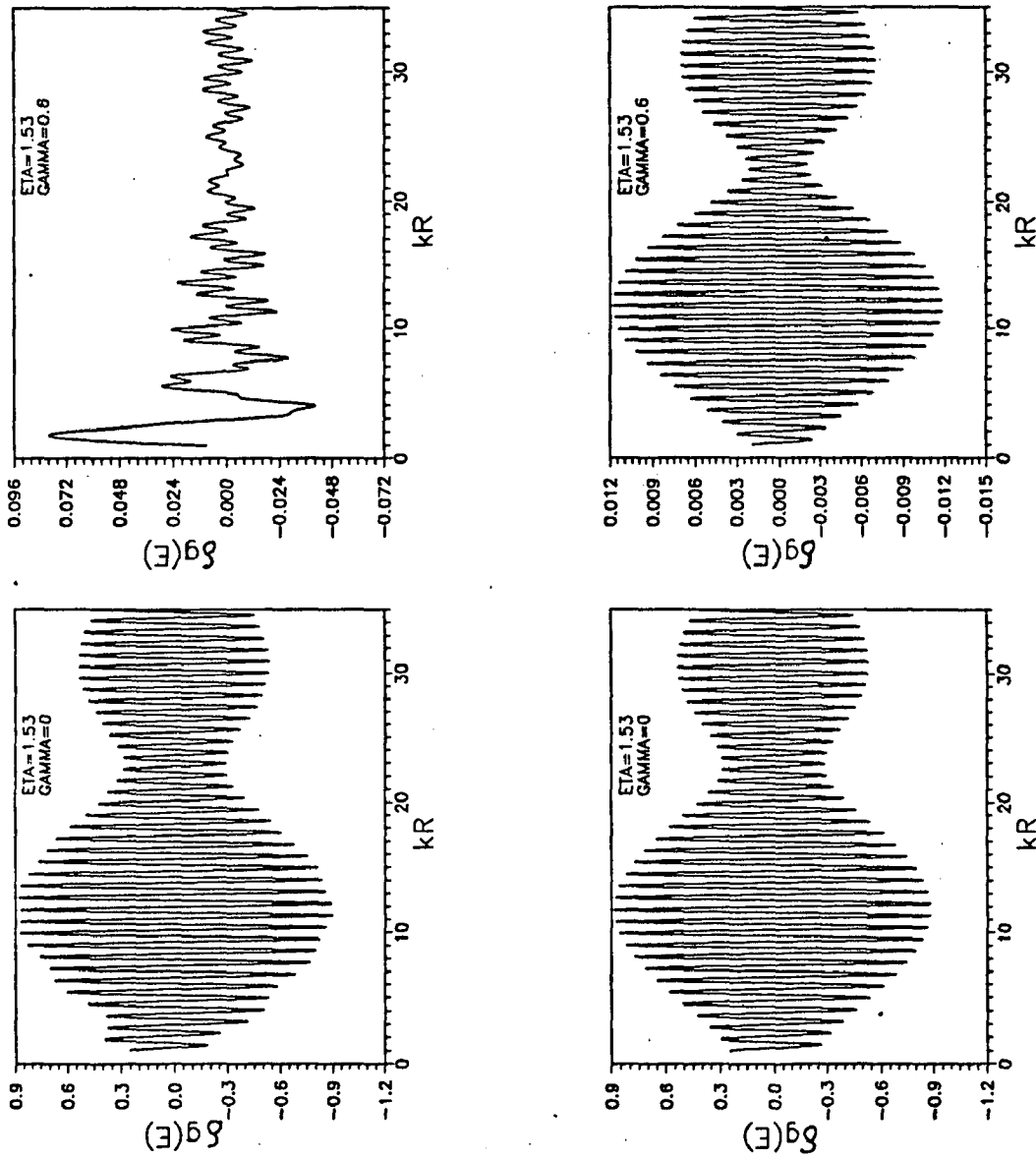


FIG. 6.7 Plots of  $\delta g(E)$  vs.  $kR$  for the orbits in the plane of axis of symmetry in spheroidal cavity with and without smoothing at  $\eta = 1.53$  by summing over  $n_u : n_v = 1:3, 1:4, 1:5, 1:6$  orbits in the lower panels and  $1:2, 1:3, 1:4, 1:5, 1:6$  orbits in the upper panels.

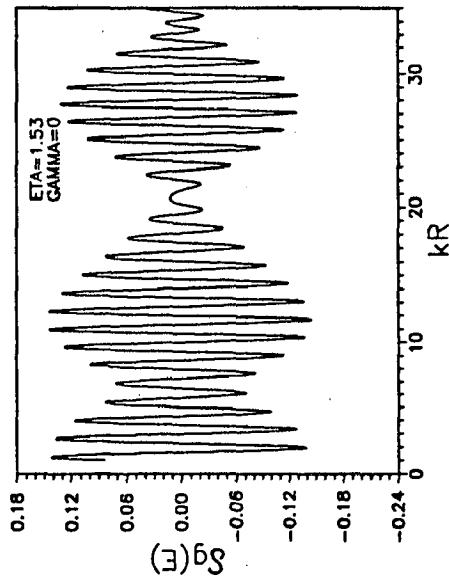
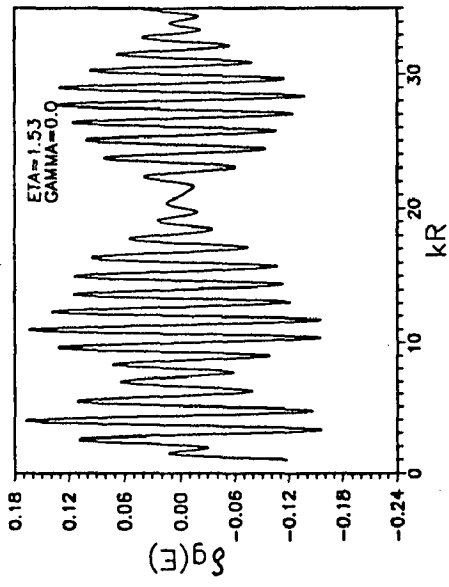
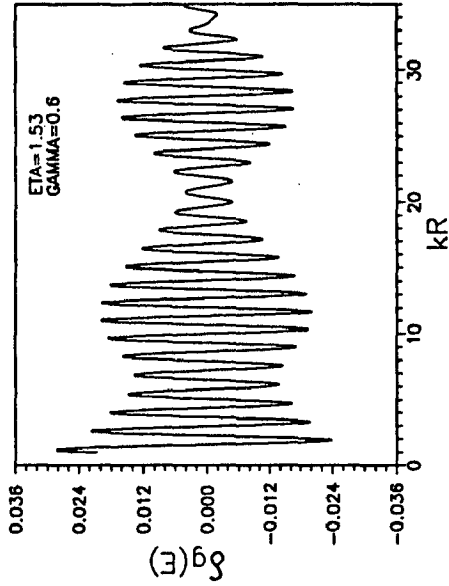
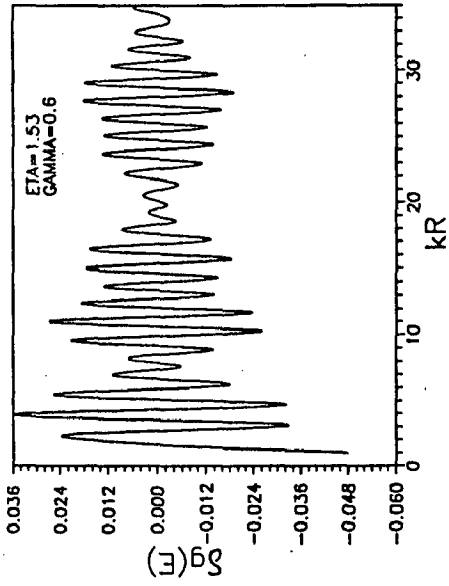


FIG. 6.8 Plots of  $\delta g(E)$  vs.  $kR$  for the orbits in the equatorial plane in spheroidal cavity with and without smoothing at  $\eta = 1.53$  by summing over  $n_u : n_v = 1:3, 1:4, 1:5, 1:6$  orbits in the lower panels and  $1:2, 1:3, 1:4, 1:5, 1:6$  orbits in the upper panels.

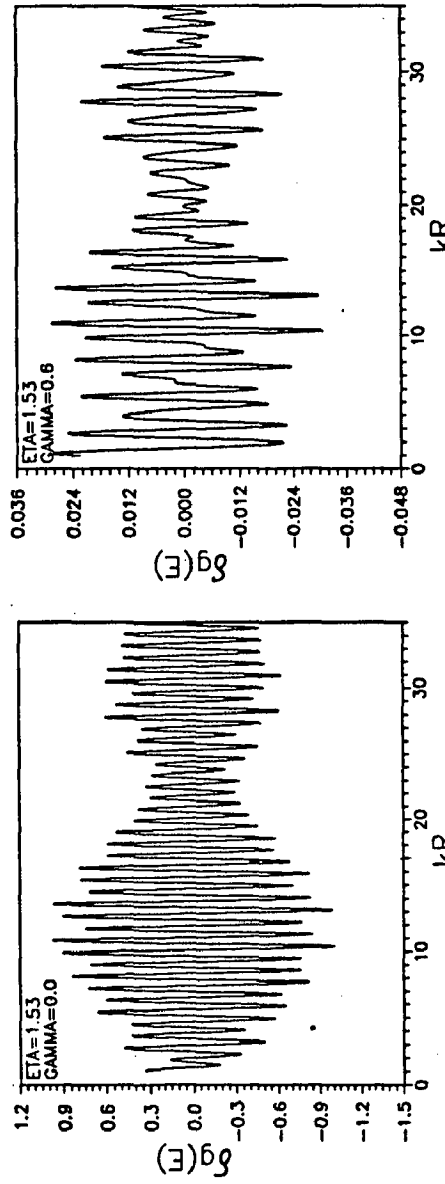
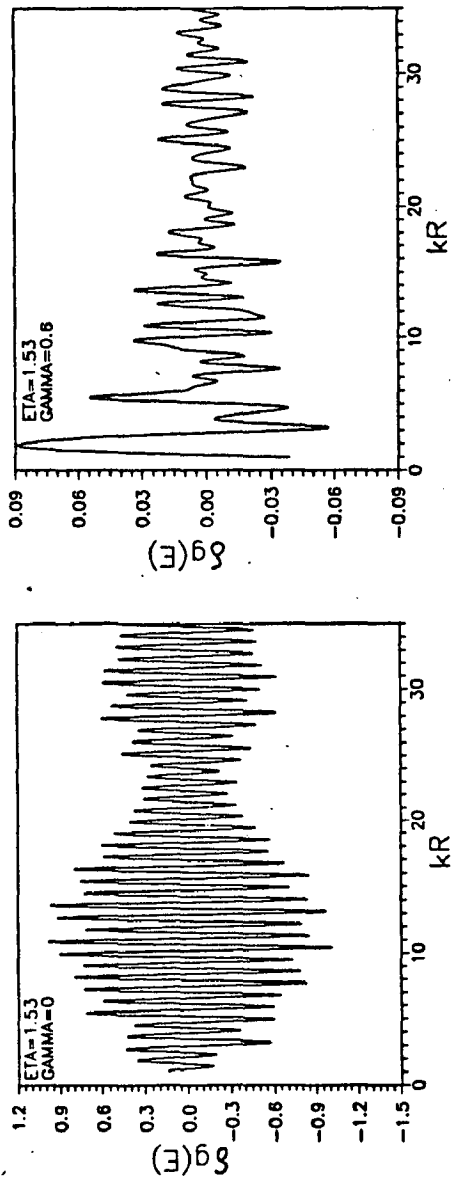


FIG. 6.9 Plots of total  $\delta g(E)$  vs.  $kR$  due to the orbits in the plane of symmetry and the orbits in the equatorial plane in spheroidal cavity with and without smoothing at  $\eta = 1.53$  by summing over  $n_u : n_v = 1:3, 1:4, 1:5, 1:6$  orbits in the lower panels and  $1:2, 1:3, 1:4, 1:5, 1:6$  orbits in the upper panels.

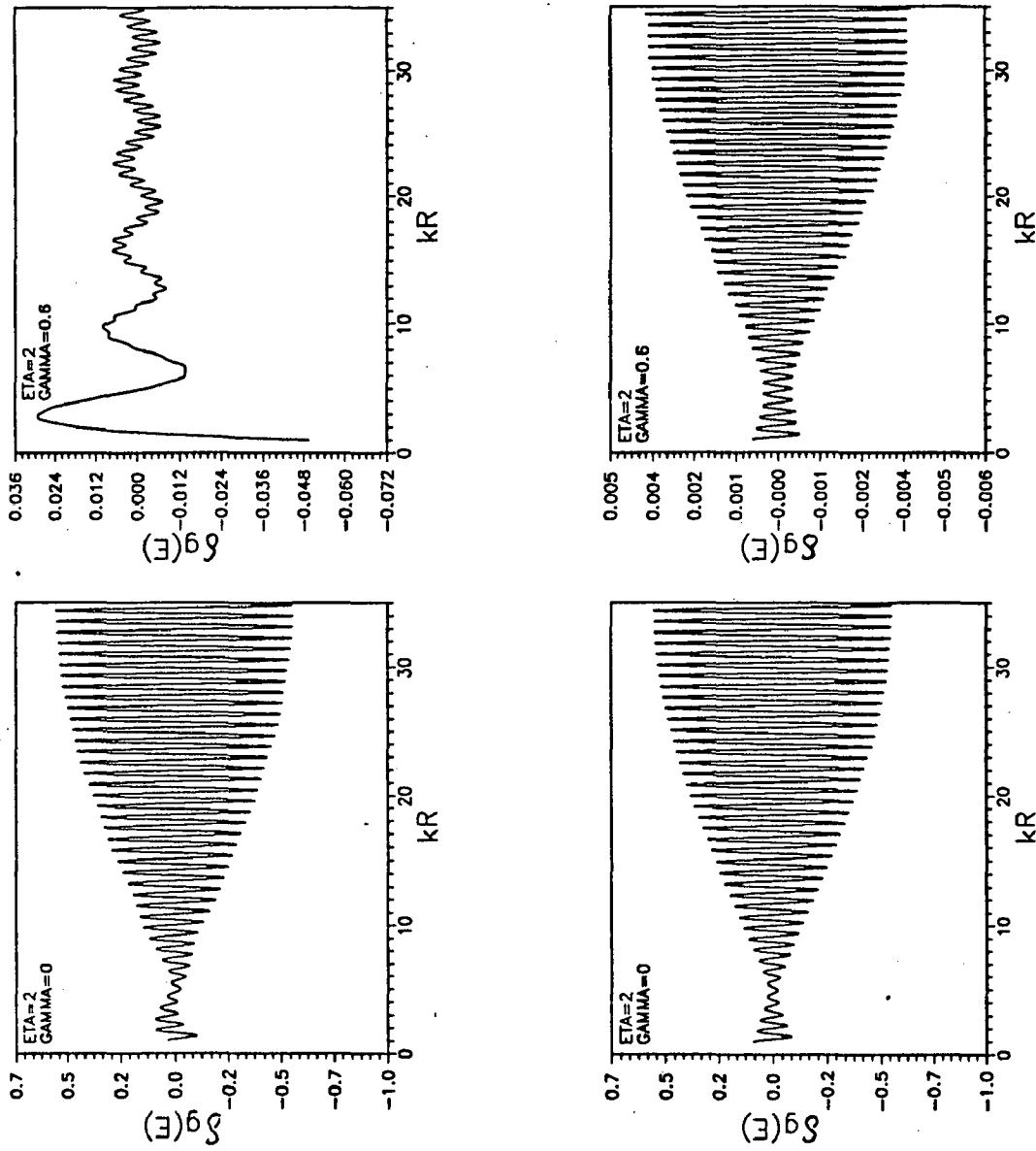


FIG. 6.10 Plots of  $\delta g(E)$  vs.  $kR$  for the orbits in the plane of axis of symmetry in spheroidal cavity with and without smoothing at  $\eta = 2$  by summing over  $n_u : n_v = 1:3, 1:4, 1:5, 1:6$  orbits in the lower panels and  $1:2, 1:3, 1:4, 1:5, 1:6$  orbits in the upper panels.



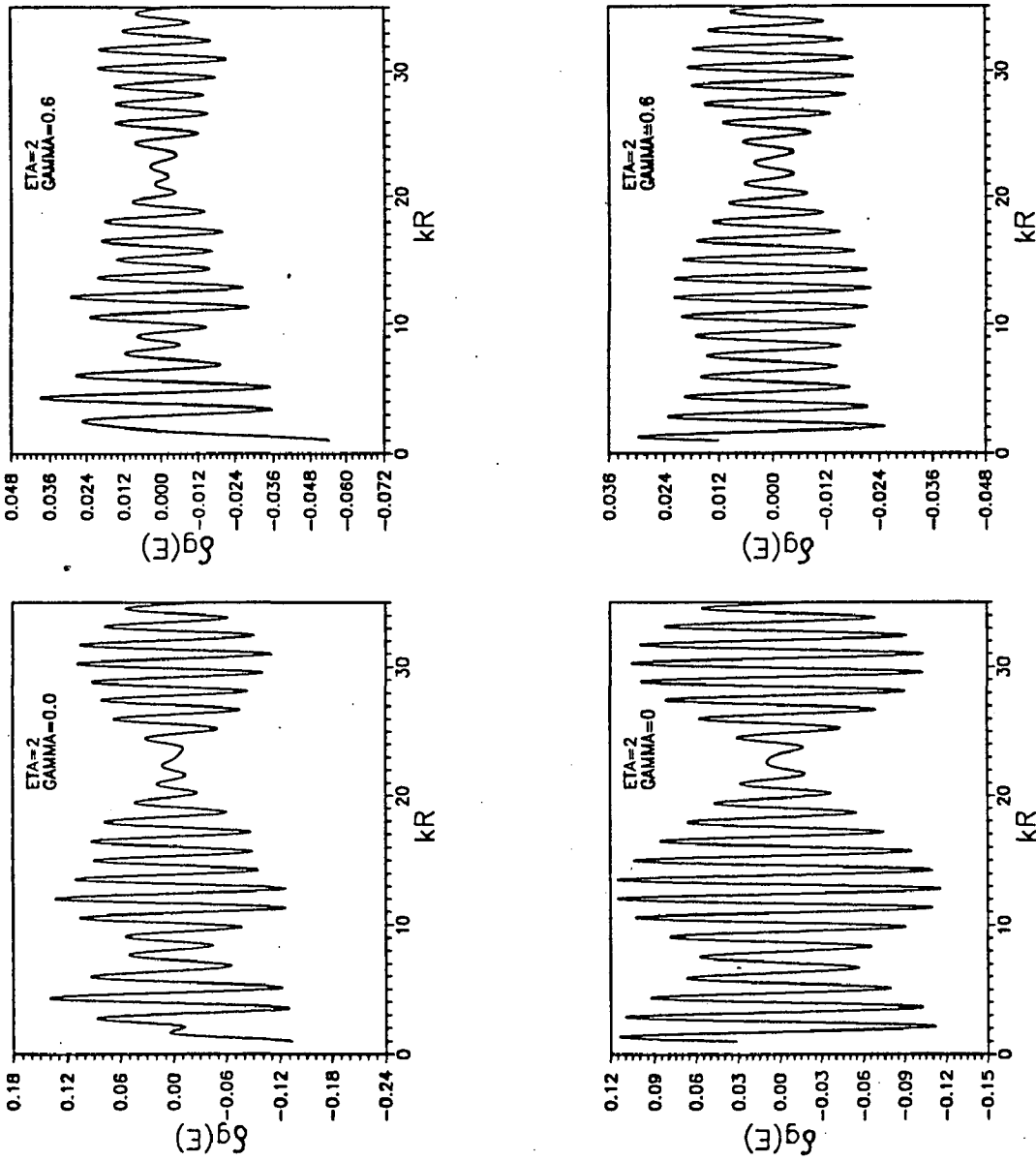


FIG. 6.11 Plots of  $\delta g(E)$  vs.  $kR$  for the orbits in the equatorial plane in spheroidal cavity with and without smoothing at  $\eta = 1.2$  by summing over  $n_u : n_u = 1:3, 1:4, 1:5, 1:6$  orbits in the lower panels and  $1:2, 1:3, 1:4, 1:5, 1:6$  orbits in the upper panels.

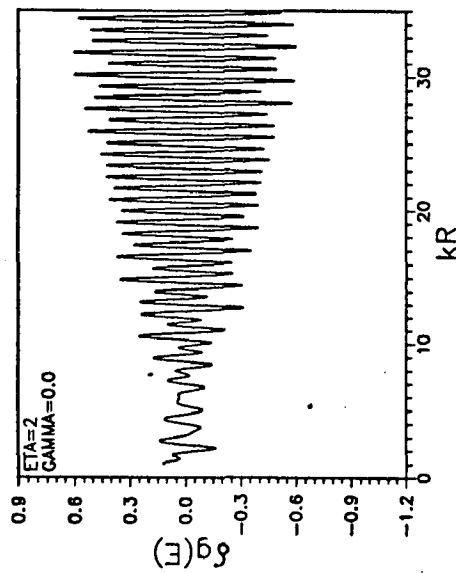
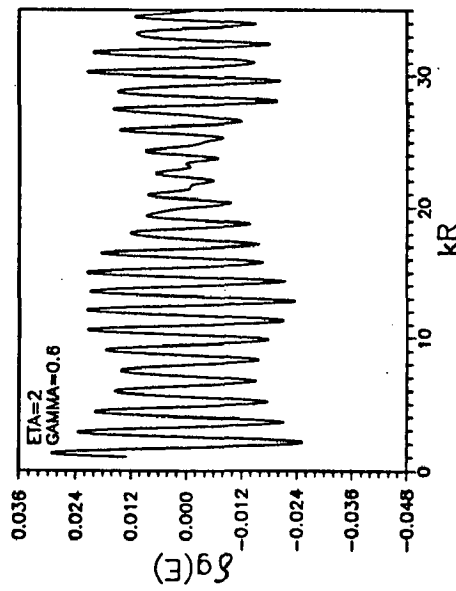
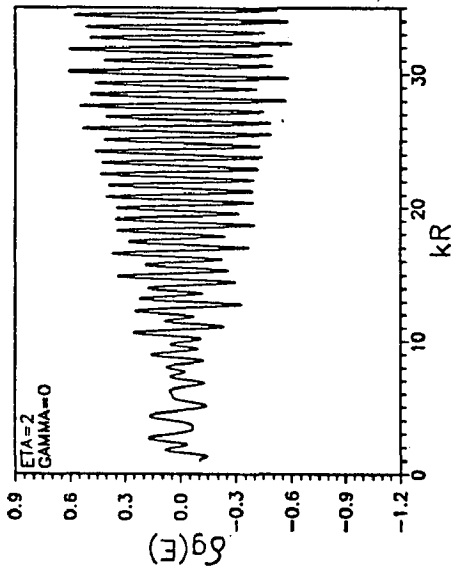
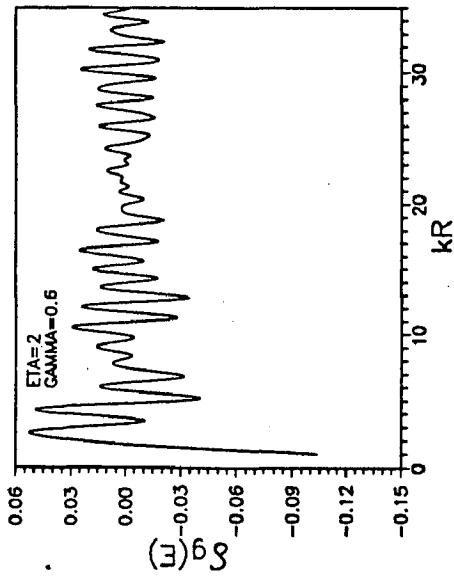


FIG. 6.12 Plots of total  $\delta g(E)$  due to the orbits in the plane of symmetry and the orbits in the equatorial plane vs.  $kR$  in spheroidal cavity with and without smoothing at  $\eta = 1.2$  with  $n_u : n_v = 1:3, 1:4, 1:5, 1:6$  orbits in the lower panels and  $1:2, 1:3, 1:4, 1:5, 1:6$  orbits in the upper panels.

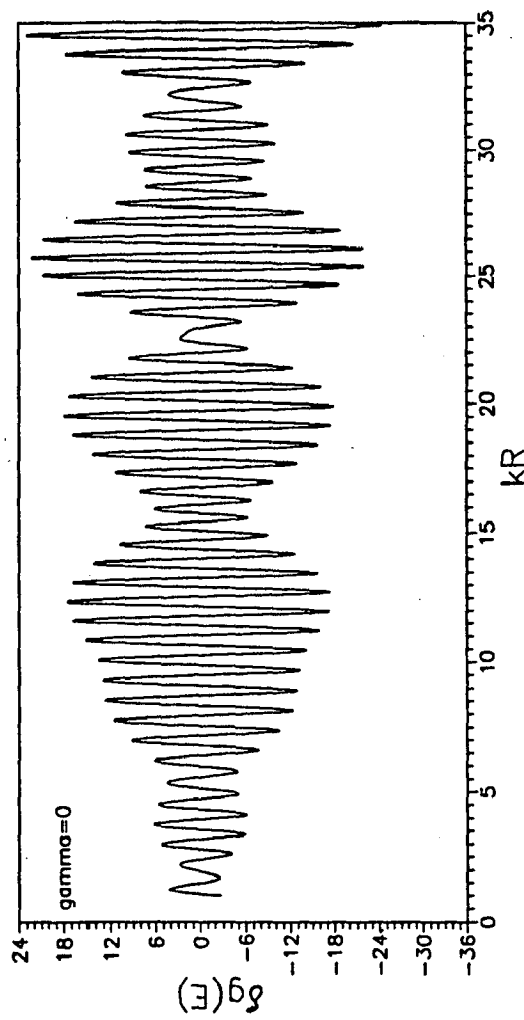
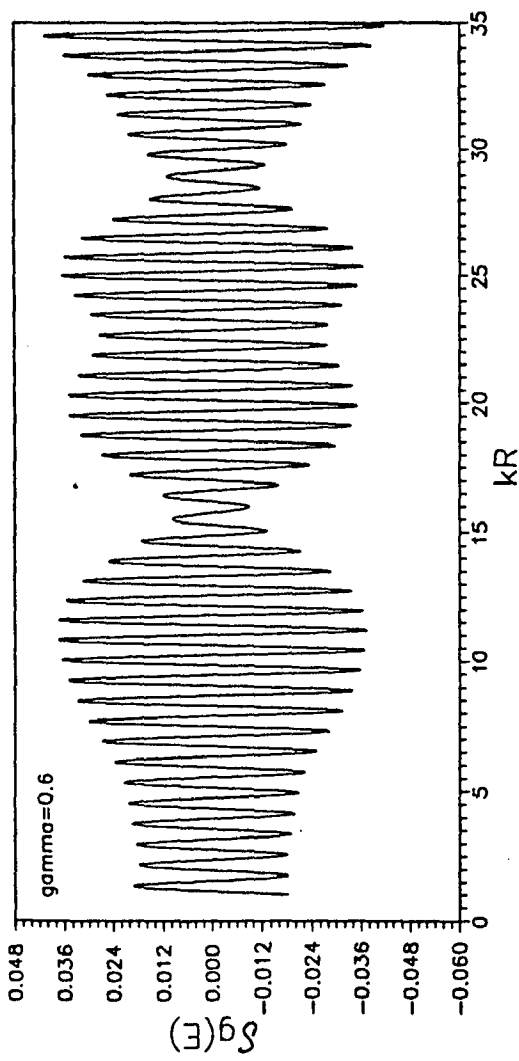


FIG. 6.13 Plots of  $\delta g(E)$  vs.  $kR$  obtained by summing over six 3-dimensional orbits in spheroidal cavity at  $\eta = 2$ ;  $n_u = 1$ ,  $n_\phi = 2$  and  $n_v$  varies from 5 to 10;  $\gamma=0$  and  $\gamma=0.6$  in upper and lower panels respectively.

# CHAPTER VII

## CONCLUSIONS

The two major themes of this thesis have been the Superdeformed bands in nuclei and application of semi-classical methods to them. The semi-classical physics has recently acquired a new vigour and vitality and its successful applications have been made in diverse areas of physics. Such studies have provided new insights into the dynamics of quantal systems. Of particular interest has been the Gutzwiller's periodic orbit theory, which provides a direct link between the classical concepts of orbits and quantised energy levels. An attempt has been made in this thesis to fuse the observation of varied features of SD bands with the ideas of the classical dynamical theories and the periodic orbits.

Following this philosophy, we have presented in chapter II a rather complete discussion of the dynamics of the particle-rotor model for high- $j$  orbitals which also considered the effect of the nonlinear term in the equation of motion. This work draws upon the earlier work of Bohr and Mottelson. Several interesting conclusions have emerged from this study. The most surprising was the emergence of rotational bands at the twin stable fixed points  $c_{\pm}$  which lie beyond the separatrix. The motion in  $j_3$  (the third component of  $j$ ) controls the overall dynamics and is dictated by the duffing oscillator which has a double well potential. The effect of tunnelling between the wells was exactly considered and two solutions ( $p=0$  and  $p=1$ ) were obtained for each quantum number  $n = 1, 2, 3, \dots$  etc. It has been shown that the system undergoes a second order phase transition when going from the yrast (aligned) regime to the nonlinear regime of duffing oscillator. The rotational bands built at  $c_{\pm}$  are thus phase separated from those built near the aligned configuration (fixed point  $a$ ); they will therefore connect with the yrast configurations with great difficulty.

The level energies at  $c_{\pm}$  follow an exact rotational relationship implying a linear  $I$  vs.  $E_{\gamma}$  behaviour. Inclusion of the non-linear effect and semi-classical quantisation revealed that very weak oscillations develop in the linear  $I$  vs.  $E_{\gamma}$  plots. Further, we found that the intercept of this overall linear graph of  $I$  vs.  $E_{\gamma}$ , on the  $I$ -axis is mostly negative. In the later chapter, we interpret this intercept as an average aligned angular momentum. Among other important features exhibited by these bands at  $c_{\pm}$ , are the finite starting angular momentum for each band and a negative alignment. The aligned angular momentum which

is negative at the lower angular momentum, increases with angular momentum, becomes positive and saturates at higher angular momenta. We have also found that the dynamical moment saturates at higher angular momenta and also exhibits a downtrend. This may be directly correlated with the saturation of aligned angular momentum.

In chapter III, we have tried to connect these findings with some of the well-known and also some newly pointed out features of the SD bands. Among the most important new features, which were established in this work are, (i) a weak oscillation in the  $I$  vs.  $E_\gamma$  plots, (ii) a negative aligned angular momentum and (iii) a feature of general identical band. The first of these is immediately understood in terms of the results of Chapter II, if we associate the SD bands with the bands located at or, near the fixed points  $c_\pm$ . By using a simple empirical formula for the SD bands, it is possible to associate the negative intercept found in the  $I$  vs.  $E_\gamma$  plots on the  $I$ -axis, with an averaged aligned angular momentum. This interpretation also fits well with the explanation of most of the SD bands as located at  $c_\pm$  point.

If we accept this interpretation of the SD bands, we find that a very simple explanation of the  $\Delta I = 2$  staggering also emerges. Arguing that the weak oscillations are a first order effect, we show that the  $\Delta I = 2$  staggering is a third order effect and must follow from an explanation for the oscillations. Since the system experiences a motion confined to a double well at  $c_\pm$ , a tunnelling between the two wells will lead to a shift in the levels of the two wells. This effect has been taken into account in our calculations presented in Chapter II. It is most interesting that the double well has a depth which is dependent on  $I$  and therefore levels with different  $I$  will shift with different amount. We find that the resultant spectrum does exhibit a  $\Delta I = 2$  staggering in many situations. The pattern is however irregular in most of the cases, as is experimentally observed to be the case.

We have also arrived at a systematics in the value of the angular momentum at which the SD bands start. This starting angular momentum has a typical range for each mass region. We have shown that it is possible to partially understand this systematics within the framework of the model calculations of Chapter II.

We have also presented some numerical results to test this formula. Besides the gross shell structure, where we obtained the beat pattern in level density, we have also shown that the formula leads to the exact quantum spectrum if a summation over sufficiently large number of orbits is carried out. This calculation serves the purpose of a text-book example to illustrate the basic ideas and concepts involved in these calculations.

A natural extension of a spherical billiard, to study deformed nuclei, is to consider deformed cavities. Many such studies have already been carried out in recent past. We have also extended the work of Chapter V to include three-dimensional spheroidal cavity which is a good approximation of prolate deformed nuclei. In Chapter VI, we have used the periodic orbit trace formula for continuous symmetries and obtained a general result for the shell correction part of the level density which is valid for three-dimensional orbits. This formula reduces to give the results of planar orbits when  $\sigma_2 = 0$ . To calculate the contribution of the planar orbits in equatorial plane, we use results of the spherical billiard from Chapter V. In an interesting application, Strutinsky and co-workers had obtained the variation in nuclear deformation with mass number  $A$  near the shell closure  $A=208$  by considering only the rhomboidal orbits in the axis-of-symmetry plane. The result was obtained under approximations and gives remarkable fit to the almost linear variation of deformation before the shell closure at  $A=208$ . We have calculated these results more exactly by using numerical methods and find that it was indeed fortuitous for Strutinsky to have reproduced these results. Various families of shortest periodic orbits (1:3, 1:4, 1:5,.. etc.) give a variation which is not too different from each other and they all appear to converge at value of  $\delta \approx 0.3$ ; this value of nuclear deformation, where most of the stable deformed nuclei are concentrated, thus appears to have a special status.

We have carried out some tests of the trace formula for spheroidal billiard by calculating the gross shell structure for three deformations  $\eta=1.2, 1.53$  and  $2$ . It is clear from these results that the most important contribution at lower deformation comes from the leading orbits which are 1:3 and 1:4. The planar equatorial orbits also appear to play an important role particularly as the deformation increases and the length of these orbits decreases.

At higher deformations, when  $\eta > \eta_{min}$ , the three dimensional (3-d) orbits make an appearance. We find that the gross shell structure of the 3-d orbits exhibits a beat pattern which has a small 'wave-length'. The 3-d orbits thus would have magic shell closures which are more closer to each other. This gives rise to the possibility of observing the beat pattern in SD nuclei. Also, as pointed out in Chapter VI, the planar orbits will get more disturbed when rotation is introduced. Therefore, the 3-d orbits are expected to become more important at large deformation and higher angular momenta, which is the case with SD nuclei. We therefore believe that a detailed study of the role of 3-d orbits would be very crucial in understanding the nature of SD bands.

Finally, we make some observations about the future directions of this work. The studies performed in this thesis have been based on the simplest possible versions of the models. This has had an advantage in terms of correlating the effects with the basic causes and physics. But it also means that we cannot make calculations for specific nuclei. This is one direction in which progress could be made in future. Further, a direct correlation of these studies with exact quantum mechanical studies offers a very important line of study. As is clear from the foregoing discussions, it has been possible to understand many features of the SD bands in a single model. Yet, many features like the phenomenon of identical bands remain untouched. This continues to be a challenge to theorists to explain this feature along with other features in a unified manner.

The results on periodic orbit theory presented in this thesis, represent the formation of a base from which a large number of studies can be started. Before this, it is still necessary to carry out detailed tests of the convergence of the summation over trace formula for the spheroidal cavity presented by us. Further, calculation of the shell correction to energy and its comparison with exact results in specific cases also needs to be carried out.

The simplest results of the spherical cavity immediately suggest applications to spherical nuclei like  $^{40}\text{Ca}$  or,  $^{41}\text{Ca}$  where a scaling in the energy levels with mass number  $A$  must exist. The results of the spheroidal shape offer a large number of applications to the deformed nuclei such as understanding their behaviour in terms of planar and 3-d orbits. The occurrence of



identical bands in different nuclei can be explored in terms of scaling of the spectrum with mass number  $A$  for very large deformation. Introduction of high spin by rotating the cavity may further expand the area of work. These studies also open the route to study the onset of chaos in nuclei under specific conditions.

# REFERENCES

## REFERENCES

- [1] Aberg, Sven, Superdeformation-A theoretical overview, Invited talk in "Nuclear Structure in the Nineties" , Oak Ridge, April (1990).
- [2] Ahmed, Zafar, Double well potential, Private communication (1996).
- [3] Ayant, Y. and Arvieu, R., Semiclassical study of particle motion in elliptical boxes: I, J. Phys. A20, 397 (1987).
- [4] Arvieu, R. and Ayant, Y., Semiclassical study of particle motion in elliptical boxes: II, J. Phys. A20, 1115 (1987).
- [5] Baktash, C., Hass, B. and Nazarewicz, W., Identical bands in deformed and superdeformed nuclei, Annu. Rev. Nucl. Part. Sc., 45, 485 (1995).
- [6] Balian, R. and Bloch, C., Distribution of eigenfrequencies for the wave equation in a finite domain: III Eigenfrequency density oscillations, Ann. Phys. (N.Y.), 69, 76 (1972).
- [7] Balian, R. and Bloch, C., Asymptotic evaluation of the Green's function for large quantum numbers, Ann. Phys. (N.Y.), 60, 401 (1970).
- [8] Bazzacco, D., Brandoline, F., Burch, R. et al., Complete decay out of the SD band in  $^{133}\text{Nd}$ , Phys. Rev., C49, R2281 (1994).
- [9] Bengtsson, R., Larsson, S.E. et al., Yrast bands and high spins potential-energy surfaces, Phys. Lett., 57B, 310 (1975).
- [10] Berry, M.V. and Tabor, M., Closed orbits and regular bound spectrum, Proc. Roy. Soc. Lond., A349, 101 (1976).
- [11] Berry, M.V. and Tabor, M., Calculating the bound spectrum by path summation in action angle variables, J. Phys. A10, 371 (1977).

- [12] Bjorholm, S. and Lynn, J.E., The double humped fission barrier, *Rev. Mod. Phys.* 52, 725 (1980).
- [13] Bohr, A., The coupling of nuclear surface oscillations to the motion of individual nucleons, *K. Dan. Vid. Selsk. Mat. Fys. Medd.* 26, No. 4 (1952).
- [14] Bohr, A. and Mottelson, B.R., Collective and individual particle aspects of nuclear structure, *K. Dan. Vid. Selsk. Mat. Fys. Medd.* 27, No. 16 (1953).
- [15] Bohr, A. and Mottelson, B.R., *Nuclear Structure, Vol II, Nuclear deformation*, Benjamin, New York, (1975).
- [16] Bohr, A. and Mottelson, B.R., Solutions for Particle-Rotor and Cranking Models for single- $j$  configuration, *Physica Scripta* 22, 461 (1980).
- [17] Bonche, P., Krieger, S.J., Quentin, P. et al., Superdeformation and shape isomerism at zero spin, *Nucl. Phys.*, A500, 308 (1989).
- [18] Brack, M., Creagh, S., Meier, P., Reimann, S.M. and Seidl, M., Semiclassical methods for the description of large metal clusters, Invited talk at the NATO, ASI Large Clusters of Atoms and Molecules, Erice, (1995).
- [19] Brack, M. and Jain, S.R., Analytical tests of Gutzwiller's trace formula for harmonic-oscillator potentials, *Phys. Rev.*, A51, 3462 (1995).
- [20] Brack, M. and Bhaduri, R.K., *Semiclassical Physics*, Addison-Wesley Pub. Comp., Inc., (1997).
- [21] Brack, M., The physics of simple metal clusters: shell consistent jellium model and semiclassical approaches, *Rev. Mod. Phys.*, 65, 677 (1993).
- [22] Brack, M., Damgaard, J., Pauli, H.C., Strutinsky, V.M., Wong, C.Y., Funny hills: The shell correction approach to nuclear shell effects and its applications to the fission process, *Rev. Mod. Phys.*, 44, 320 (1972).

- [23] Brack, M., Lecture notes on Gutzwiller's periodic orbit theory, at Konan University, Kobe, Japan, Sept. (1994).
- [24] Brack, M., Blaschke, J., Creagh, S.C., Magner, A.G., Meier, P. and Reimann, S.M., On the role of classical orbits in mesoscopic electronic systems, *Z. Phys.* D40, 276 (1997).
- [25] Byrski, T., Beck, F.A., Curien, D. et al., Observation of identical superdeformed bands in  $N=86$  nuclei, *Phys. Rev. Lett.* 64, 1650 (1990).
- [26] Caiwan, Shen, Wendong, Luo and Chen, Y.S., Identical bands and quantized alignments in superdeformed nuclei, *Phys. Rev.* C55, 1762 (1997).
- [27] Carbonell, J., Brut, F., Arvieu, R. and Touchard, J., Classical properties and semiclassical quantisation of a spherical nuclear potential, *J. Phys.* G11, 325 (1985).
- [28] Chasman, R.R., Superdeformation in the rare earth region, *Phys. Lett.*, B187, 219 (1987).
- [29] Cederwell, B., Janssens, R.V.F., Brinkman, M.J., New features of SD bands in  $^{194}\text{Hg}$ , *Phys. Rev. Lett.* 72, 3150 (1994).
- [30] Cederwell, B., Hackman, G., Galindo-Uribarri, A. et al., Properties of superdeformed bands in  $^{153}\text{Dy}$ , *Phys. Lett.* B380, 18 (1996).
- [31] Creagh, S.C. and Littlejohn, R.G., Geometrical properties of Maslov indices in the semiclassical trace formula for the density of states, *Phys. Rev.* A42, 1907 (1990).
- [32] Creagh, S.C. and Littlejohn, R.G., Semiclassical Trace formula in the presence of continuous symmetries, *Phys. Rev.* A44, 836 (1991).
- [33] Dagnall, P.J., Smith, A.G., Lisle, J.C. et al., The observation of a superdeformed structure in  $^{82}\text{Y}$ , *Z. Phys.* A353, 251 (1995).
- [34] Deleplanque, M.A., Beausang, C.W., Burde, J., Diamond, R.M., Stephens, F.S., McDonald, R.J., Draper, J.E., Superdeformation in Odd-Odd nucleus  $^{150}\text{Tb}$ : Experiment-

- tal search for superdeformed configurations, Phys. Rev. C39, 1651 (1989).
- [35] de Voigt, M.J.A., Dudek, J. and Szymanski, Z., High spin phenomena in atomic nuclei, Rev. Mod. Phys. 55, 949 (1983).
- [36] Draper, J.E., Stephens, F.S., Deleplanque, M.A. et al., Spins in SD bands in the mass 190 region, Phys. Rev. C42, R1791 (1990).
- [37] Dudeja, M., Malik, S.S. and Jain, A.K., An empirical analysis of superdeformed bands: A semiclassical view, Phys. Lett. B412, 14 (1997).
- [38] Dudeja, M., Semiclassical quantisation of cranking model and SD bands, Talk presented at IV National Workshop on nuclear structure physics, Puri (1997).
- [39] Dudek, J., Nuclear superdeformation at high spins, Report of Centre de Recherches Nucleaires, IN2P3-CNRS/ Universite Louis Pasteur BP20, F-67037, Strasbourg, Cedex, France (1987).
- [40] El-Aouad, N., Burglin, O., Dudek, J., Heydon, B., Rowley, N. and Szymanski, Z., Correlation between quantized-alignment and identical-band mechanisms, Phys. Rev. C49, R1246 (1994).
- [41] Flibotte, S., Hackman, G., Ragnarsson, I. et al., Multiparticle excitations in the superdeformed  $^{149}\text{Gd}$  nucleus, Nucl. Phys. A584, 373. (1995).
- [42] Flibote, S., Andrews, H.R., Ball, G.C. et al.,  $\Delta I = 4$  bifurcation in a superdeformed band: Evidence for a  $C_4$  symmetry, Phys. Rev. Lett. 71, 4299 (1993).
- [43] Fluggae, Siegfried, Practical Quantum Mechanics I, pg. 154, Springer-Verlag, Berlin (1971).
- [44] Frisk, H., Shell structure in terms of periodic orbits, Nucl. Phys. A511, 309 (1990).
- [45] Frisk, H. and Arvieu, R., Transition order-chaos in a rotating billiard, Z. Phys. A495, 291c (1989).

- [46] Goel, A. and Jain, A.K., Coriolis coupling in two-quasiparticle rotational bands of deformed even-even nuclei, *Phys. Rev. C* 45, 221 (1992).
- [47] Goldstein, H., *Classical mechanics*, Addison-Wesley Publ. Co. (1950).
- [48] Gradshteyn, I.S. and Ryzhik, I.M., *Table of integrals, series and products*, Academic Press, New York (1983).
- [49] Gutzwiller, M.C., *Chaos in classical and quantum mechanics*, Springer-Verlag, New York Inc. (1990).
- [50] Gutzwiller, M.C., Phase-integral approximation in momentum space and the bound states of an atom, *J. Math. Phys.* 8, 1979 (1967); Periodic orbits and classical quantisation conditions, *J. Math. Phys.* 12, 343 (1971).
- [51] Hackman, G., Khoo, T.L., Caarpenner, M.P. et al., Spins, parity, excitation energies and octupole structure of an excited superdeformed band in  $^{194}\text{Hg}$  and implications for identical bands, *Phys. Rev. Lett.* 79, 4100 (1997).
- [52] Hamamoto, I. and Mottelson, B., Superdeformed rotational bands in the presence of Y-44 deformation, *Phys. Lett.* B333, 294 (1994).
- [53] Hass, B., Vivien, J.P., Basu, S.K. et al., Feeding of the superdeformed yrast band in  $^{149}\text{Gd}$ , *Phys. Lett.* B245, 308 (1991).
- [54] Hara, K. and Lalazissis, G.A., Analysis of  $\Delta I = 2$  staggering in nuclear rotational spectra, *Phys. Rev. C* 55, 1789 (1997).
- [55] Haslip, D.S., Flibotte, S., France, G.de et al.,  $\Delta I = 4$  bifurcation in identical superdeformed bands, *Phys. Rev. Lett.* 78, 3447 (1997).
- [56] Haxel, O., Jensen, J.H.D. and Suess, H.E., On the 'Magic Numbers' in nuclear structure, *Phys. Rev.* 75, 1766 (1949).
- [57] Huang, K., *Statistical Mechanics*, II edition, John Wiley and Sons, New York, Chap

17 (1987).

- [58] Inglis, D.R., Particle derivation of nuclear rotation properties associated with a surface wave, *Phys. Rev.* 96, 1059 (1954).
- [59] Jain, S.R., Jain, A.K. and Ahmad, Z., Nonlinear dynamics of high-j cranking model, *Phys. Lett.* B370, 1 (1996).
- [60] Jain, A.K., Strongly coupled bands as effectively decoupled bands, *Z. Phys.* A317, 117 (1984).
- [61] Jain, A.K. and Dudeja, M., Some new universal features of superdeformed bands, *J. of Korean Phys. Soc.* 23, S361 (1996).
- [62] Jain, A.K. and Jain, S.R., Superdeformation -Present status and some new universal features, *Proc. of National Workshop on Nuclear Structure Physics, Roorkee*, pg. 57 (1995).
- [63] Jain, A.K., Dudeja, M., Malik, S.S. and Ahmad, Z., Nonlinear dynamics of particle-rotor model and superdeformed bands, *Phys. Lett.* B392, 243 (1997).
- [64] Jain, A.K. Casten, R.F., Observation of  $\pm F_0$  symmetry in F-spin multiplets, *Modern Phys. Lett.* A3, 743 (1988).
- [65] Jain, A.K. and Sood, P.C., *Proc. of Int. Conf. on Band Structure and Nucl. Dynamics*, Vol. I, pg. 23, New Orleans, U.S.A. (1980).
- [66] Jain, K. and Jain, A.K., Rotational bands in deformed odd-A nuclei in the actinide region, *At. Data and Nucl. Data Tables* 50, 269 (1992).
- [67] Jain, A.K., Sheline, R.K., Sood, P.C., Jain, K., Intrinsic states of deformed odd-A nuclei in the mass regions ( $151 \leq A \leq 193$ ) and ( $A \geq 221$ ), *Rev. Mod. Phys.* 62, 393 (1990).
- [68] Jain, A.K., Sheline, R.K., Headly, D., Sood, P.C., Bruke, D., Hrivnoacova, I., Kvasil,



- J., Nosek, D. and Hoff, R.W., Nuclear structure in odd-odd nuclei  $144 \leq 194$ , Rev. Mod. Phys. in press (July 1998).
- [69] Jain, A.K., Dudeja, M., Jain, S.R., Ahmed, Zafar and Malik, S.S., Superdeformed bands as the rigid rotor bands, Proc. of DAE symposium on Nuclear Physics 39B, 74 (1996).
- [70] Jain, A.K., Kvasil, J., Sheline, R.K. and Hoff, R.W., Coriolis coupling in the rotational bands of deformed odd-odd nuclei, Phys. Rev. C90, 432 (1989).
- [71] Jain, K., Jain, A.K., Decoupling from the Particle-Rotor model, Phys. Rev. C30, 2050 (1984).
- [72] Jain, A.K., A new look at the decoupled bands, Proc. of the Int. Conf. on Nuclear Physics, Florence, Italy, (Tipografia- Compositori, Bologna), Vol I, pg. 178 (1983).
- [73] Jennings, B.K., Bhaduri, R.K. and Brack, M., Semiclassical approximation in a one body potential, Phys. Rev. Lett. 34, 228 (1975).
- [74] Joyce, M.J., Sharpey-Schafer, J.F., Riley, M.A. et al.,  $N=7$  unfavoured superdeformed band in  $^{193}\text{Hg}$  coriolis splitting and neutron shell structure at extreme deformation, Phys. Lett. 340B, 150 (1994).
- [75] Kerman, A.K., Rotational perturbation in nuclei- application to Wolfram 183, Dan. Mat. Fys. Medd. 30, No. 15 (1956).
- [76] Khoo, T.P. et al., Excitation energies and spins of a superdeformed band in  $^{194}\text{Hg}$  from one-step discrete decays to the yrast line, Phys. Rev. Lett. 76, 1583 (1996).
- [77] Kota, V.K.B., Phys. Rev. C53, 2550 (1996).
- [78] Lauritsen, T., Janssens, R.V.F., Carpenter, M.P. et al., Dynamic moment of inertia of the  $^{192}\text{Hg}$  superdeformed band at high rotational frequencies, Phys. Lett. 279B, 239 (1992).

- [79] Macchiavelli, A.O., Cederwall, B., Clark, R.M. et al. C-4 symmetry effects in nuclear rotational motion, Phys. Rev. C51, R1 (1995).
- [80] Magner, A.G., Fedotkin, S.N., Ivanyuk, F.A., Meier, P., Brack, M., Reimann, S.M. and Koizumi, H., Semiclassical analysis of shell structure in large prolate cavities, Ann. Physik 6, 555 (1997).
- [81] Meir, P., Brack, M. and Creagh, S.C., Semiclassical description of large multipole-deformed metal clusters, Z. Phys. D41, 281 (1997).
- [82] Mayer, M.G., On the closed shells in nuclei II, Phys. Rev. 75, 1969 (1949).
- [83] Mikhailov, I.N. and Quentin, P., Band staggering in superdeformed states and intrinsic vortical motion, Phys. Rev. Lett. 74, 3336 (1995).
- [84] Neergard, K. and Pashkevich, V.V., Shell corrections to the deformation energies of very high spin nuclei, Phys. Lett. 59B, 218 (1975).
- [85] Nilsson, S.G., Binding states of individual nucleons in strongly deformed nuclei, K. Dan. Vid. Selsk. Mat. Fys. Medd. 29, No. 16 (1955).
- [86] Nolan, P.J., Superdeformation and high spin states, Nucl. Phys. A553, 107C (1993).
- [87] Pavlichenkov, I.M., Nonadiabatic mean field effects in the  $\Delta I = 2$  staggering of superdeformed bands, Phys. Rev. C55, 1275 (1997).
- [88] Pavlichenkov, I.M. and Flibotte, S., C-4 symmetry and bifurcation in superdeformed bands, Phys. Rev. C51, R460 (1995).
- [89] Pavlichenkov, I.M., Bifurcation in quantum rotational spectra, Phys. Reports 226, 173 (1994).
- [90] Pederson, J., Bjorholm, S., Borggreen, J., Hansen, K., Martin, T.P. and Rasmussen, H.D., Observation of quantum supershells in clusters of sodium atoms, Nature 353, 733 (1991).

- [91] Petrache, C.M., Duchené, G., Kharraja, B. et al., Detailed level scheme of  $^{151}\text{Tb}$  and the feeding of the normal deformed states by the superdeformed bands, Nucl.Phys. A579, 285 (1994).
- [92] Piepenberg, R. and Protasov, K.V., Model of superfluid liquid with triplet pairing, cranking model and model of variable moment of inertia in superdeformed bands in  $A=190$  mass region, Z. Phys. A346, 7 (1993).
- [93] Percival, I.C., Semiclassical theory of bound states, Adv. Chem. Phys. 36, 1 (1997).
- [94] Reichi, L.E. and Zheng, W.M., Field-induced barrier penetration in the quartic potential, Phys. Rev. A29, 2186 (1984).
- [95] Reimann, S.M., Persson, M., Lindelof, P.E. and Brack, M., Shell structure of circular quantum dot in weak magnetic fields, Z. Phys. B101, 377 (1996).
- [96] Schuk, C., Hannachi, F., Gall, B. et al., Study of superdeformation in  $^{192}\text{Hg}$  with Eurogam and Gammasphere, Preprint CSNSM-94-15, Paper presented at the XXXII International winter meeting on nuclear physics, Bormio (1994).
- [97] Schutz, Y., Vivien, J., Beck, F.A. et al., Search for collective effects in very high spin states of  $^{152}\text{Dy}$ , Phys. Rev. Lett. 48, 1534 (1982).
- [98] Sheline, R.K., Ragnersson, I. and Nilsson, S.G., Shell structure for deformed nuclear shapes, Phys. Lett. B41, 115 (1972).
- [99] Singh, B., Firestone, R.B. and Frank Chu, S.Y., Table of superdeformed nuclear bands and fission isomers, Nucl. Data Sheets 78, 1 (1996).
- [100] Sood, P.C. and Jain, A.K., Description of multiband structure in  $^{154}\text{Gd}$  on symmetry consideration, Z. Physik A320, 645 (1985).
- [101] Stephens, F.S., Deleplanque, M.A., Draper, J.E. et al., Spin alignment in superdeformed  $\text{Hg}$  nuclei, Phys. Rev. Lett. 64, 2623 (1990).

- [102] Stephens, F.S., Deleplanque, M.A., Macchiavelli, A.O., Diamond, R.M., Fallon, P. and Lee, I.Y. et al., Alignment and pseudospin symmetry, *Phys. Rev. C* 57, R1565 (1998).
- [103] Stutinsky, V.M., Shell effects in nuclear masses and deformation energies, *Nucl. Phys. A* 95, 420 (1967).
- [104] Stutinsky, V.M., Shells in deformed nuclei, *Nucl. Phys. A* 122, 1 (1968).
- [105] Stutinsky, V.M. and Magner, A.G., Trace formula for the systems with continuous symmetries, *Sov. J. Part. Nucl. Phys.* 7, 138 (1976).
- [106] Stutinsky, V.M., Magner, A.G., Ofengenden, S.R. and Dossing, T., Semiclassical interpretation of the gross-shell structure in deformed nuclei, *Z. Phys. A* 283, 269 (1977).
- [107] Sun, Y., Zhang, J. and Guidry, M.  $\Delta I = 4$  bifurcation without explicit four fold symmetry, *Phys. Rev. Lett.* 75, 3398 (1995).
- [108] Svensson, C.E., Baktash, C., Cameron, J.A. et al., Observation and quadrupole-moment measurement of the first superdeformed bands in the  $A \approx 60$  mass region, *Phys. Rev. Lett.* 79, 1233 (1997).
- [109] Toki, H. and Wu, L.,  $\Delta I = 4$  bifurcation in ground bands of even-even nuclei and the interacting boson model, *Phys. Rev. Lett.* 79, 2006 (1997).
- [110] Twin, P.J., Nayko, B.M., Nelson, A.H. et al., Observation of discrete-line superdeformed band up to  $60\hbar$  in  $^{152}\text{Dy}$ , *Phys. Rev. Lett.* 57, 811 (1986).
- [111] Werner, T.R. and Dudek, J., Shape coexistence effects of super- and hyperdeformed configurations in rotating nuclei with  $42 \leq Z \leq 56$  and  $74 \leq Z \leq 92$ , *Atomic Data and Nucl. Data Tables* 59, No.1, 1 (1995).